

Understanding and Controlling the Morphology of Organic Thin Films

by

Jongchan Kim

A dissertation submitted in partial fulfillment
of the requirements for the degree of
Doctor of Philosophy
(Electrical and Computer Engineering)
in the University of Michigan
2021

Doctoral Committee:

Professor Stephen R. Forrest, Chair
Assistant Professor Parag B. Deotare
Professor L. Jay Guo
Professor Max Shtein

“After all, tomorrow is another day.”

— S. O’Hara, *Gone with the Wind*

Jongchan Kim

jongckim@umich.edu

ORCID iD: [0000-0003-3005-9268](https://orcid.org/0000-0003-3005-9268)

© Jongchan Kim 2021

All Rights Reserved

Acknowledgements

Life is an exciting journey since one can interact with numerous inspiring people. Science is no different than life, therefore good science comes from interactions with good people. I was fortunate to meet countless kind, smart and intuitive people who have taught me in various ways, which is an unforgettable memory. While I cannot describe how grateful I feel for all the support I received during my Ph.D., here I try to express my best gratitude in this short text.

The first and foremost appreciation goes to my advisor, Professor Stephen Forrest who showed me how a true researcher should think, act and behave. Throughout the course of my Ph.D., he has been the person who challenged my capability by letting me think outside the box, and guided me in how to approach scientific problems. He always asks, “*so what did you learn from this?*” which I personally think is the best question showing the attitude of how a good researcher should approach every experiment without being biased. In addition, his unparalleled trust and perseverance with students let a student mature into an independent scientist. Furthermore, he is a great life mentor, giving students lessons much more than solely transferring knowledge. In short, he is a role model of an ideal advisor and I appreciate every moment working with him.

I am also grateful for the support and guidance from my mentors and colleagues. My great mentors, Jaesang, Yue and Caleb, guided me through the knowledge of OLEDs, Xiao and Panda taught me everything about optics, Kyusang, Byungjun and Dejiu taught me how to fabricate in the clean room. I also appreciate the assistance on projects, Shaocong who enabled me to work with Fourier optics, Haonan who gave me insights in the optical modeling, Siwei who endeavored

to assist me in making hybrid LEDs, Xiaheng who worked on 2D materials together with me and Kan who gave me physical insights through many discussions. I also appreciate Quinn and Yongxi, for imparting knowledge of OPVs and thank Claire, Boning, Changyeong and Haonan for maintaining the tools together. I was also fortunate to have great collaborators outside the campus, Peter, Thilini, Moon Chul, Daniel, Jie, John and Professor Thompson at the University of Southern California, Julie, and Mike at Universal Display Corp., Professor Vinod Menon's group at City University of New York, and Professor Mohammad Omary at the University of Northern Texas.

I am also grateful for the people who gave me a lot of good memories during my Ph.D. Eva, our group mom, has given me and our group members countless support for every difficulty we encountered, and I thank all the past and present group members, Michael, Kevin, Xin, Amy, Joosung, Charles, Olga, Ardavan, Qi, Lise, John, Hafiz, Xinjing, Jeffrey, Rebecca, Joon and many others. I would also like to acknowledge numerous support from the technical staffs, Pilar, Dennis, Sandrine from the Lurie Nano Fab, and Sean from Angstrom engineering who taught and assisted me every time I had trouble with the apparatus. I also give special thanks to all my friends outside the group, who gave me various life experiences beyond research.

Above all, I would like to appreciate my parents and family who have given me constant trust, support, care, and love. Their support and love enabled me to keep going every day, therefore this thesis would not have been done without them.

Jongchan Kim

Ann Arbor, MI,

April, 2021

Table of Contents

Acknowledgements	ii
List of Tables	viii
List of Figures	ix
List of Appendices	xiii
List of Abbreviations	xiv
Abstract	xvi
Chapter 1 Introduction to Organic Semiconductors	1
1.1 Organic semiconductors	1
1.1.1 Defining organic semiconductors	1
1.1.2 Types of organic semiconductors	6
1.2 Fabrication process	9
1.2.1 Vacuum thermal evaporation	9
1.2.2 Organic vapor phase deposition	10
1.2.3 Organic vapor jet printing	12
Chapter 2 Organic Small Molecules	14
2.1 Polarons and excitons	14
2.2 Singlet and triplet excitons	17
2.3 Energy transfer	20
2.4 Charge transport	24
2.5 Fluorescence and phosphorescence	27
2.6 Types of ligands in heavy-metal phosphorescent complexes	29
Chapter 3 Bulk Organic Film and Morphology	31
3.1 Bonds of organic film	31

3.1.1 Covalent bonds	32
3.1.2 Van der Waals bonds	37
3.2 Morphology of small molecule organics	40
3.2.1 Static and transition dipole moments	41
3.2.2 π - π interactions	42
3.2.3 Molecular alignment	44
3.2.3.1 Measurements of molecular alignment	44
3.2.3.2 Control of molecular alignment	47
3.2.4 Crystallinity	53
3.3 Impact of organic thin film morphology	54
3.3.1 Electrical aspect	54
3.3.2 Optical aspect	55
Chapter 4 Organic Light Emitting Devices	58
4.1 Device structure and operating principle of OLEDs	58
4.2 OLED benchmarks	61
4.2.1 Colorimetry	61
4.2.2 Performance parameters	65
4.3 Optics of OLEDs	67
4.3.1 Optical loss channels	67
4.3.2 In-plane wavevector	68
4.3.3 Mode analysis for waveguide and SPP modes	69
4.3.3 TDM orientation and optical power loss	73
Chapter 5 Using Fourier Plane Imaging Microscopy for Determining Transition Dipole Moment Orientations in Organic Light Emitting Devices	76
5.1 Introduction	76
5.2 Theory of the optical model for analysis	77
5.3 Experimental methods	83
5.4 Impact of TDM alignment on OLED performance	85
5.5 Conclusion	89
Chapter 6 Nanoscale Morphological Mapping of Organic Thin Films	91
6.1 Introduction	91
6.2 Experimental Methods	92
6.2.1 Sample preparation	92

6.2.2 Optical measurement	93
6.2.3 Optical simulation	93
6.2.4 X-ray diffraction measurements	94
6.3 Concept of using morphological sensing layer with Fourier imaging microscope	94
6.4 Use of morphological sensing layers for single layer systems.....	97
6.5 Criteria of optimum molecules for morphological sensing layers	99
6.6 Use of morphological sensing layers for multilayer systems.....	102
6.7 Merits of the technique.....	105
6.8 θ_{hor} conversion of PtOEP	107
6.9 Error analysis.....	109
6.9.1 Surface Roughness Errors	109
6.9.2 Fitting errors	111
6.9.3 Density analysis.....	111
6.9.4 Depth of field.....	112
6.10 Conclusion.....	112
Chapter 7 Systematic Control of the Orientation of Organic Phosphorescent Pt Complexes in Thin Films for Increased Optical Outcoupling	114
7.1 Introduction	115
7.2 Experimental methods.....	116
7.2.1 Sample preparation.....	116
7.2.2 Optical measurements	117
7.2.3 X-ray diffraction measurements	117
7.2.4 Single crystal structure determination	118
7.2.5 DFT calculations of TDM and molecular orbitals	118
7.3 Morphological control via modifying the molecular structure	119
7.4 Morphological control via structural templating.....	121
7.5 How interaction of ligands determines the orientation of Pt complex	128
7.6 Theory for vertical orientation of Pt complexes.....	130
7.7 Structural analysis of PtD film	131
7.8 Structural templating of PtD film with varied crystallinity.....	133
7.9 Controlling the TDM orientation of a mixed emissive layer film.....	136
7.10 Conclusion.....	137
Chapter 8 Large Area Organic-Transition Metal Dichalcogenide Hybrid Light Emitting Device	139

8.1 Introduction	139
8.2 Experimental methods.....	140
8.2.1 Device fabrication	140
8.2.2 Dry transfer process.....	141
8.2.3 Device characterization	142
8.2.4 Electron- and hole-only device photoluminescence spectral fitting.....	142
8.2.5 Exciton formation analysis	142
8.3 LED fabrication and testing	144
8.4 Device structure design concept.....	149
8.5 Cause of limited external quantum efficiency.....	150
8.6 Trion emission in device spectrum.....	150
8.7 Conclusion.....	152
Chapter 9 Summary and Outlook	153
Appendix	156
Bibliography	170

List of Tables

Table 1.1 Comparison of properties between inorganic and organic semiconductors.....	3
Table 3.1 Ir complexes used for alignment studies.....	50
Table 7.1 Thin film morphology of CzSi films doped with PtD.....	127
Table 7.2 Summarized results in Fig. 7.14.....	132
Table 7.3 Structural and emission data of reference Pt complexes.....	133
Table 7.4 Measured results in Fig. 7.16.	135
Table B.1 Modal power distribution of scattering and specular (metal) reflector substrates. ...	164

List of Figures

Figure 1.1 Energy diagram of inorganic semiconductors.	4
Figure 1.2 Comparison of energy diagrams.	5
Figure 1.3 Two types of organic molecules.	7
Figure 1.4 Molecular structure of Anthracene, a typical aromatic molecule.	7
Figure 1.5 A schematic of a vacuum thermal evaporation chamber.	10
Figure 1.6 Schematic of an organic vapor phase deposition chamber.	11
Figure 1.7 A schematic of an organic vapor jet printing chamber.	13
Figure 2.1 Illustration of the different types of excitons.	15
Figure 2.2 Energy diagram of dimer vs. excimer.	17
Figure 2.3 Illustration for the concept of singlet and triplet states.	19
Figure 2.4 Jablonski diagram.	20
Figure 2.5 Types of energy transfers according to the interaction distances	21
Figure 2.6 Exchange energy transfer between neighboring molecules	23
Figure 2.7 Energy level diagram of the band and hopping transport.	24
Figure 2.8 Marcus charge transfer	26
Figure 2.9 Illustration of Marcus charge transfer with different free energies (ΔG^0).	27
Figure 3.1 Diagram showing the potential energy of two separate hydrogen atoms.	32
Figure 3.2 Examples of sigma bonds with various types of overlap between different orbitals.	33
Figure 3.3 Schematic of two p-orbitals forming a π -bond.	34
Figure 3.4 Schematic explaining the coordinate bond.	35
Figure 3.5 Electron distribution within a polar molecule.	35
Figure 3.6 The periodic table with electronegativity values.	36
Figure 3.7 Different types of van der Waals bonding between two Arene moieties.	38
Figure 3.8 Electrostatic interaction of two ideal aromatic molecules with π -electrons with different orientation.	43

Figure 3.9 Cross-sectional illustration of the set up for angle dependent photoluminescence spectroscopy.....	44
Figure 3.10 Angle dependent photoluminescence spectra with and without the half-glass cylinder.	45
Figure 3.11 Angle dependent photoluminescence spectra of varied θ_{hor}	46
Figure 3.12 General relationship between the molecular shape and orientation.	48
Figure 3.13 Molecular structures and their TDM orientation used in the experiment.....	49
Figure 3.14 Calculated outcoupling efficiency and measured EQE for the three TADF molecules of varied molecular lengths.....	49
Figure 3.15 DFT calculation for the molecules used in the alignment studies.....	51
Figure 3.16 Ir-complexes used for the organic surface-ligand interaction experiment.	52
Figure 3.17 Measured orientation of the Ir-complexes.....	53
Figure 3.18 Measured exciton diffusion length.	54
Figure 3.19 Influence of morphology on the electrical performance	55
Figure 3.20 Emission profile from varied orientations of TDMs	56
Figure 4.1 Schematic illustration of the OLED structure and its energy levels.....	59
Figure 4.2 Approaches to obtain white light from OLED EMLs.	61
Figure 4.3 An eye retina covered with light-sensitive rod and cone cells.	62
Figure 4.4 Luminous efficacy curves for human vision.	63
Figure 4.5 CIE color matching function and CIE 1931 color space chromaticity diagram.....	64
Figure 4.6 PLQY vs. dopant concentration.....	67
Figure 4.7 Optical loss channels in OLEDs and their power distribution.	67
Figure 4.8 In-plane wavevectors in OLEDs.....	69
Figure 4.9 Waveguide modes.....	71
Figure 4.10 Surface plasmon polariton modes.....	72
Figure 4.11 Dipole field coupling with the SPP mode in the near-field regime.....	73
Figure 4.12 Modal power distribution of different TDMs.....	74
Figure 4.13 Modal power distribution of different TDMs.....	75
Figure 4.14 Varied light trapping with TDM orientation	75
Figure 5.1 Illustrations for understanding Fourier plane imaging microscopy.....	77
Figure 5.2 FIM results from the three dopants.....	85
Figure 5.3 Transition dipole orientation measurement in a birefringent host matrix.	86
Figure 5.4 Performance of OLEDs with the three dopant emitting molecules in Fig. 5.2.	87

Figure 5.5 Measurement evaluation.....	88
Figure 6.1 The morphological sensing layer concept.	94
Figure 6.2 Morphology investigation of a 30 nm thick CBP film.	97
Figure 6.3 Imaging the morphology of a bilayer thin film.	102
Figure 6.4 Mapping of the structure of a crystalline grain.....	103
Figure 6.5 Dendritic growth of CBP on TPBi with annealing.....	104
Figure 6.6 Morphological investigation of Tint film via PtOEP MSL.	107
Figure 6.7 TDM within the PtOEP molecule.....	107
Figure 6.8 θ_{hor} conversion of PtOEP.....	108
Figure 6.9 Correlation between θ_{hor} of PtOEP vs. various values.	109
Figure 6.10 Rough surface errors.....	109
Figure 6.11 Surface scanning for rough surface errors.....	110
Figure 6.12 Fitting errors.	111
Figure 7.1 Controlling molecular orientation in light emitting layers.	115
Figure 7.2 Orientation analysis of (dbx)Pt(dpm).	119
Figure 7.3 Orientation analysis of Pt complex dopants.	120
Figure 7.4 Photoluminescence spectra of films of Pt complexes doped into CBP.....	121
Figure 7.5 Photophysical and structural characteristics of neat films of PtD and PtOEP doped Tint.	122
Figure 7.6 Control of the PtD TDM via templating.....	123
Figure 7.7 Measured single crystal structure and cell parameters of PtD and Tint based on single crystal XRD.	124
Figure 7.8 Measuring the birefringence of a neat NTCDA film via refractive index.....	124
Figure 7.9 Bragg-Brentano x-ray diffraction pattern of the PtD film on different substrates. ..	125
Figure 7.10 Relation between crystallinity and structural templating.	126
Figure 7.11 Refractive index measurement for neat CzSi film.....	127
Figure 7.12 Control of the PtOEP:Tint TDM via templating.	127
Figure 7.13 Calculated electrostatic potential surface of a (dpm)Pt(dbx) molecule via DFT geometry optimization.	130
Figure 7.14 DFT calculation for PtD.	132
Figure 7.15 Spectrum vs. doping concentration of PtD in CzSi.....	133
Figure 7.16 Time resolved photoluminescence of CzSi:PtD by varied doping concentration..	135
Figure 8.1 Schematic illustration of the monolayer WS ₂ dry transfer procedure.	141

Figure 8.2 Calculated outcoupling efficiency of the sensing layers at various positions in the emissive layer.....	143
Figure 8.3 Device structure of the hybrid 2D-organic LED.	144
Figure 8.4 The TDM orientation of monolayer WS ₂ in a CBP host matrix.	144
Figure 8.5 Calculated distribution of the modal power distribution vs. average TDM orientation.	145
Figure 8.6 Exciton density profiles in the EML.....	146
Figure 8.7 Performance characteristics of the hybrid LED.	147
Figure 8.8 Photoluminescence of monolayer WS ₂ embedded in single-charge device.	148
Figure 8.9 J-V characteristics of mWS ₂ in the electron- and hole- only-device.....	149
Figure B.1 Schematic illustration of the PHOLED on a diffuse reflector.	159
Figure B.2 Reflectance and outcoupling efficiency of the diffuser.	161
Figure B.3 Modal power distribution vs. in-plane wave vector for various waveguide layer refractive indices.	162
Figure B.4 Characteristics of PHOLEDs fabricated on metal mirror and diffuse reflector substrates.....	162
Figure B.5 Radiant power intensity profile for PHOLEDs on diffuse reflector and Al mirror substrates.....	165
Figure B.6 Simulated fraction of light outcoupled from the light diffusing substrate vs. the size of the OLED.	166
Figure B.7 Emission profile of the white PHOLED on the diffuser.....	167
Figure B.8 Modal power distribution evolution with number of reflections.	168

List of Appendices

A. List of Chemicals	156
B. Efficient outcoupling of organic light emitting devices using a light scattering dielectric layer	158

List of Abbreviations

Angle PL angle dependent photoluminescence spectroscopy

AFM atomic force microscopy

CCD charge coupled device

CT charge transfer

CVD chemical-vapor-deposition

DFT density functional theory

EQE external quantum efficiency

EBL electron blocking layer

EIL electron injection layer

EML emissive layer

EOD electron-only device

ETL electron transport layer

FIM Fourier plane imaging microscopy

FMM fine metal mask

FRET Förster (or fluorescent) resonant energy transfer

GIWAXD grazing incidence wide angle x-ray diffraction

HIL hole injection layer

HTL hole transport layer

HBL hole blocking layer

HOD hole-only device

HOMO highest occupied molecular orbital

LED light emitting device

L_D diffusion length

LUMO lowest unoccupied molecular orbitals

OLED organic light emitting devices

OPV organic photovoltaics

OVPD organic vapor phase deposition
OVJP organic vapor jet printing
PLQY photoluminescence quantum yield
pPP p-polarized plane
PHOLED phosphorescent OLED
PL photoluminescence
SOC spin-orbit coupling
sPP s-polarized plane
SPP surface plasmon polariton
TADF thermally activated delayed fluorescent
TD-DFT Time-dependent density functional theory
TDM transition dipole moment
TE transverse electric
TIR total internal reflection
 T_g glass transition temperature
TM transverse magnetic
TMDC transition metal dichalcogenide
TRA transmission, reflection and absorption
vdW van der Waals
VTE Vacuum thermal evaporation
VASE variable angle spectral ellipsometry
XRD X-ray diffraction
ZORA zero order regular approximation

Abstract

Display panels today open the door to the repository of knowledge, and their use is expanding from conventional home appliances to transparent, wearable and mobile devices. Organic semiconductors are a perfect candidate for this ubiquitous use of display panels since organics are flexible, transparent with high brightness and capable of good color rendering. The expanding outdoor use of organic devices poses questions whether: i) the devices are bright enough to be visible under daylight, and ii) the devices can withstand extreme conditions such as the interior of an automobile in the summer. Organic light emitting devices (OLEDs) achieved ~100% internal quantum efficiency with phosphorescence in 1998 [1], and since then the bottle neck for OLED brightness has been the outcoupling efficiency. The capability of organics to withstand severe conditions is closely related to their morphological stability. Thus, improving the outcoupling efficiency and controlling the morphology of OLEDs are the two crucial aspects in the future display technology. In this sense, this thesis mainly deals with the methods to improve the light outcoupling of OLEDs by morphological control. Also, methods for understanding organic film morphology are discussed.

In this thesis, we demonstrate a measurement technology to obtain precise nanoscale information about the morphologies of several organic thin film structures using Fourier plane imaging microscopy (FIM). We use FIM to detect the orientation of molecular transition dipole moments from an extremely low density (i.e. small fractions of a monolayer) of luminescent dye

molecules, which we call “morphology sensors.” The orientation of the sensor molecules is driven by the local film structure, and thus can be used to determine details of the host morphology without influencing it. We use symmetric planar phosphorescent dye molecules as the sensors that are deposited into the bulk of organic film hosts during the growth. Furthermore, we monitor morphological changes arising from thermal annealing of metastable organic films that are commonly employed in photonic devices.

Methods to control the organic film morphology to improve the light outcoupling are also demonstrated. Here we control the orientation of Pt complex molecules during the growth of emissive layers by two different methods: modifying the molecular structure, and using structural templating. Pt complex dopant molecules whose structures are modified by adjusting the ligands show an approximately 20% increased fraction of horizontally aligned transition dipole moments compared to the original molecule while being diluted in the host matrix. Alternatively, we pre-deposit a highly ordered structural template layer, which results in a 60% increase in horizontally aligned transition dipole moments compared to the film deposited in the absence of the template.

Finally, we employ a 2-dimensional transition metal dichalcogenides as the active luminescent layer due to its optimum emission profile for efficient outcoupling. Therefore, a hybrid light emitting device (LED) is fabricated employing a chemical-vapor-deposition grown, centimeter-scale monolayer of WS₂ (mWS₂), embedded within conductive organic layers. As a result, LEDs with an average external quantum efficiency of $0.3 \pm 0.3\%$ and with the highest efficiency of 1% were achieved. Also, we show that negatively charged excitons, also known as trions, are generated in the mWS₂ with the injected current, causing an efficiency roll-off at high current densities.

Chapter 1 Introduction to Organic Semiconductors

Organic semiconductors have features that have been difficult to realize with inorganic semiconductors, such as flexible films or film deposition on any substrate, while demonstrating efficient emission or absorption of light. These distinct properties stem from the material characteristics of organic semiconductors. In this chapter we discuss the fundamental properties of organic semiconductors with their physical origins. Then, the deposition techniques of organic films used for the device fabrication are introduced.

1.1 Organic semiconductors

1.1.1 Defining organic semiconductors

Organic materials are chemical compounds containing one or more carbon-hydrogen bonds. The particular focus of this thesis on organic materials is put in the category of *organic semiconductors*, which conduct current with moderate energy gaps of $\sim 0.5\text{-}3$ eV. These materials differ from the conventional semiconductors, which are often called *inorganic semiconductors*, in terms of electrical, optical and morphological characters.

Inorganic semiconductors are comprised of highly ordered crystallites built up with single or multiple types of atoms. The latter is also known as a compound semiconductor, with an example of GaN, which is an essential material used in numerous areas such as high-power, high-speed-switching and light-emitting device industries today. An example of a single-atom inorganic

semiconductor is Si, which is the most common material for all semiconductor business today due to its abundance and high-quality processing technology. Inorganic semiconductors have strong covalent bonds between the atoms, which is the reason for their physical characteristics which include brittleness, stiffness and a high melting temperature ($> 1000^{\circ}\text{C}$), only a few exceptions such as HgCdTe [2].

Organic semiconductors exhibit different features compared to inorganic semiconductors. The key difference between organic and inorganic semiconductors stems from the building blocks and the bonds between them. The building block of organic films is an organic molecular compound or polymer, which is an electrically neutral group comprising several C and H atoms held together by covalent bonds. Due to carbon's ability to catenate, meaning that it forms chains with other carbons, millions of organic compounds have been identified and synthesized so far with still an infinite amount of room left to be explored. The cohesive force that combines the building blocks of organic film is mainly van der Waals bonds, a relatively weak bond compared to a covalent or ionic bond. The different building blocks and bonds which cause vastly different material properties between organic and inorganic semiconductors will be discussed with a summary in Table 1.1.

Table 1.1 Comparison of properties between inorganic and organic semiconductors. (Adapted from Forrest, *Organic Electronics*, 2020)

Property	Organics	Inorganics
Bond type	van der Waals	Covalent/ionic
Intermolecular bond Energy	0.1 eV	1–5 eV
Energy band width	0.01–0.5 eV	1–4 eV
Charge transport	Polaron hopping	Band transport
Charge mobility	$\leq 1 \text{ cm}^2/\text{V s}$	$\sim 1000 \text{ cm}^2/\text{V s}$
Conduction levels	Frontier orbitals	Bands
Dielectric constant (Refractive index)	2–3 (1.5–2)	10–15 (3–5)
Peak absorption (Oscillator strength)	$10^5\text{--}10^6 \text{ cm}^{-1}$ (High)	$10^3\text{--}10^4 \text{ cm}^{-1}$ (Low)
Exciton species	Frenkel	Wannier–Mott
Exciton binding energy	$\sim 500\text{--}1000 \text{ meV}$	$\sim 5\text{--}10 \text{ meV}$
Exciton radius	$\sim 10 \text{ \AA}$	$\sim 100 \text{ \AA}$
Hardness	Soft	Hard
Flexibility	Flexible	Brittle

Hardness and flexibility

Bond strength is an important element determining the rigidity of the material. Inorganic solids are combined with strong chemical bonds with a dissociation energy of $\sim 1\text{--}5 \text{ eV}$, which is at least an order of magnitude higher than organic compounds combined with van der Waals bonds. Therefore, unlike the hard, brittle inorganic materials, organic films tend to be soft and elastic, enabling their use for flexible and rollable devices. Also, the smaller intermolecular binding energy of organic compounds leads to a relatively low evaporation temperature ($\sim 100\text{--}500^\circ\text{C}$). However, the decomposition of the organic compounds usually happens at a much higher temperature due to the strong covalent bonds.

The flexible character of organic thin films is also related to their morphology. Unlike highly crystalline inorganic semiconductors, the majority of organic films are amorphous. Therefore, organic films are less brittle but more flexible compared to the film comprising inorganic semiconductors. Due to the amorphous film structure of organic films, their

morphological stability is often exhibited by the glass transition temperature (T_g), which is the temperature when a gradual and reversible transition from a hard and relatively brittle state into a viscous or rubbery state occurs at an elevated temperature. More details about organic film morphology are discussed in Chapter 3.

Frontier Energy levels

Electrons in an atom occupy discrete energy levels as shown in Fig. 1.1a. When two atoms are in close proximity, the energy level of each orbital splits into two different levels, according to the Pauli Exclusion Principle. As the number of atoms approaches infinity, forming a single crystal, the interval between the discrete energy levels becomes negligible, forming a continuous ‘energy band’ as shown in Fig. 1.1b. Thus, the energy band is a continuum of a large number of energy states. Electrons within the crystal fill the band from the lowest energy state, with the top, nearly filled band called the valence band and the lowest nearly empty band called the conduction band. The energy difference between the conduction and valence band edge is called the band gap.

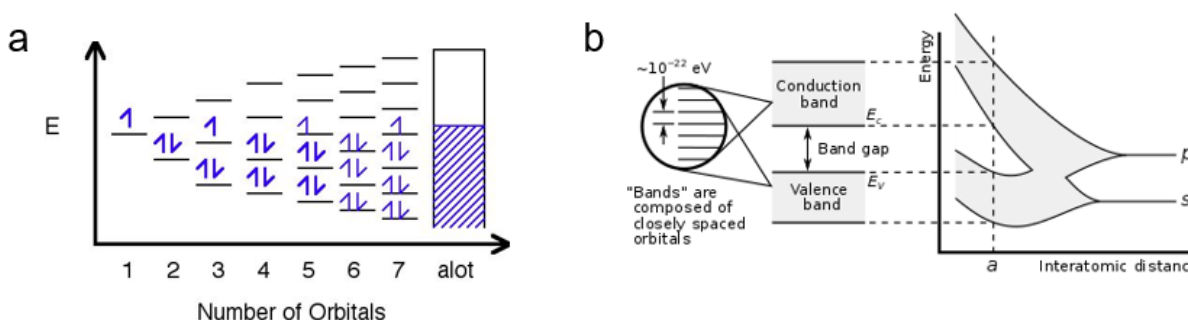


Figure 1.1 Energy diagram of inorganic semiconductors.

(a) Energy diagram of atomic frontier energies as a function of number of orbitals. The energy levels eventually form energy bands for a large number of atoms. (b) Energy band diagram for inorganic semiconductors.

On the other hand, organic molecules are comprised of a limited number of atoms. Thus rather than forming a band, the highest and lowest frontier molecular electronic orbitals are typically identified as shown in Fig. 1.2. The highest occupied molecular orbital (HOMO) is filled

with the most energetic electrons within the molecular π -conjugate system, which is similar to the valence band edge in inorganic single crystals. Electrons in the lowest unoccupied molecular orbitals (LUMO) comprise the least energetic conduction states, which is similar to the conduction band edge in inorganic crystals. The energy level of a molecule is found via density functional theory (DFT), which calculates electron distributions in relatively small molecular ensembles. The energy levels are measured with cyclic voltammetry as well as ultraviolet photoelectron spectroscopy (for HOMO) and inverse photoelectron spectroscopy (for LUMO).

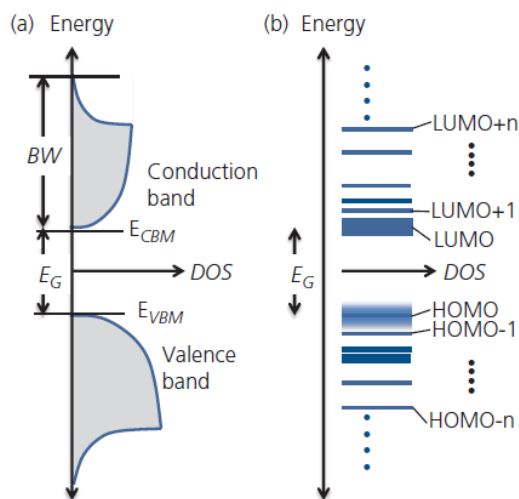


Figure 1.2 Comparison of energy diagrams. Energy diagram of inorganic (a) and organic (b) semiconductors (Adapted from Forrest, *Organic Electronics*, 2020).

Charge transport

Crystalline and molecular solids exhibit vastly different charge transport phenomena. Within atomic single crystalline solids, electronic wavefunctions are delocalized over the entire volume, thus showing ballistic transport, also known as band transport. As a result, the mean free path is larger than the inter-atomic distance (< 1 nm) and shows relatively high mobility, typically larger than $1 \text{ cm}^2/\text{V}\cdot\text{sec}$. The charge transport decreases with temperature since nuclear scattering prevents ballistic transport and reduces the electron speed.

In molecular solids, on the other hand, the charge transport is intermolecular, which is also known as hopping transport. This mostly appears in disordered solids such as amorphous or polycrystalline (at grain boundaries) semiconductors. Since the wavefunction overlap is small, the charge transport in organic film is not ballistic, thus electrons tunnel through the potential barriers, causing much lower charge mobility (typically less than $0.01 \text{ cm}^2/\text{V}\cdot\text{sec}$) compared to crystalline inorganic semiconductors. The mechanism of charge transport in organic molecules is discussed in more detail in Chapter 2.4.

1.1.2 Types of organic semiconductors

Small molecule vs. polymer organic

Organic materials are usually classified into small molecules and polymers. Small molecules are organic compounds with a well-defined molecular weight as shown in Fig. 1.3a. These are also referred to as monomers. On the other hand, polymers are long-chain compounds with an indeterminate number of molecular units being repeated as shown in Fig. 1.3b. Due to the structural differences, small molecules and polymers exhibit different physical characters. One of the important differences is the higher boiling point of polymers due to their entangled long chains which prevents them from being evaporated in vacuum chambers as can occur with small molecule organic materials. This difference causes the two materials to be deposited in different ways, which will be discussed in Chapter 1.2.

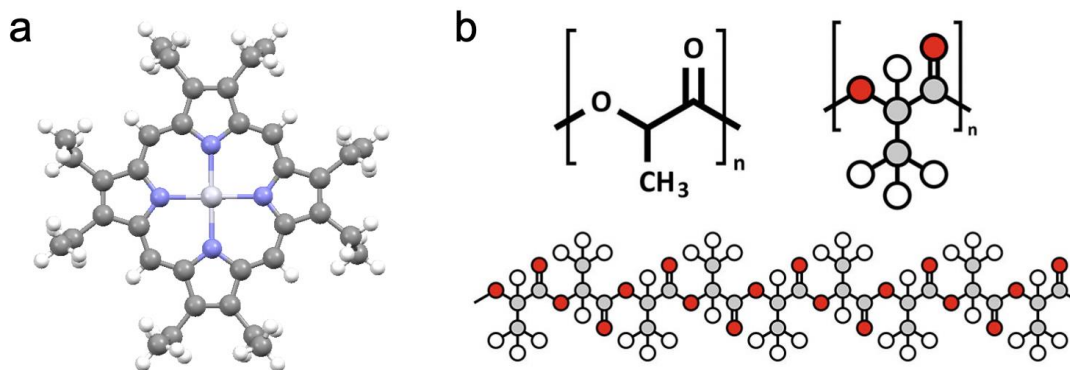


Figure 1.3 Two types of organic molecules.

(a) Small molecules represented by a monomer of octaethylporphyrin-Pt (III) (PtOEP) with a “ball and stick” style. The metal (Pt) atom is shown in light grey sphere at the center, N atoms are shown in light purple, N atoms are shown in grey, and H atoms are shown in white spheres. (b) Polymeric materials, represented by polylactic acid (PLA), which is used in various places from food packing to medical implants. Polylactic acid is formed from building blocks comprising C, O and H atoms (top left and right). That building block, called a monomer, repeats over and over to form a long chain (bottom).

Aromatic vs. aliphatic compounds

Covalent bonds are formed when two or more nuclei share the valence electrons to form lower energy states. Covalent bonds include different bonds such as sigma (σ) and pi (π) bonding. Sigma (σ) bonds are the strong type of covalent bonds, with shared electrons localized between the two atoms. Pi (π) bonds are weaker compared to the sigma bonds due to a reduced overlap of orbitals. More details about the bonds will be discussed in Chapter 3.1.

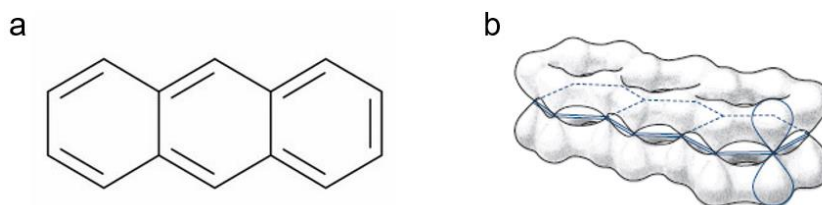


Figure 1.4 Molecular structure of Anthracene, a typical aromatic molecule.

(a) Chemical formula of Anthracene. (b) Anthracene viewed from the molecular plane with the electron cloud showing the conjugated π -electron system (Adapted from Forrest, *Organic Electronics*, 2020).

When consecutive π bonds are continuously linked within a molecule, a delocalized chain of shared electrons is formed, known as a conjugated π -system. Especially, molecules with cyclic

(ring-shaped), planar structures with π bonds in resonance are referred as aromatic molecules. They are called aromatic molecules due to the strong odors associated with them. Aromatic rings are stable and do not break apart easily. The most common aromatic compounds are derivatives of benzenes. Due to the delocalized conjugated pi-system, aromatic compounds are frequently used as organic semiconductors.

Non-aromatic compounds are called aliphatic compounds. Aliphatic compounds also can be cyclical, however, the cyclic aliphatic compounds do not obey Hückel's rule and, thus, do not exhibit aromatic properties. Hückel's rule estimates whether a planar ring molecule would have aromatic properties, requiring the number of π -electrons to be $4n+2$, where n is a non-negative integer. Saturated aliphatic hydrocarbons, which consist entirely of single bonds, are called alkanes, which are described by the formula C_nH_{2n+2} . Unsaturated aliphatic compounds are referred to as alkene (C_nH_{2n}) or alkyne (C_nH_{2n-2}), depending on their formulas.

Fluorescent vs. phosphorescent compounds

Fluorescence is an emission of light by a substance that has absorbed light or is electrically excited. The light emission has a lower energy (longer wavelength) than the absorbed radiation due to the thermal relaxation during the emission. Fluorescence only occurs from spin-conserving transitions, therefore limits the overall emission efficacy when electrically excited. In contrast, phosphorescence is emission associated with the spin-forbidden transition which overcomes the emission efficacy limit of fluorescence. The differences between fluorescent and phosphorescent molecules will be discussed more in detail in Chapter 2.5.

1.2 Fabrication process

1.2.1 Vacuum thermal evaporation

Vacuum thermal evaporation (VTE) is the most commonly used processing technique for organic film growths so far. The apparatus is comprised of a vacuum chamber, substrate holder, crucible, and pump as shown in Fig. 1.5. The materials to be evaporated are placed in the crucible, and then the chamber is pumped down to vacuum. The pressure of the chamber is maintained below 10^{-6} torr to enable a ballistic transfer of the sublimed molecule and preventing it from being scattered by the background gas molecules. The use of vacuum provides flexibility in choosing materials, unlike solution processing where the solvent of the material being deposited has a chance to chemically attack the predeposited films. The VTE process is capable of handling a sequential growth of films and co-evaporation is possible by evaporating multiple materials at the same time. The rate and thickness of the film growth are monitored by a quartz crystal monitor, which measures the varied vibration frequency of the quartz due to the material deposited on the crystal. The substrate holder rotates during the deposition to enable a uniform film thickness, and sometimes the substrate temperature is controlled via the stage heater/cooler with a feedback thermal controller. This heating/cooling of the substrate helps controlling the morphology of the film since it promotes/prevents molecular kinetic movement during the condensation of the organic vapor on the substrate.

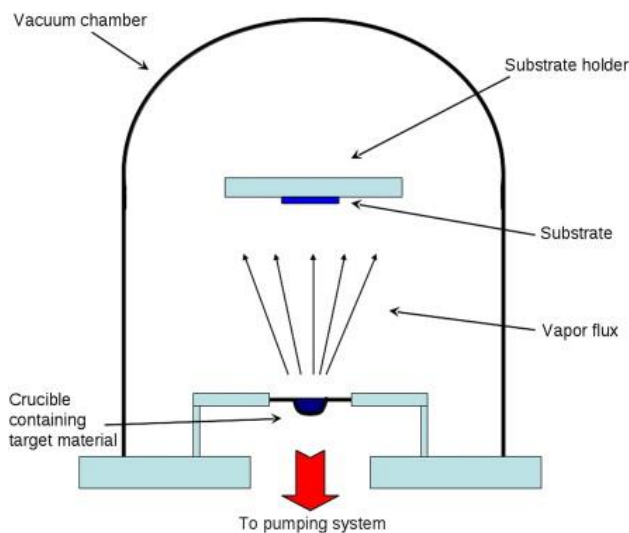


Figure 1.5 A schematic of a vacuum thermal evaporation chamber.
 (Adapted from R. J. Martín-Palma, et al., chap. 15, *Engineered Biomimicry*, 2013).

Albeit VTE offers a number of advantages, there are also several shortcomings of the process. The most critical drawback is the low material usage efficiency. This is because much of the evaporated material is wasted by being deposited outside the substrate. Also, VTE is not capable of depositing polymers. This is because the carbon chains of polymers are so severely entangled, which causes a break of the backbone before the evaporation is enabled. Thus, most polymers are diluted in solvents and spin-coated on the substrate. In addition, achieving a uniform deposition rate is limited due to the thermally insulating organic materials in the crucible where, during heating, only the organic materials in contact with the most intensely heated region is evaporated, which causes a fluctuation of rates when the organics in the region are exhausted.

1.2.2 Organic vapor phase deposition

To overcome the shortcomings of the VTE, organic vapor phase deposition (OVPD), a method using an inert carrier gas such as N_2 or Ar was introduced [3,4]. This technique uses a chamber with heated walls, and flows a hot carrier gas to evaporate the organic material. In an OVPD chamber, no materials are deposited on the walls due to its high temperature and the

substrate zone is kept cool to induce deposition as shown in Fig. 1.6. Due to the cold substrate temperature, organic vapor condenses on the substrate and coats the surface uniformly.

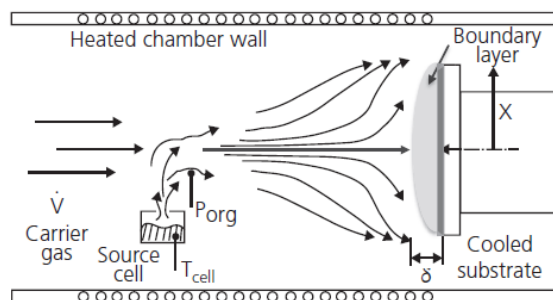


Figure 1.6 Schematic of an organic vapor phase deposition chamber. (Adapted from Shtein, et al., 2001)

The pressure within the chamber usually ranges from 10s of mtorr to several torr. The base pressure of the pump (typically a roughing pump) is around 10^{-3} torr, meaning that the chamber is filled with the carrier gas. This is the starkest difference of OVPD from other vacuum based deposition techniques, which enables a uniform evaporation of organic material in the crucible since the organic material surface is uniformly heated in an equilibrium environment with the hot carrier gas (at low gas flow rate). In addition, with OVPD, deposition occurs with a uniform coating of the substrate surface when it is at the equilibrium state regardless of the substrate position and shape, unlike VTE where the thickness profile is dependent on the relative position of the evaporation source and the substrate.

Also, OVPD has a number of levers affecting the organic film morphology, such as the pressure of the chamber, flow rate of the source carrier gas, temperature of the carrier gas. An optimized morphology utilizing these elements of OVPD has been thoroughly demonstrated for various organic electronic devices, since the morphology acts a critical role in its performance. Also, due to its high material usage with numerous control methods, OVPD can achieve an

extraordinarily fast growth of organic devices, capable to be utilized for roll-to-roll deposition schemes, enabling a lower cost of production for a commercialized use [5].

1.2.3 Organic vapor jet printing

The pixel size of OLEDs in cutting-edge smart phones measure at several tens of micrometers, and are patterned with a metal shadow mask. While shadow masking is a simple and effective method to pattern the current displays, it has a serious limit in reducing the pixel size due to a shadowing effect. Also, as the pattern size decreases, the region deposited via material spreading beneath the mask becomes a larger fraction of the total device area. To resolve this problem, an ultra-thin fine metal mask (FMM) with a thickness of 30-200 μm is utilized. However, the use of an ultra-thin mask causes other difficulties in substrate handling, such as mask sagging during a large-scale deposition.

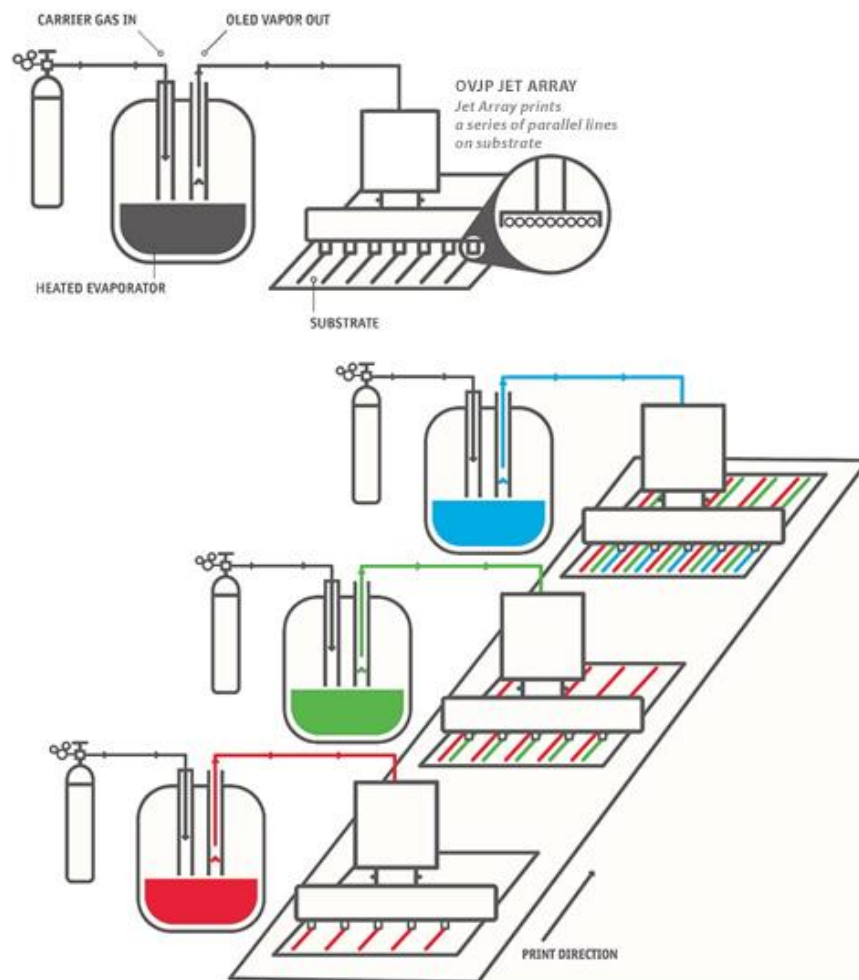


Figure 1.7 A schematic of an organic vapor jet printing chamber.
 (Adapted from Universal Display Corporation, UNIVERSAL OVJP®)

Organic vapor jet printing (OVJP) is a method proposed to solve the patterning issue. It is a solvent-less deposition, which does not require shadow masks for depositing organic materials. OVJP uses a microscopic nozzle to focus the hot carrier gas, which carries the source organic material as in the OVPD, onto the substrate. The deposition profile is controlled by different conditions, such as the gas jet profile and substrate temperature [6,7]. Therefore, OVJP is a technology that can liberate the organic deposition from any patterning issue, enabling various form factors of organics devices in lighting [8], displays [8] and thin film transistors [9].

Chapter 2 Organic Small Molecules

A molecule is the most fundamental building block of an organic thin film. Thus, it is essential to understand the characteristics of a molecule to understand organic electronic devices. In this chapter, we discuss the quasiparticles carried by small molecules and how they transfer between the molecules. Also, ligands comprising heavy metal complex molecules, an important component for modern phosphorescent OLEDs, are discussed.

2.1 Polarons and excitons

An injected electron in an organic film ionizes a molecule, causing a local displacement of molecules from their equilibrium positions for relaxation. This adjustment of position leads to a polarization locally centered at the charge carrier. A quasiparticle including the charge and its surrounding local polarization is defined as a ‘polaron.’ Polarons exist in all condensed matter solids, although the degree of local polarization depends on material characteristics. The more localized the polaron is, the more difficult it becomes to be transferred between the molecules, causing reduced charge mobility throughout the film.

An exciton is a quasiparticle describing a bound excited state of an electron and a hole which are attracted to each other by the Coulombic force. An exciton is formed by optically exciting an electron in the ground state to an excited state of a molecule, or by electrically exciting via injection of charge carriers at conductive contacts. The Coulombic force binding an electron

and a hole leads to a net neutral particle, therefore, excitons are transferred by diffusion without being affected by external electric fields.

The binding energy and its change with distance are given by the Bohr model, which describes the orbit of an electron around the positively charged particle. The Bohr model energy is $E = e^2/(8\pi\epsilon r)$, where e is the electron charge, ϵ is the dielectric constant, and r is the distance between the charges. From this model, we deduce that the binding energy decreases with the dielectric constant of a medium, which is due to the electric field screening that reduces the Coulomb interaction. Inorganic semiconductors typically demonstrate high dielectric constant ($\epsilon_r > 10$) and, therefore, have a small binding energy (5-10 meV) with an exciton radius typically larger than the lattice spacing as shown in Fig. 2.1. These are called ‘Wannier-Mott’ excitons, usually with binding energies smaller than the thermal energy at room temperature and, thus are easily dissociated into free carriers. Therefore, in the absence of a quantum confinement, the absorption of a photon in inorganic semiconductors results in a band-to-band generation of free charge without generating an exciton. As a result, the absorption spectrum appears to be broad and the oscillator strength is relatively lower than the organic materials due to the smaller spatial overlap of the orbitals.

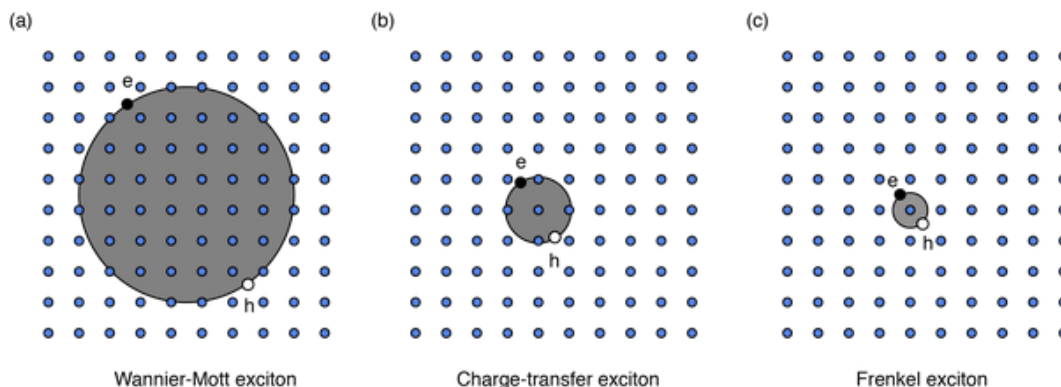


Figure 2.1 Illustration of the different types of excitons.
(Image by Edoardo Baldini)

Organic semiconductors typically show smaller dielectric constants than inorganic semiconductors due to the limited polarizability, resulting in larger binding energies (0.5-1eV) with smaller exciton radii. These tightly bound, localized excitons in a single molecule are called Frenkel excitons. Due to their strong binding energy, Frenkel excitons diffuse long distances without being dissociated and relax to the ground state. Also, the tightly bound local Frenkel excitons demonstrate large oscillator strengths, enabling a highly absorptive feature with narrow spectral widths (~100 nm full width at half maximum [10]) and effective optical emission stemming from an efficient radiative recombination. These features of organic materials help produce efficient, light weight photonic devices.

An excited electron within the Frenkel exciton can momentarily transfer to a neighboring molecule, creating an anion-cation pair of neighbors. This type of delocalized pair of excitons is called a charge transfer (CT) exciton. Due to the enlarged exciton radius (r), the binding energy of a CT exciton decreases substantially (~0.1-0.5 eV) compared to a Frenkel exciton. As this separation extends over multiple sites, the exciton becomes a Wannier-Mott-like exciton and eventually becomes separated as an electron and a hole.

A CT exciton formed between two molecules is referred to as a dimer, excimer or exciplex depending on the environment. Dimer indicates an exciton formed between two molecules that are bound even in the ground state, whereas an excimer or an exciplex refers to an exciton between two molecules only bound when excited. An exciplex differs from an excimer in that the former refers to an exciton between heterogeneous molecules. The difference between an excimer and a dimer is observed from their luminescent spectrum as shown in Fig. 2.2. For dimers, the vibronic progression is observable in the spectrum since the ground state is a bound state with different vibronic states, whereas for excimers, charges in different molecules are separated in the ground

state without any vibronic states resulting in a broad and featureless spectrum. Also, the displacement of molecules is relatively larger in excimers due to the lack of attraction in the ground state. It is worthwhile to mention that the difference between an excimer and dimer is solely from the resonance interaction and the concomitant geometric relaxation of the two molecules. Therefore, it is possible that the two cases occur in parallel depending on the different extent of the mutual geometrical variation during excitation. For example, with planar molecules, a herringbone arrangement typically prevents closer approach of molecules during the excitation compared to a parallel stack geometry, leading to a higher chance to show dimeric emission than excimers [11].

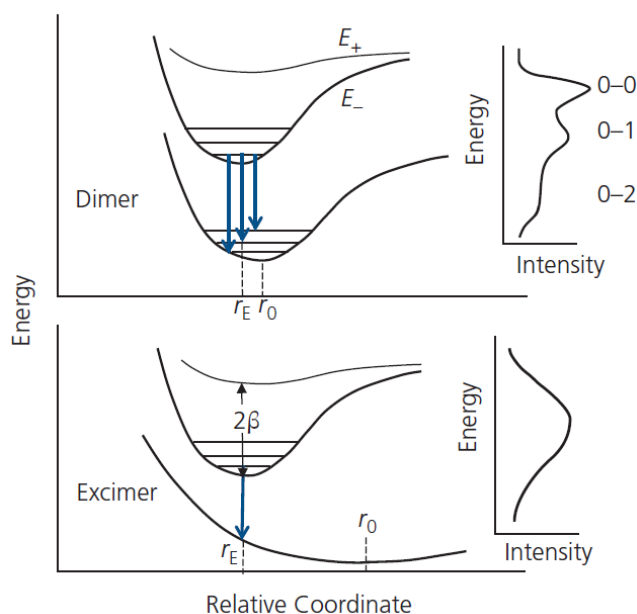


Figure 2.2 Energy diagram of dimer vs. excimer.
(Adapted from Forrest, *Organic Electronics*, 2020)

2.2 Singlet and triplet excitons

The spin of a state is given by the total spin of all electrons in all orbitals. Since no two Fermions (in this case, electrons) occupy the same state (n, l, m_l, m_s) in a single molecule according to the Pauli Exclusion Principle, electrons in each filled orbital are paired with anti-parallel spins

and therefore do not contribute to the total spin. However, the electrons in the frontier orbitals are free to be excited or to hop onto an adjacent molecule, thus they should be considered to count the total spins of the system. In the ground state, all electrons are paired with anti-parallel spins resulting in a total spin of 0 ($S=0$), however, in the excited state two different cases can occur. First are excitons comprising two electrons with anti-parallel spins, deemed a singlet state exciton, i.e.

$\psi_{spin,S} = \frac{1}{\sqrt{2}}(|\uparrow\downarrow\rangle - |\downarrow\uparrow\rangle)$. Singlets only have one possible value of the z -component, that is $m_S = 0$, which is where the name comes from. In this case, the total spin adds up to zero ($S = 0$). In contrast, excitons with spins of even symmetry between the excited and ground state electrons, i.e.

$$\begin{aligned}\psi_{spin,T+} &= |\uparrow\uparrow\rangle \\ \psi_{spin,T0} &= \frac{1}{\sqrt{2}}(|\uparrow\downarrow\rangle + |\downarrow\uparrow\rangle), \\ \psi_{spin,T-} &= |\downarrow\downarrow\rangle\end{aligned}\tag{2.1}$$

are called as triplet states, where the total spin adding up to one ($S = 1$). Different illustrations of singlet and triplet excitons are given in Fig. 2.3.

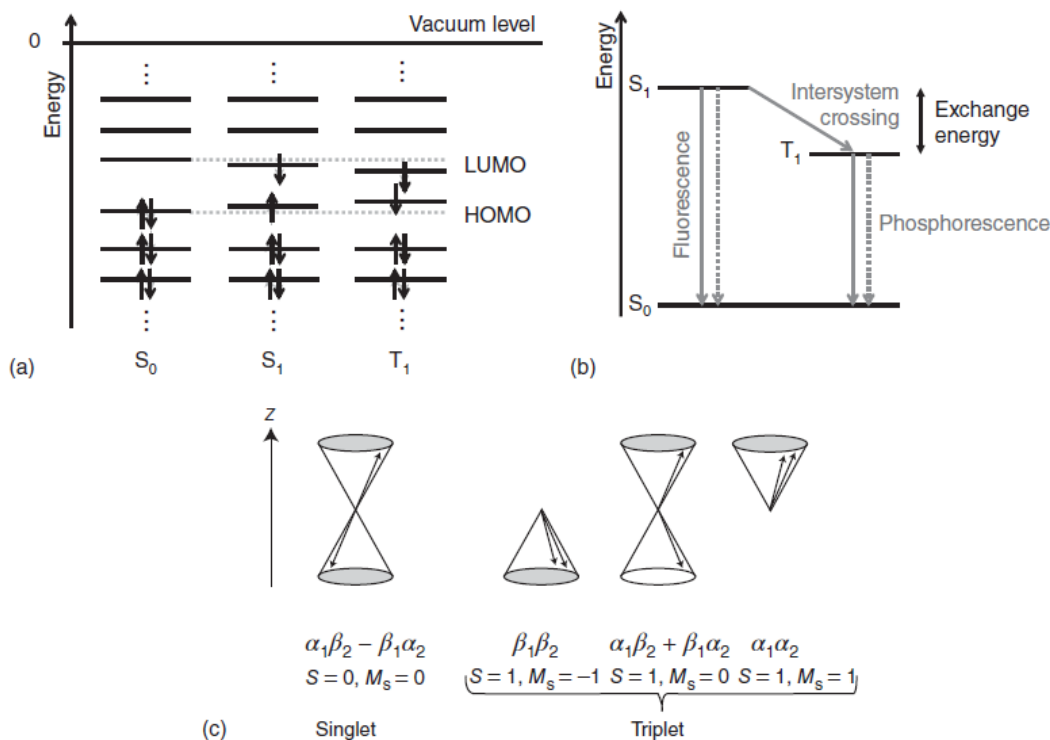


Figure 2.3 Illustration for the concept of singlet and triplet states.

(a) Singlet and triplet states in an orbital configuration scheme. (b) Singlet and triplet excitons in a state diagram. (c) Singlet and triplet states in a vector diagram describing the relative orientations of the two electron spins for each state. The singlet state shows a 180° out-of-phase configuration with antiparallel vectors, while the triplet states show in-phase configurations. α and β denote the up and down spin wavefunctions, where S and m_s shows the total spin and its value in the z -component, respectively. (Adapted from Köhler and Bässler, *Electronic Process in Organic Semiconductors*, 2015)

The lowest triplet state (T_1) has a lower energy than the lowest singlet state (S_1) and the energy difference between the two states are referred to as ‘exchange energy’, twice the value of the exchange integral. This occurs because the anti-symmetric spin of singlet excitons requires spatially symmetric states, which require closer proximity of electrons than triplet states that leads to a larger Coulomb repulsive energy. The exchange interaction exponentially increases with overlap of the HOMO and LUMO, in the first order approximation. Thus, for a molecule with significant HOMO/LUMO overlap, the exchange energy is large, on the order of 0.7-1.0 eV [11], whereas for a molecule with small overlap, the exchange energy can even become comparable to the room temperature thermal energy, demonstrated by thermally activated delayed fluorescent compound molecules [12].

2.3 Energy transfer

As previously discussed, an exciton is a quasiparticle that transfers energy throughout the organic film. Therefore, understanding how excitons are distributed enables comprehending how energies are propagated within an organic film. The Jablonski diagram shown in Fig. 2.4 illustrates the relationship between energies, spins, vibronic levels and transition processes of excitons, thus is an important figure for understanding the energy transfer in an organic film. In the diagram, there are basically two important manifolds, singlet and triplet states. The transition within the manifold (internal conversion) is allowed, however the transition between different manifolds (intersystem crossing) is prohibited by the Laporte spin selection rule. However, when the system is strongly perturbed by an intense spin orbit coupling, the intersystem crossing becomes possible, enabling an efficient transfer of lowest singlet excitons into the triplet manifold, known as phosphorescence. This will be discussed more in detail in Chapter 2.5.

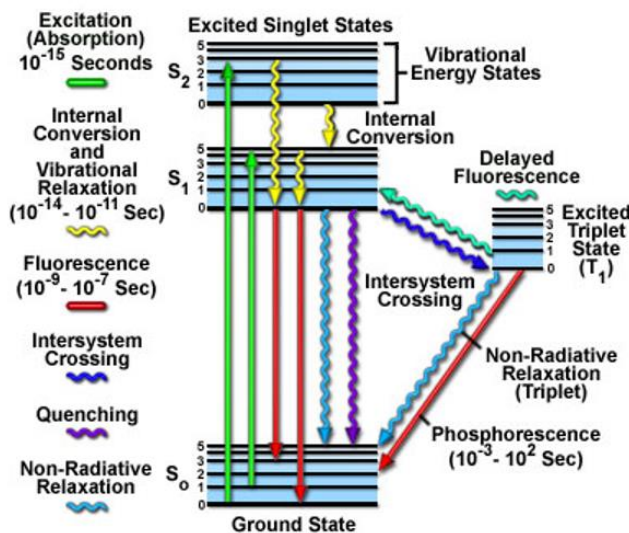


Figure 2.4 Jablonski diagram.

Jablonski diagram for a molecular system with singlet (S) and triplet (T) manifolds with vibronic levels in each manifold. The approximate time constants for each emissive decay are designated. Solid lines designate radiative processes whereas the wiggly lines show non-radiative processes (Adapted from micro.magnet.fsu.edu).

Energy transfer occurs primarily in three different categories depending on the interaction distances: i) long range radiative transfer (trivial energy transfer); ii) Förster (or fluorescent) resonant energy transfer (FRET); and iii) Dexter transfer (or exchange transfer). An illustration describing these three types of energy transfers is shown in Fig. 2.5.

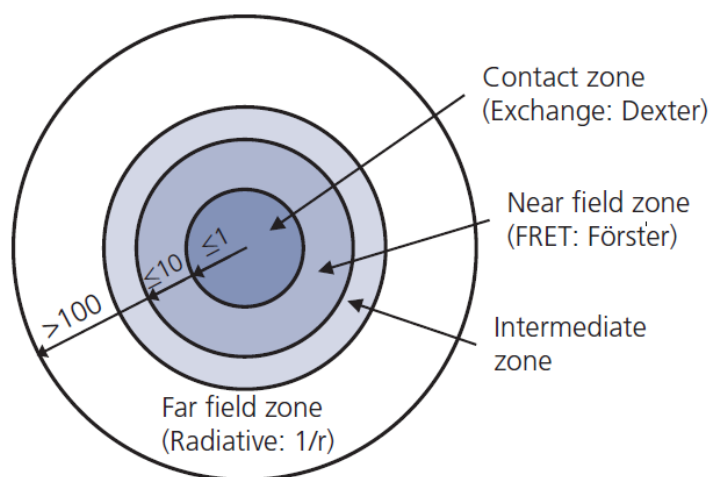


Figure 2.5 Types of energy transfers according to the interaction distances (Adapted from Forrest, *Organic Electronics*, 2020)

Long range radiative transfer (trivial transfer) occurs when an exciton is transferred from one molecule to another by emission and reabsorption of the light. Trivial transfer requires an efficient emission and absorption of photons by the molecules and does not involve any interaction between the molecules. Therefore, a good overlap between the emission and absorption spectra of the donor and the acceptor molecules is required for an efficient long range radiative transfer.

Förster resonant energy transfer is a near-field non-radiative energy transfer between molecules via dipole-dipole interactions. It is a process where the excited state donor molecule is relaxed while the ground state acceptor molecule is excited via coupling interactions. The Laporte selection rule requires that the donor and acceptor transition should not change the total spin states. Therefore, singlet excitons can freely Förster transfer, however, the first level triplet excitons (T_1)

cannot since the ground state relaxation is prohibited. However, such a transfer between the triplet excitons in the triplet manifold (T_n) is allowed.

The transfer rate and the radius of FRET is derived from the Fermi's golden rule [11] as [10]:

$$k_{ET} = \frac{9(2303)c^4}{128\pi^5} \frac{\kappa^2 \Phi_D}{n_r^4 \tau_D N_A R_{DA}^6} \int \frac{f_D(\nu) \alpha_A(\nu)}{\nu^4} d\nu \quad (2.2)$$

$$R_0^6 = \frac{9c^4}{128\pi^5} \frac{\kappa^2 \Phi_D}{N_A n_r^4} \frac{M_{\omega A}}{\rho_{MA}} \int \frac{f_D(\nu) \alpha_A(\nu)}{\nu^4} d\nu \quad (2.3)$$

where k_{ET} is the Förster transfer rate, R_0 is the Förster radius, R_{DA} is the distance between the donor and acceptor molecule, τ_D is the lifetime of the donor without the acceptor, c is the speed of light, N_A is Avogadro's number, n_r is the refractive index of the medium, Φ_D is the quantum yield of the donor, $M_{\omega A}$ is the molar molecular mass, ρ_{MA} is the mass density of the acceptor mixture, ν is the frequency, f_D/α_A are the emission/absorption spectrum of the donor/acceptor, and κ^2 is the dipole orientation factor. The dipole orientation factor varies with the arrangement of donor and acceptor transition dipole moments (TDMs) ranging between 0 and 4, with $\kappa^2=2/3$ for an isotropic arrangement. Equation (2.2) shows that the Förster transfer rate increases with a shorter donor-acceptor distance and a larger spectral overlap. A rule of thumb of the Förster radius is ~ 5 nm, not more than 10 nm for typical organic films.

Dexter transfer, also known as the exchange transfer, is an electron hopping transport between the contacting molecules, therefore is the shortest range energy transfer, usually less than ~ 1 nm. During Dexter transfer, the electron of an excited molecule transfers to a neighboring ground state molecule, whereas an electron in the ground state molecule is transferred back to the originally excited molecule as shown in Fig. 2.6. Dexter transfer occurs while the spin states of

the excited and ground state excitons are preserved. Therefore, triplet states are free to transfer via Dexter exchange process.

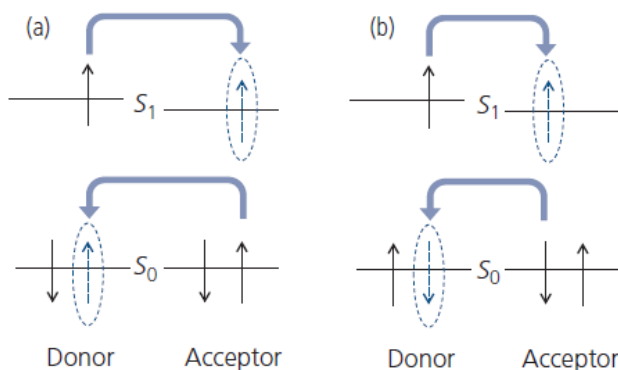


Figure 2.6 Exchange energy transfer between neighboring molecules
Exchange energy transfer between the neighboring molecules of singlet (a) and triplet (b) excitons. (Adapted from Forrest, *Organic Electronics*, 2020)

Dexter transfer also depends on overlap of the emission and absorption spectra and the distance between the donor and acceptor molecules as:

$$k_{ET} \propto \frac{J_{\omega}}{R_{DA}^2} \exp(-2R_{DA} / L) \quad (2.4)$$

where J_{ω} is the spectral overlap integral and L is the effective average radius of the excited and ground states involved. Unlike Förster transfer, the Dexter transfer rate in Eq. 2.4 does not show an orientation dependence and occurs preferentially to the closest molecule with the largest contact area. Also, it is important to note that the transfer rate of a Dexter transfer exponentially depends on R_{DA} , and thus decreases much faster with the donor-acceptor distance compared to the Förster transfer.

Both Förster and Dexter transfers show that the energy transfer highly depends on the molecular distance and spectral overlap. This implies that the molecular structure and its packing, which affect the mean distance between molecules, are important elements of the energy transfer within a film. For example, tightly π -stacked planar molecular crystals with minimal disorder would show a more efficient energy transfer compared to an amorphous film comprising bulky

molecules with large steric hindrance, when the spectral overlap is identical. Furthermore, a decrease in crystallinity, which leads to an increased disorder, decreases the exciton diffusion length [13]. Meanwhile, it should be noted that the alignment between the acceptor and donor molecules only affects the rate of the Förster transfer, implying that the disorder of the molecule is more critical for Förster transfer.

2.4 Charge transport

In an ideal crystal with no lattice scattering, the energy level at each lattice site is depicted as a straight line with the charge carrier wavefunction delocalized, and the charge moves as a plane wave (Block wave) as shown in Fig. 2.7a. In a real crystal, however, lattice vibrations, or phonons, disrupt the crystal symmetry, which scatter electrons and thereby reduce charge mobility. Lowering the temperature will therefore increase the mobility in this case. This type of charge transport is called band transport, which is typically observed in highly crystalline inorganic semiconductors. Charge diffusion usually dominates in inorganic semiconductors, since the potential differences are typically small due to the efficient dielectric screening ($\epsilon_r > 10$) and good band alignment.

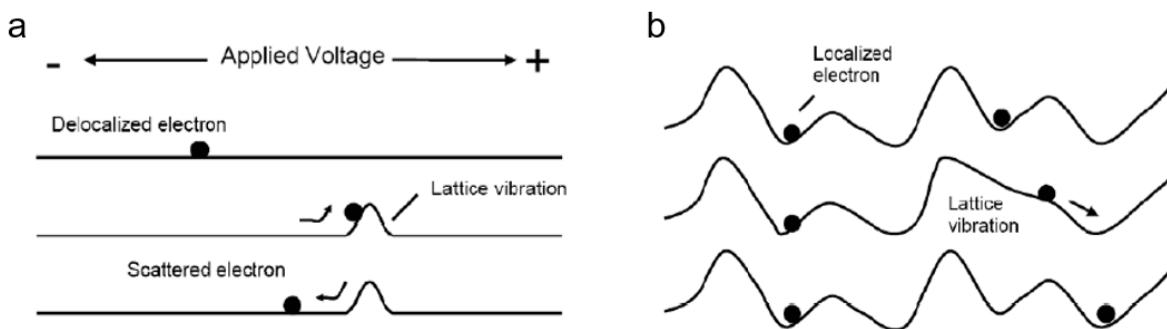


Figure 2.7 Energy level diagram of the band and hopping transport
 The energy level of band transport is mostly constant when no lattice vibrations occur (a), whereas for the hopping transport the localized charge needs to overcome the energy barrier every time it tries to transfer (b).

For most organic semiconductors, however, weak intermolecular forces are predominant among molecules or polymers. In this case, a discrete energy band structure is dominant in the bulk. The free propagation of charge, as usually seen in inorganic semiconductors, no longer exists. As a result, carrier transport in organic semiconductors becomes a hopping process that involves thermionic emission and tunneling of carriers between localized sites, as shown in Fig. 2.7b. This means that the charges are more difficult to transport in organic films (especially for an amorphous phase) thus one can imagine the charges in organic semiconductors as ‘sticky’ particles, which takes an energy to activate hopping over the barrier at the edge of the potential energy wall. Therefore, the current is mainly controlled by the charge drift until the current reaches the space charge limited (SCL) regime, where the charge diffusion also plays a significant role.

There are two models describing the hopping process in the presence of static disorder within an organic film, Miller-Abrahams and Marcus electron transfer theory. The Miller-Abrahams theory describes the conduction of charges that occur via hopping from the donor to the acceptor molecule, with the rate of hopping from site i to j is shown as:

$$k_{ET} = v_0 \exp(-2\gamma_{ij}R_{ij}) \begin{cases} \exp\left(-\frac{E_j - E_i}{k_B T}\right) & E_j > E_i \\ 1 & E_j < E_i \end{cases} \quad (2.5)$$

where E_i and E_j are the energy levels of initial and final states with the separation of R_{ij} , and γ_{ij} is the overlap of orbital between the initial/final orbital wavefunctions, and v_0 is the frequency of charge attempting to overcome the barriers to hop onto the nearest neighbors. From Eq. (2.5), we are able to conclude that the charge transport is more efficient with larger orbital wavefunction overlap, less separation (higher mass density), and larger initial and final energy difference. The exponential dependence of the transfer rate to the distance is a similar result from Dexter transfer, since both transfers result from charge tunneling between the adjacent molecules.

Another theory explaining charge transfer is the Marcus electron transfer, which is a more physically consistent model. Marcus transfer theory explains the charge transfer as depicted in the reaction coordinate vs. Gibbs free energy diagram as shown in Fig. 2.8.

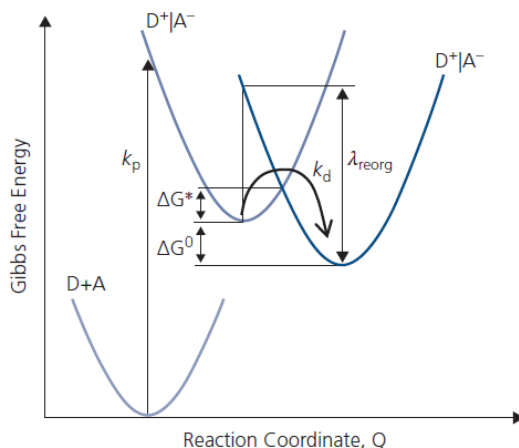


Figure 2.8 Marcus charge transfer

An illustration of the charge transfer process according to the Marcus theory. The lower parabola shows the initial precursor whereas the top two parabolas show the donor (left) and the acceptor (right) states with the energy barrier of ΔG^* to be overcome by the charge. (Adapted from Forrest, *Organic Electronics*, 2020)

The transfer rate of the Marcus theory is as follows:

$$k_{ET} \propto \exp\left(-\frac{(\lambda_{reorg} + \Delta G^0)^2}{4\lambda_{reorg}k_B T}\right) \quad (2.6)$$

where λ_{reorg} is the reorganization energy that describes the height of the potential difference in the perspective of the destination potential, and ΔG^0 is the difference between the lowest energy levels of each parabola. Unlike Miller-Abraham theory of electron transfer where the transfer rate saturates in an exergonic reaction, in Marcus theory the electron transfer rate does not simply increase as ΔG^0 decreases. As shown in Fig. 2.9, when $\Delta G^0 < 0$ and $|\Delta G^0| > \lambda_{reorg}$, the activation energy (ΔG^*) should increase with decreasing ΔG^0 which causes the rate to decrease, also known as the Marcus inverted region. This was shown for organic materials by Rand, et al. and Liu, et al. [14,15]

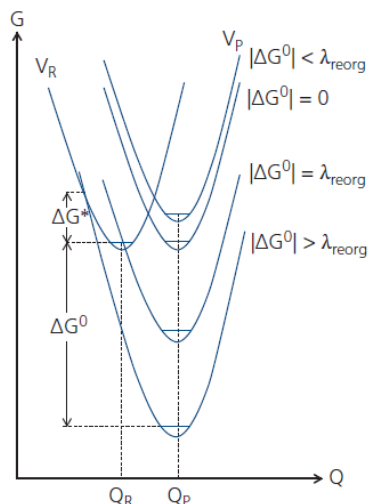


Figure 2.9 Illustration of Marcus charge transfer with different free energies (ΔG^0).
(Adapted from Forrest, *Organic Electronics*, 2020)

As with Dexter energy transfer, the charge transport rate is highly dependent on the distance between the donor and acceptor molecules since charge transfer is also caused by intermolecular tunneling. Thus, highly crystalline tightly π -stacked molecular crystals show much higher charge transport rate, and thus have higher charge mobility, compared to the amorphous films with less ordered film morphology. Therefore, controlling the film morphology in a desired way increases the film mobility by orders of magnitude.

2.5 Fluorescence and phosphorescence

Fluorescence and phosphorescence are different types of molecular luminescence processes, which result from the relaxation of excitons to the ground state. Fluorescence occurs without a change of spin state, thus is an allowed transition. Since fluorescence is an allowed transition, the exciton decay time is relatively short ($10^{-9} - 10^{-7}$ sec). This “allowed transition” is produced in reference to the selection rules in quantum mechanics.

In contrast, phosphorescence is a decay of excitons by “forbidden energy state” transitions, accompanying a spin state variation. Since it is a forbidden transition, the emission is inefficient

and exhibits a long decay time. However, Baldo, et al. [16] showed that the use of molecules comprising a heavy metal atom center coordinated with organic ligands enable a dramatically improved quantum yield by incorporating a strong perturbation due to the spin-orbit coupling (SOC) to the center metal, mixing the singlet and triplet states. The strong SOC perturbs the spin of the electron by interacting with its orbital angular momentum, where the strength of it is expressed as [10]:

$$H_{soc} = \frac{q}{\hbar m_e^2 c^2} \frac{1}{r} \frac{dV(r)}{dr} \mathbf{l} \cdot \mathbf{s} = \frac{Zq^2}{8\pi\epsilon_0 m_e^2 c^2} \frac{1}{r^3} \mathbf{l} \cdot \mathbf{s}, \quad (2.7)$$

where $V(r)$ is the potential of an electron in the hydrogenic atom with atomic number Z , $V(r) = -Zq/4\pi\epsilon_0 r$, \mathbf{l} and \mathbf{s} are the angular momentum and spin angular momenta, respectively. The expectation value of $1/r^3$ in the spherical coordinate is:

$$\left\langle \frac{1}{r^3} \right\rangle = \frac{2(Z/a_0)^3}{n^3 l(l+1)(2l+1)}, \quad (2.8)$$

where $a_0 = \frac{4\pi(\epsilon_0\epsilon_r)\hbar^2}{m_e q^2}$ is the Bohr radius. The expectation value of the $\mathbf{l} \cdot \mathbf{s}$ coupling is written as:

$$\langle \mathbf{l} \cdot \mathbf{s} \rangle = \frac{1}{2} (\langle \mathbf{j} \rangle^2 - \langle \mathbf{l} \rangle^2 - \langle \mathbf{s} \rangle^2) = \frac{\hbar^2}{2} [j(j+1) - l(l+1) - s(s+1)]. \quad (2.9)$$

Thus, the SOC energy is obtained:

$$E_{so} = -Z^4 \cdot \frac{\hbar^2 q^2}{8\pi\epsilon_0 m_e^2 c^2 a_0^3} \frac{j(j+1) - l(l+1) - s(s+1)}{n^3 l(l+1)(2l+1)}, \quad (2.10)$$

showing that the SOC interaction has a Z^4 dependence on the atom number. Therefore, the SOC increases drastically by employing heavy metal centers such as Ir, Pt or Au, which are typically used to promote phosphorescence in a molecule. Also, E_{so} decreases with increasing the principal quantum number (n), meaning that the effect of SOC drops dramatically for higher excited state manifolds.

2.6 Types of ligands in heavy-metal phosphorescent complexes

Ligand is a functional group that binds to a central metal atom to form a coordination complex. Since heavy metal complex phosphorescent emitters are comprised of transition metal centers, understanding ligands is important to understand the construction of phosphorescent molecules.

Transition metals, which are typically used for phosphorescent emitters, form complex ions which are metal ions surrounded by ligands. They are attached to the ligands via coordinate covalent bonds, a type of covalent bond that is formed without sharing electrons and instead formed by one nucleus providing the entire electron-pair for the bond. The number of bonds formed between the center metal and ligands is called the coordination number which varies between 2 and 8 depending on the charge and electron configuration. The most common coordination number is 6, and then 4. Complex ions with a coordination number of 6 usually have an octahedral arrangement, whereas those with a coordination number of 4 have either a square-flat or tetrahedron structure.

Some ligands have two or more electron lone pairs, and thus form multiple coordinate bonds with the center metal. These ligands are called chelating ligands and, depending on the numbers of coordinate bonds, are deemed n -dentate ligands. For example, when it binds with two lone pairs, it is called as bidentate ligand, for three lone pairs, it is called as tridentate ligand and so on. The most commonly used heavy-metal complexes are Ir(III) and Pt(II) complexes. Ir(III) complexes are octahedral molecules with the coordination number of 6 and Pt(II) complexes are square-flat bidentate molecules with the coordination number of 4.

A heavy metal complex comprised of same/different types of ligands is called a homoleptic/heteroleptic compound. Since a heteroleptic compound has different ligands attached to the center metal atom, an emission from a molecule only happens from the ligand with the lowest excitation energy. This ligand is called a chromophoric ligand since it emits photons, whereas the other ligands are known as ancillary ligands which do not emit photons.

Chapter 3 Bulk Organic Film and Morphology

Morphology of a thin film usually refers to film structures shown by crystallinity, orientation, stiffness, homogeneity, and thermal stability, and is one of the key factors governing the properties of a solid. It determines essentially every element of a film such as the thermal, optical and electrical characteristics, which are critical features for a device [17–19]. Precise understanding and control of the film morphology is, therefore, crucial for developing high performance devices. Understanding the morphology of a film starts from how each molecule is bonded with another. Therefore, in this chapter, we start from discussing the different bonds comprising an organic film, investigate how the morphology is affected by the bonds, and eventually describe how different morphology affects the characteristics of the film.

3.1 Bonds of organic film

A bond is a cohesive force holding the building blocks (atoms or molecules) of a material together. When an energy similar or higher than the bond energy is applied, the building blocks fall apart, causing the phase to change or molecules to fracture. In addition, the type of bond determines how electrons are distributed within a system (films or devices), affecting the electrical and optical characteristics of the system. As such, the bond is closely related to numerous aspects of a material, therefore understanding bonds is an essential base to comprehending the material characteristics. In this chapter we discuss the bond characteristics in detail.

3.1.1 Covalent bonds

Covalent bonds are formed when two or more nuclei share valence electrons to form a lower energy state. This occurs since an electron in an atom is stabilized by being attracted to the proton in another atom, causing the entire system to be stabilized. The spins of the two electrons comprising the bond are antiparallel to each other. Covalent bonds are strong bonds with a dissociation energy of $\sim 1-5$ eV, depending on its type and polarity.

The energy of molecular hydrogen (H_2) as a function of internuclear distance is plotted in Fig. 3.1. The plot shows that the system becomes stable as the two atoms approach each other until a certain point ($r_0 = 74$ pm for H_2 molecules). In the long-distance regime, the attraction between electron-proton dominates, thus the energy of the system decreases as the atoms approach each other until this attraction is maximized. When the interatomic distance is closer than r_0 , the system becomes unstable. This is due to the proton-proton and electron-electron Coulombic repulsive interactions, which causes the energy to increase rapidly. This behavior is similar with the case of ionic bonding since they both result from attractive and repulsive forces between the charged entities.

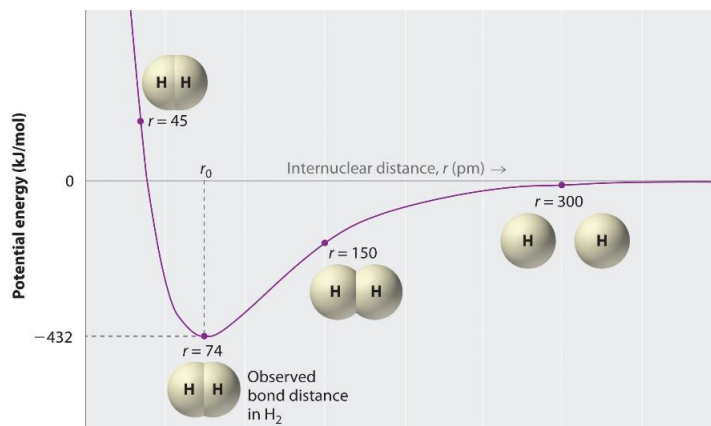


Figure 3.1 Diagram showing the potential energy of two separate hydrogen atoms. (Adapted from chem.libretexts.org)

Covalent bonds include various ranges of bonds such as sigma (σ), pi (π) and coordinate bonding as discussed in Chapter 1.1.2. They are formed by sharing the valence electrons, however the distribution of the shared electrons is different between each other. Sigma (σ) bonds are formed by head-on overlapping of atomic orbitals as shown in Fig. 3.2. This bond is the strongest type of covalent bond due to the large overlapping of the participating orbitals. The electrons forming the sigma bond is often referred to as σ -electrons which are localized between the two atoms joined by the bond. All single bonds are sigma bonds, which enable rotational freedom within the molecule when they are not interlocked.

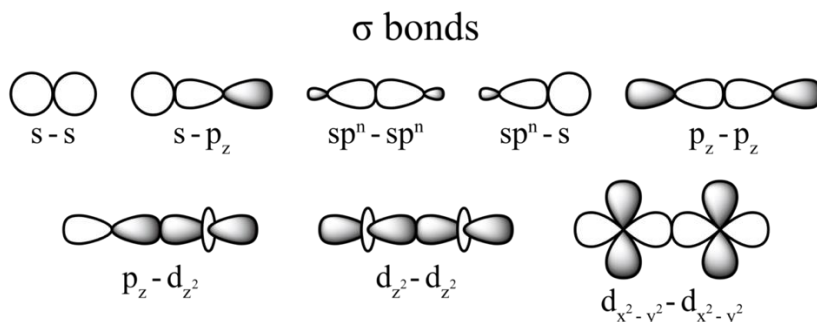


Figure 3.2 Examples of sigma bonds with various types of overlap between different orbitals. (Adapted from brilliant.org)

Pi (π) bonds are formed due to the overlapping of adjacent atomic orbitals as shown in Fig. 3.3. They are formed above and below the plane of the molecule occupied by a sigma bonds, with the axes of the atomic orbitals parallel to each other. Therefore, the overlap between the orbitals is less than the directly overlapped sigma bonds, leading to weaker bond energies. Double bonds consist of one sigma and one pi bond, whereas a triple bond is comprised of one sigma and two pi bonds.

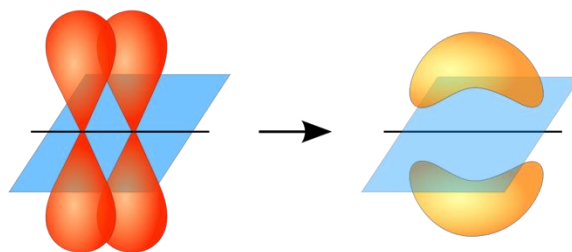


Figure 3.3 Schematic of two p -orbitals forming a π -bond.
(Adapted from wikipedia.org)

An important aspect of π bonds in organic materials is the formation of π -conjugation. A conjugated system is a system of connected p -orbitals with delocalized electrons in a molecule which typically lowers the overall energy of the molecule and increases its stability. They allow a delocalization of π -electrons across all adjacent aligned p -orbitals. Thus, in the π -conjugated system, the π -electrons do not belong to a single bond or atom, but rather to a region of atoms. Therefore, by elongating this region of π -electron conjugation, producing a conductive chain within a molecule is possible. Furthermore, conjugated systems are not only conductive, but they easily accept or donate electrons, which makes it an indispensable element for all organic electronic devices. As a result, all organic electronic devices today comprise of organic materials with π -conjugated systems.

Coordinate bonds, also known as dative bonds, are another type of covalent bond. Unlike other covalent bonds which share the electron from two different nuclei, the coordinate bond happens when one nuclei provides the entire electron-pair for the bond formation as shown in Fig. 3.4. It is formed between a central electrophile (low electron density such as metal cations) and one or more nucleophiles (high electron density such as anion ligands) around the center. The high electron density ligands supply two electrons per coordinate bond to the central electrophile to satisfy the octet rule. Unlike ionic compounds, coordinate bonding between oppositely charged ionic species still holds the covalent character where the bonding electrons are shared between the

atoms. Coordinate bonds are typically observed in transition metal complexes, which are an important type of phosphorescent molecule often used for OLEDs.

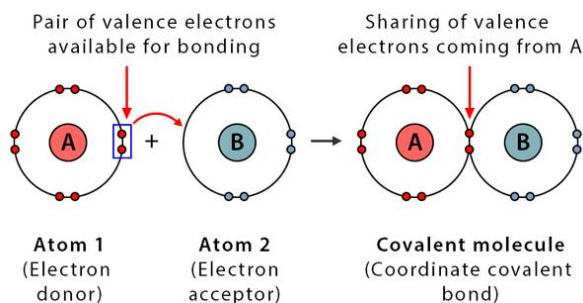


Figure 3.4 Schematic explaining the coordinate bond. (Adapted from chemistrylearner.com)

Polarity of the covalent bond is another important element which determines its strength. When the atoms forming a covalent bond are identical, such as a C-C bond, the electrons in the bond are shared equally with no polarity. These are often referred to as pure covalent bonds. In contrast, when the atoms linked by a covalent bond are different, the bonding electrons are unequally shared, meaning that they are more attracted to one atom than the other, giving rise to the electron density toward that atom. Therefore, when two different atoms form a covalent bond, a local polarity is created, with one part more positive and the other part more negative compared to the neutral potential. An example is shown in Fig. 3.5, showing a higher electron density around the Cl atom. The Greek letter delta (δ) is used to indicate whether the atom has a partial positive or negative charge compared to the neutral potential.

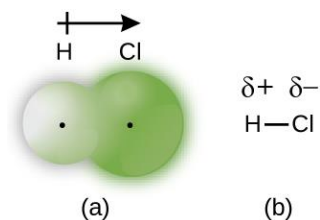


Figure 3.5 Electron distribution within a polar molecule. (a) The distribution of electron density within the HCl molecule showing higher density around Cl nucleus. The black dots indicate the location of the H and Cl nuclei. (b) δ^+ and δ^- shows the partial positive and negative charges within the molecule. (Adapted from chem.libretexts.org)

The distribution of electrons within the bond is determined by the electronegativity of the participating atoms. Electronegativity is a measure of the tendency of an atom to attract electrons (i.e., electron density) towards itself. Therefore, electronegativity determines how the shared electrons are placed between the atoms within a bond. An atom with larger electronegativity has stronger attraction towards the electrons within the bond, therefore, the atom with larger electronegativity shows partial negative charge. As the difference in electronegativity increases, the electron distribution becomes more polarized and partial charges of the atoms rise. Thus, an organic molecule with a substantial difference of electronegativity between the atoms shows a non-uniform distribution of positive and negative charges that leads to a static dipole moment of the molecule. Organic molecules typically show negative potentials near the halide atoms compared to the region with C atoms. In addition to the atoms, some groups also show strong electron withdrawing or donating character, such as halide, cyano groups (withdrawing) / -OH, -NH₂ groups (donating), which are often used to decrease/increase the orbital energy of the molecules by inducing less/more electron-electron repulsion to the molecular system. However, a drastic change of electron density using strong electron withdrawing groups have been known to risk the stability of the molecule, as demonstrated by adding fluorine groups for blue dopants in OLEDs [10].

← Increasing electronegativity →																		
																H 2.1		
	Li 1.0	Be 1.5												B 2.0	C 2.5	N 3.0	O 3.5	F 4.0
	Na 0.9	Mg 1.2												Al 1.5	Si 1.8	P 2.1	S 2.5	Cl 3.0
	K 0.8	Ca 1.0	Sc 1.3	Ti 1.5	V 1.6	Cr 1.6	Mn 1.5	Fe 1.8	Co 1.9	Ni 1.9	Cu 1.9	Zn 1.6	Ga 1.6	Ge 1.8	As 2.0	Se 2.4	Br 2.8	
	Rb 0.8	Sr 1.0	Y 1.2	Zr 1.4	Nb 1.6	Mo 1.8	Tc 1.9	Ru 2.2	Rh 2.2	Pd 2.2	Ag 1.9	Cd 1.7	In 1.7	Sn 1.8	Sb 1.9	Te 2.1	I 2.5	
	Cs 0.7	Ba 0.9	La-Lu 1.0-1.2	Hf 1.3	Ta 1.5	W 1.7	Re 1.9	Os 2.2	Ir 2.2	Pt 2.2	Au 2.4	Hg 1.9	Tl 1.8	Pb 1.9	Bi 1.9	Po 2.0	At 2.2	
Decreasing electronegativity ↓	Fr 0.7	Ra 0.9	Ac 1.1	Th 1.3	Pa 1.4	U 1.4	Np-No 1.4-1.3											

Figure 3.6 The periodic table with electronegativity values. Electronegativity increases toward the upper right of the table. (Adapted from chem.libretexts.org)

3.1.2 Van der Waals bonds

A van der Waals (vdW) bond is an intermolecular interaction. It is the most typical cohesive force which combines the organic molecular and polymer films. Unlike the case of ionic or covalent bonds which are bound by strong chemical bonds, vdW bonds are induced by a temporary Coulombic force due to the fluctuation of polarization. A vdW bond is comparatively weaker than ionic or covalent bonds and therefore is more susceptible to disturbance, and quickly vanishes at longer distances. The weak bond strength of vdW bonds causes the organic film to be soft and flexible, enabling various form factors of organic electronic devices. As the distance-dependent potential of the multipoles decays fast with its number of charge moments as $1/r^{n+1}$ [10], we mainly discuss the dipolar interactions in this thesis.

As vdW force occurs by a superposition of electrostatic interactions within each molecule, it is be decomposed into four different elements:

- 1) repulsion between molecules preventing the overlap of orbital states to follow the Pauli Exclusion Principle.
- 2) attraction/repulsion by the electrostatic interaction between the static dipoles;
- 3) induction, also known as polarization, which refers to the electrostatic attraction between a static dipole and induced charges caused by that static dipole, which is also known as polarization. This force is also known as Debye force. And, finally,
- 4) dispersion, which refers to the attraction between the molecules due to the instant fluctuation of charges. Dispersion occurs regardless of the polarity of the molecule, including non-polar atoms.

Therefore, we subdivide the vdW bonds, i) dipole-dipole interaction, ii) dipole-induced dipole interaction, and iii) interaction between induced dipole interactions as illustrated in Fig. 3.7. The third case is often called the London dispersion force.

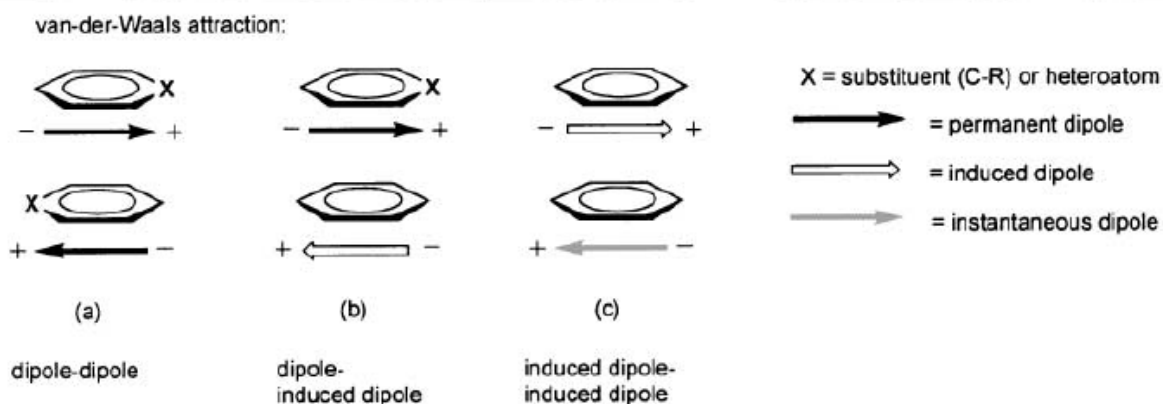


Figure 3.7 Different types of van der Waals bonding between two Arene moieties. (Janiak, 2000)

Dipole-dipole forces (Keesom force)

This force occurs between molecules that have static dipoles. This is also known as Keesom force, and the angle averaged result is given by:

$$U_{ij} = -\frac{m_1^2 m_2^2}{24\pi^2 \epsilon_0^2 \epsilon_r^2 k_B T |r_i - r_j|^6} \quad (3.1)$$

where m is the static dipole moment. As shown, the force decays swiftly following $1/r^6$, demonstrating that the bonds quickly vanish at longer distances. A static dipole of a molecule with local polarity occurs due to the difference of electronegativity of each atom, especially when an atom has lone electron pairs that cause an unequal electron distribution, as discussed in Chapter 3.1.1. As static dipoles have a spatial field distribution across the molecular surface, the dipole-dipole forces depend on the mutual orientation of the molecules, i.e., the molecules tend to align toward a relaxed state by reducing the dipole-dipole repulsion and inducing more attraction. This is a strong driving force that aligns small molecules during the growth of a film in vacuum since

the vacuum/organic boundary allows the molecules to be oriented before being buried by the next layer of film; this vdW force-driven molecular alignment does not appear in the spin-coated organic films since the entire ensemble is placed together with no surface boundary [20].

Dipole-induced dipole forces (Debye force)

The angle averaged result of a dipole-induced dipole force also shows a $1/r^6$ dependence as:

$$U_{ij} = \frac{-\alpha m_1^2}{(4\pi\epsilon_0\epsilon_r)^2 |r_i - r_j|^6} \quad (3.2)$$

where α is the polarizability of the molecule being induced. This dipole-induced dipole force occurs when one molecule with a static dipole repels/attracts another molecule's electrons. The molecule with larger π -conjugation, therefore, has a larger dipole-induced dipole force since more electrons are delocalized, which enhances the polarizability (α) of a molecule. The dipole-induced dipole force is far weaker than dipole-dipole interaction, however, stronger than the London dispersion force.

London dispersion force

London dispersion force is an interactive force between instantaneous multipoles in molecules caused by the charge fluctuation. Since charge fluctuation is the main cause, the polarizability of the molecule is the key factor of the London dispersion force. The expression is also known as the Buckingham potential, which follows:

$$U_{ij} = \alpha_{ij} \exp(-\beta_{ij} |r_i - r_j|) - \frac{A_{disp}}{|r_i - r_j|^6} \quad (3.3)$$

where β is a constant, and A_{disp} is a constant related to the coupling of the dipoles of each molecule. An alternative form showing the attraction and repulsion between two non-polar molecules is the Lennard-Jones 6-12 potential, which follows:

$$U_{ij} = 4\varepsilon_{ij} \left[\left(\frac{\sigma_{ij}}{|r_i - r_j|} \right)^{12} - \left(\frac{\sigma_{ij}}{|r_i - r_j|} \right)^6 \right] \quad (3.4)$$

where ε_{ij} is the depth of the potential well, which shows the strength of the attraction between two particles, and σ is the distance at which the potential energy between the molecules become zero, which shows how close the two nonbonding particles can approach. The first term of the equation describes the Pauli repulsion at short ranges between the molecules, whereas the second term describes the attractive binding force at long ranges due to the dispersion interaction. The range difference between the the Pauli repulsion and the attraction by the dispersion interaction results in a distance with the lowest potential, known as the van der Waals radius, which is the closest location a molecule can reach to its neighboring molecule.

Van der Waals force is important in analyzing organic morphology since it describes the interaction between molecules which plays the main role in forming bulk films. The π - π interaction between π -conjugated molecules is one of the important aspects that determines the morphology of a molecular film. This will be discussed more in detail in Chapter 3.2.

3.2 Morphology of small molecule organics

Morphology is, by definition, a study of the forms of things. In semiconductor physics, morphology describes the distribution of phases and structure of the film. Morphology of a film is shown by multiple aspects such as crystallinity, orientation, stiffness, homogeneity, and thermal stability of a film. Since morphology deals with how the building block is arranged, it significantly affects the overall properties of a film. For example, with the same C atoms, graphite and diamond show totally different mechanical, optical and electrical characteristics due to their different

arrangements. In this chapter, we discuss how molecular arrangement occurs during the deposition of an organic film.

3.2.1 Static and transition dipole moments

Molecular dipoles occur due to the disproportionate sharing of electrons in a molecule as discussed in Chapter 3.1.1. Depending on the time scale of this unequal distribution of electrons, the dipole moment is subdivided into two categories. Electrons pulled by more electronegative atoms within a molecule build up a discrete region of high electron density, producing a static dipole moment. The static dipole moment measures the separation of positive and negative electrical charges within a molecule, showing the polarity as $p(r) = \int_V \rho(r_0)(r_0 - r) d^3r_0$, where ρ is the charge density and r_0 denotes the position of the dipole. The static dipole of a molecule causes an enhanced intermolecular Coulombic interaction leading to a stronger van der Waals or even hydrogen bond.

On the other hand, the excitation of a molecule induces a temporary high electron density within a molecule which induces the TDM. The TDM is associated with the transition between the initial (ψ_i) and the final (ψ_f) states, with its transition rate (k_{if}) depending on the Hamiltonian H' which describes the perturbation caused by the absorption of a photon ($H = H_0 + H'$). The transition rate is determined by Fermi's golden rule as [10,11,21]:

$$k_{if} = \frac{2\pi}{\hbar} \left| \langle \psi_i | H' | \psi_f \rangle \right|^2 \rho, \quad (3.5)$$

where ρ is the density of the final states. Equation (3.5) shows that to increase the transition rate, one should either increase the coupling between the initial and final states, or increase the density of the final states. The direction of the TDM shows how a molecule interacts with an

electromagnetic wave of a given polarization, while the magnitude of the TDM gives the strength of the interaction between the molecule and the wave, known as the oscillator strength. Since the dipole oscillates with the charge transfer during relaxation, the TDM of an emitting molecule is regarded as a small dipole antenna. Therefore, when a light emitting molecule is located inside an optical waveguide, the orientation of the TDM severely affects the amount of the light trapped in, or extracted from, the waveguide. Likewise, for light absorbing molecules in photovoltaics, the orientation significantly affects the amount of light absorbed. Therefore, controlling the orientation of the TDM is crucial for an advanced performance of optoelectronic devices, which will be discussed in detail in Chapter 7.

3.2.2 π - π interactions

Organic electronic devices used today are comprised of aromatic rings due to their high conductivity and ease of electron donating/accepting properties as discussed in Chapter 3.1.1. With the aromatic compounds, the polarizability increases due to the delocalized electrons, thus enhancing the vdW bonding. Especially, for aromatic molecules with a large π -system, π - π interaction between the π -conjugates plays a significant role in molecular arrangement. Thus, it is important to understand the nature of π - π interaction, which has been investigated in the previous works of Hunter, et al., Janiak, and Sinnokrot, et al. [22–24].

An aromatic molecule is comprised of a delocalized π -electron and a σ -framework that form the backbone of a molecule. Since a molecule holds electrostatic neutrality, the π -electron solely comprising electronegative electrons shows negative potential, while the σ -framework shows relatively positive electrostatic potential. Therefore, there is a competition between the repulsion of π -electrons and the attraction between π -electrons and the σ -framework (π - σ

attraction), which varies depending on the molecular size and the arrangement of different atoms within the molecule. The balance of interactions between the π -electrons and σ -framework is the key factor determining how the molecules align with each other as shown in Fig. 3.8.

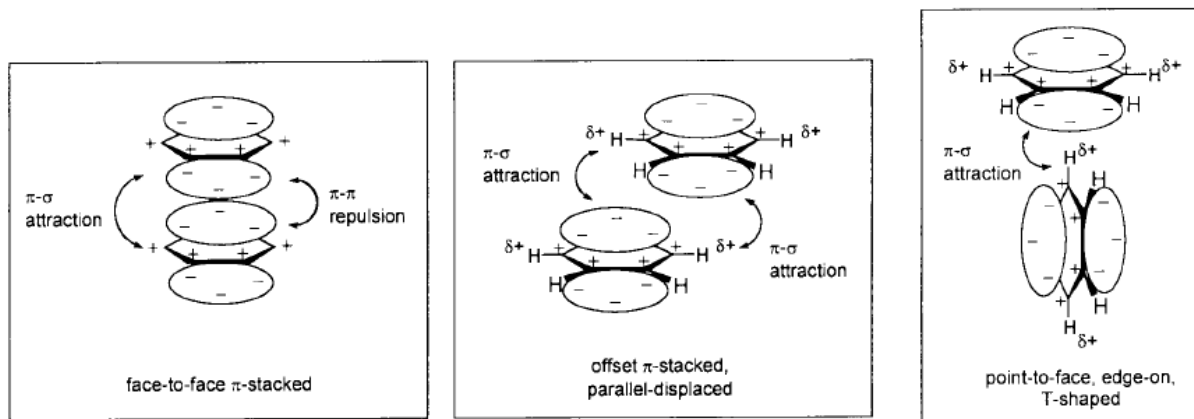


Figure 3.8 Electrostatic interaction of two ideal aromatic molecules with π -electrons with different orientation. (Janiak, 2000)

To understand and analyze the interactions between aromatic molecules, Hunter and Sanders suggested a set of rules based on a simple model of charge distribution. The rules for arenes such as benzene are as follows: i) π - π repulsion dominates in a π -stacked geometry; ii) π - σ attraction is stronger than the π - π repulsion in the offset π -stacked geometry; and iii) π - σ attraction dominates in the edge-on or T-shaped geometry.

A substituent or heteroatom within an arene perturbs the π -system and the uniform charge distribution no longer holds. The distortion of the static dipole results in an electrostatic dipole-dipole and dipole-induced dipole interactions as in Fig. 3.7. The experimental results [22,25] show that the electron withdrawing substituent shows stronger intermolecular attraction than the uniform charge distribution due to the reduced repulsion between the π -electrons. Thus, an electron donating substituent shows the weakest intermolecular attraction. An example of electron withdrawing/donating groups are F, NO₂ and CN / R, OR, NH₂ and NR₂ (R=alkyl).

3.2.3 Molecular alignment

Orientation of a molecule is one of the key aspects of organic film morphology. It is determined by different factors such as molecular shape, film growth kinetics, and anisotropy between the ligands in the case of phosphorescent emitters. Here, we discuss how to measure the orientation of molecules within an amorphous film, and cover the different elements that affect molecular alignment.

3.2.3.1 Measurements of molecular alignment

As mentioned in Chapter 3.2.1, the TDM of a molecule is a small dipole antenna, thus the orientation of the TDM is correlated to the angular intensity profile of the light emission. Therefore, we obtain the TDM orientation by measuring the angle dependent photoluminescence spectra. While measuring the angle dependent spectra, the organic film-deposited glass substrate is attached onto a half-cylinder prism to extract the light trapped in the glass substrate as shown in Fig. 3.9 [26]. This is because a significant portion of the light emitted from the TDM within an organic film is trapped in the glass substrate, which is necessary to achieve an accurate measure of the angular emission intensity profile of the TDM.

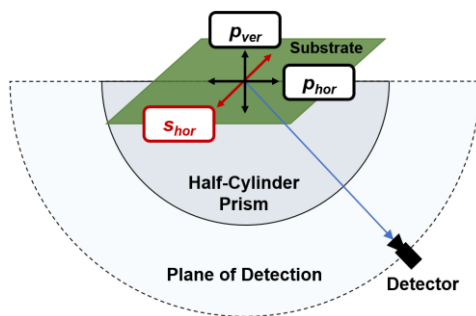


Figure 3.9 Cross-sectional illustration of the set up for angle dependent photoluminescence spectroscopy.

The light trapped in the glass substrate is due to the total internal reflection at the air-glass interface caused by the higher refractive index of the glass ($n_{glass} = 1.45$) versus that of the air ($n_{air} = 1.0$), also known as ‘glass mode’, as shown in Fig. 3.10.

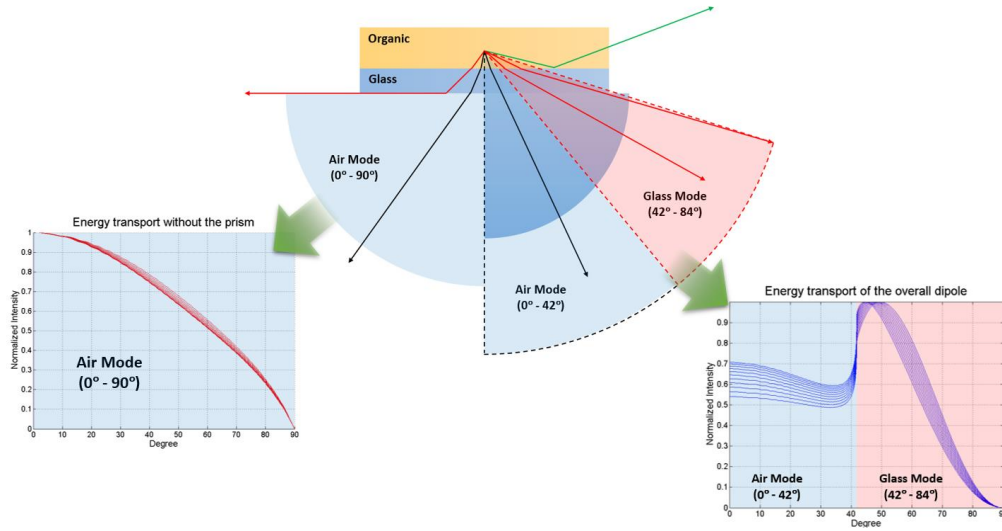


Figure 3.10 Angle dependent photoluminescence spectra with and without the half-glass cylinder.

As shown in the theoretical calculation in Fig. 3.10, the angular intensity profile of the air mode shows a Lambertian profile with no distinct features, therefore the glass mode information is necessary for higher accuracy to fit the measured result to the optical model. In the model, the emission from horizontally aligned TDMs is decomposed into transverse electric (S_{hor}) and magnetic (p_{hor}) modes, whereas the vertically aligned TDM emits into the p_{ver} mode. Then the ratio of horizontal-to-vertical TDMs (θ_{hor}) becomes:

$$\theta_{hor} = \frac{S_{hor} + P_{hor}}{S_{hor} + P_{hor} + P_{ver}}, \quad (3.6)$$

leading to $\theta_{hor} = 0.67$ for random alignment ($S_{hor} = P_{hor} = P_{ver}$), and $\theta_{hor} = 1.0$ for TDMs oriented parallel to the substrate. The angular photoluminescence is measured in the detection of the plane with a linear polarizer parallel to the plane, thus leading to the total intensity profile as:

$$I_{total} = \theta_{hor} \cdot I_{p-hor} + (1 - \theta_{hor}) \cdot (I_{p-ver}). \quad (3.7)$$

The light trapped in the glass substrate increases as the fraction of horizontally aligned TDM decreases since the majority of the light emission power is focused in the direction perpendicular to the TDM. Therefore, as shown in Fig. 3.11, the glass mode peak value decreases with the θ_{hor} .

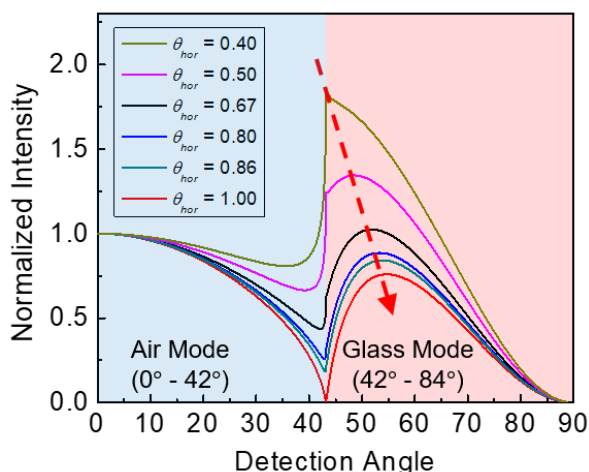


Figure 3.11 Angle dependent photoluminescence spectra of varied θ_{hor} .

The most commonly used methods for measuring molecular orientation are variable angle spectral ellipsometry (VASE), grazing incidence wide angle x-ray diffraction (GIWAXD), and angle dependent photoluminescence spectral measurements (Angle PL) [26–28]. Despite their simplicity and precision, VASE and GIWAXD do not have the sensitivity to resolve the alignment of the dopant emitters in dilute thin films. On the other hand, Angle PL overcomes this problem by directly measuring the emitting dopant orientation. However, Angle PL suffers from the need for precise alignment of the optical components and a slow rate of data acquisition along only a single axis. Since angle dependent photoluminescence spectroscopy requires rotational movement, with distance from the detector to the sample on the scale of the lens focal length, a small tilt or shift of the sample holder causes significant measurement inaccuracies. On the other hand, using a Fourier plane imaging microscope simultaneously measures the radiation at all angles, providing

a sensitive, simple and precise measurement of the TDM orientation in real time [13,14,25]. The use of a Fourier plane imaging microscope for determining the TDM orientation will be discussed in Chapter 5 in detail.

3.2.3.2 Control of molecular alignment

Molecular films deposited in high vacuum have been shown to have superior physical properties compared to the solution-processed samples due to the higher packing density [32], lower enthalpies [33] and reduced reorganization via post thermal annealing [34,35]. One additional advantage of vacuum deposition is the controllability of the molecular orientation during the growth. This is achieved either via shape of the molecule or growth kinetics. In this chapter, we discuss the methods to control the molecular alignment in vacuum deposited films in detail.

Via Molecular shape

The shape of a molecule, including its length, bulkiness, and planarity is one of the factors affecting its orientation. The dependence of molecular orientation on its shape was shown by Yokoyama, et al., demonstrating that the optical anisotropy of an organic film increases with the aspect ratio or flatness of the molecule. The optical anisotropy of a film is correlated with the orientation of the molecule since the refractive index of a film is proportional to the polarizability as:

$$\varepsilon_r(\omega) = [n(\omega) + ik(\omega)]^2 = 1 + 4\pi\chi(\omega) \quad (3.8)$$

where ε_r is the relative dielectric constant, and χ is the susceptibility of the ensemble of molecules. Since the molecular polarizability is enhanced along the direction of π -conjugation, as mentioned

in Chapter 3.1.2, the direction of higher refractive index corresponds to the direction of molecular axis for molecules with long chain π -conjugation. By comparing the ordinary/extraordinary refractive indices of the film, Yokoyama, et al., concluded that as the molecule is longer or have a planar shape, the molecule shows more horizontal orientation with respect to the substrate plane as shown in Fig. 3.12.

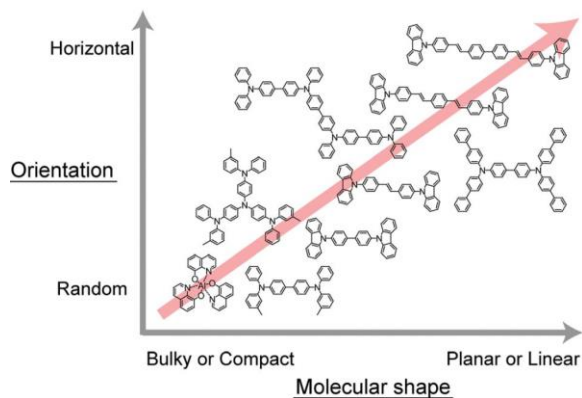


Figure 3.12 General relationship between the molecular shape and orientation.
(D. Yokoyama, 2011)

Referring to this trend, Byeon and Kim, et al., [36] used three thermally activated delayed fluorescent (TADF) molecules, CzTrz, BCzTrz, and TCzTrz, which are molecules of different lengths comprising carbazole, biscarbazole and triscarbazole donor units, respectively (molecular structures in Fig. 3.13a). The molecules show different fractions of horizontally aligned TDM depending on the length of the molecules as shown in Fig. 3.13b.

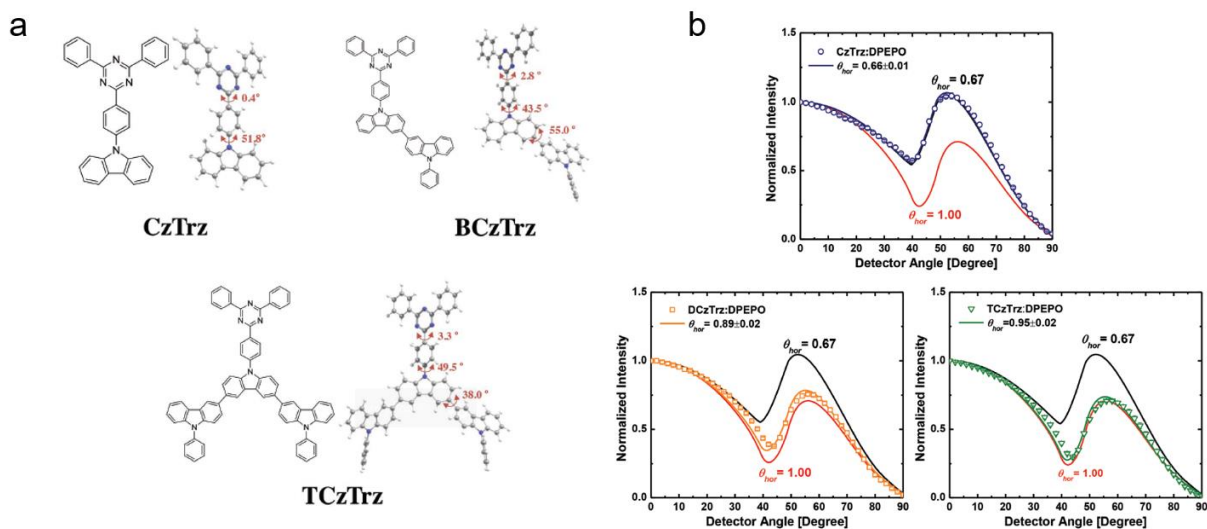


Figure 3.13 Molecular structures and their TDM orientation used in the experiment. (Byeon and Kim, et al., 2018)

As a result of the increased fraction of horizontally aligned molecules, the outcoupling efficiency was significantly improved, therefore leading to an increased external quantum efficiency as shown in Fig. 3.14.

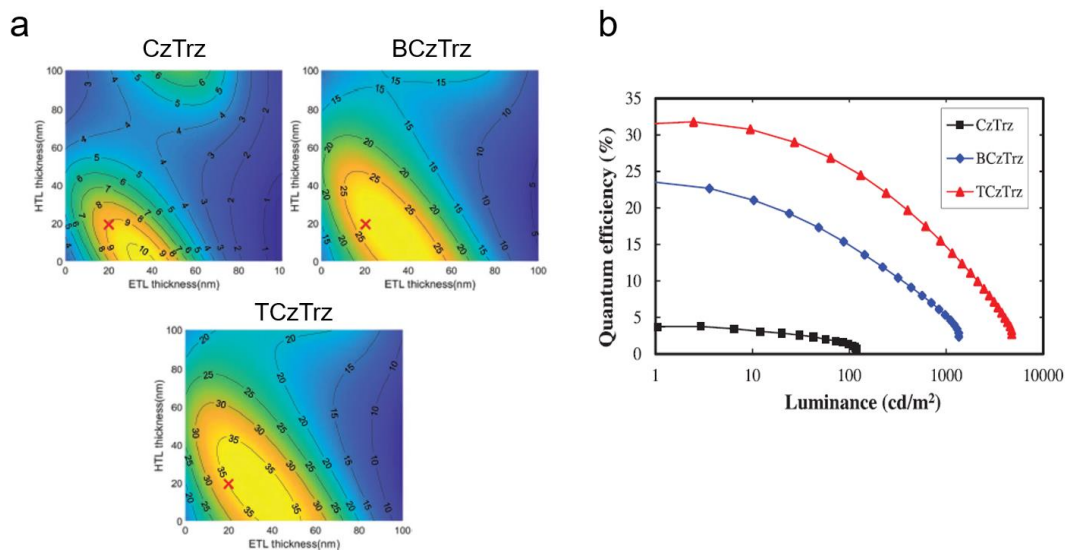


Figure 3.14 Calculated outcoupling efficiency and measured EQE for the three TADF molecules of varied molecular lengths. (a) Calculated based on the horizontally aligned TDM. (b) Identical device structures with varied dopant emitter molecules. (Byeon and Kim, et al., 2018)

Via Growth Kinetics and Ligands

Organic materials are charge neutral particles, thus the elements comprising a film are physically bonded by either Coulombic interaction or van der Waals bonds. Therefore, the understanding of which of these forces dominates the growth kinetics is the key to efficiently controlling the molecular orientation during film growth in a vacuum. Three different mechanisms have been proposed: i) large dipole-dipole interaction of a dopant molecule showing strong Keesom force causes molecular aggregation that leads to randomization of the TDM orientation [37–40]; ii) the Coulombic attraction of the electro-negative and positive regions of molecules cause the molecular alignment [41–45]; and iii) the anisotropic interaction of aliphatic and aromatic regions of the molecule drives the alignment [20,46].

Theory (i) was proposed by Graf, et al. [37] with various Ir-complexes of different static dipole moments and molecular diameters as shown in Table 3.1. Here the dipole-dipole attraction induced molecular aggregation was suggested as the main cause of the random orientation of Ir(ppy)₃. The other Ir-complex dopants showed anisotropic horizontal alignment of dopant TDMs due to the weaker dipole potential compared to Irppy₃.

Table 3.1 Ir complexes used for alignment studies.

Calculated result of static dipole moment (μ), molecular diameter (r), dipole–dipole potential U relative to the dipole–dipole potential of Irppy₃ and the anisotropy factor ($a = 1 - \theta_{\text{hor}}$). (Graf, et al., 2014)

	μ [D]	r [Å]	$U/U_{\text{Ir(ppy)}_3}$	a
Ir(ppy) ₃	6.40	11.4	1.00	0.31
Ir(ppy) ₂ (acac)	1.66	11.0	0.08	0.23
Ir(chpy) ₃	2.02	11.6	0.09	0.23
Ir(dhfp) ₂ (acac)	1.16	17.7	0.01	0.25
Ir(BT) ₂ (acac)	1.76	12.6	0.05	0.22
Ir(MDQ) ₂ (acac)	1.75	13.8	0.04	0.24
Ir(piq) ₃	5.20	13.5	0.39	0.22

Theory (ii) is shown by a set of host and dopant molecules with various surface potentials, demonstrating the effect of different electrostatic interaction energies. Here, the surface potentials

of different molecules were calculated via DFT calculations shown in Fig. 3.15. Moon, et al., [42,44] and Huh, et al., [45], showed that the fraction of horizontally aligned TDMs of a dopant molecule varies when doped into different host matrices. From the calculation and the measured orientation, it was shown that the extent of intermolecular binding energy between the molecules is positively correlated with the fraction of horizontally aligned TDMs. The binding energy was shown to depend on the electrostatic interaction and the geometry. This demonstrates that the electrostatic interaction between the host and dopant drives the orientation of the molecule.

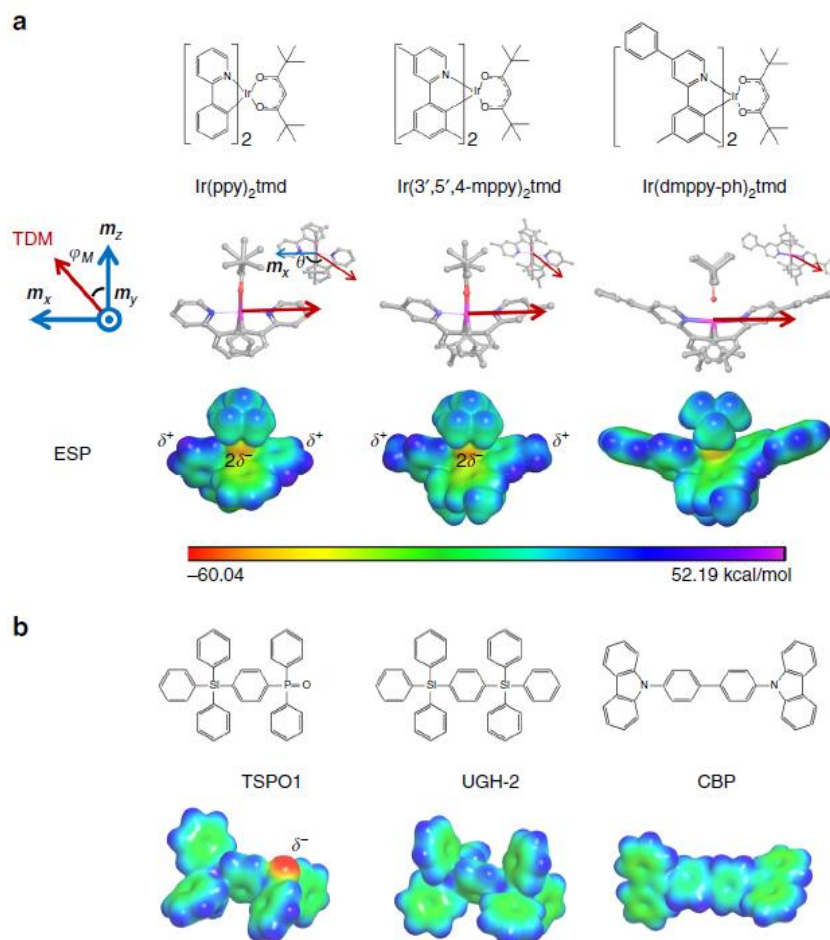


Figure 3.15 DFT calculation for the molecules used in the alignment studies. Ir-complexes dopants (a) and host molecules (b) used for the experiment. The calculated electrostatic potential contour is shown on the bottom with the colored scale bar indicating the potential quantity. (Moon, et al., 2017)

In theory (iii), tridentate heteroleptic Ir-complexes comprising 1 aliphatic and 2 aromatic ligands [(bppo)₂Ir(acac)], and two different types of aromatic ligands [(ppy)₂Ir(bppo)]/[(ppy)₂Ir(bpp)] were synthesized as shown in Fig. 3.16. The carbonyl (C=O) group in bppo was employed due to the large static dipole moment. This is important since, in theory (i) and (ii), the static dipole moment is the key element driving the molecular orientation.

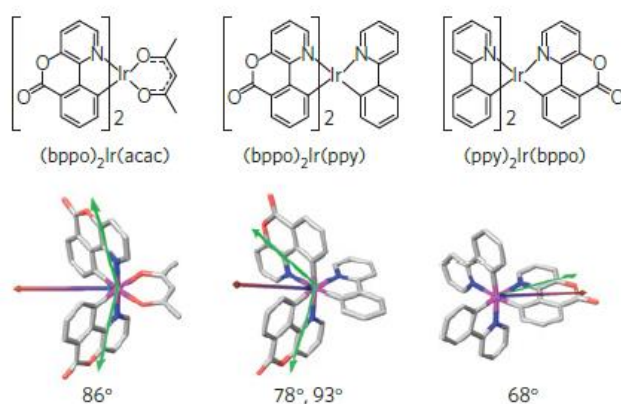


Figure 3.16 Ir-complexes used for the organic surface-ligand interaction experiment. (Jurow, et al., 2015)

The measured orientation in Fig. 3.17 shows that only (bppo)₂Ir(acac) shows horizontal alignment whereas (bppo)₂Ir(ppy) and (ppy)₂Ir(bppo) show random orientation even though they have strong static dipole moments. This phenomenon is explained by the surface boundary created between the pre-deposited organic host matrix surface and the vacuum environment during film growth, forcing asymmetric interactions of the dopant molecule which drives it to orient before being buried by the next amorphous layer of the host material. However, which ligand among the aliphatic or aromatic ligands interacts with the host matrix is unclear from this work, which is investigated in Chapter 7.

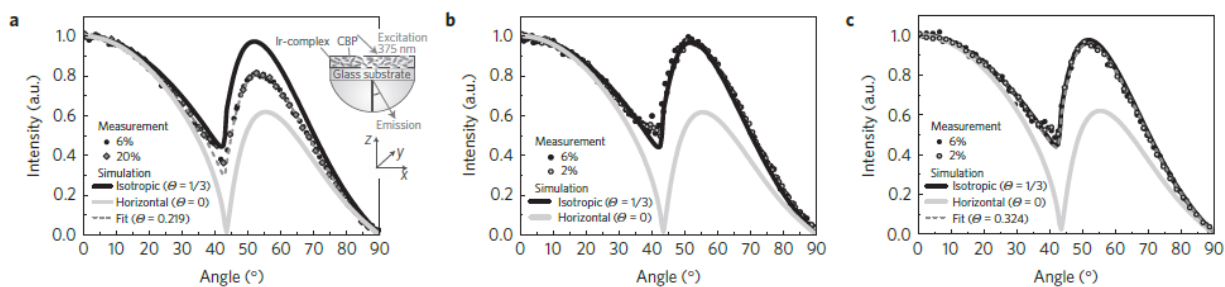


Figure 3.17 Measured orientation of the Ir-complexes $(ppy)_2Ir(bppo)$ shows horizontal orientation (a), and $(bppo)_2Ir(ppy)$ and $(bppo)_2Ir(ppy)$ shows random orientation (b and c). (Jurow, et al., 2015)

3.2.4 Crystallinity

Unlike the devices based on inorganic materials, crystalline films are not necessary for OLEDs since the hopping-type conductivity in amorphous thin film is adequate. However, charge conduction and extraction are critical in organic photovoltaics (OPVs) and organic field effect transistors. There are numerous advantages to using crystalline organic films such as: i) tunable optical/electrical properties depending on the packing direction and morphology [47,48]; ii) long exciton diffusion length [13,49]; and iii) flexibility and elasticity [50].

Structural templating is a method to control the morphology of a crystalline organic film via π - π interaction. The varied morphology of crystalline films via molecular template growth leads to the modified physical properties of the film [51,52]. For template growth, a thin molecular template layer is pre-deposited on the surface, where the next organic semiconductor film is grown on top of it. The template layer induces the growth of organic semiconductor molecules by intermolecular interactions such as lattice matching and π - π interactions, thus controlling the orientation, crystal size, film morphology, and electronic structure [46,52,53]. The control of molecular orientation of light emitting molecules using the molecular template growth is explored in Chapter 7.

The exciton diffusion length and charge mobility are also closely linked with the crystallinity of an organic film since the exciton diffusion is primarily attributed to Förster-assisted migration, closely correlated with the molecular orbital wave function overlap. Lunt, et al., [52] showed the correlation between the exciton diffusion length and the crystallite size of the PTCDA film by controlling the growth conditions with organic vapor phase deposition. As shown in Fig. 3.18, the exciton diffusion length increases with the fluorescence quantum yield and the mean crystal size since the non-radiative losses at grain boundaries is found to be $\sim 10^4$ times larger than in bulk crystals. This shows that the film becomes less defective as the film crystallinity (\propto mean grain size) increases, leading to an increased exciton diffusion length.

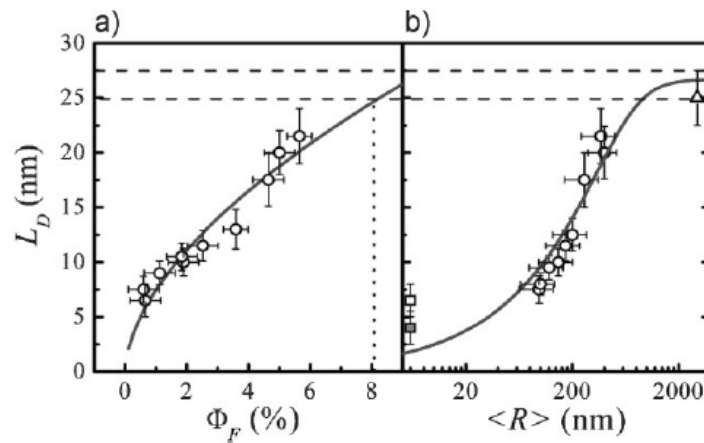


Figure 3.18 Measured exciton diffusion length. Exciton diffusion length (L_D) vs. fluorescence quantum yield (a) and mean crystal diameter (b). (Lunt, et al., 2010)

3.3 Impact of organic thin film morphology

3.3.1 Electrical aspect

As mentioned in Chapter 3.1.2, a current path in an organic film forms through π -conjugation and the overlap between the π -conjugates. Therefore, aligning the π -conjugation and π - π overlap with the current path direction becomes crucial for improving the device current characteristics. Sullivan, et al., [47] used PTCDA as the template layer to self-assemble the CuPC,

a planar molecule with a large π -system that enables efficient π - π stacking, in a CuPC-C₆₀ OPV system as shown in Fig. 3.19a to improve the short circuit current density and achieve a ~60% enhancement by modifying the crystal orientation of CuPC molecules. For vertical devices such as OLEDs or OPVs, the current path is perpendicular to the substrate, meaning that the planar molecules which π - π overlap should be horizontally aligned. In contrast, the current path of organic thin film transistors is parallel to the substrate plane where π -stacking should occur between the vertically aligned planar molecules for an optimal current flow.

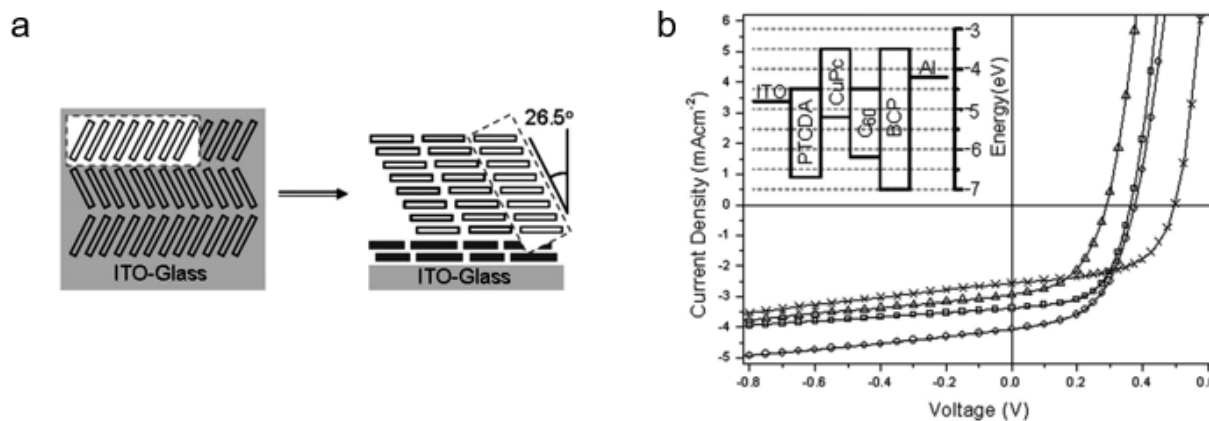


Figure 3.19 Influence of morphology on the electrical performance

(a) Schematic illustration showing the structure of CuPc film with (left) and without (right) the PTCDA templating layer. (b) J-V curves for a series of OPV devices with the varied thickness of the PTCDA template layer (0 Å crosses, 10 Å circles, 20 Å squares, and 50 Å triangles). (Sullivan, et al., 2007)

3.3.2 Optical aspect

Solvation effect

The solvation effect occurs when an excited molecule interacts with its environment, also known as solvatochromism. When an excited molecule is surrounded by a dielectric environment, the molecule polarizes the surrounding medium, causing a relaxed excited state energy. Since the effect is caused by polarization of the surrounding environment, solvation effects are correlated to the static dipole of the excited molecule and its surrounding molecules. Nonpolar molecules tend to show a weaker solvation effect than polar molecules, since nonpolar molecules exhibit weak

London dispersion forces at a very short range ($\sim 1/r^6$) compared to polar molecules showing dipole-induced forces ($\sim 1/r^3$). The degree of freedom of the surrounding molecules is another important element for the solvation effect, since the higher the degree of freedom of the surrounding molecules, the better they realign to reduce the excited state energy.

In- and out-coupling of light absorption/emission for OPV/OLEDs

As discussed in Chapters 3.2.1 and 3.2.3, an emitting or an absorbing molecule in an OLED or OPV can be regarded as a small dipole antenna. Since a dipole antenna emits or absorbs a majority of light in the direction perpendicular to its TDM, as shown in Fig. 3.20a, the orientation of the emitting and absorbing molecule is a crucial element that determines the coupling of emitted or absorbed light into different optical modes. The different optical modes within an OLED optical microcavity and the relation with the TDM orientation will be discussed in detail in Chapter 4.3.3.

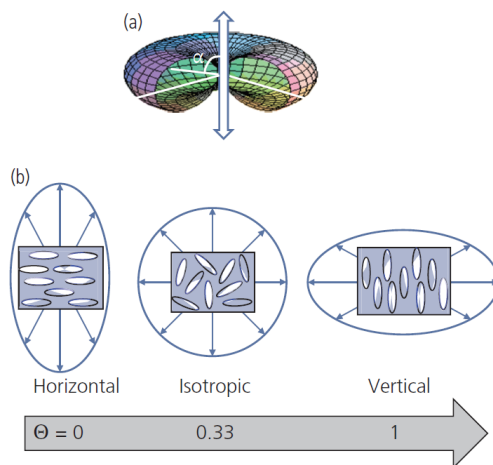


Figure 3.20 Emission profile from varied orientations of TDMs
 (a) Schematic illustration of a dipole antenna radiation. The white arrow shows the TDM vector and the contour shows the E-field.
 (b) Varied orientation of the molecules (white oval) with the TDM along its long axis, changing the angular emission profile (blue lines). θ shows the fraction of the vertically aligned TDM. (Adapted from Forrest, *Organic Electronics*, 2020)

Since the coupling of optical modes varies depending on molecular orientation, the external quantum efficiency of OLEDs and OPVs are correlated with the molecular orientation. Therefore, research on molecular alignment has been done as discussed in Chapter 3.2.3.2.

Chapter 4 Organic Light Emitting Devices

The most successful organic electronic devices today are OLEDs, creating a multi-billion dollar display industry due to the massive success of mobile displays. Furthermore, OLEDs are extending their markets to various light emission industries such as televisions, transparent displays and lighting due to the high color purity, power conversion efficiency, flexibility, transparency, and facile fabrication process (especially in large-scale). In this chapter, we discuss the basic principles of OLEDs with their benchmarks and characterization methods. We also investigate optical modes in the weak optical microcavity of OLEDs and discuss different optical loss channels.

4.1 Device structure and operating principle of OLEDs

In its simplest form, an OLED consists of semiconductor layers sandwiched between two contacts. Depending on the opacity of the top and bottom contact, an OLED is referred to as a top or bottom emitting or transparent OLED. Top or bottom emitting OLEDs have a transparent electrode on one side, usually comprised of ITO or IZO, paired with a reflective metal mirror electrodes at the other side, usually comprised of Al or Ag. In a conventional, bottom-emitting OLED, the anode comprises transparent ITO, and Al is used as the reflecting cathode as shown in Fig. 4.1. To prevent the oxidation of organic molecules during operation, devices are encapsulated in an oxygen- and water-free environment after the fabrication.

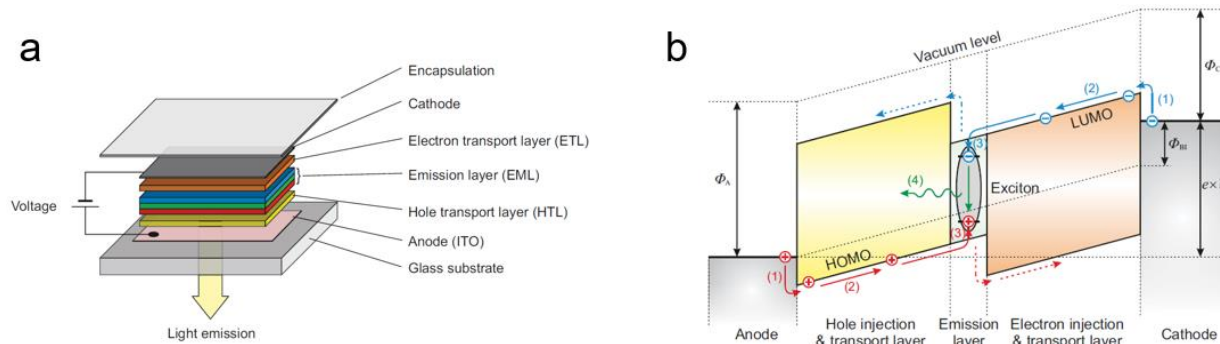


Figure 4.1 Schematic illustration of the OLED structure and its energy levels. (W. Brütting, et al., 2013)

An OLED comprises of multiple layers with different purposes, such as charge injection/transport/blocking or exciton generation/recombination/blocking layers. Organic materials of different energy levels and work functions are chosen for these specific traits.

Hole and electron injection layers (HIL, EIL) are deposited right after the anode and before the cathode, respectively, which facilitate charge injection into the device. The primary function of injection layers is to reduce the injection barriers, which is done by either depositing a small amount of dipolar materials to tilt the energy level [54], to shift the work function of the cathode [55], or to dope the interface organic materials [56–58]. Al / LiQ works well for the electron injection since Li ions are liberated from LiQ during the Al deposition and dope the interface to reduce injection barrier of the electrons [59]. For hole injection, MoO₃ or HATCN is often deposited on the ITO anode due to the efficient formation of an Ohmic contact at the ITO/HIL/hole-transport layer heterojunction interface as a result of its high work function that causes electrons to transfer from the HIL to the ITO [60].

The purpose of a charge transport layer is two-fold: i) to transport charge carriers to the emissive layer; and ii) block the leaking charge carriers and excitons from the emissive layer. Therefore, it is common to use a high-mobility material as the charge transport layer (hole- and electron-transport layer, HTL and ETL) while using a ~5 nm thick charge or exciton blocking layer

(XBL) for optimized device performance. For efficient charge blocking, the EBL should have energetically shallower LUMO and the HBL should have deeper HOMO energies with respect to the vacuum level compared to the emissive layer (EML) molecules. Since the generated excitons should not leak from the EML, the blocking layers should show equal (or larger) exciton energy states than those of the EML.

The EML of an OLED is where the holes and electrons recombine, generating excitons. The EML comprises a mixture of different types of molecules depending on its purpose. Phosphorescent OLEDs (PHOLEDs) generally employ a host-guest system with dopant emitter molecules mixed into the host matrix at a concentration ranging from 1 to 20% depending on the device characteristics. The host matrix usually has a larger energy gap than the dopant to enable exothermic energy transfer of excitons from the host to the dopant, which enables an efficient light emission from the dopant. Since most organic molecules are unipolar, i.e. the charge mobility for holes and electrons are significantly different, two host molecules of different polarities are often mixed together in the EML for efficient hole and electron conduction, also known as the “co-host EML” [61,62]. Also, an EML covering a broad visible wavelength spectrum for white OLEDs is also often used, with multiple dopants mixed together or deposited in separate regions as shown in Fig. 4.2 [63–65].

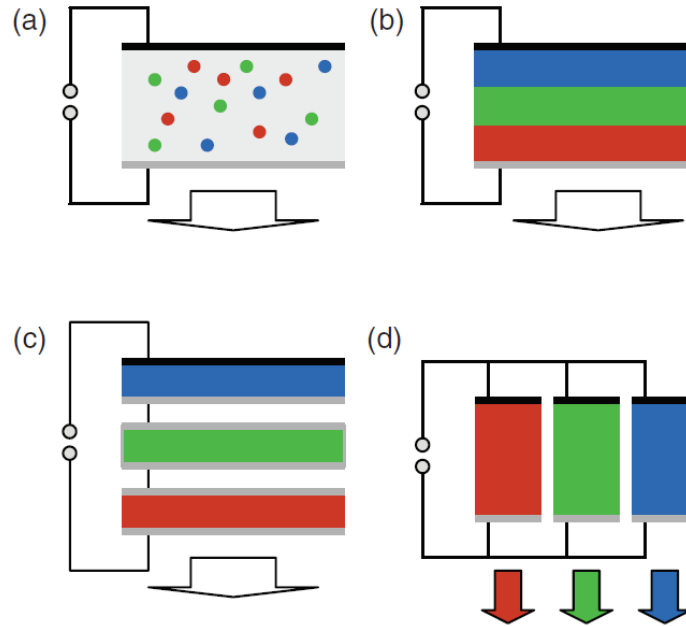


Figure 4.2 Approaches to obtain white light from OLED EMLs.
 (a) Blended dyes in a single layer (b) Single stack comprising layers emitting different colors (c) Separated OLED stacks connected via charge generation layers (d) OLEDs emitting different colors deposited side by side. (Gather, et al., 2011)

4.2 OLED benchmarks

4.2.1 Colorimetry

Displays and lighting are related to how humans perceive an image. An experience through the display becomes livelier as an image approaches the real color of the object. Also, as the spectrum of a lighting fixture is closer to the black body radiation, the experience becomes more natural since the sun is a near perfect black body radiator (surface temperature of 5780 K). How the perceived color from an object or an image differ from its real color is closely related to the function of human eyes. Thus it is important to understand how human eyes perceive color.

Humans only perceive a specific range of wavelengths between $\lambda=380$ to 780 nm (visible spectrum). Eyes are comprised of different types of acceptor cells, three cone cells and one rod cell, as shown in Fig. 4.3a, which differentiate the chromaticity and luminance, respectively. Three types of cones cells cover the spectral ranges as shown in the responsivity spectrum in Fig. 4.3b.

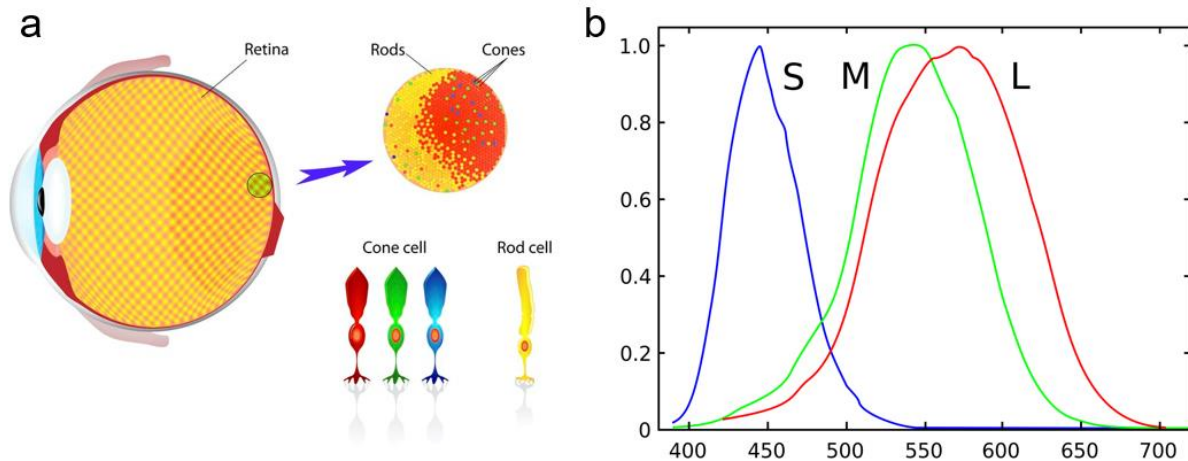


Figure 4.3 An eye retina covered with light-sensitive rod and cone cells. (Adapted from Designua/Shutterstock.com)

There are different modes of the eye vision depending on the illumination condition. In low luminance (10^{-6} to 10^{-3} cd/m^2) conditions, cone cells are nonfunctional and only rod cells are operational, known as scotopic vision. In normal light conditions (10 to 10^8 cd/m^2) photopic vision occurs, which is a mode when the vision of cone cells dominate enabling color perception having a significantly improved visual acuity and temporal resolution compared to scotopic vision. Mesopic vision occurs in intermediate lighting conditions (10^{-3} to $10^{0.5}$ cd/m^2) and a combination of scotopic and photopic vision gives an inaccurate visual acuity and color discrimination. Due to the different acceptors activated in different modes, the spectral sensitivity varies in each mode as shown in Fig. 4.4.

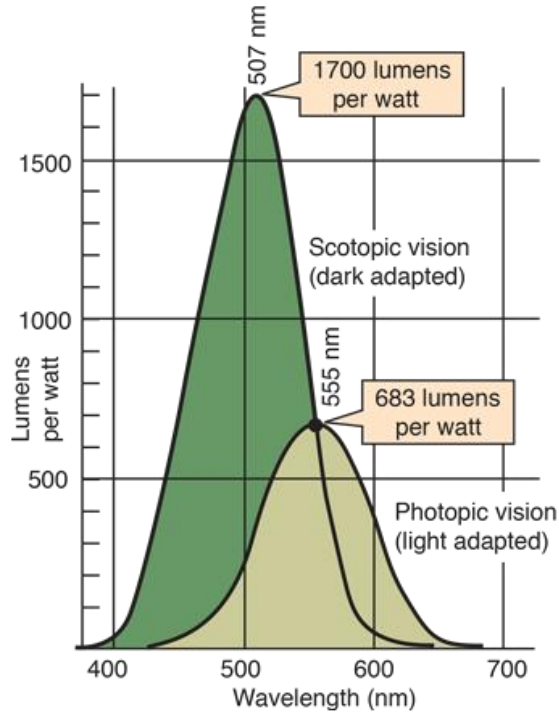


Figure 4.4 Luminous efficacy curves for human vision. Lumens is defined to be 683 lumens/watt at the peak efficacy of the photopic vision curve. The efficacy of photopic and scotopic curves meet at 555 nm. (Adapted from Williamson & Cummins)

Chromaticity of a light source is quantified by the Commission Internationale de l’Eclairage (CIE) 1931 (x, y) chromaticity diagram. The diagram is based on the color matching functions (CMF) shown in Fig. 4.5a which gives a numerical description of the chromatic response of a standard colorimetric observer. The x and y chromaticity coordinates for the CIE chart are then determined as:

$$x = \frac{X}{X + Y + Z}, \quad y = \frac{Y}{X + Y + Z} \quad (4.1)$$

where X , Y and Z are the tristimulus values determined for a source with a spectral radiance, $L(\lambda)$, as:

$$\begin{aligned}
 X &= \int_{380}^{780} L(\lambda) \bar{x}(\lambda) d\lambda \\
 Y &= \int_{380}^{780} L(\lambda) \bar{y}(\lambda) d\lambda \cdot \\
 Z &= \int_{380}^{780} L(\lambda) \bar{z}(\lambda) d\lambda
 \end{aligned}
 \tag{4.2}$$

The resulting CIE coordinate diagram is shown in Fig. 4.5b, which shows the visible chromaticity of an average person. The curved boundary shows monochromatic light while the straight boundary is known as the line of purples. If one chooses any two points of the diagram, then all colors within the line is produced by mixing the two colors of the points. When three points are selected, all colors inside the triangles are be formed by mixing the three point colors. Therefore, it is better to have the three points in the CIE diagram further apart, forming a larger triangle, to achieve a better color rendering capacity with an RGB display.

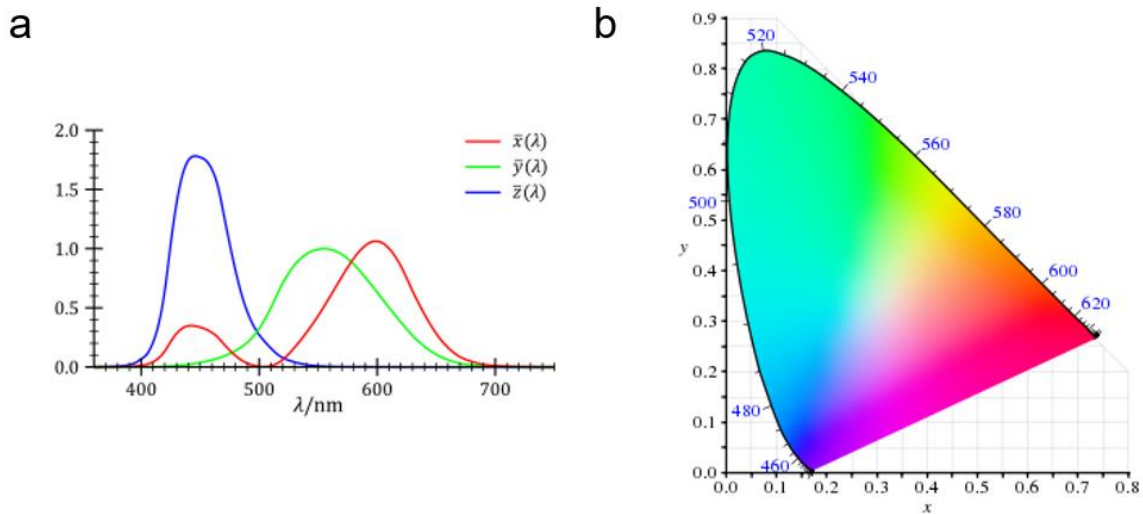


Figure 4.5 CIE color matching function and CIE 1931 color space chromaticity diagram. (Adapted from wikipedia.org)

4.2.2 Performance parameters

External quantum efficiency (EQE) is a ratio between the number of emitted photons towards the viewing direction vs. number of injected electrons. EQE is expressed as:

$$\eta_{EQE} = \eta_{IQE} \cdot \eta_{out} = (\gamma \cdot \chi_{ST} \cdot \Phi_{PL}) \cdot \eta_{out} \quad (4.3)$$

where η_{IQE} is the internal quantum efficiency which shows the ratio between the number of generated photons inside the OLED structure vs. number of injected electrons, η_{out} is the outcoupling efficiency which shows the ratio between the number of generated photons vs. number of emitted photons towards the viewing direction from the OLED structure, γ is the charge carrier balance factor, χ_{ST} is the spin factor describing the number of emitted photons compared to the number of generated excitons, and Φ_{PL} is the photoluminescence quantum yield (PLQY).

The charge carrier balance factor (γ) is the ratio between the recombined electrons and the injected electrons. In modern OLEDs, γ is near unity due to the efficient confinement of the injected charges and generated excitons. The spin factor (χ_{ST}) varies depending on the type of emitter molecules. Fluorescent molecules show negligible spin orbit coupling, only being able to emit singlet excitons. Therefore, fluorescent molecules show $\chi_{ST} = 25\%$ due to the singlet-to-triplet exciton formation rate of 1:3 from the injected charge carriers. Recently, however, fluorescent molecules showing much higher χ_{ST} by triplet-triplet fusion ($\sim 83\%$) [66] or delayed fluorescence (100%) [67] are being actively explored.

Photoluminescence quantum yield (Φ_{PL}) measures the ratio between the absorbed and emitted number of photons. It is also described as the ratio between the radiative decay to the total decay rate of the excited state as:

$$\Phi_{PL} = \frac{k_r}{k_r + \sum k_{nr}} \quad (4.4)$$

where k_r and k_{nr} denote the radiative and non-radiative decay rates, respectively. The decay rate of a material is closely related to the natural decay lifetime (τ) as

$$\tau = \frac{1}{k_r + \sum k_{nr}}. \quad (4.5)$$

Since the decay lifetime, rate and quantum yield of a material are closely related, understanding the decay characteristics of a material enables determining whether a system is suitable for LEDs or solar cells.

The radiative decay rate can be modified by varying the optical microcavity conditions, which is also known as the Purcell effect. The Purcell effect describes the change of spontaneous emission rate according to its environment, showing that the radiative decay rate of an excited state is proportional to the cavity quality factor (Q) and inversely proportional to the mode volume (V) of a cavity [68–70]. The non-radiative decay of the system includes several elements, such as exciton annihilation due to an Auger-recombination type of energy transfer, thermal relaxation, trap-assisted quenching, etc. [71]

The optimal dopant concentration in the OLED EML comprising host-dopant mixtures depends on the PLQY. The PLQY decreases with the dopant concentration due to concentration quenching as in Fig. 4.6 [72]; thus, a low doping concentration tend to increase the *EQE* of an OLED. However, low doping concentration does not always maximize the *EQE* of an OLED since the charge carrier balance and exciton density profile are also affected by the doping concentration when the dopant molecule carries the charge carriers within the EML. Thus, an optimal design of the device structure by tuning the different conditions is necessary.

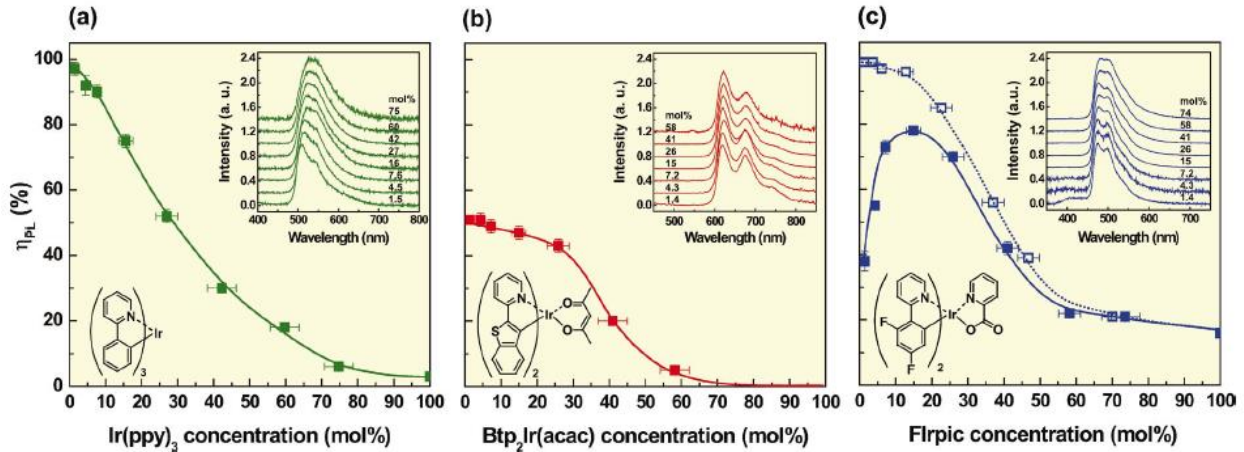


Figure 4.6 PLQY vs. dopant concentration Measured in Irppy₃:CBP (a) Ir(btpp₂)(acac):CBP (b) and Irfpic:CBP (c) and Irfpic:mCBP EMLs. (Kawamura, et al., 2005)

4.3 Optics of OLEDs

4.3.1 Optical loss channels

A significant proportion of photons emitted within an OLED is trapped in an optical microcavity structure due to the optically dense organic material and glass substrate compared to the air. Also, light is trapped in the metal cathode-organic interface due to the strong interaction between photons and electrons at the metal surface, which are also known as ‘polaritons.’ The generated photons couple into different optical modes depending on their propagation direction as shown in Fig. 4.7a.

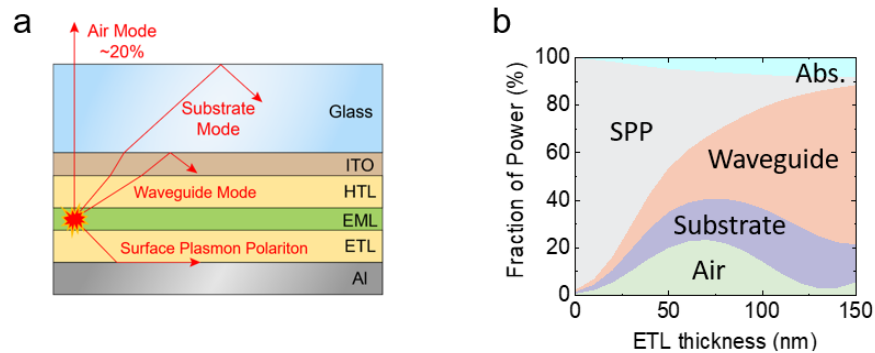


Figure 4.7 Optical loss channels in OLEDs and their power distribution. (a) Schematic illustration of different optical loss channels in OLEDs. (b) Modal power distribution of optical loss channels in OLEDs as a function of ETL thickness.

Air modes are the photons emitted to the viewing direction, which consist of only ~20% of the generated light power for conventional glass substrates. Fig. 4.7b illustrates the significance of outcoupling schemes to improve the performance of OLEDs. Substrate modes are trapped in the substrate due to the total internal reflection (TIR) at the glass-air interface. Substrate modes are efficiently outcoupled by structuring the glass-air interface using microlens arrays [73–75] and other methods [75,76]. Photons emitted at larger angles than substrate modes couple into waveguide modes, confined within the high refractive index active organic and transparent contact layers. Photons can also couple into lossy surface plasmon polariton (SPP) modes at the metal contact [77], where they are trapped at the organic/metal interface.

4.3.2 In-plane wavevector

An OLED is a multilayer stacked dielectric waveguide as shown in Fig. 4.8a [78], thus the propagation direction of a wave varies depending on the refractive index of the layer. Therefore, a quantity which remains constant regardless of the layer properties is required, which is the in-plane component of a wavevector. A wavevector is a quantity associated with the momentum of the light, carrying information about the medium in which the wave propagates as well as the propagation direction as,

$$\vec{k} = \frac{\vec{p}}{\hbar} = \frac{2\pi n}{\lambda} \quad (4.6)$$

where p is the momentum of a traveling wave, n is the refractive index of the layer, and λ is the wavelength. Then the in-plane wavevector is:

$$\kappa = |\vec{k}| \sin \theta = \left| n \frac{2\pi}{\lambda} \right| \sin \theta = \left| n \frac{\omega}{c} \right| \sin \theta = |nk_0| \sin \theta \quad (4.7)$$

where θ is the angle of light propagation with respect to the interface normal. The magnitude of the in-plane wavevector contains information about the propagation angle and remains constant regardless of the propagation medium according to the boundary conditions dictated by Maxwell's equations. Therefore, a dispersion diagram with respect to the in-plane wavevector can be plotted as shown in Fig. 4.8b.

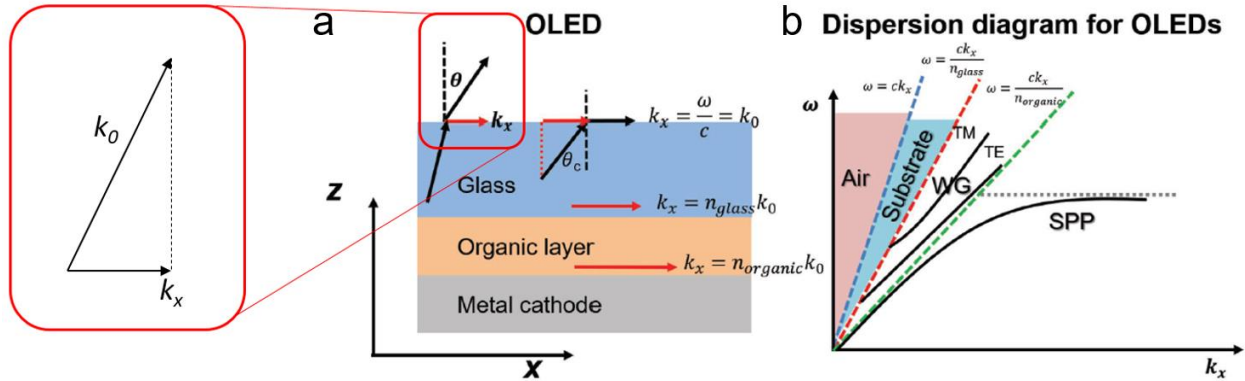


Figure 4.8 In-plane wavevectors in OLEDs. (a) Schematic illustration of multilayer stacked OLED with propagating waves. (b) Dispersion diagram for a bottom emitting OLED. (Salehi, et al., 2019)

In the dispersion diagram, the four different modes -- air, substrate, waveguide and surface plasmon polariton -- are shown. The air, substrate, and waveguide modes are waves propagating with in-plane wavevectors between 0 and k_0 , k_0 and $n_{\text{glass}}k_0$, $n_{\text{glass}}k_0$ and $n_{\text{org}}k_0$, respectively, whereas the SPP modes are waves with in-plane wavevectors larger than $n_{\text{org}}k_0$. As such, the refractive index of each layer plays a role determining how the light emission power is distributed [78].

4.3.3 Mode analysis for waveguide and SPP modes

The spontaneous emission rate of an emitter follows Fermi's golden rule as [21]

$$\Gamma_{ij} = \frac{2\pi}{\hbar} |M_{ij}|^2 \rho(\nu_{ij}) \quad (4.8)$$

where Γ is the transition rate between the excited state (i) and the lower energy state (j) of the emitter, M is the coupling rate between the initial and final states depending on the perturbing Hamiltonian that causes the transition, and ρ is the density of photonic states at the transition frequency, ν . The coupling rate, M , is mostly dictated by the material character of an emitter or the film morphology such as the oscillator strength and TDM orientation whereas the photonic density of states is usually managed by the properties of the optical microcavity (Purcell effect). Therefore, optimizing the optical microcavity plays a significant role in device performance by determining the decay lifetime of excitons and affecting the waveguide mode environment.

Waveguide modes appear due to the interference of the propagating waves, therefore only a certain number of modes, satisfying the standing wave conditions in the z -direction, are supported by the optical microcavity as shown in Fig. 4.9. The lowest frequency of a wave that exist in a slab waveguide is known as the cutoff frequency. This discrete nature of waveguide modes differs from the continuous substrate modes. The difference occurs from the thin slab of the waveguide mode, enabling the light reflected from the top and bottom interfaces to interfere with each other as a Fabry-Perot Etalon. Also, due to the different interference environment, the two different polarizations, transverse electric (TE) and transverse magnetic (TM) modes show different eigenmodes within the waveguide. Therefore, the TE and TM modes should be treated separately.

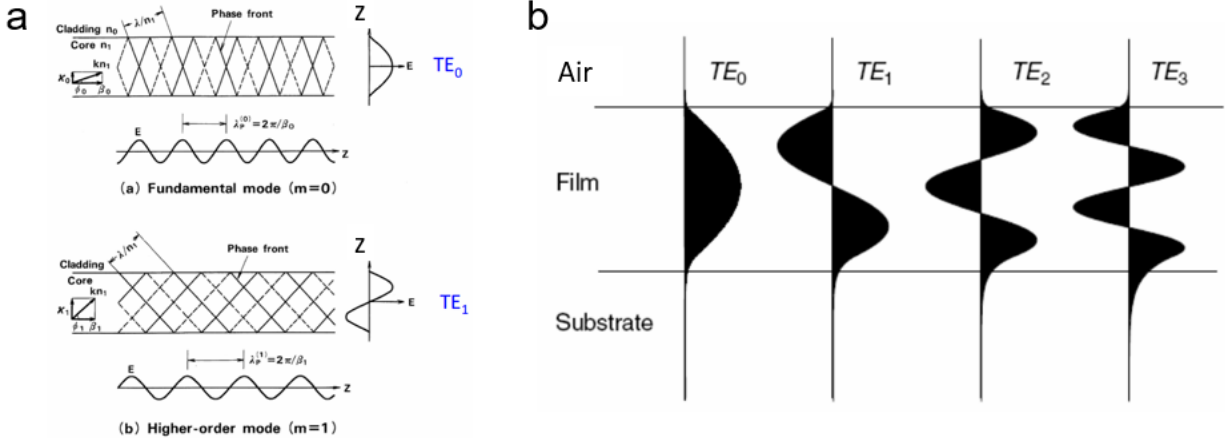


Figure 4.9 Waveguide modes

(a) Schematic illustration of wave propagation in a slab waveguide. (b) Field distribution in the slab waveguide. (Adapted from G. Lifante, *Integrated Photonics Fundamentals*)

Surface plasmons are quanta describing the longitudinal oscillation of free electrons at the metal surface. These are transverse magnetic in character, and the generation of surface charges by the oscillation requires an electric field perpendicular to the surface as shown in Fig. 4.10a. Thus, only light with TM (p) polarization is coupled into SPP modes. The dispersion of SPP modes is strongly dependent on the permittivity of the metal and the dielectric material as,

$$k_{SP} = k_0 \sqrt{\frac{\epsilon_d \epsilon_m}{\epsilon_d + \epsilon_m}} \quad (4.9)$$

where ϵ_m and ϵ_d are the frequency-dependent permittivities of the metal and dielectric materials, respectively. The in-plane wavevectors of SPs are usually larger than the dielectric, leading the SPP modes to be non-radiative. Thus, as shown in Fig. 4.10b, the field in the z -direction is evanescent, preventing the power from propagating away and strictly confined within the surface, causing it to be the most challenging loss channel in OLEDs to overcome. A method to eliminate the SPP losses in OLEDs is discussed in Appendix B.

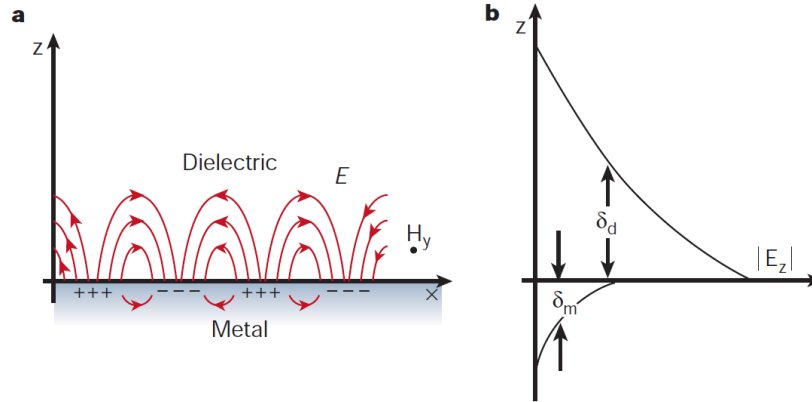


Figure 4.10 Surface plasmon polariton modes

(a) Schematic illustration of SPP mode propagation viewed at the plane of incidence. (b) Field distribution of SPP modes. δ is the decay length of the field, where δ_d is the order of half the wavelength of light involved, whereas δ_m is determined by the skin depth of the metal. (Barnes, 2003)

In the far-field regime, light with an in-plane wavevector greater than the magnitude of the wavevector in free space ($\kappa > k_0$) is evanescent in nature. This is shown in the dispersion diagram as the in-plane wavevector of SPPs being larger than the same frequency light in the dielectric as shown in Fig. 4.8b. Therefore, momentum matching techniques such as prism or grating coupling are required to couple the far-field light into SPP modes. As a result, the light emitted from an OLED in the far-field regime does not couple into SPP modes, and does not contribute to the efficiency loss. However, when an excited molecule is in close proximity (scale of emission wavelength, λ), the evanescent field of the SPP reaches the molecular dipole oscillator as shown in Fig. 4.11a, thus the dipole impart the emissive power into the SPP mode. For a dipole located near a planar surface, a wide range of in-plane wavevector exists as shown in Fig. 4.11b. Thus, the light with in-plane wavevector of $\kappa > k_0$ exists when the dipole is located very near to the metal surface, satisfying the momentum conservation, enabling the dipole to couple into inaccessible modes in the far-field, e.g. SPP modes [79]. Therefore, the excited state molecule dissipates its energy via the optical near-field coupling into the SPP modes.

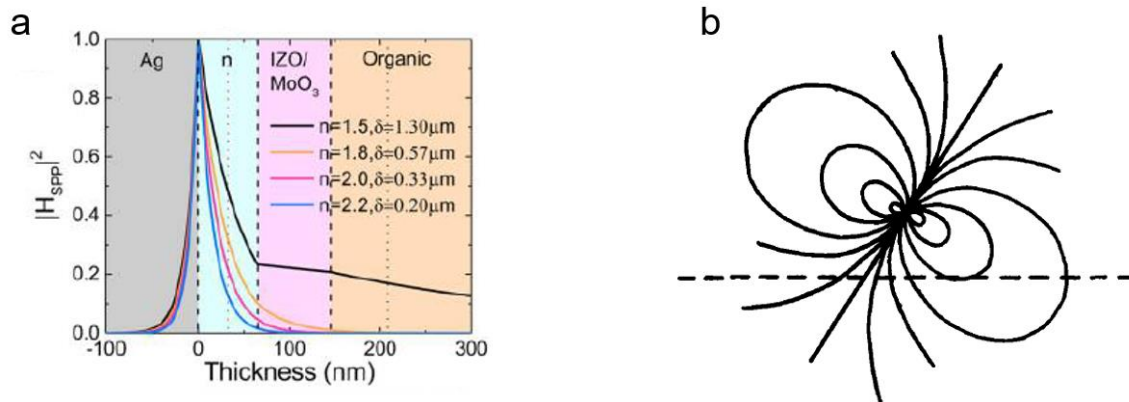


Figure 4.11 Dipole field coupling with the SPP mode in the near-field regime (a) Surface plasmon mode magnetic field intensity across the organic multilayer stack with different refractive indices, n . The SPP mode propagation length, δ , is shown as well. (Qu, et al., 2017). (b) Electric field lines of an electric dipole in the near-field regime. The broken line indicates the surface plane interface. The wavevector near the interface in this case is not a one component. (Barnes, 1998)

The extent of this near-field coupling into the SPP mode exponentially decreases with the distance of the dipole emitter to the metal surface, therefore a thicker ETL suppresses the outcoupling efficiency losses caused by the SPP mode coupling as shown in Fig. 4.7b. However, the number of supported modes within a slab waveguide increases with the film thickness, causing an increased outcoupling efficiency loss into the waveguide mode.

4.3.3 TDM orientation and optical power loss

The TDM orientation of an emitting molecule is a different way to avoid the SPP mode coupling losses. By orienting the TDM horizontally, i.e. parallel to the substrate plane, the coupling losses into the SPP modes are significantly suppressed since only TM polarized light is allowed to couple into the SPP mode. This is shown by the simulated power dissipation spectra for three orthogonal TDMs in a prototypical OLED with the device structure in Fig. 4.12. As shown, the vertical (p_z) TDM dissipates most of its power into the SPP mode, whereas the horizontal TDMs (p_x, p_y) distribute their power into various optical modes.

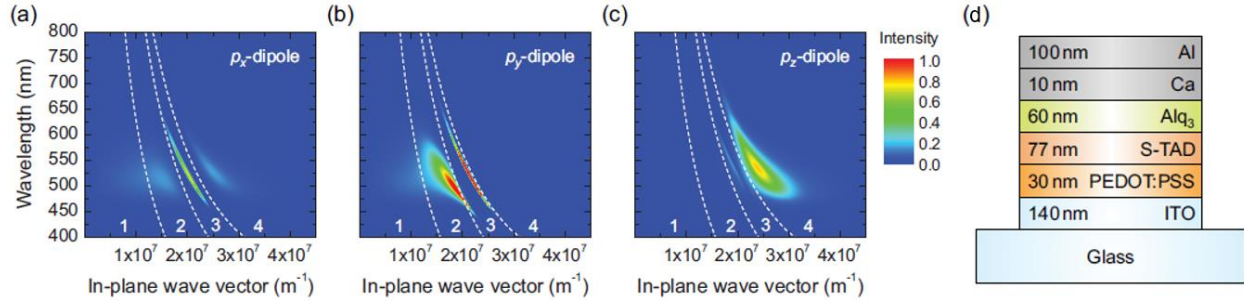


Figure 4.12 Modal power distribution of different TDMs
 Simulated power dissipation of prototypical OLED in each mode for horizontal TDMs (a, b) and vertical TDM (c). The x, y axis is parallel to the substrate plane whereas the z-axis is orthogonal to the plane. Zone 1,2,3 and 4 refer to air, substrate, waveguide and SPP mode, respectively. (d) Device structure of the OLED used for the simulation. (Brütting, et al., 2013)

The simulated power dissipation of the TDMs with perfect horizontal and vertical orientations with respect to the substrate plane are shown in Fig. 4.13. As expected from Fig. 4.12, the light power coupled into SPP mode is significantly increased for a vertically aligned TDM than the horizontal case. The amount of light power coupled into the waveguide mode is also highly dependent on the polarization, increasing with the fraction of vertically aligned TDMs since the light power emitted by the TDM is focused in the direction perpendicular to the charge transfer vector, as shown in Fig. 4.14. Therefore, the light coupled into the waveguide mode for a vertically oriented TDM is approximately twice of a horizontally aligned TDM for an OLED with thick ETLs (> 200nm), as shown in Fig. 4.13. As a result, the outcoupling efficiency of a TDM with a perfect horizontal orientation is enhanced by roughly a factor of 1.5 compared to the randomly aligned TDM [70]. This result emphasizes the importance of suppressing the fraction of a vertically aligned TDM for improving the OLED performance. Specific methods to increase the fraction of horizontally aligned TDMs will be discussed in Chapter 7.

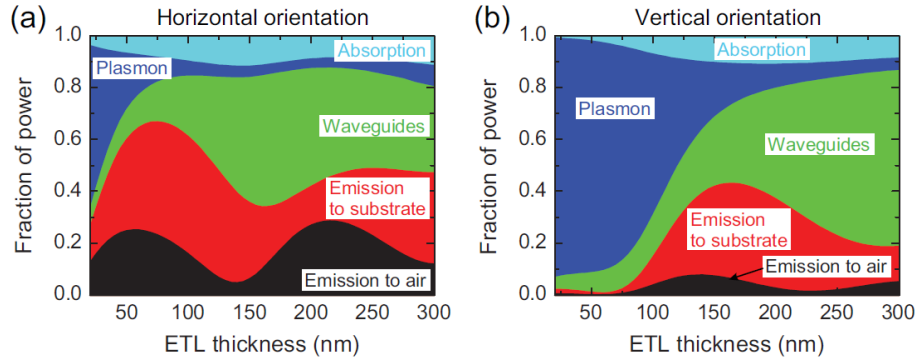


Figure 4.13 Modal power distribution of different TDMs
 Simulated modal power dissipation for (a) perfect horizontal and (b) vertical TDM orientation with respect to the ETL thickness. The quantum yield for both cases was set to be 100%. (Brütting, et al., 2013)

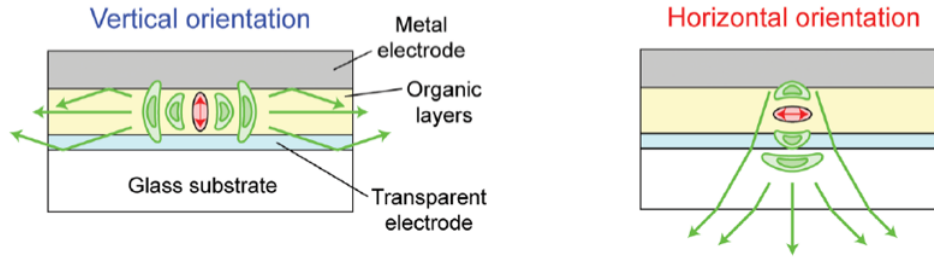


Figure 4.14 Varied light trapping with TDM orientation
 Schematic illustration showing varied light trapping in the optical waveguide depending on the TDM orientation. (Yokoyama, 2011)

Chapter 5 Using Fourier Plane Imaging Microscopy for Determining Transition Dipole Moment Orientations in Organic Light Emitting Devices

The orientation of molecules affects various aspects of an organic film as discussed in Chapter 3.3 [36,47,80–82]. Therefore, a number of methods have been proposed to reveal the orientation of molecules within the organic thin films, although many entail complex experimental setups and may lack the sensitivity required for a given application as mentioned in Chapter 3.2.3.1 [83–85,26–28]. Recently, Fourier plane imaging microscopy (FIM), which is a class of fluorescence microscopy measuring the angular emission intensity distribution from the film, has been used to identify the orientation of the emissive TDM in various materials [29–31,86–92]. In FIM, a large proportion of the light emitted into the substrate is simultaneously collected by the objective lens, and imaged by a 2D charge coupled device (CCD), resulting in a dramatically reduced measurement time and improved precision compared to conventional 1D scanning methods [26].

5.1 Introduction

In this chapter, we use FIM to determine the TDM orientation for different luminescent dopants used in the OLED EML. We present an optical model to interpret the FIM polar images following the dyadic Green's function method in cylindrical coordinates that is based on the dipole model of Chance, Prock and Silbey (CPS) [93]. The method determines the Poynting vector within a birefringent medium, from which we obtain the angular intensity distribution that reveals the

TDM orientation. The dipole model is an extension of previous work [94] that includes consideration of birefringent media commonly used in organic electronic structures. The cylindrically symmetric solution is compact, and enables straightforward application to stratified birefringent multilayers. We validate our model by measuring the orientation of three emissive dopants: Ir(ppy)₃, Ir(ppy)₂(acac) and (MAC)CuCz doped in CBP, and compare the FIM data with the outcoupling efficiency from the OLEDs incorporating these same emissive layers.

5.2 Theory of the optical model for analysis

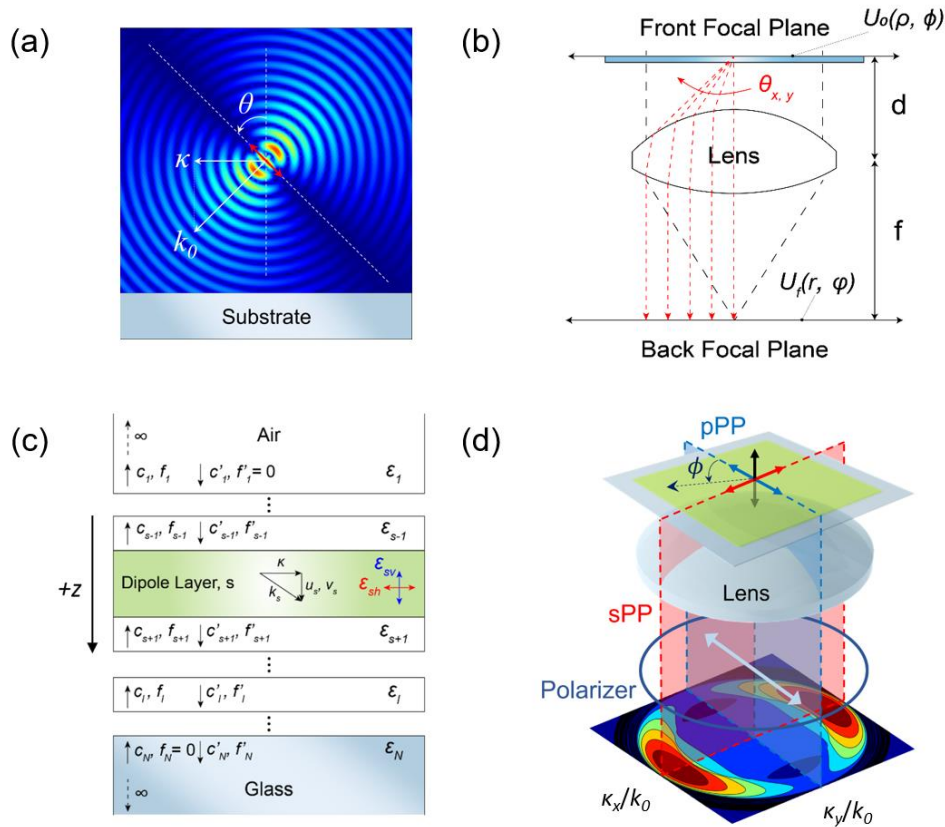


Figure 5.1 Illustrations for understanding Fourier plane imaging microscopy. (a) Calculated electric field of an oscillating dipole whose TDM is at angle, θ , relative to the substrate normal. The wave vector, k_0 , and its in-plane component, κ , are shown. (b) Geometries for the Fourier transform operation of a Fourier lens. (c) A stratified multilayer structure used for the optical calculation defining the various wavevectors (κ , k , u , v), coefficients of the travelling wave eigenfunctions (c , f) and dielectric components (ϵ) in each layer. The subscripts s and l denote the source and arbitrary layer within the multilayer, respectively. (d) A schematic showing how FIM pole plot is obtained from a point dipole. The two orthogonal planes, sPP and pPP, are defined by the linear polarizer.

Light emitted from a dopant molecule has a dipole radiation pattern shown in Fig. 5.1a, allowing for identifying its orientation from its angular emission profile. The analysis is done by decomposing the light intensity from different directions, characterized by the in-plane wave vector, $\kappa = k_0 \cdot n \cdot \sin\theta$, where k_0 is the wave vector in free space, n is the refractive index of the medium, and θ is the angle between the substrate normal and the propagation direction.

Fraunhofer and Fresnel approximations are used for analyzing diffraction patterns at different distances from the source to the image plane. The Fraunhofer approximation simplifies the calculations due to the suppressed phase factor, however, it can only be applied at large distances from the source [95]. The Fraunhofer approximation can be used at small distances, however, by placing a Fourier lens between the source and the image plane that transforms a parabolic wave in the near-field into a plane wave. Fourier plane imaging, also known as back-focal plane imaging, decomposes an image into the weighted sum of its plane wave components. Placing the source in the front focal plane of a Fourier lens as in Fig. 5.1b results in a Fraunhofer diffraction pattern of the input field in the back focal plane described by: [95]

$$\begin{aligned}
 U_f(r, \varphi) &= \frac{\exp\left[i \frac{k}{2f} \left(1 - \frac{d}{f}\right) r^2\right]}{i\lambda f} \int_0^{2\pi} \int_0^\infty U_0(\rho, \phi) \exp\left[-i \frac{2\pi}{\lambda f} \{\rho r \cos(\phi - \varphi)\}\right] \rho d\rho d\phi \\
 &= m(r) \cdot F_0(k_\rho, \varphi),
 \end{aligned} \tag{5.1}$$

where ρ , ϕ and r , φ are the polar coordinates of the front and back focal planes, respectively. $U_0(\rho, \phi)$ and $U_f(r, \varphi)$ are the input and output intensity distributions, respectively, f is the lens focal length, d is the propagation distance, λ is the wavelength, $F_0(k_\rho, \varphi)$ is the Fourier transform of the input function, $U_0(\rho, \phi)$, and $k_\rho (= \kappa/k_{||})$ is the normalized in-plane wave vector in the front focal plane with $k_\rho = \frac{1}{2\pi} k_0 \sin \theta_x \approx r/\lambda f$ for paraxial plane waves when $\phi = \varphi$. Note that $U_f(r, \varphi)$ is a Fourier transform of the input function in k -space, with a quadratic phase factor, $m(r)$. Here, $m(r)$

is a complex number for $d \geq f$. Thus, the phase curvature disappears for the sample plane at $d = f$, resulting in an output function in the back focal plane of the Fourier transform of $U_0(\rho, \phi)$.

In Eq. (5.1), $F_0(k_\rho, \varphi)$ corresponds to the far-field angular profile of a point dipole. Here, we follow the formulation of the CPS model [93] and previous work [94] to derive F_0 in a birefringent medium using dyadic Green's functions for the multilayer reference structure in Fig. 5.1c. The use of a dyadic Green's function assumes cylindrical symmetry of emission from a dipole source. This enables a compact solution compared to previous scattering matrix methods [96,97]. The dipole source at the origin, $\xi' = (0, 0, 0)$, is embedded in the s^{th} layer, with either a vertical or horizontal orientation. We assume all layers are uniaxial with a complex dielectric tensor, ϵ_l :

$$\epsilon_l = \begin{pmatrix} \epsilon_{lh} & 0 & 0 \\ 0 & \epsilon_{lh} & 0 \\ 0 & 0 & \epsilon_{lv} \end{pmatrix}, \quad (5.2)$$

where ϵ_{lh} , ϵ_{lv} are dielectric eigenvalues of the l^{th} layer in the ordinary, extraordinary directions, respectively. The system is isotropic when $\epsilon_{lh} = \epsilon_{lv}$. Here we assume a lossless source layer, i.e. $\epsilon_s = \text{Re}[\epsilon_s]$. The subscripts l and s represent variables or constants in the l^{th} and the source layer. The electromagnetic wave can be decomposed into TE and TM modes (s - and p -polarizations). The dispersion relations for both polarizations are:

$$\begin{aligned} \frac{u_l^2}{\epsilon_{lh}} + \frac{\kappa^2}{\epsilon_{lh}} &= k_0^2 \quad (\text{TE}) \\ \frac{v_l^2}{\epsilon_{lh}} + \frac{\kappa^2}{\epsilon_{lv}} &= k_0^2 \quad (\text{TM}) \end{aligned} \quad (5.3)$$

where u_l and v_l are the substrate-normal wavevectors of the TE and TM modes. The dipole source is characterized by an oscillating current with unit strength following:

$$\begin{aligned} \mathbf{J}(\xi) &= -i\omega \mathbf{p}_0 \delta(\xi), \quad |\mathbf{p}_0| = 1 \\ \mathbf{E}(\xi) &= -i\omega \int \mathbf{G}(\xi, \xi') \cdot \mathbf{J}(\xi') d^3 \xi' \end{aligned} \quad (5.4)$$

where ω is the oscillation frequency, \mathbf{p}_0 is the dipole vector, $\mathbf{G}(\xi, \xi')$ is the dyadic Green's function and $\mathbf{J}(\xi)$ is the current density. To evaluate the time-harmonic electromagnetic wave in a stratified anisotropic structure, we consider the dyadic Green's function of a dipole source embedded in an infinite anisotropic medium as described in [98]:

$$\mathbf{G}_\infty(\xi, \xi') = -\frac{1}{i\omega \varepsilon_0 \varepsilon_h} \left[\nabla \nabla + k_h^2 \varepsilon_v \boldsymbol{\varepsilon}^{-1} \right] \frac{e^{ik_h \xi_e}}{4\pi \xi_e} - i\omega \mu_0 \left\{ \left(\frac{\varepsilon_v e^{ik_h \xi_e}}{\varepsilon_h 4\pi \xi_e} - \frac{e^{ik_h \xi}}{4\pi \xi} \right) \boldsymbol{\varphi} \boldsymbol{\varphi} + \frac{e^{ik_h \xi_e - ik_h \xi}}{4\pi i k_h \rho^2} (\boldsymbol{\rho} \boldsymbol{\rho} - \boldsymbol{\varphi} \boldsymbol{\varphi}) \right\} \quad (5.5)$$

where $\boldsymbol{\varepsilon}^{-1}$ is the inverse of dielectric tensor, $k_h^2 \equiv \omega^2 \mu_0 \varepsilon_0 \varepsilon_h$, and $\xi_e^2 = \frac{\varepsilon_v}{\varepsilon_h} \rho^2 + z^2$, $\xi^2 = \rho^2 + z^2$. Using

the Sommerfeld identity [99], we expand the non-zero electric field components into cylindrical waves:

$$\begin{aligned} E_{tz}^\perp &= -\frac{\omega \mu_0 P_0^\perp}{4\pi} \frac{\varepsilon_{sh}}{\varepsilon_{sv}} \frac{\varepsilon_{lh}}{\varepsilon_{lv}} \int_0^\infty \frac{\mathbf{K}^3}{v_s k_{sh} k_{lh}} \left(f_{l\perp}' e^{iv_l z} + f_{l\perp} e^{-iv_l z} + \delta_{ls} e^{iv_l |z|} \right) J_0(\kappa \rho) d\kappa \\ E_{l\rho}^\perp &= -\frac{i\omega \mu_0 P_0^\perp}{4\pi} \frac{\varepsilon_{sh}}{\varepsilon_{sv}} \int_0^\infty \frac{\kappa v_l}{v_s k_{sh} k_{lh}} \left(f_{l\perp}' e^{iv_l z} - f_{l\perp} e^{-iv_l z} + \frac{\delta_{ls}}{\text{sgn}(z)} e^{iv_l |z|} \right) \frac{\partial J_0(\kappa \rho)}{\partial \rho} d\kappa \\ E_{tz}^\parallel &= \frac{i\omega \mu_0 P_0^\parallel}{4\pi} \int_0^\infty \frac{\kappa^2}{k_{sv} k_{lv}} \left(f_{l\parallel}' e^{iv_l z} + f_{l\parallel} e^{-iv_l z} + \frac{\delta_{ls}}{\text{sgn}(z)} e^{iv_l |z|} \right) J_1(\kappa \rho) \cos \phi d\kappa \\ E_{l\rho}^\parallel &= -\frac{\omega \mu_0 P_0^\parallel}{4\pi} \int_0^\infty \left[\frac{v_l}{k_{sv} k_{lv}} \frac{\varepsilon_{lv}}{\varepsilon_{lh}} \left(f_{l\parallel}' e^{iv_l z} - f_{l\parallel} e^{-iv_l z} + \delta_{ls} e^{iv_l |z|} \right) \frac{\partial J_1(\kappa \rho)}{\partial \rho} \cos \phi - \frac{1}{u_s} \left(c_l' e^{iu_l z} + c_l e^{-iu_l z} + \delta_{ls} e^{iu_l |z|} \right) \frac{J_1(\kappa \rho)}{\rho} \cos \phi \right] d\kappa \\ E_{l\phi}^\parallel &= \frac{\omega \mu_0 P_0^\parallel}{4\pi} \int_0^\infty \left[\frac{v_l}{k_{sv} k_{lv}} \frac{\varepsilon_{lv}}{\varepsilon_{lh}} \left(f_{l\parallel}' e^{iv_l z} - f_{l\parallel} e^{-iv_l z} + \delta_{ls} e^{iv_l |z|} \right) \frac{J_1(\kappa \rho)}{\rho} \sin \phi - \frac{1}{u_s} \left(c_l' e^{iu_l z} + c_l e^{-iu_l z} + \delta_{ls} e^{iu_l |z|} \right) \frac{\partial J_1(\kappa \rho)}{\partial \rho} \sin \phi \right] d\kappa \end{aligned} \quad (5.6)$$

where $k_{lh}^2 \equiv \omega^2 \mu_0 \varepsilon_0 \varepsilon_{lh}$, $k_{lv}^2 \equiv \omega^2 \mu_0 \varepsilon_0 \varepsilon_{lv}$, p_0^\parallel and p_0^\perp are the horizontal and vertical dipole moment components, and the source terms are indicated by δ_{ls} . The result becomes identical to the optically isotropic system when $\varepsilon_{lh} = \varepsilon_{lv}$ [94].

The coefficients of the top (-z) and bottom (+z) traveling eigenfunctions (**M** and **N** in CPS model [93]), c_l, f_l and c_l', f_l' , are determined by the boundary conditions of Maxwell's equations as:

$$\begin{aligned}
k_{lh} \left(f'_{l\perp} e^{iv_l z_{0l}} + f_{l\perp} e^{-iv_l z_{0l}} \right) &= k_{l+1,h} \left(f'_{l+1,\perp} e^{iv_{l+1} z_{0l}} + f_{l+1,\perp} e^{-iv_{l+1} z_{0l}} \right) \\
\frac{v_l}{k_{lh}} \left(f'_{l\perp} e^{iv_l z_{0l}} - f_{l\perp} e^{-iv_l z_{0l}} \right) &= \frac{v_{l+1}}{k_{l+1,h}} \left(f'_{l+1,\perp} e^{iv_{l+1} z_{0l}} - f_{l+1,\perp} e^{-iv_{l+1} z_{0l}} \right) \\
k_{lv} \left(f'_{l\parallel} e^{iv_l z_{0l}} + f_{l\parallel} e^{-iv_l z_{0l}} \right) &= k_{l+1,v} \left(f'_{l+1,\parallel} e^{iv_{l+1} z_{0l}} + f_{l+1,\parallel} e^{-iv_{l+1} z_{0l}} \right) \\
\frac{v_l}{k_{lv}} \frac{\varepsilon_{lv}}{\varepsilon_{lh}} \left(f'_{l\parallel} e^{iv_l z_{0l}} - f_{l\parallel} e^{-iv_l z_{0l}} \right) &= \frac{v_{l+1}}{k_{l+1,h}} \frac{\varepsilon_{l+1,v}}{\varepsilon_{l+1,h}} \left(f'_{l+1,\parallel} e^{iv_{l+1} z_{0l}} - f_{l+1,\parallel} e^{-iv_{l+1} z_{0l}} \right) \\
c'_{l\parallel} e^{iu_l z_{0l}} + c_{l\parallel} e^{-iu_l z_{0l}} &= c'_{l+1,\parallel} e^{iu_{l+1} z_{0l}} + c_{l+1,\parallel} e^{-iu_{l+1} z_{0l}} \\
u_l \left(c'_{l\parallel} e^{iu_l z_{0l}} - c_{l\parallel} e^{-iu_l z_{0l}} \right) &= u_{l+1} \left(c'_{l+1,\parallel} e^{iu_{l+1} z_{0l}} - c_{l+1,\parallel} e^{-iu_{l+1} z_{0l}} \right)
\end{aligned} \tag{5.7}$$

where z_{0l} is the z -coordinate of the interface between the l^{th} and $(l+1)^{\text{th}}$ layer. The source terms are omitted for simplicity. With the relations in Eq. (5.7), the coefficients are obtained via numerical calculations as described by Celebi, et al. [24]. With the coefficients determined, energy transfer into different layers is obtained by calculating the time-averaged divergence of the Poynting vector normalized to the dipole decay rate [93]:

$$b = \frac{e^2 k_s^3}{6\pi m \omega \varepsilon} \left[1 + \frac{3q\varepsilon}{2p_0 k_s^3} \text{Im}(E_0) \right] \tag{5.8}$$

or:

$$\frac{b}{b_0} = 1 - q + q \left(1 + \frac{\text{Im}(\mathbf{p} \cdot \mathbf{E}(\boldsymbol{\xi}'))}{\text{Im}(\mathbf{p} \cdot \mathbf{E}_\infty(\boldsymbol{\xi}'))} \right), \tag{5.9}$$

where b (b_0) is the exciton decay rate in an optical cavity (free space), $\mathbf{E}_\infty(\boldsymbol{\xi}')$ is the electric field with a dipole embedded in an infinite anisotropic source layer in free space, $\mathbf{E}(\boldsymbol{\xi}')$ is the electric field with a dipole embedded in a source layer that is in a stratified cavity structure, and q is the radiative quantum yield. Birefringence is calculated by expressing b separately for substrate-parallel and normal orientations. The total decay rate is obtained by the weighted average of the two decay rates:

$$b_{tot} = \theta_{hor} \cdot b_{\parallel} + (1 - \theta_{hor}) b_{\perp}, \quad (5.10)$$

Next, we calculate the divergence of the normalized Poynting vector. Assuming the structure is infinite in the x - y plane, we get [94]:

$$\int \nabla \cdot \mathbf{S} dV \approx \oint \mathbf{S} \cdot \hat{\mathbf{z}} d\sigma = S_z^+ - S_z^-, \quad (5.11)$$

$$S_z = \frac{i}{2\mu_0\omega} \left[E_{\rho} \left(\frac{\partial E_{\rho}}{\partial z} - \frac{\partial E_z}{\partial \rho} \right)^* + E_{\phi} \left(\frac{\partial E_{\phi}}{\partial z} - \frac{\partial E_z}{\rho \partial \phi} \right)^* \right],$$

where the superscripts + and - denote the forward- (+ z) and backward- (- z) propagating energy flux through the bottom and top interfaces of the l^{th} layer, respectively. Defining $k_{\rho} = \kappa / k_{sh}$ as the normalized surface-parallel wave vector, we calculate the normalized perpendicular components of the Poynting vector by inserting the electric field into Eq. (5.11). Integrating over x - y and applying the Bessel function closure relation, we get:

$$\begin{aligned} \text{Re}[S_{l,z}^{\perp}(k_{\rho})] &= \frac{3q}{4} \left| \frac{\varepsilon_{sh}}{\varepsilon_{sv}} \right|^2 \text{Re} \left\{ \sqrt{\frac{\varepsilon_{lh}^*}{\varepsilon_{lv}}} \frac{k_{\rho}^3 \sqrt{\varepsilon_{lv} / \varepsilon_{sh} - k_{\rho}^2}}{|1 - \varepsilon_{sh} / \varepsilon_{sv} \cdot k_{\rho}^2|} (f'_{l\perp} e^{iv_l z_{0l}} - f_{l\perp} e^{-iv_l z_{0l}}) \times (f'_{l\perp} e^{iv_l z_{0l}} + f_{l\perp} e^{-iv_l z_{0l}})^* \right\} \\ \text{Re}[S_{l,z}^{\parallel}(k_{\rho})] &= \frac{3q\varepsilon_{sh}}{2(3\varepsilon_{sh} + \varepsilon_{sv})} \text{Re} \left\{ \frac{\varepsilon_{sh}}{\varepsilon_{sv}} \sqrt{\frac{\varepsilon_{lh}^*}{\varepsilon_{lv}}} \left[k_{\rho} \sqrt{\frac{\varepsilon_{lv}}{\varepsilon_{sh}} - k_{\rho}^2} (f'_{l\parallel} e^{iv_l z_{0l}} - f_{l\parallel} e^{-iv_l z_{0l}}) (f'_{l\perp} e^{-iv_l z_{0l}} + f_{l\perp} e^{iv_l z_{0l}})^* \right. \right. \\ &\quad \left. \left. + \frac{k_{\rho} \sqrt{\varepsilon_{lh} / \varepsilon_{sh} - k_{\rho}^2}}{|1 - k_{\rho}^2|} (c'_l e^{iu_l z_{0l}} + c_l e^{-iu_l z_{0l}}) (c'_l e^{iu_l z_{0l}} - c_l e^{-iu_l z_{0l}})^* \right] \right\} \end{aligned} \quad (5.12)$$

which becomes identical to the result in isotropic medium when $\varepsilon_{lh} = \varepsilon_{lv}$ [94].

Then,

$$F_{0,\perp}(k_{\rho}) = \frac{n_{glass}}{n_{sv} k_{\rho}} \text{Re}[S_{N,z}^{\perp}(k_{\rho})] \quad (5.13)$$

$$F_{0,\parallel}(k_{\rho}) = \frac{n_{glass}}{n_{sh} k_{\rho}} \text{Re}[S_{N,z}^{\parallel}(k_{\rho})]$$

where $F_{0,\perp}$ and $F_{0,\parallel}$ correspond to the field intensity for substrate-normal (\perp) and -parallel (\parallel) dipoles, which corresponds to the Fourier transform of the input photoluminescence as previously

shown in Eq. (5.1). Unlike the angular spectrum of a point source which has a tangential relationship (u/k_ρ or v/k_ρ) between the Poynting vector and the field intensity, $1/k_\rho$ appears in Eq. (5.13). This difference stems from the detection of FIM using a planar CCD, where Lambert's cosine law does not apply. The fraction of energy transferred from the source to each layer is obtained by integrating $\text{Re}[S_{i,z}(k_\rho)]$ for all k_ρ and then dividing by the corresponding decay rate b/b_0 .

The lens projects a polar plot in the back focal plane with an angle of in-plane rotation, φ , as shown in Fig. 5.1d. Molecules deposited during layer growth often lack an in-plane rotational (φ) preference. Thus, the output intensity distribution in the focal plane shows an in-plane symmetry. Placing a linear polarizer in front of the back focal plane breaks the symmetry, leading to an improved fitting accuracy of the polar intensity information to Eq. (5.13). Then we define two orthogonal planes, one parallel (blue plane, Fig. 5.1d) and the other perpendicular (red plane) to the polarizer, defined as p-polarized (pPP) and s-polarized (sPP) dipole planes, respectively. As shown in Fig. 5.1d, pPP includes vertically and horizontally aligned TDMs relative to the substrate, whereas sPP includes only one horizontally aligned TDM. The projected k -space image in the back focal plane then follows the cosine square law of a linear polarizer:

$$U_f(r, \varphi) = \frac{1}{i\lambda f} \left\{ \left((1 - \theta_{hor}) F_{0, \perp, pPP}(k_\rho) + \theta_{hor} F_{0, \parallel, pPP}(k_\rho) \right) \cos^2 \varphi + \left(\theta_{hor} F_{0, \parallel, sPP}(k_\rho) \right) \sin^2 \varphi \right\} \quad (5.14)$$

5.3 Experimental methods

Films for Fourier plane imaging microscope measurement were grown on pre-cleaned 0.2 mm thick fused silica substrates by VTE in a chamber with a base pressure of 1×10^{-7} torr. The deposition rates of the molecules were adjusted to achieve the desired dopant concentrations in the host, and the film thicknesses were controlled using quartz crystal thickness monitors. We

deposited a 50 nm thick Al marker on the samples to precisely focus the microscope on the film on the front focal plane. Following the deposition, devices were encapsulated using an epoxy seal around the edge of a cover glass in a N₂ environment.

The Fourier microscope consists of two parts, (i) an inverted fluorescence microscope comprising a 325 nm He-Cd continuous-wave laser with an inverted microscope (Olympus IX73), and (ii) a system of optical components comprising a Fourier lens (Thorlabs), optical filters, a linear polarizer, and a 1024×1024 CCD array (Princeton Instruments). The photoluminescence of the sample was coupled through an oil immersion objective (×100, NA=1.40, Olympus). The Fourier lens ($f = 300$ mm) reconstructed the Fourier image plane on the CCD. A long-pass filter was used to prevent the reflected laser beam to be incident on the CCD, while a filter with the pass band near the peak wavelength of the dopant photoluminescence was also placed in the optical path. A linear polarizer separates the emission into two the orthogonal planes corresponding to the pPP and sPP modes. To suppress imaging artefacts in the high- k region, the k -space fitting in pPP was performed over a limited range of $-1.1 < k_x/k_0 < 1.1$ [29,86,87,100].

OLEDs were grown on 1 mm thick cleaned glass substrates with a pre-deposited, patterned 150 nm-thick ITO layer (Thin Film Devices, Inc.). Prior to film deposition by VTE, the ITO-coated substrates were treated in a UV-ozone chamber for 15 min. CBP, Ir(ppy)₂(acac), Ir(ppy)₃, TAPC and BP4mPy, were purchased from Luminescence Technology, Corp. The device area of 2 mm² was defined by the intersection of a pre-patterned 1 mm wide ITO strip and an orthogonal 2 mm wide Al cathode strip patterned by deposition through a metal shadow mask. The current density–voltage (J – V) characteristics were measured using a parameter analyzer (HP4145, Hewlett–Packard) and a calibrated photodiode (FDS1010-CAL, Thorlabs) following standard

procedures [101]. The emission spectra at $J = 100\text{mA}/\text{cm}^2$ were recorded using a calibrated spectrometer (USB4000, Ocean Optics) coupled to the device with an optical fiber.

5.4 Impact of TDM alignment on OLED performance

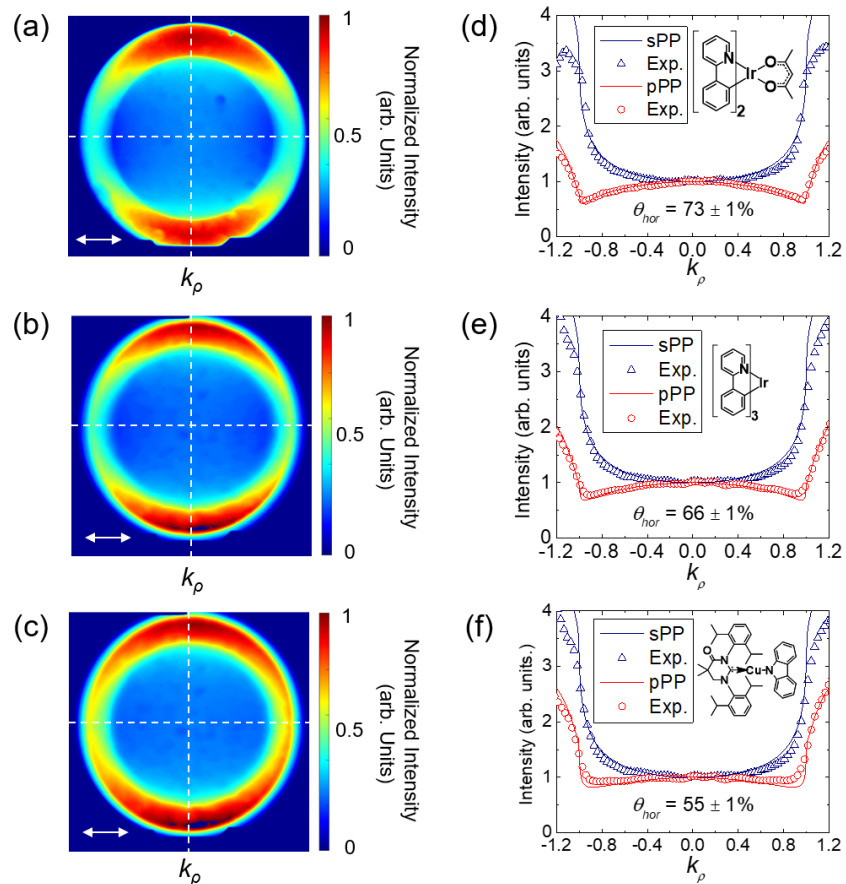


Figure 5.2 FIM results from the three dopants.

Measured pole plots (a-c) and intensity profiles in the pPP and sPP (d-f, data points), along with the simulated fits (solid lines) for $\text{Ir}(\text{ppy})_2(\text{acac})$ (a, d), $\text{Ir}(\text{ppy})_3$ (b, e), and $(\text{MAC})\text{CuCz}$ (c, f) doped at 10 vol.% into a CBP host. Insets: Molecular structural formulae of each dopant.

Figure 5.2a-c show measured intensity patterns for thin films comprising $\text{Ir}(\text{ppy})_2(\text{acac})$, $\text{Ir}(\text{ppy})_3$ and $(\text{MAC})\text{CuCz}$ doped at 10 vol.% into a CBP host matrix. The measured pPP and sPP intensity profiles compared with the simulation fits in Fig. 5.2d-f show a horizontal and isotropic orientation of the TDM respect to the substrate from $\text{Ir}(\text{ppy})_2(\text{acac})$, and $\text{Ir}(\text{ppy})_3$ doped in CBP

($\theta_{hor} = 73 \pm 1\%$ and $66 \pm 1\%$), respectively, which are consistent with previous measurements [37,40,102], whereas (MAC)CuCz in CBP shows a relatively vertically aligned TDM ($\theta_{hor} = 55 \pm 1\%$) as shown in Fig. 5.2f.

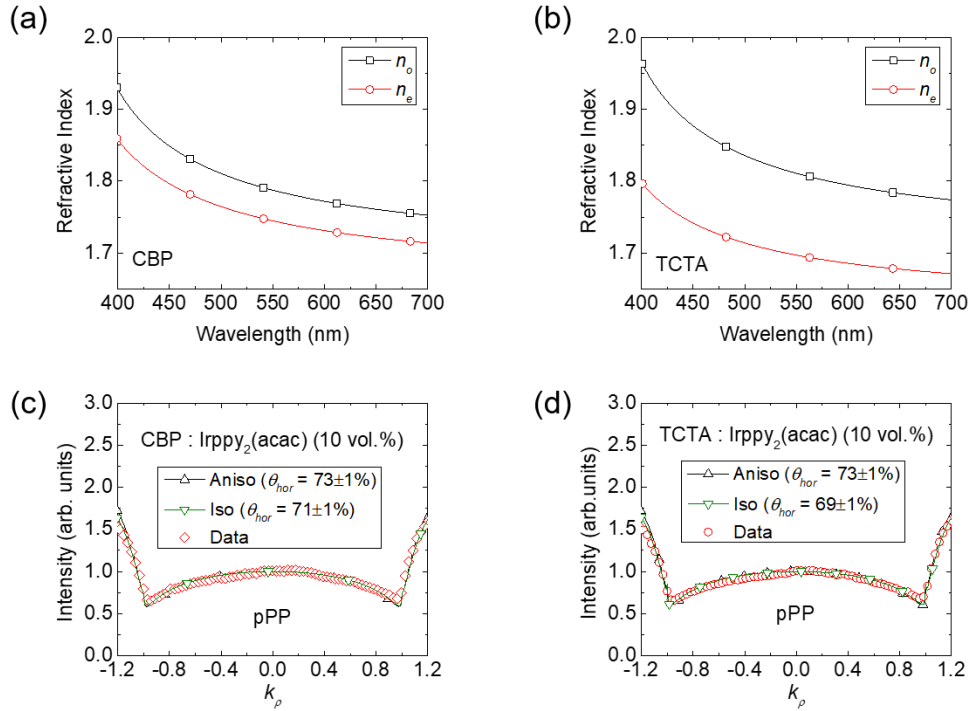


Figure 5.3 Transition dipole orientation measurement in a birefringent host matrix. Refractive index of (a) CBP, and (b) TCTA. Here n_o and n_e are the indexes of refraction along the ordinary and extraordinary optical axes, respectively. Measured intensity profiles of Ir(ppy)₂(acac) doped in (c) CBP and (d) TCTA at 10 vol.%. Note that there is an error in the orientation measurement of 2% for CBP and 4% in TCTA with its larger birefringence.

Ir(ppy)₂(acac) is doped in a birefringent host in Fig. 5.3, tris(4-carbazoyl-9-ylphenyl)amine (TCTA), to show the effect of an anisotropic medium on the emission. The measured refractive index of CBP and TCTA are shown in Fig. 5.3a and 5.3b, demonstrating a larger birefringence of TCTA. The FIM intensity patterns in pPP for CBP and TCTA hosts are shown in Fig. 5.3c and 5.3d. Two different fit results based on isotropic and anisotropic media are used to compare each measurement, showing an increased discrepancy when assuming an anisotropic dielectric constant for TCTA compared to the CBP host matrix.

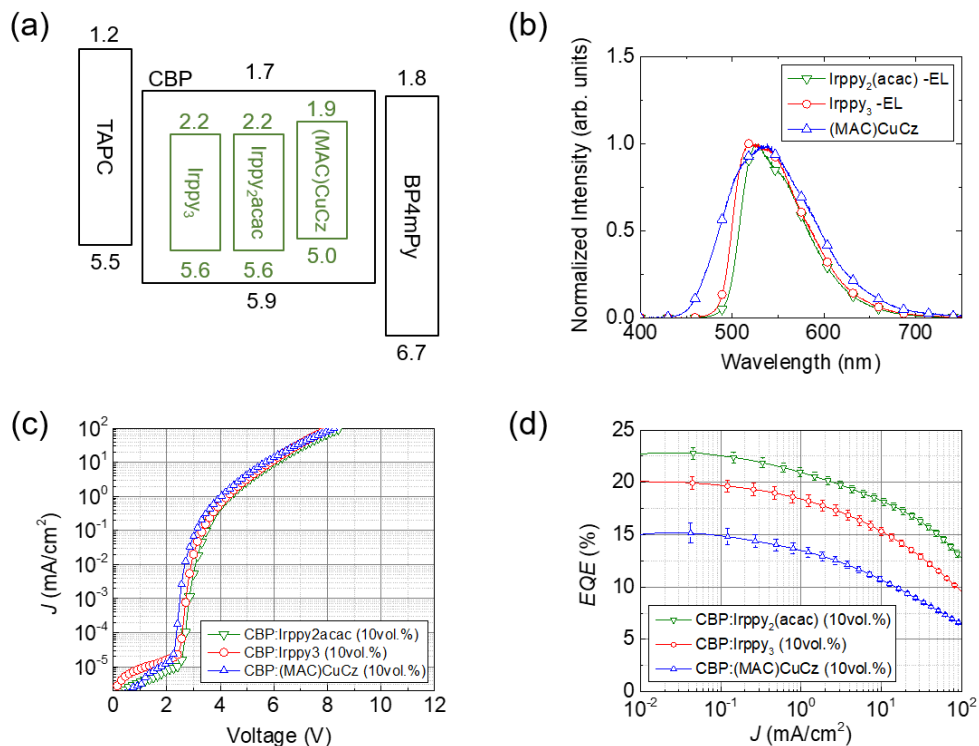


Figure 5.4 Performance of OLEDs with the three dopant emitting molecules in Fig. 5.2. (a) Frontier orbital energies of the materials in eV. The electroluminescence spectra (b), current density-voltage (J - V) characteristics, (c) and the current density vs. external quantum efficiency (J - η_{EQE}) characteristics (d) of the OLEDs.

OLEDs comprising these dopants were fabricated with the following structures: Al 100 nm / LiQ 1.5 nm / BP4mPy 50 nm / CBP: Dopant (10 vol.%) 15 nm / TAPC 40 nm / MoO₃ 2 nm / ITO 150 nm. Figure 4a shows the frontier orbital energies for the OLEDs, and Fig. 5.4b shows the corresponding OLED electroluminescent spectra. The J - V characteristics of the devices in Fig. 5.4c show negligible differences due to the identical device structures. The peak EQE in Fig. 5.3d is approximately 1.3 times higher for Ir(ppy)₂(acac) than (MAC)CuCz.

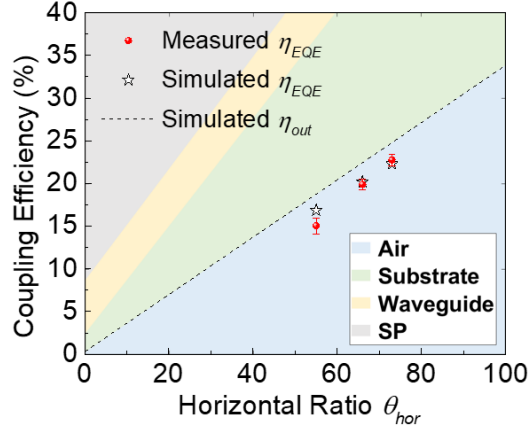


Figure 5.5 Measurement evaluation.

Calculated distribution of the emitted power into different modes depending on the average orientation of the TDM within the emissive layer. The data points show the measured and simulated η_{EQE} of the OLEDs comprising different dopant emitters. The simulated points are based on FIM measurements of the dopant molecule orientations relative to the substrate. The color bands indicate the proportion of light power coupled into each mode.

In Fig. 5.5, the simulated coupling efficiency of each mode as a function of θ_{hor} at 530 nm is compared with the measured peak EQE of the OLEDs (data points). Here, the simulated fraction of the emitted light power coupled into each mode is shown along the vertical axis. The fraction of air and substrate mode coupling increases with θ_{hor} , whereas coupling to SPP mode decreases.

The external quantum efficiency of an OLED is given by:

$$\eta_{EQE} = \eta_{int} \cdot \eta_{out} = \gamma \chi_{ST} \eta_{PL} \eta_{out} \quad (5.15)$$

where η_{int} is the internal quantum efficiency, which is the ratio of the number of photons generated to the number of injected charges. The internal efficiency is the product of the charge balance factor (γ), spin formation ratio (χ_{ST}), and photoluminescence quantum yield (η_{PL}). The χ_{ST} is 100% for electrophosphorescent (PHOLED) and TADF devices. Also, η_{out} is the outcoupling efficiency, which is the fraction of photons coupled into air modes vs. the total number of photons generated.

The Ir-based PHOLEDs and the (MAC)CuCz TADF OLEDs in Fig. 5.4 have identical device structures. The J - V characteristics in Fig. 5.4c show no noticeable differences since the energy levels of all dopants are nested in the host matrix energy gap, thus experiencing similar

charge transfer efficiencies from host to dopant. Therefore, we conclude that the three devices have similar γ . Also, $\eta_{PL} > 90\%$ for all three molecules [40,72,103], leading to nearly identical η_{int} . However, the EQE in Fig. 5.4d shows noticeable differences from device to device, reaching approximately 1.3 times higher for the Ir(ppy)₂(acac) device compared to the (MAC)CuCz OLED.

From the above, the relative differences of EQE between the dopant molecules can, therefore, be attributed to differences in outcoupling efficiency resulting from variations in TDM orientation. The coupling into different modes as a function of TDM orientation is simulated in Fig. 5.5. The vertical TDM emits TM polarized light primarily in the substrate-parallel direction. Therefore, the majority of power from the vertical TDM is coupled to either SP modes, or waveguide and substrate modes, depending on the ETL thickness that determine the distance between the metal cathode and the emitting dipoles. A thin ETL results in a larger fraction of power to be coupled to SP modes due to near-field coupling. Consequently, the fraction of light coupled into air modes decreases with an increasing fraction of vertically oriented TDMs as shown in Fig. 5.5. The simulation shows peak outcoupling efficiencies of 24.8%, 22.4% and 18.7% for OLEDs with $\theta_{hor} = 73\%$, 66% and 55%, respectively. Assuming $\gamma = \chi_{ST} = 100\%$ and $\eta_{PL} = 90\%$ for the three dopant molecules [40,72,103], the simulated $\eta_{EQE} = 22.3\%$, 20.2% and 16.9%, which corresponds to the experimental result, $\eta_{EQE} = 22.8 \pm 0.7\%$, $19.2 \pm 0.6\%$ and $15.1 \pm 0.9\%$.

5.5 Conclusion

We combine the CPS dipole model with Fourier optics to describe the far-field radiation distribution pattern in the back focal plane of a converging lens originating from a light emitting point dipole within a stratified birefringent thin film. By comparing the measured emission pattern using Fourier imaging microscopy with simulations, we determine the average orientation of the

TDM vectors within an organic film. We apply this technique to measure the TDM orientations of three different molecules, namely Ir(ppy)₂(acac), Ir(ppy)₃ and (MAC)CuCz doped into a CBP host matrix. The OLED outcoupling efficiencies agree to within experimental error with that obtained using FIM. This technique can be used to understand and optimize light outcoupling in a variety of materials systems and device structures.

Chapter 6 Nanoscale Morphological Mapping of Organic Thin Films

As discussed in Chapter 3, understanding morphology is fundamental to revealing the structure-property relationships of solids [104,105]. Disordered materials are of particular interest since their morphology is rarely in the lowest energy, equilibrium state, and hence can be complex and metastable, or even unstable over time [17,106]. Organic molecular solids, which are the foundation of a large range of devices such as OLEDs and OPVs, are particularly important members of the class of disordered materials since they are bonded by relatively weak vdW forces [19]. For this reason, considerable work has been done to develop methods for revealing their morphologies, including reciprocal and real space measurements from X-ray [107], electron and light sources [26,108,109], and scanning probe microscopies [110,111]. Unfortunately, the access to detailed bulk or interface structures using these techniques has been limited by the spatially averaged information of the bulk, the potential damage that they inflict on the sample due to physical contact or by high energy probe beams [112], their difficulty of use and complexities in data analysis, or their shallow probing depth.

6.1 Introduction

In this chapter, we reveal the detailed nanoscale morphology within archetype organic electronic thin films using FIM, which is a class of fluorescence microscopy that has been used for detecting emissive transition dipole orientations in various materials [29–31,86–88,90–

92,113]. Advantages of fluorescence microscopy arise from a wide selection of dye molecules available for tagging the structural elements, highly sensitive and position-dependent measurement, and the opportunity to monitor dynamic processes in real time. With an appropriate selection of dye molecules and analysis techniques, determining the local film morphology is possible. By depositing phosphorescent dye molecules at strategic positions within a host organic thin film, their luminescence provides high resolution, depth and area-dependent structural maps of the host. The FIM-plus-dye molecule combination is used to create 3D morphological maps of changes arising from thermal annealing in a stacked bilayer film, and at the interfaces. The volume resolution of the measurements is limited by the flatness of the predeposited film and the ability to accurately determine layer thickness during deposition in the direction normal to the film plane, and has a resolution of approximately half the visible wavelength (~ 200 nm) within the plane. Therefore, an Ångstrom-level resolution in the depth axis can be achieved for an ideal case, with precise deposition and measurement techniques, and a flat surface.

6.2 Experimental Methods

6.2.1 Sample preparation

Films are grown on pre-cleaned, 0.2 mm thick fused silica substrates (Technical Glass Products) by vacuum sublimation in a chamber with a base pressure of 1×10^{-7} torr. The 30 nm thick films were deposited at 0.5 \AA/s , and $\sim 1 \text{ \AA}$ thick MSLs were deposited at 0.1 \AA/s . The deposition rate and film thicknesses were controlled using a quartz crystal thickness monitor. A 50 nm thick Al fiducial mark was deposited on the sample surface to aid in precise focusing. Following deposition, devices were encapsulated using an epoxy seal around the edge of a cover glass in a N_2 environment.

6.2.2 Optical measurement

The Fourier microscope consists of a 532 nm wavelength, continuous-wave laser, an inverted microscope (Olympus IX73), optical filters, a linear polarizer, a Fourier lens (Thorlabs) and a 1024×1024 CCD array (Princeton Instruments). The sample was placed at the front focal plane of the Fourier microscope. Both the excitation laser beam and photoluminescence from the sample were coupled through an oil immersion objective ($\times 100$, NA=1.40, Olympus) to extract all glass modes. The lens with a focal length of 300 mm was used to reconstruct the Fourier image plane onto the imaging CCD. A 550 nm long-pass filter was used to reject the reflected laser beam, and a filter with a pass band near the peak wavelength of the sensor molecule photoluminescence (650 nm for PtOEP) was placed in the optical path. A linear polarizer was used to select the emission along the orthogonal pPP and sPP planes. The k -space fitting of pPP modes was performed over the domain, $-1.1 < k_\rho < 1.1$, to minimize imaging artefacts in the high- k region [29]. The linear polarizer was removed for the measurement when capturing the in-plane (azimuthal) pattern was required.

6.2.3 Optical simulation

The pole plot simulations in Fig. 6.1 are calculated based on the dyadic Green's function in a birefringent medium with the model presented elsewhere [113]. The film structure used for the simulation is 30 nm CBP (Fig. 6.2), and 30 nm CBP / 30 nm TPBi (Fig. 6.3) on glass with refractive indices at $\lambda = 650$ nm corresponding to the peak emission wavelength of PtOEP. The dipole depth position is assumed to be in the center of the CBP layer in Fig. 6.2, and as defined in Fig. 6.3a.

6.2.4 X-ray diffraction measurements

X-ray measurements for thin film samples were made in the Bragg-Brentano geometry using the Cu-K α radiation source operated at 40kV and 44mA in a Rigaku Ultima IV X-Ray Diffractometer.

6.3 Concept of using morphological sensing layer with Fourier imaging microscope

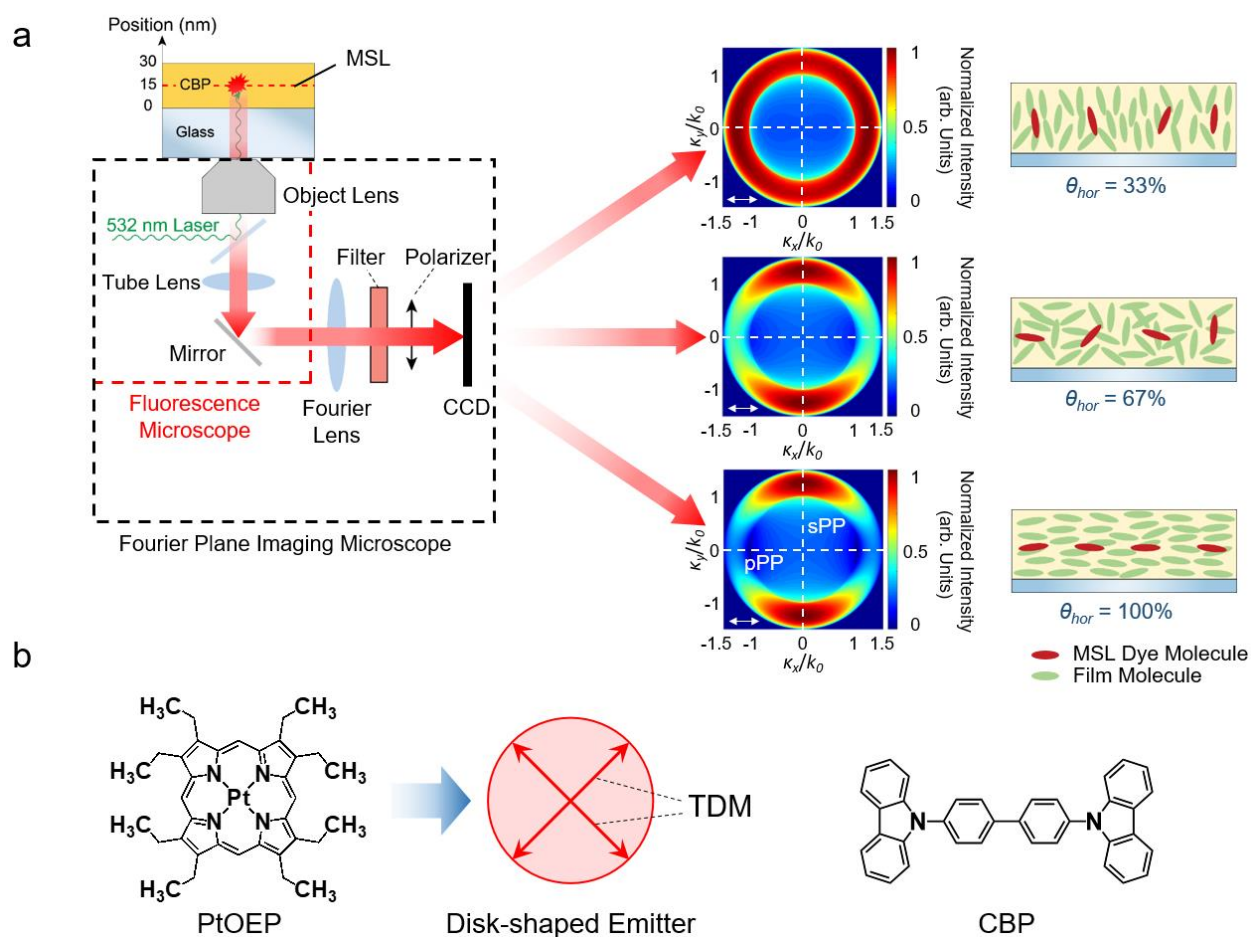


Figure 6.1 The morphological sensing layer concept.

(a) The red dashed line box shows a schematic of the fluorescence microscope, and the black box shows the imaging system. Polar images (center) at different polarizations (shown by arrows) corresponding to the emission due to orientation of the dye molecules in the MSL (red ovals, illustration to right) in the morphology of the host matrix (green ovals). (b) Molecular structural formulae of PtOEP and CBP. Due to its square planar D_{4h} symmetry, PtOEP has two orthogonal TDMs.

Morphology measurements comprise two parts, dye sensor layer placement followed by polarization and spatially sensitive optical observation of the dye emission pattern. We start by depositing a sub-monolayer ($<1\text{\AA}$) of dye molecules, called morphological sensing layers (MSLs), at a desired position in the film under test, as illustrated in Fig. 6.1a. With an appropriate selection of dye molecule, the orientation of the TDMs of the population is correlated with its environment, thus revealing the morphology at the deposited position [45]. In this work, red emitting PtOEP is used for the sensor molecule. This is a square, dihedral Pt-complex with a 4-fold symmetry (D_{4h} symmetry). We use the technologically significant CBP as the material under study due to its well-known structure, film forming properties, and low T_g that enables a facile change of morphology via thermal annealing [102,105].

The MSL orientation is determined using FIM images that are highly sensitive to the orientation of the radiative TDM relative to the substrate plane [29,86]. The FIM comprises two parts, a fluorescence microscope and a system of lenses that capture the angular dependence of the emission in a spatial image acquired in a single shot by a CCD image sensor. The optical pump of the fluorescence microscope locally excites the MSL, as shown in Fig. 6.1a, and the photoluminescence of the dye molecules is incident on the CCD array through the objective lens. The incident photoluminescence is transformed by placing the CCD at the Fourier plane of the lens, resulting in a k -space pole plot at the image plane. The orientation of the dye molecules is determined by comparing the obtained pole plot with a simulation based on a dipole model using dyadic Green's function analysis [113].

We show simulated pole plots in Fig. 6.1a corresponding to θ_{hor} from 33% to 100% (simulation details in Methods). The pole plot is a graph showing the photoluminescence intensity at different angles.

The direction of each emitted wave is described by the in-plane wavevector, $\kappa = k_0 \cdot n \cdot \sin\theta$, where k_0 is the free space wave vector, n is the refractive index of the medium, and θ is the angle between the substrate normal and the propagation direction. The CCD is a 2-dimensional array that can be used to decompose κ into two orthogonal wavevectors in each coordinate, κ_x and κ_y . The region bounded by $0 \leq k_\rho \leq n_{air}$ ($n_{air} = 1.0$), where k_ρ is the normalized in-plane wave vector ($k_\rho = \kappa/k_0$), corresponds to the air modes. The substrate modes occur for higher in-plane wave vectors, $n_{air} \leq k_\rho \leq n_{glass}$ ($n_{glass} \approx 1.5$). A linear polarizer (whose directions are indicated by arrows in the bottom-left corners of the simulations) is used to separate the emission in the two orthogonal planes, corresponding to p -polarized (pPP) and s -polarized (sPP) planes. These are indicated with horizontal and vertical dashed cross-hairs, respectively. The orientation of the sensor molecule (defined by θ_{hor}) is determined by comparing the measured emission intensity profile (I) in pPP to the weighted sum of the simulated p -polarized dipoles aligned horizontally (p_{hor}) and vertically (p_{ver}) to the substrate plane, as follows [40],

$$I(\kappa_x / k_0) = \theta_{hor} \cdot I_{p-hor}(\kappa_x / k_0) + (1 - \theta_{hor}) \cdot I_{p-ver}(\kappa_x / k_0). \quad (6.1)$$

Here, I_{p-hor} and I_{p-ver} are the intensities of the orthogonal p -polarized dipoles for each normalized wavevector (κ_x/k_0). Since the dipole emits the majority of its power perpendicular to the TDM, $I_{p-hor}(k_\rho)$ is dominant in the air modes, whereas $I_{p-ver}(k_\rho)$ is prevalent in the substrate modes. Therefore, the substrate mode peak intensity in pPP decreases with increasing θ_{hor} . In contrast, the substrate mode peak intensity in sPP increases with the θ_{hor} , as emission from only one horizontal dipole is uniformly distributed over all angles in sPP plane.

PtOEP is a disk-shaped molecule comprising two orthogonal TDMs in the molecular plane, as shown in Fig. 6.1b [45]. Therefore, 50% of the emission from a perfectly vertically oriented PtOEP molecule is from the horizontally aligned TDM, leading to θ_{hor} between 50% and 100%,

otherwise $\theta_{hor} = 67\%$ for isotropic (i.e. random) molecular orientation. This misrepresents the alignment of PtOEP when compared with a less symmetric molecule that has a single, average TDM with θ_{hor} ranging from 0% to 100%. For this reason, we remove the contribution from one of the two orthogonal TDMs in the PtOEP molecular plane by converting the θ_{hor} of PtOEP molecules using the transform shown in chapter 6.7. The transformed value is denoted θ_{h-conv} .

6.4 Use of morphological sensing layers for single layer systems

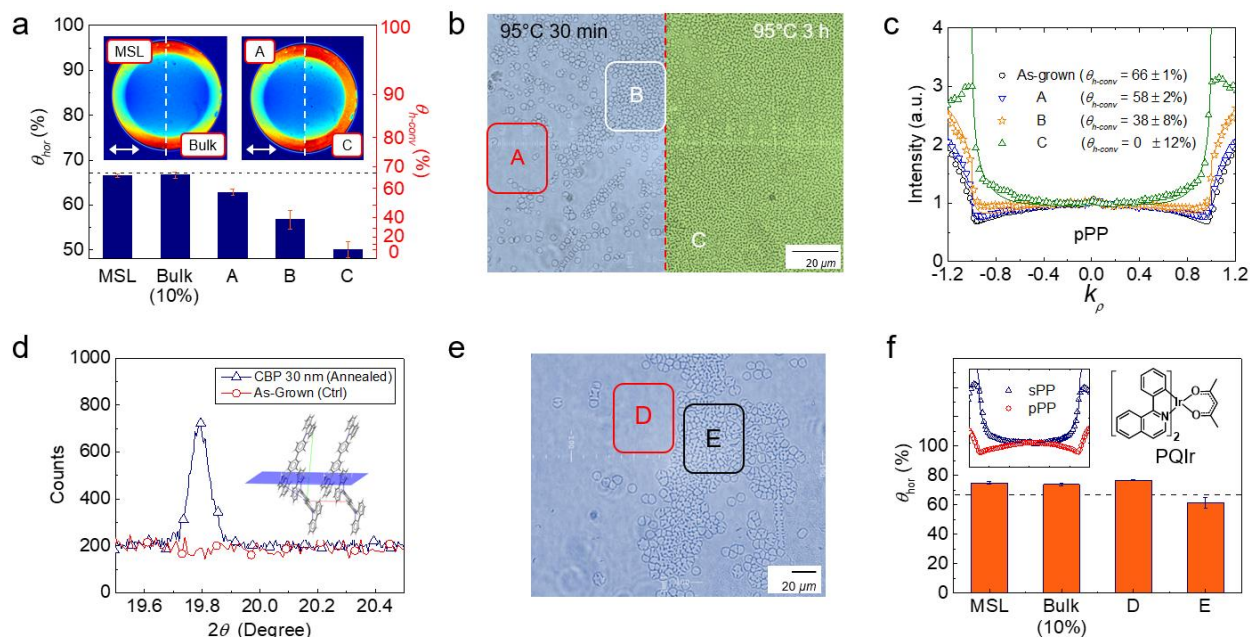


Figure 6.2 Morphology investigation of a 30 nm thick CBP film.

(a) Measured θ_{hor} (θ_{h-conv}) from the CBP film comprising a sub-monolayer PtOEP MSL in its center, and 10 vol.% PtOEP uniformly doped throughout the bulk film. The θ_{hor} (θ_{h-conv}) from the annealed MSL sample in regions A, B and C are shown in the histogram, where the horizontal dashed line indicates isotropic, random alignment ($\theta_{hor} = \theta_{h-conv} = 0.67$). The polar plots from each sample are shown at top, with arrows indicating the polarizer direction. (b) Optical micrograph of the 30 nm thick CBP film comprising a PtOEP MSL in its center (15 nm from the substrate) annealed at 95°C for 30 min (left) and 3 h (right). Colors of the micrographs are added after the measurement for clarity. (c) pPP intensity profile of the as-grown sample, and after annealing in regions A-C. Data are shown by points, and fits are indicated by lines (see Methods). (d) XRD pattern of a 30 nm thick CBP film on a sapphire substrate before and after annealing. Inset: CBP crystal structure with its (031) plane (blue) oriented parallel to the substrate. (e) Optical micrograph of the CBP film with PQIr as the MSL, annealed at 95°C for 3 h. (f) Measured θ_{hor} (θ_{h-conv}) of as-grown, 30 nm thick CBP films comprising a PQIr MSL placed in the film center (MSL), PQIr uniformly doped throughout the bulk at 10 vol.% (Bulk 10%), and of the annealed MSL sample in regions D and E. Inset: Measured p-polarized (pPP) and s-polarized (sPP) planes intensity profiles (data points) along with simulated fits (solid lines) from the as-grown MSL sample. The vertical axis shows the intensity, and the horizontal axis shows the normalized in-plane wave vector (k_p). Molecular formula of PQIr is shown on the right.

Figure 9.2a shows the measured orientation from two samples; one with the MSL deposited in the center of a 30 nm thick CBP film, and the other with CBP uniformly doped with 10 vol.% PtOEP. Both samples indicate a random orientation as found previously [45,102,105]. The negligible difference between the two samples shows that the MSL precisely and locally represents the amorphous morphology of the bulk film. We then annealed the CBP film at 95°C, above its T_g (62°C) [102] for 30 min, resulting in no visible change in some regions (A) in the optical micrograph in Fig. 6.2b, whereas there is evidence of crystallization in regions B. After 3 h, the film becomes uniformly crystallized (image C). Figure 9.2c shows the measured intensity profiles (data points) along with the simulation fits (solid lines) in pPP, normalized to values at $k_p = 0$ in regions A, B and C. The fits indicate that θ_{h-conv} decreases with annealing from $66 \pm 1\%$ to $0 \pm 12\%$, corresponding to a shift from random to principally vertical orientation. XRD patterns in the Bragg-Brentano geometry of a 30 nm thick neat CBP film are provided in Fig. 6.2d. These data reveal the cause of the decrease in θ_{h-conv} in the annealed CBP film. The amorphous, as-deposited film lacks X-ray peaks, whereas after annealing, the film shows a distinct (031) peak corresponding to vertical alignment of the CBP molecules [114]. This is illustrated in the inset showing the orientation of the (031) plane in blue relative to the molecules. In this case, the substrate plane is parallel to (031). We conclude that the reduced θ_{h-conv} of the PtOEP MSL is a result of changes in morphology of the CBP film.

Our results demonstrate that the combination of Fourier plane imaging microscopy and morphological sensing layers can be used to create high resolution 3D maps of the morphologies of vdW-bonded solids. Crystallization features witnessed by PtOEP occur after only a 30 min anneal at 95°C (Fig. 6.2b). The energy provided by annealing at $T > T_g = 62^\circ\text{C}$ of CBP [102] liberates the molecules to form crystallites. In region A, a slight decrease ($\sim 10\%$) of θ_{h-conv} is

observed due to morphological changes so small that they do not appear in the micrograph, showing the sensitivity of the method. The crystallization of CBP molecules is visible in region B, corresponding to an additional decrease in θ_{h-conv} . After 150 min, uniform crystallization spreads across the entire film (region C). The difference in the film appearance between regions B and C is not conspicuous, however, θ_{h-conv} decreases after 3 h of annealing, demonstrating continued morphological changes with time. The (031) plane observed via XRD in Fig. 6.2d shows that the CBP molecules in the crystallites formed by annealing are vertically oriented with their c_2 axis tilted approximately $9\text{--}17^\circ$ from the substrate normal. This corresponds to $\theta_{h-conv} = 9\text{--}28\%$, similar to the decrease in Fig. 6.2c. Thus, the decrease in θ_{h-conv} measured for PtOEP accurately represents the change in CBP film morphology. Similarly, in Fig. 6.4c and 4d, the in-plane orientation of PtOEP corresponds to the direction of spherulite growth, as illustrated in Fig. 6.4e.

6.5 Criteria of optimum molecules for morphological sensing layers

The same annealing procedure is followed by using the red emitting sensor molecule, PQIr. This pseudo-octahedral molecule features a bulky, tridentate structure. As before, the sample comprises a $\sim 1\text{\AA}$ thick, sensor layer deposited in the middle of a 30 nm thick CBP film. The as-grown sample shows a primarily horizontal sensor orientation ($\theta_{hor} = 75 \pm 1\%$). Unlike PtOEP, the complete crystallization of CBP does not occur in the presence of PQIr, even after several hours of annealing, as shown in Fig. 6.2e. Amorphous regions (D) do not show any change of TDM orientation. Indeed, PQIr molecular orientations are randomized even in the crystallized region (E), with significantly lower signal intensity than the as-grown sample. The measured θ_{hor} from all samples are summarized in Fig. 6.2f, showing that PQIr does not clearly describe the structure of CBP, in contrast to PtOEP.

The measurement precision is, in part, determined by the choice of sensor molecule. This is illustrated by comparing the results in Fig. 6.2 for PtOEP and PQIr, respectively. Compared to planar PtOEP, pseudo-octahedral Ir-complexes show less orientation dependence on the host matrix due to the small π -interactions arising from steric hindrance of their bulky molecular structures with the surrounding environment [102,115]. Furthermore, the orientation of heteroleptic Ir-complexes with an aliphatic ligand as in PQIr introduce anisotropic interactions, and hence anisotropic orientations with the organic surface during deposition, regardless of the host matrix composition. [20] This can cause a misrepresentation of the host morphology. Furthermore, steric hindrance can impede the ability of the molecules to follow the host morphology, and can even interfere with the progress of crystallization of the host. This is shown by the micrograph in Fig. 6.2e, where only local CBP crystallization occurs, even after hours of annealing above T_g . Amorphous regions (D) show no change in θ_{hor} after annealing, demonstrating morphological pinning by the PQIr sensors. Indeed, crystallization only takes place when phase separation of CBP and PQIr molecules occurs, as in region E. This, in turn, significantly decreases the PQIr emission intensity due to concentration quenching in sensor aggregates, and randomizes their orientation due to the elevated entropy of PQIr molecules [116]. In conclusion, bulky sensors not only misrepresent the morphology of the surrounding environment, but can also impede the host matrix from achieving its equilibrium structure. Hence, planar molecules are better suited for use in 3D FIM + MSL imaging, whereas doping sterically bulky molecules may improve morphological stability of the host even when used in sub-monolayer quantities. Indeed, FIM in this case has proven to be a useful tool in selecting molecules, while determining their efficacy in stabilizing thin film morphologies.

This leads us to identify the following properties of an appropriate morphological sensor molecule. It should (i) be intensely emissive at wavelengths distinct from that of the host, (ii) have a uniquely defined TDM axis relative to the molecular plane, (iii) be planar to avoid interfering with the morphological development of the host solid, and (iv) be symmetric to prevent the sensor orientation being driven by the molecular anisotropy [20,46,102]. Following these criteria, planar phosphorescent molecules with D_{nh} symmetry having cyclic conjugated π -systems, i.e. disk-shaped phosphors or fluorophores, are preferred. Polycyclic conjugated π -systems are sensitive to small changes of environment via large π - π interactions [45]. Additionally, it is a simple matter for disk-shaped molecules to convert θ_{hor} to the average tilt angle of the molecular plane [45]. On the other hand, asymmetric planar molecules with one molecular axis larger than the other, i.e. with an aspect ratio >1 , have distinct edges for a molecule to contact the substrate, causing difficulties distinguishing the high θ_{hor} either from a flat-lying or an edge-on configuration with the TDM axis parallel to the substrate plane. An example is dibenzo- (f,h) quinoxaline (Pt dipivaloylmethane)₂ in Chapter 7, that shows a horizontally aligned TDM with an edge-on configuration to the substrate. The complication becomes even more pronounced when the dye molecule has rotary σ -bonded aromatic chains that randomize the TDM orientation. Therefore, metal porphyrins or phthalocyanines are optimal sensing molecules for unambiguous orientation assignment.

6.6 Use of morphological sensing layers for multilayer systems

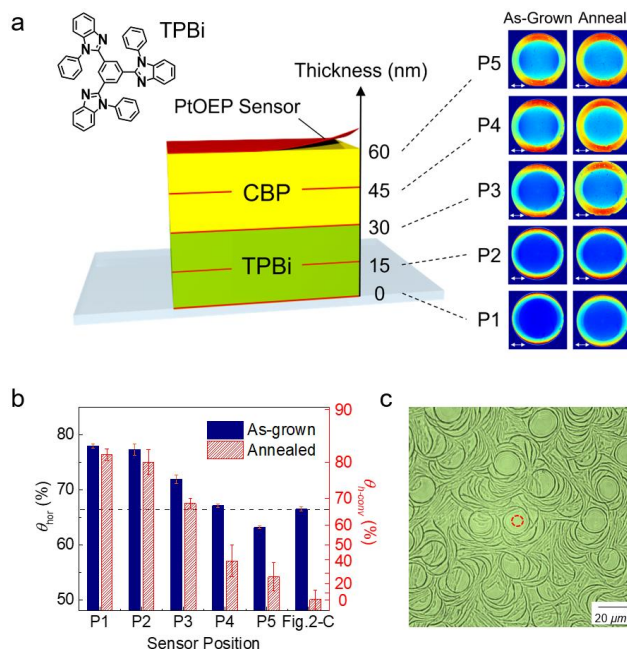


Figure 6.3 Imaging the morphology of a bilayer thin film.

(a) Illustration showing the placement of the PtOEP MSLs within a CBP/TPBi bilayer, with the measured polar plots before and after annealing at the right. Molecular formula of TPBi is shown. (b) Measured θ_{hor} (θ_{h-conv}) of the as-grown samples, and after annealing for 3 h. The dashed line indicates isotropic alignment. (c) Optical micrograph of the annealed sample. The red circle indicates the area excited by the laser.

We extended the measurement into the vertical (z) axis to obtain depth-related morphological data. Five samples are prepared comprising a planar heterojunction bilayer of 30 nm TPBi and 30 nm CBP, with PtOEP sensing layers placed in different positions in each of the various samples, labelled P1-P5 in Fig. 6.3a. All films are annealed at 95°C for 3 h. The pole plots in Fig. 6.3a show a small change in P1-P2 before and after annealing. This contrasts with significant differences observed in positions P4-P5. Measurements of θ_{h-conv} for each film are provided in Fig. 6.3b. Figure 9.3c shows an optical micrograph of the film after annealing, with the red circle showing the optically pumped region in the experiment. The patterns in the micrograph indicate local crystallization of CBP. The θ_{h-conv} is reduced by annealing to less than half of its original value in positions P4-P5, while it remains almost constant in P1-P2 in

TPBi [102] due to its $T_g = 122^\circ\text{C}$, which is higher than the annealing temperature. However, the decrease in P4-P5 is still less than in Fig. 6.2b, region C, in the neat CBP film. This suggests that the morphologically stable TPBi film partially “pins” the CBP structure due to contact at the heterointerface, similar to that found for metastable organic mixtures stabilized by including small concentrations of dopant molecules (e.g. PQIr) [117], or by the attachment of a metal cap [118].

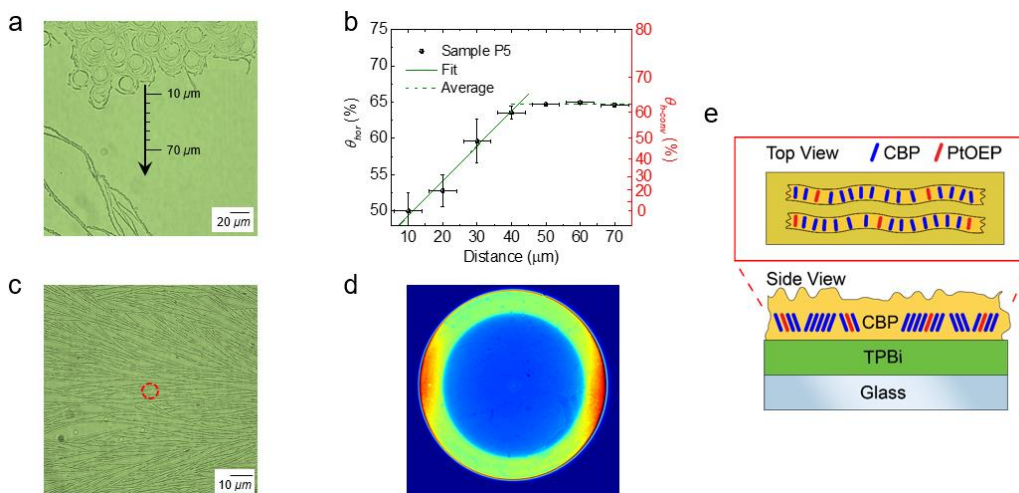


Figure 6.4 Mapping of the structure of a crystalline grain.

(a) Optical micrograph at the periphery of a spherulite in sample P5 after annealing. The arrow shows the line-scan path with measurements made at 10 μm intervals. (b) Measured θ_{hor} ($\theta_{\text{h-conv}}$) following the scanning path in (a). The solid line shows a linear regression fit to the data vs. distance from the spherulite, until the structure stabilizes close to a random orientation at distances $> 40 \mu\text{m}$ (dashed line). (c) Optical micrograph of a polycrystalline fiber of a spherulite in sample P4 after annealing. The red circle indicates the laser excitation area. (d) polar plot from the red-circled region in (c) using FIM with the linear polarizer removed. e. Schematic illustration of the configuration of the PtOEP sensor molecules within the CBP polycrystalline fibers.

Annealed CBP on a glass substrate in Fig. 6.2 forms a randomly oriented powder in the substrate plane. In contrast, the annealed CBP on TPBi forms spherulites of radially propagating polycrystals. Spherulites appear during diffusion-limited growth [119], which is caused by the underlying TPBi layer impeding the movement of CBP molecules. In Fig. 6.4a, we used FIM to map morphological variations of sample P5, by moving the beam radially away from the spherulitic region, with a 10 μm interval between each measurement. The orientation of the MSL gradually changes from vertical to random orientation, and stabilizes at 40 μm distance from the

spherulite periphery, as shown in Fig. 6.4b. The solid line shows the linear regression of the variation near the spherulitic region, whereas the dashed line shows the average $\theta_{h\text{-conv}}$ in the region of constant morphology.

Also, FIM was used to investigate one of the polycrystalline fibers within a spherulite in sample P4 (see image, Fig. 6.4c). The linear polarizer was removed for this measurement to capture the in-plane (azimuthal) pattern. The pole plot in Fig. 6.4d shows the substrate mode intensity has peaks in the direction parallel to the crystal branch direction. This phenomenon is similarly observed in other regions along different crystal dendritic growth directions, as shown in Fig. 6.5.

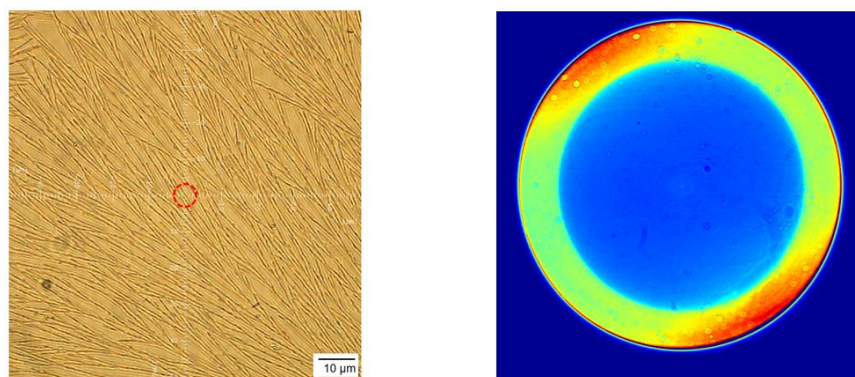


Figure 6.5 Dendritic growth of CBP on TPBi with annealing. Optical micrograph (left) and the FIM pole plot (right) measured from the polycrystalline fiber of CBP spherulite in sample P4 after annealing

The orientational conformation for this phenomenon is illustrated in Fig. 6.4e. Due to its disk-like structure, PtOEP emits the majority of its power perpendicular to the molecular plane, causing the vertically aligned PtOEP molecules to show peaks at high- k (corresponding to substrate modes). Also, the peak positions that are parallel to the fibers indicate that the molecular plane aligns perpendicular to the microfiber axis. These data reconfirm that PtOEP *follows* the CBP host matrix, giving information about the π - π stacking direction of CBP after annealing.

6.7 Merits of the technique

In FIM, the majority of emission towards the substrate is collected by the objective lens. Also, the intensity profile of the entire k -space is simultaneously acquired in a single snapshot, enabling a dramatically reduced time for measurement compared to conventional, 1D angle scanning methods [26]. Consequently, it is possible to observe the emission from minute dye molecule concentrations. Indeed, sub-monolayer coverage by sensor molecules enables their precise placement at well-defined depths within the host as in Fig. 6.3, enabling a depth resolution that is limited by the flatness of the predeposited film and the ability to accurately determine layer thickness during deposition. This means that for an ideal case, where the most precise deposition and measurement techniques are used with a flat surface, an Ångstrom-level resolution in the depth axis can be achieved. This is compared with commonly used morphological measurements such as atomic force microscopy (AFM), ellipsometry, and X-ray or electron beam diffractometry that are only capable of revealing either surface structure or averaged information of the bulk. Electron tomography is another means for investigating the bulk morphology of the film. However, it requires crystalline film structures and atoms with high contrast (e.g. metals) to resolve the orientation or the arrangement of the molecules. Moreover, the high energy electron beam inflicts damages to the sample, especially for soft materials as organics. The position-selective character of the MSL enables investigating the interface morphology at planar heterojunctions or within donor-acceptor domains in mixed heterojunctions, which can be helpful in optimizing organic electronic device performance [120]. An example of an interface morphology measurement is sample P3 in Fig. 6.3, determined by locating a sub-monolayer sensor layer between the CBP and TPBi layers. The horizontal alignment of the as-grown P3 sample shows that the initially deposited CBP molecules at the interface follow the morphology of the underlying layer (TPBi). However,

the orientation in P4 is identical to the bulk CBP, demonstrating that effects of the underlying layer are not preserved as the deposition continues. At the air-CBP interface (P5), the orientation becomes increasingly vertical compared to P4, showing that surface crystallization of CBP is encouraged as its degrees of freedom increase with distance from the pinning interface. The change of θ_{h-comv} in P3 after annealing is smaller than P4 - P5, which is still less than in Fig. 6.2, region C. This suggests that depositing CBP on a stable layer suppresses morphological changes *throughout the bulk of the film*. This is similar to the structural forcing induced by molecular alignment to an underlying template layer [46,121].

Recent studies on small molecule orientation has, to this point, primarily focused on dopant emitters [82]. Nevertheless, the morphology of buffer layers such as host or transport layers is also important, since π - π stacking affects charge birefringence, conductivity and the exciton transfer efficiency. Ellipsometry has been commonly used for investigating the structure of buffer layers via analysis of the difference between ordinary and extraordinary refractive indices [122] as shown in Fig. 6.6. The refractive index of a 30 nm thick Tint film in Fig. 6.6 demonstrates vertically aligned molecules, consistent with the result from XRD and FIM+MSL. However, the birefringence of the film does not always reveal the actual molecular configuration since it solely probes the polarizability and the TDM of the film. For example, TPBi shows nearly isotropic orientation by ellipometry [123], whereas the result for P2 in Fig. 6.3, and the previous report from Mayr, et al. [102] indicate the molecules have a preferred horizontal alignment. This difference arises from the molecular structure of TPBi (Fig. 6.3a, inset) comprising three rotary σ -bonded aromatic chains that are randomized in the solid, resulting in suppressed birefringence for molecules that are horizontally aligned.

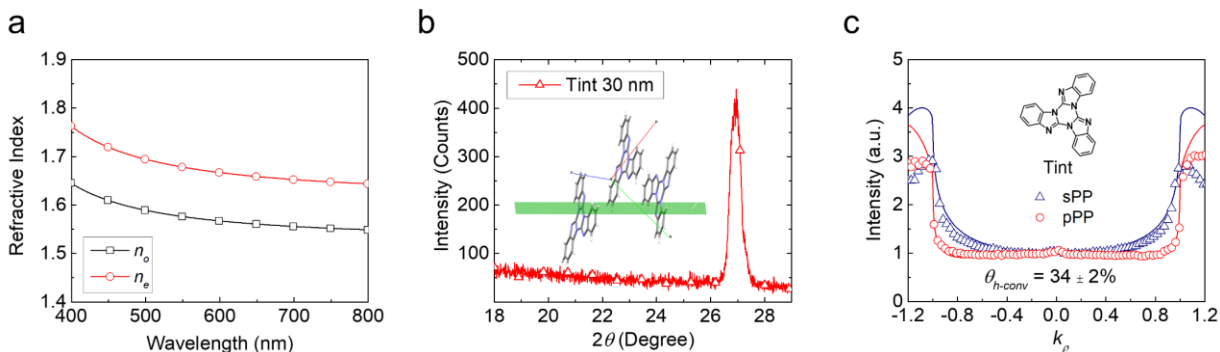


Figure 6.6 Morphological investigation of Tint film via PtOEP MSL. Morphological investigation of a 30 nm thick Tint film by the PtOEP MSL. (a) Measured refractive index by ellipsometry, (b) X-ray diffraction pattern showing the $(\bar{2}20)$ peak, Inset: Tint crystal structure and $(\bar{2}20)$ plane (green) parallel to the substrate (CCDC-1919336). (c) Measured angular intensity profile in pPP and sPP (data points) via FIM and the simulation fits (solid lines), Inset: Molecular formula of Tint. The refractive index in (a), $n_e > n_o$, shows stronger polarizability in the substrate normal than the in-plane direction due to the vertically oriented Tint molecules, which is consistent with the XRD and FIM measurements.

6.8 θ_{hor} conversion of PtOEP

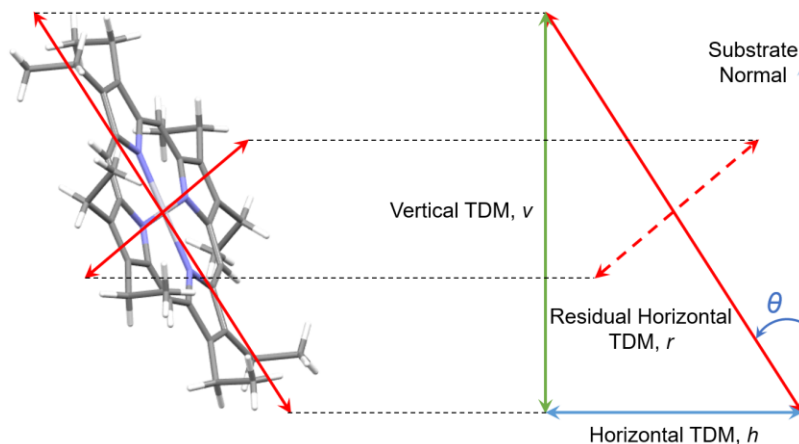


Figure 6.7 TDM within the PtOEP molecule.

PtOEP is a disk-shaped molecule comprising two orthogonal TDMs in the molecular plane, as shown in Fig. 6.1b. It has 4-fold symmetry, hence its TDM exhibits this same symmetry in the molecular plane. This causes the measured θ_{hor} to include a residual horizontal TDM regardless of the orientation of the molecule, denoted as r in Fig. 6.7. Thus the measured $\theta_{hor} = \frac{1}{2} + \frac{1}{2} \cdot \sin^2 \theta$, reducing the range of θ_{hor} from 50% to 100%. Here, we obtain the θ_{h-conv} excluding the contribution from the residual dipoles for a better understanding of the PtOEP orientation.

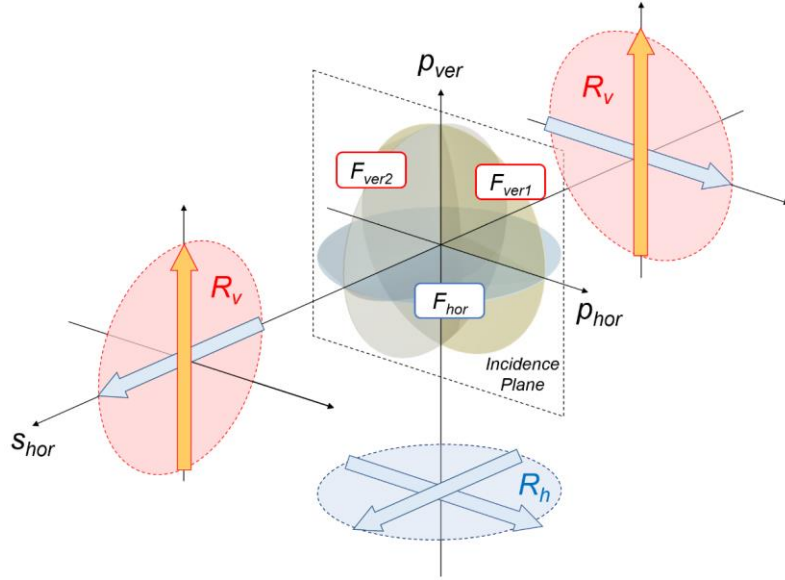


Figure 6.8 θ_{hor} conversion of PtOEP.
Unit orthogonal planes for PtOEP. Arrows indicate the TDMs.

We decompose the emission from PtOEP into three orthogonal planes denoted as F_{hor} , F_{ver1} and F_{ver2} in Fig. 6.8. The ratios are R_h and R_v for each horizontally and vertically aligned plane, respectively. Then the sum becomes, $2R_v + R_h = 1$. Each plane is decomposed into two orthogonal dipoles (see Fig. 6.8), giving:

$$\theta_{hor} = \frac{2(R_v + R_h)}{2(R_v + R_h) + 2R_v} = R_v + R_h = 1 - R_v = \frac{1}{2} + \frac{1}{2} R_h, \quad (6.2)$$

giving,

$$\begin{cases} R_v = 1 - \theta_{hor} \\ R_h = 2\theta_{hor} - 1 \end{cases} \quad (6.3)$$

The residual horizontal TDMs in Fig. 6.7 are the two TDMs described in the R_v and one TDM in R_h . After excluding the residual TDMs, each PtOEP molecule includes one TDM. Then the θ_{h-conv} is the fraction of two orthogonal horizontal TDMs ($s_{||}$, $p_{||}$) to the total as,

$$\theta_{h\text{-conv}} = \frac{p_{\parallel} + s_{\parallel}}{p_{\perp} + p_{\parallel} + s_{\parallel}} = \frac{2R_h}{2R_h + R_v} = \frac{2(2\theta_{hor} - 1)}{3\theta_{hor} - 1} \quad (6.4)$$

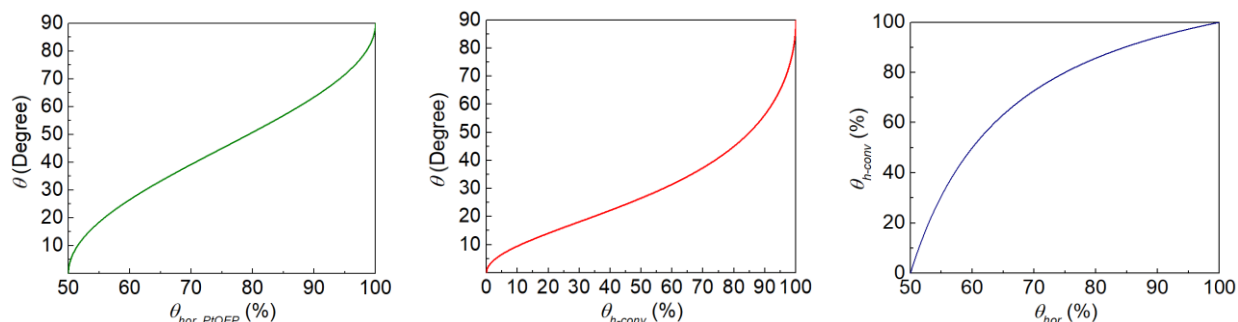


Figure 6.9 Correlation between θ_{hor} of PtOEP vs. various values. Measured θ_{hor} vs. molecular tilt angle θ (left), $\theta_{h\text{-conv}}$ vs. molecular tilt angle θ (middle), and measured θ_{hor} vs. $\theta_{h\text{-conv}}$ (right).

6.9 Error analysis

6.9.1 Surface Roughness Errors

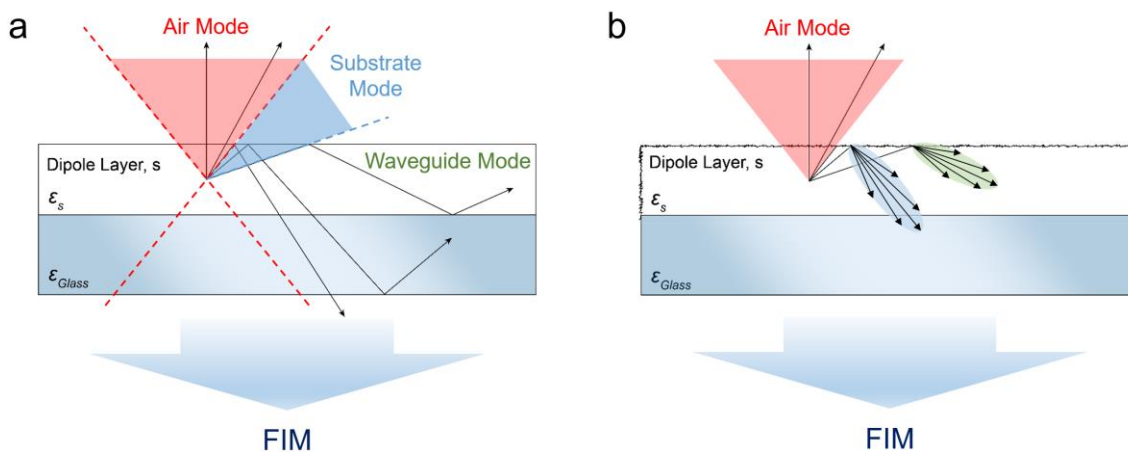


Figure 6.10 Rough surface errors. Schematic illustration of the sample for FIM. In theory, all layers are perfectly flat (a), however, in some cases the surface roughness is comparable to the scale of the wavelength (b). Then a broader specular lobe occurs at the rough surface, causing errors in the data.

Dyadic Green's function analysis is based on a planar multilayer stack. When the standard deviation of the height across the surface-air interface of a film is comparable to the wavelength, the reflected light from the interface creates a broader reflectance lobe as shown in Fig. S6-1(b). The reflectance lobe redirects a fraction of the substrate modes into the air mode. This causes the

air mode intensity to increase, especially near the air / substrate mode interface, leading to error. The error increases as the fraction of vertically aligned TDM increases since the majority of the light emitted from the vertically aligned TDM is coupled into substrate modes.

The effect of the surface roughness error is investigated by comparing the θ_{hor} of sample P5 at $x = 10 \mu\text{m}$ in Fig. 4b ($\theta_{hor} = 50 \pm 2\%$) with the results from the rough spherulitic region, $\theta_{hor} = 47 \pm 2\%$. As in Fig. S1, PtOEP cannot show $\theta_{hor} < 50\%$ ($\theta_{h-conv} < 0\%$), however, the rough spherulite surface causes a broad reflectance lobe leading to an under estimation of θ_{hor} by 3-5%. However, the smooth regions within the spherulites show negligible roughness compared to the as-grown sample shown in the cross-sectional profile in Fig. S6-2(c). Therefore, the laser beam is positioned within the smooth circular regions to measure θ_{hor} from the spherulite region as shown in Fig. 3c to minimize error.

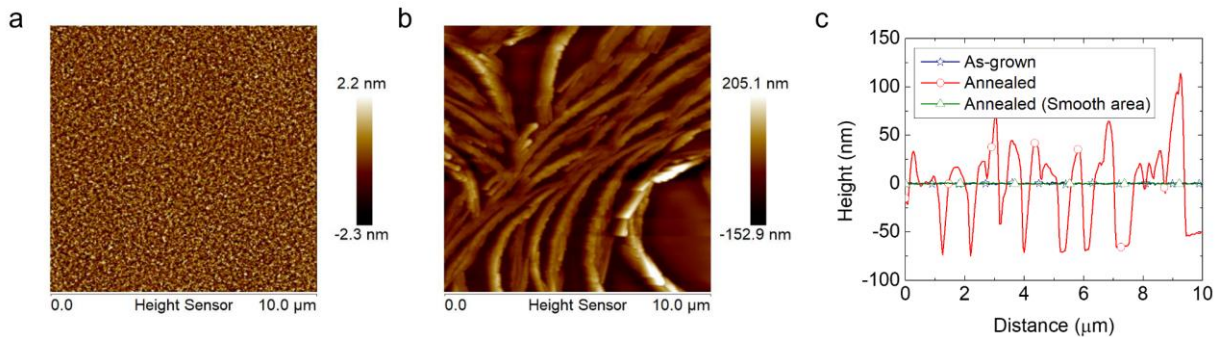


Figure 6.11 Surface scanning for rough surface errors. Atomic force micrograph of the surface of (a) as-grown and (b) annealed (95°C, 3 h) organic bilayer films comprising CBP 30nm / TPBi 30 nm on the substrate. (c) Cross-sectional profile of each sample.

6.9.2 Fitting errors

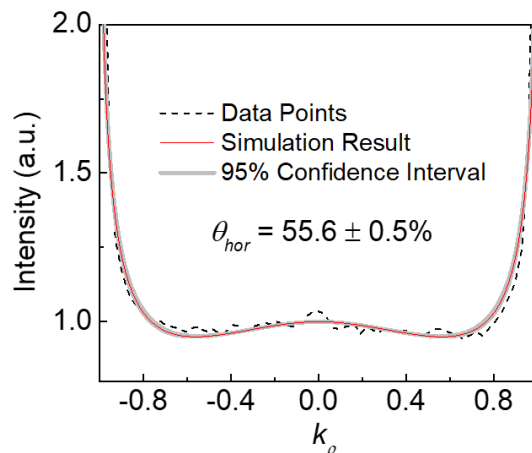


Figure 6.12 Fitting errors.

Measured pPP intensity profile (dashed line) via FIM along with the simulation fit (solid lines, red) from a PtOEP MSL in the middle of a 30 nm Tint film. The grey solid line shows the upper and lower bound of the 95% confidence interval of the linear regression.

We used least squares method for the mathematical regression analysis (function ‘*lsqcurvefit*’ in MATLAB), with the variable θ_{hor} as follows:

$$\min_{\theta_{hor}} \sum_{k_i} \left(F(\theta_{hor}, k_i) - data_{k_i} \right)^2 \quad (6.5)$$

where $F(\theta_{hor}, k_i)$ is the simulated radiative intensity at $k_\rho = k_i$ with θ_{hor} as an input variable, and $data_{k_i}$ is the experimental result at $k_\rho = k_i$. The k -space fitting is performed over the domain, $-1.1 < k_\rho < 1.1$, to minimize imaging artefacts in the high- k region. The fitting error denotes the standard deviation of the θ_{hor} with 95% confidence level.

6.9.3 Density analysis

In the previous work of H-F. Xiang et al. [124], density of the films comprising different small organic molecules were measured. Here, CuPC, which shares a similar molecular structure as PtOEP, shows a density of $1.54 \pm 0.02 \text{ g/cm}^3$. This is the density of the bulk film (3D) whereas the morphological sensing molecules are spread in 2-dimensional slab. The molecular weight of

PtOEP is 727.84 g/mol, leading to 1.27×10^{21} molecules/cm³. Then, we could obtain the density in 2D by taking a 2/3 power of the molecules/cm³, which becomes 1.18 molecules/nm².

6.9.4 Depth of field

Depth of field is determined from the nearest object plane in focus to that of the farthest plane also simultaneously in focus. In microscopy, the depth of field is usually in the scale of microns. Depth of field varies with numerical aperture and magnification of the objective lens, and usually high numerical aperture systems, which typically have high magnification, have shorter depth of field as:

$$DOF = \frac{\lambda \cdot n}{NA^2} + \frac{n}{M \cdot NA^2} \cdot e \quad (6.6)$$

where λ is the wavelength of the light source, n is the refractive index of the medium (air or oil), NA is the numerical aperture of the objective lens, and e is the smallest distance that can be resolved by a detector placed in the image plane of the microscope objective with a lateral magnification of M . For example, the objective lens used in this experiment ($\times 100$, NA=1.40) shows a depth of field of 531.5 nm for a light source of $\lambda = 650$ nm with an assumption of $e = 4\mu\text{m}$. This means that the image plane position should be adjusted when the measurement range in the depth axis exceeds 531.5 nm.

6.10 Conclusion

We introduce a method to spatially resolve the 3D morphology within thin films by measuring the orientation of an ultrathin, luminescent morphological sensing layer using Fourier plane imaging microscopy. The MSL is deposited at the position of interest in a sub-monolayer quantity that has a minimal influence on the morphology of the film under study. The sensing

molecules with discotic molecular structures are optimal for precisely representing the local structure. With this method, we measured the morphology at multiple depth positions within a planar heterojunction bilayer comprising films with different T_g , showing different morphological evolutions across the bilayer bulk with annealing. In addition, we investigated the morphology of the annealed film in various in-plane positions with micrometer scale features using a high magnification objective lens in the FIM. The resolution of our technique is at the Ångstrom scale in the direction normal to the film plane, and is optically diffraction limited within the plane. This capability is used to generate precise, 3D maps of film morphology. Importantly, given that each polar image revealing the molecular orientation within the field of focus is taken in a single shot, changes in morphology can be observed in real time by recording a sequence of images as the film is heated or exposed to solvent vapors in ambient or other selected environments (vacuum, inert gas, etc.).

Chapter 7 Systematic Control of the Orientation of Organic Phosphorescent Pt Complexes in Thin Films for Increased Optical Outcoupling

To date, studies on phosphorescent emitter orientation have largely focused on Ir complexes [20,37,40,41,44,102,125–127]. While the common Ir (III) complexes used in OLEDs have octahedral geometries, related Pt (II) complexes have planar geometries. In this context, there has been a rapid progress in developing high external quantum efficiency Pt complex emitters [128,129] for PHOLEDs with favorable color characteristics [130,131], and long operational lifetimes [132]. Highly efficient PHOLEDs using these complexes have been enabled by increasing the fraction of light outcoupled from the PHOLED by aligning the TDM of the light emitting molecules parallel to the substrate [27,69,133]. Controlling the molecular alignment, therefore, can play a role in improving the efficiency of Pt complex-based PHOLEDs. The planar structure of Pt complexes has a better chance of forming π -stacking networks than bulky, 3 dimensional molecules, potentially enabling control of the molecular orientation in films via external forces such as structural templating [52].

7.1 Introduction

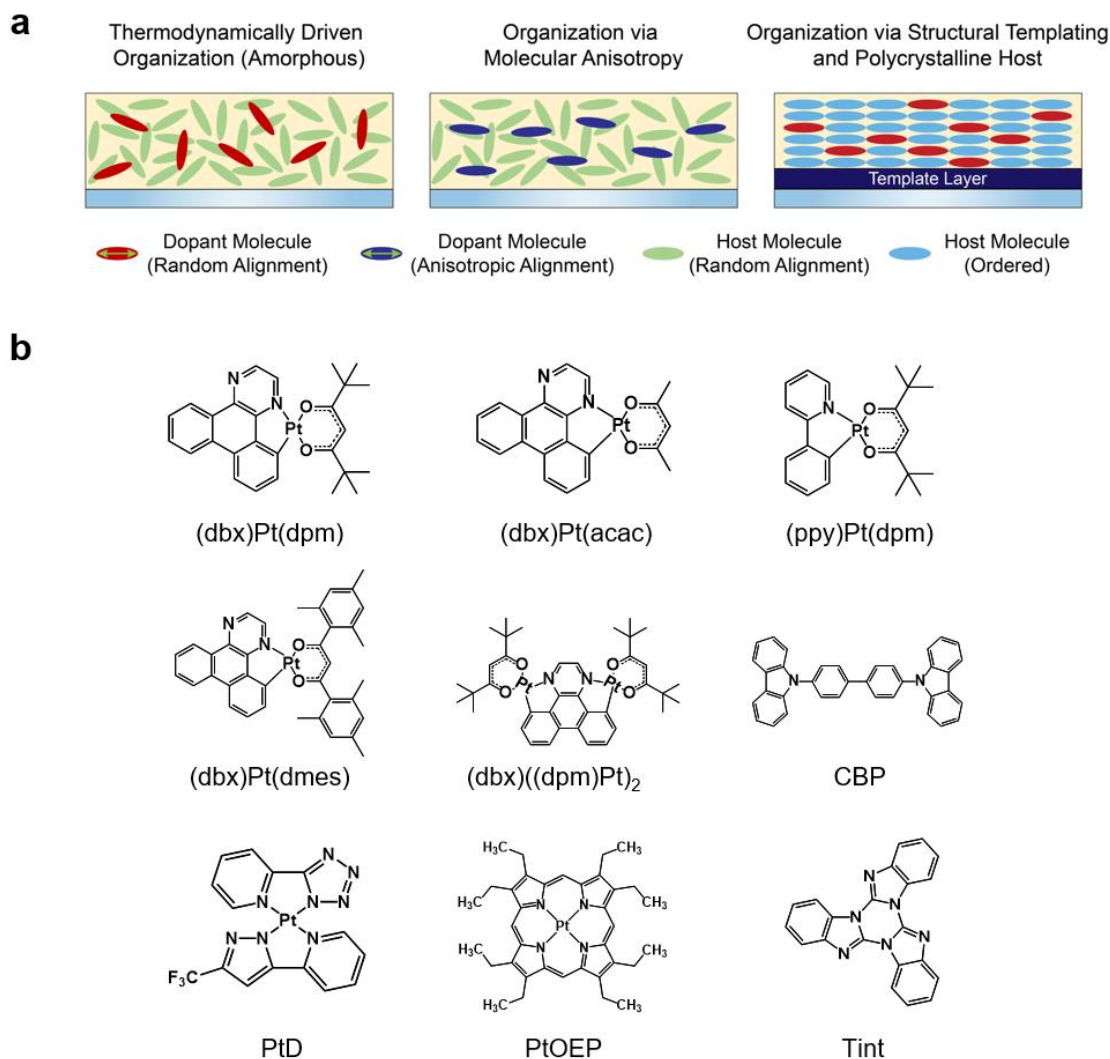


Figure 7.1 Controlling molecular orientation in light emitting layers.

(a) Amorphous growth leads to random alignment of molecules relative to the substrate (left). Molecular anisotropy can lead to preferable alignment of light emitting species (middle). Growth of an ultrathin templating layer forces the subsequently deposited molecules to lie flat on the substrate (right). (b) Molecular structural formulae of the Pt complexes and small molecules used for the experiments are shown.

In this chapter, we control the Pt complex orientation relative to the substrate plane during the film growth using two different approaches. The first is to modify the molecular structure of heteroleptic bidentate Pt complexes to induce preferred horizontal alignment of the molecule via molecular anisotropy as illustrated in Fig. 7.1a. Angle dependent p-polarized photoluminescence of a film comprising (dbx)Pt(dpm) (see Fig. 7.1b), doped in the organic host, CBP, revealed that

the dopant TDMs are preferentially oriented perpendicular to the substrate. Studies of modified complexes of (dbx)Pt(dpm) showed that the aromatic ligands control molecular orientation. The second approach achieves the preferred orientation of the emitter by pre-depositing a thin (< 2 nm) layer of a molecular template on the substrate that promotes the horizontal alignment of subsequently deposited emissive Pt complexes (Fig. 7.1a) [52,134].

The relationship between TDM orientation and film morphology are investigated via a combination of angle-dependent PL and x-ray diffraction. Correlations between film crystallinity and orientation controlled via structural templating are investigated by varying the concentration of a polycrystalline host in the emissive layer, revealing that a host concentration of > 70 vol.% is required to achieve significant control over otherwise randomly distributed phosphor orientations. An increase of nearly 60% in horizontally aligned molecules is obtained using a molecular template compared with films deposited directly onto bare sapphire and fused silica substrates. We find that by varying the details of molecular and substrate structures provide a systematic route for controlling molecular alignment during layer growth, and ultimately to enhance the optical outcoupling of the emitting species, making these effective strategies for increasing OLED efficiency.

7.2 Experimental methods

7.2.1 Sample preparation

Thin films were deposited at 1.0 Å/s on 0.2 mm thick fused silica glass by vacuum thermal evaporation in a chamber with a base pressure of 1×10^{-7} torr. The deposition rate and film thicknesses were controlled using a quartz crystal thickness monitor. Following deposition, devices were encapsulated using an epoxy seal around the edge of a cover glass in a N₂

environment. The samples for angle-dependent optical characterization consist of 1.5 nm PTCDA / 1.5 nm NTCDA/ 30 nm emissive layer. PTCDA, NTCDA, PtOEP, and CBP were purchased from Luminscence Technology, Corp.

7.2.2 Optical measurements

Samples were excited with a He-Cd laser at a wavelength of 325nm. Alignment of the TDM was inferred from the angle-resolved photoluminescence of the phosphor-doped films [26,28]. The emission from horizontally aligned TDMs is decomposed into TE_{hor} and TM_{hor} modes, whereas the vertically aligned TDM emits into the TM_{ver} mode. The θ_{hor} was obtained from the intensity ratio of TM_{hor} to TM_{ver} modes by removing TE_{hor} using a polarization filter. This is compared to the simulated values calculated based on the dyadic Green's function in a birefringent medium [94]. A least-squares algorithm was used to fit the measured photoluminescence data to the simulation. The 0.2 mm thick fused silica substrate was placed perpendicular to the plane of detection and the emission was outcoupled from the substrate using a 2 cm radius, half-cylindrical lens. A motorized stage was used to position the detector. The refractive indices and extinction coefficients of materials were measured using variable-angle spectroscopic ellipsometry.

7.2.3 X-ray diffraction measurements

X-ray measurements for thin film samples were performed in the Bragg-Brentano geometry using the Cu-K α radiation source operated at 40kV and 44mA in a Rigaku Ultima IV X-Ray Diffractometer.

7.2.4 Single crystal structure determination

The plates of PtD, Tint and (dbx)Pt(dpm) were grown by 3-zone thermal gradient vacuum sublimation. The zone temperatures for PtD and Tint were 240 / 210 / 180 °C and 200 / 165 / 135 °C, respectively. For PtD and Tint crystals of dimensions of 0.04 × 0.01 × 0.01 mm and 0.01 × 0.01 × 0.01 mm were mounted on a Rigaku AFC10K Saturn 944+ CCD-based X-ray diffractometer equipped with a low temperature device and Micromax-007HF Cu-target micro-focus rotating anode ($\lambda = 1.54187 \text{ \AA}$) operated at 1.2 kW (40 kV, 30 mA). The X-ray intensities were measured at 85 K with the detector placed at a distance 42.00 mm from the crystal. Rigaku d*trek images were exported to CrysAlisPro for processing and corrected for absorption. A transparent, prism-like 0.11 mm x 0.18 mm x 0.35 mm crystal of (dbx)Pt(dpm) was used for the X-ray crystallographic analysis. The X-ray intensity data are obtained using a Bruker APEX DUO system equipped with a fine-focus tube ($\text{MoK}\alpha$, $\lambda = 0.71073 \text{ \AA}$) and a TRIUMPH curved-crystal monochromator. The frames were integrated with the SAINT V8.37A (Bruker AXS, 2013) algorithm. Data were corrected for absorption using the multi-scan method (SADABS). The structures for the three compounds were solved and refined with the Bruker SHELXTL (version 2016/6) software package.

7.2.5 DFT calculations of TDM and molecular orbitals

The ground (S_0) and triplet state (T_1) geometries of PtD and PtOEP were optimized at the B3LYP/LACV3P** level using the Jaguar (v. 9.4 release 15) program within the Material Science suite developed by Schrödinger, LLC [135]. Time-dependent density functional theory (TD-DFT) with the zero order regular approximation (ZORA) approach [136] as implemented in Jaguar to compute the TDMs for phosphorescent ($T_1 \rightarrow S_0$) emission,. The ZORA Hamiltonian incorporates

spin-orbit coupling (SOC) effects that are associated with triplet ($T_1 \rightarrow S_0$) emission. The SOC-TD-DFT calculations were performed on the T_1 optimized structures using the B3LYP functional and a mixed basis set in which the DYALL-2ZCVP-ZORA-J-Pt-Gen set was used for the Pt, while the 6-31G** set was used for the remainder of the atoms.

To simulate the T_1 state relaxation of the PtD excimers/dimers (3.41-dimer and 3.35-dimer) within the crystalline matrix, geometry optimization was performed on each dimer constrained by a molecular shell consisting of all its immediate neighbors (based on the crystal structure packing data) modeled as a rigid classical force field. This was done using a 2-layer hybrid QM/MM with an n -layered integrated molecular orbital and molecular mechanics (NIOM) scheme in which the central dimer was treated at the B3LYP/LanL2Dz level while the UFF molecular mechanics force field was used to model the surrounding molecular shell which was kept frozen during the optimization. All NIOM calculations were performed using the Gaussian 09 program [137]. Subsequently, SOC-TDDFT calculations were performed on the T_1 (NIOM:B3LYP/LanL2Dz:UFF) optimized structure of both dimers to obtain the TDVs associated with dimeric/excimeric emission. The surrounding molecular shell was ignored for the SOC-TDDFT calculations.

7.3 Morphological control via modifying the molecular structure

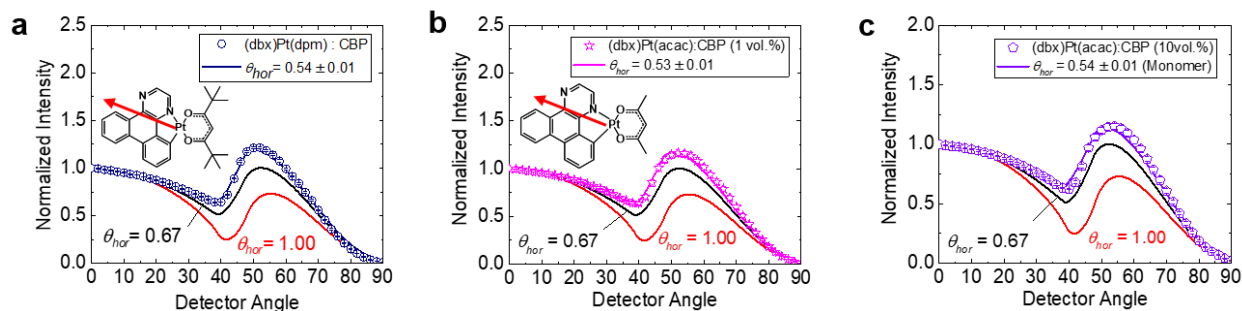


Figure 7.2 Orientation analysis of (dbx)Pt(dpm).

Angle dependent *p*-polarized photoluminescence measurements for (a) (dbx)Pt(dpm) doped at 10 vol.% and (dbx)Pt(acac) doped at (b) 1 vol.%, and (c) 10 vol.% into a CBP host. Insets show the TDM orientations in the molecules.

We study a series of bidentate Pt (II) complexes with chromophoric (C[^]N) and ancillary (L[^]X) ligands, shown in Fig. 7.1 DFT is used to determine the TDM orientation relative to the molecular frame in these complexes. The TDM of the complex lies in the (C[^]N)Pt plane with an angle δ between the TDM and the Pt-N bond, which ranges between 20° and 45° for the (C[^]N)Pt(L[^]X) complexes [138]. We chose (dbx)Pt(dpm) as the reference dopant molecule, comprising a chromophoric dibenzo-*(f,h)*-quinoxaline (dbx) aromatic ligand, and an ancillary dipivolylmethane (dpm) aliphatic ligand. The complexes are doped into CBP at 10 vol.%, and angle-dependent PL measurements of the films are analyzed to obtain the TDM orientation relative to the substrate of $\theta_{hor} = 0.54 \pm 0.01$, Fig. 7.2a. Here, θ_{hor} corresponds to fractional contribution of the net TDM direction lying in the horizontal plane parallel to the substrate, thus the fraction in the vertical direction is 0.46. An isotropic thin film gives $\theta_{hor} = 0.67$. The DFT calculation in the inset shows that $\delta = 36^\circ$. Shifting to a smaller ancillary ligand in (dbx)Pt(acac) shows similar alignment ($\theta_{hor} = 0.53 \pm 0.01$) to (dbx)Pt(dpm) when doped at 1 vol.% and 10 vol.% in CBP, see Fig. 7.2b and 2c.

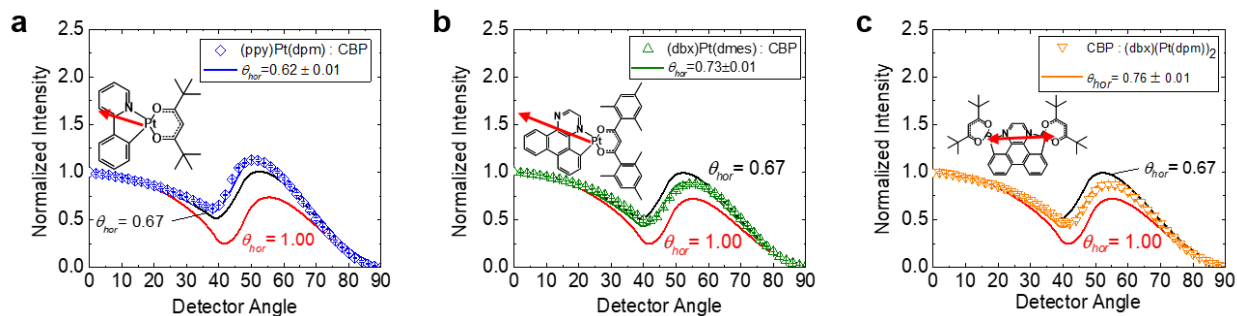


Figure 7.3 Orientation analysis of Pt complex dopants.

Angle dependent *p*-polarized photoluminescence measurement for (a) (ppy)Pt(dpm), (b) (dbx)Pt(dmes), and (c) (dbx)(Pt(dpm))₂ doped into CBP at 10 vol.%. Insets show the TDM orientations in the molecules.

Figure 7.3 shows the angle-dependent PL of several different (C^N)Pt(L^X) complexes doped at 10% in CBP. The film comprising (ppy)Pt(dpm) in Fig. 7.3a demonstrates an increased net horizontal alignment of the TDM compared to (dbx)Pt(dpm) ($\theta_{hor} = 0.62 \pm 0.01$ vs. 0.54 ± 0.01). Introduction of an aromatic ancillary ligand comprising two mesityl groups attached to the acac ligand producing (dmes)Pt(dbx), increases the horizontal component even further to $\theta_{hor} = 0.73 \pm 0.01$. Attaching an additional Pt-dpm on the opposite side of the dbx ligand in (dbx)(Pt(dpm))₂ shown in Fig. 7.3c, results in a horizontal component of $\theta_{hor} = 0.76 \pm 0.01$.

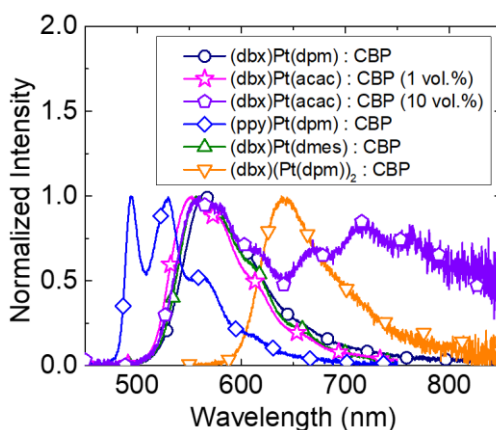


Figure 7.4 Photoluminescence spectra of films of Pt complexes doped into CBP. Measured photoluminescence of films of (dbx)Pt(dpm), (dbx)Pt(acac), (ppy)Pt(dpm), (dbx)Pt(dmes) and (dbx)(Pt(dpm))₂ doped into CBP at 10 vol.%. The (dbx)Pt(acac) was also doped into CBP at 1 vol.%.

7.4 Morphological control via structural templating

The emission spectra of Pt-complex doped CBP films are shown in Fig. 7.4. Contrary to changes in the ancillary (L^X) ligand, changes in the chromophoric (C^N) ligand leads to marked shifts in the emission spectra. In contrary, promoting molecular alignment *via* substrate structural templating provides a potential route to control the orientation of the square planar Pt-complexes within a blended film without changing the molecular structure and hence its emission spectrum. Two phosphorescent Pt complexes molecules were used explore the templating approach; one

comprising a neat PtD film, and the other consisting of PtOEP doped at 10 vol.% into Tint (see Fig. 7.1b).

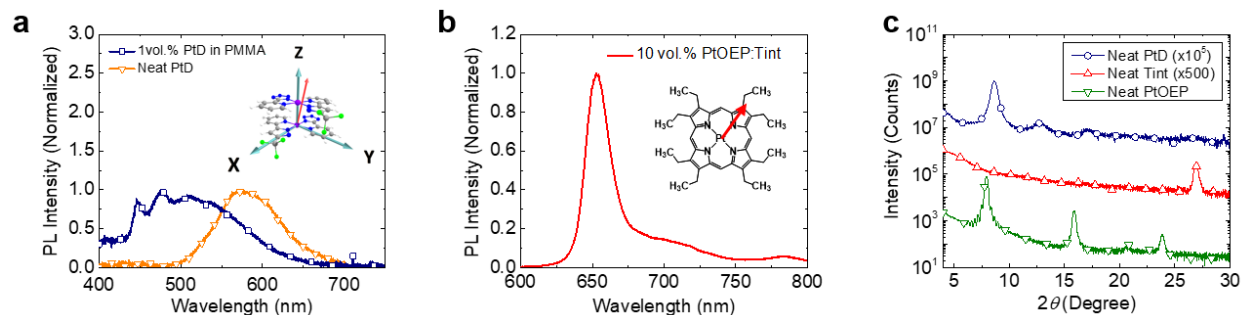


Figure 7.5 Photophysical and structural characteristics of neat films of PtD and PtOEP doped Tint.

(a) Photoluminescence spectra of films of neat PtD, and 1 vol.% PtD doped in PMMA. The arrow in the inset illustrates the dimer TDM vector formed between two PtD molecules as determined via time dependent density functional theory (TD-DFT). The z-axis is between the Pt center of the dopant molecules, whereas the PtD molecular plane lies in the x-y plane. (b) Photoluminescence spectra of PtOEP doped Tint at 10 vol.%. The arrow in the inset illustrates the TDM vector within the PtOEP molecule. (c) XRD diffraction patterns of neat PtOEP, PtD and Tint films. The data are offset for clarity.

Figure 7.5 shows the photophysical and structural characteristics of the neat PtD, Tint, PtOEP, and PtOEP-doped Tint films on sapphire substrates. The broad PL peak at a wavelength of $\lambda_{di} = 572$ nm of neat PtD in Fig. 7.5a is due to dimer emission. This feature is less pronounced in PtD diluted to 1 vol.% in a PMMA host due to monomer triplet emission at $\lambda_m = 450$ -480 nm. The PtOEP-doped Tint shows dominant monomer emission at $\lambda_m = 653$ nm in Fig. 7.5b, with the triplet, T_1 , TDM lying within the PtOEP molecular plane (see inset), and weak dimer emission at $\lambda_{di} = 783$ nm. Monomer emission is dominant since PtOEP molecules are diluted in the host matrix. Furthermore, steric hindrance between the PtOEP ethyl groups reduces coupling between the dopants. X-ray diffraction patterns of films deposited onto a sapphire substrate in Fig. 7.5c exhibit intense (200), (001) and (220) diffraction peaks of PtD, PtOEP and Tint, respectively (Fig. 7.7 for crystal structures and diffraction patterns of PtD and Tint).

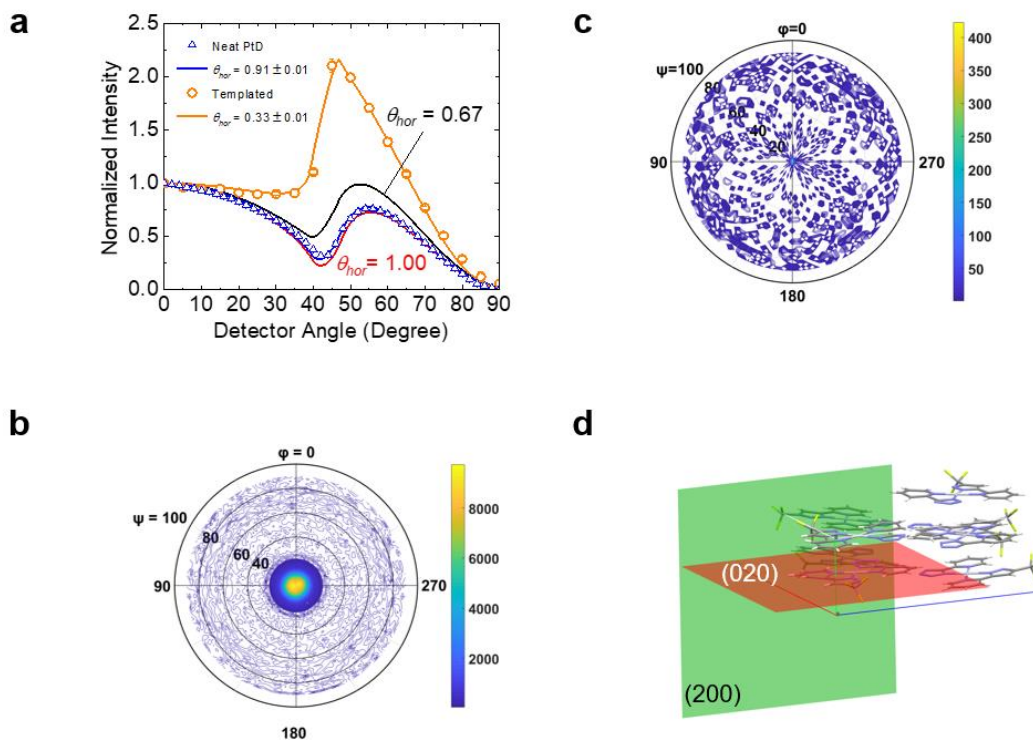
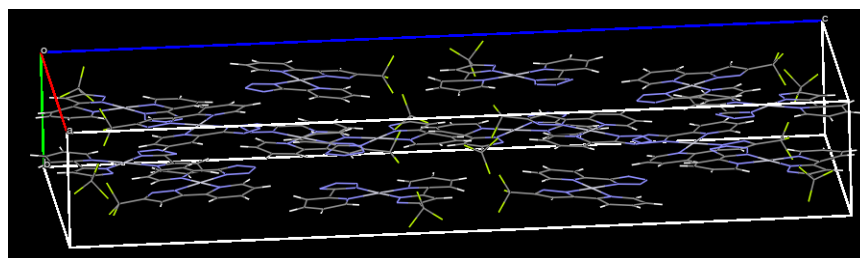


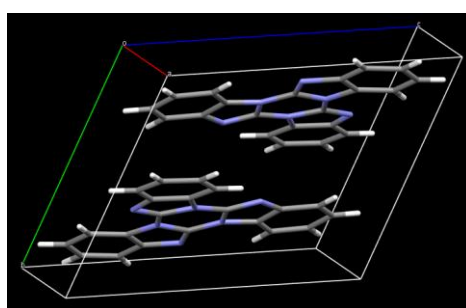
Figure 7.6 Control of the PtD TDM via templating.

(a) Angle-dependent *p*-polarized photoluminescence of a neat PtD film grown on sapphire substrate and on a pre-deposited template layer. (b) X-ray pole figure of the (200) plane ($2\theta = 8.4^\circ$) for a neat PtD film on sapphire. (c) X-ray pole figure of the (020) plane ($2\theta = 26.6^\circ$) for a neat PtD film on a PTCDA template layer. (d) PtD crystal structure showing the (200) (green) and (020) (red) planes.

Film morphology was also controlled via structural templating using a self-organized, 1.5nm (~5 monolayer) thick PTCDA layer [52,139]. The PTCDA grows in the flat-lying α -phase (102) (i.e. molecular planes of PTCDA lie parallel to the substrate), thus increasing the possibility of π -stacking with the subsequently deposited molecules [53]. For the angle-dependent PL measurement in Fig. 7.6a, a neat layer of NTCDA of the same thickness (1.5 nm) was deposited on the PTCDA prior to deposition of the emissive layer. The NTCDA/PTCDA bilayer transfers its structure to the subsequently deposited molecules (Fig. 7.8) while also blocking excitons formed in the emissive layer from quenching at PTCDA with its relatively low singlet exciton energy (1.95eV) [140].



Material	Space Group	a(Å)	b(Å)	c(Å)	α (°)	β (°)	γ (°)	Cell Volume (Å ³)
PtD	P b c a	20.9	6.7	45.0	90	90	90	6294.1



Material	Space Group	a(Å)	b(Å)	c(Å)	α (°)	β (°)	γ (°)	Cell Volume (Å ³)
Tint	P-1	8.1	9.1	11.6	109.3	101.9	100.8	750.91

Figure 7.7 Measured single crystal structure and cell parameters of PtD and Tint based on single crystal XRD.

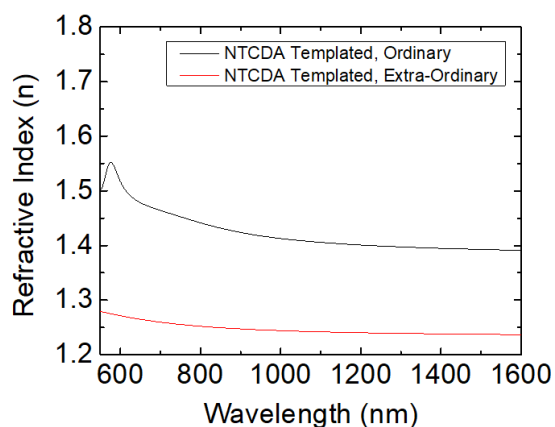


Figure 7.8 Measuring the birefringence of a neat NTCDA film via refractive index. The ordinary refractive index is larger than the extraordinary refractive index from the NTCDA film, showing the horizontal alignment of NTCDA molecules deposited on the PTCDA template [105]. This enables the monolayer thick NTCDA layer (1.5nm) to transfer the templated structure to the subsequently deposited molecules.

The PtD film deposited on the NTCDA/PTCDA template shows a decreased horizontal orientation ($\theta_{hor} = 0.33 \pm 0.01$) of the PtD dimer TDM compared to deposition on a bare fused silica substrate with $\theta_{hor} = 0.91 \pm 0.01$ (see Fig. 7.6a). To determine the relationship between TDM orientation and film morphology, x-ray pole figures of the (200) and (020) planes are provided in Fig. 7.6b and 6c. The configuration of each plane within the PtD crystal is shown in Fig. 7.6d. The film deposited directly on the sapphire substrate in Fig. 7.6b shows the (200) diffraction peak ($2\theta=8.2-8.5^\circ$) at a radial angle of $\psi = 0^\circ$, suggesting that (200) plane lies parallel to the substrate. The (200) plane lies perpendicular to the PtD molecular plane, hence the (200) diffraction peak at $\psi = 0^\circ$ indicates the molecular plane is vertically aligned to the substrate. The (020) plane ($2\theta = 26.6^\circ$) parallel to the molecular plane shows a diffraction peak at $\psi = 0^\circ$ for the film on the template layer, indicating that the PtD molecules lie with their molecular planes parallel to the templating molecules. The x-ray diffraction patterns of the 30 nm thick film of PtD deposited on sapphire, ITO and PTCDA are shown in Fig. 7.9.

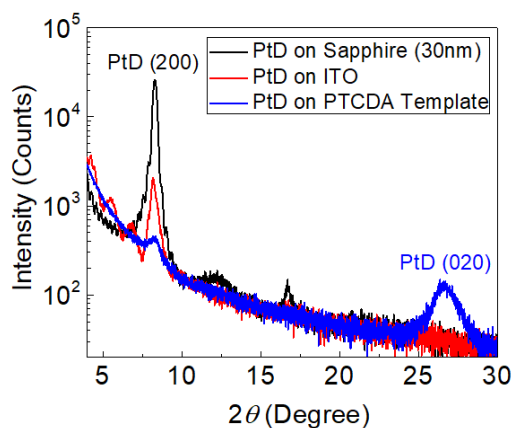


Figure 7.9 Bragg-Brentano x-ray diffraction pattern of the PtD film on different substrates. The 30nm thick film of PtD deposited on sapphire substrate exhibits intense (200) diffraction, which is also observed in a film deposited on a 15 nm thick ITO surface. However, the film deposited on a 1.5 nm thick PTCDA template layer shows significantly reduced (200) peak, whereas (020) peak appears at $2\theta=26.6^\circ$ due to the varied morphology of PtD molecules. The x-ray pole figure data are provided in Fig. 6.

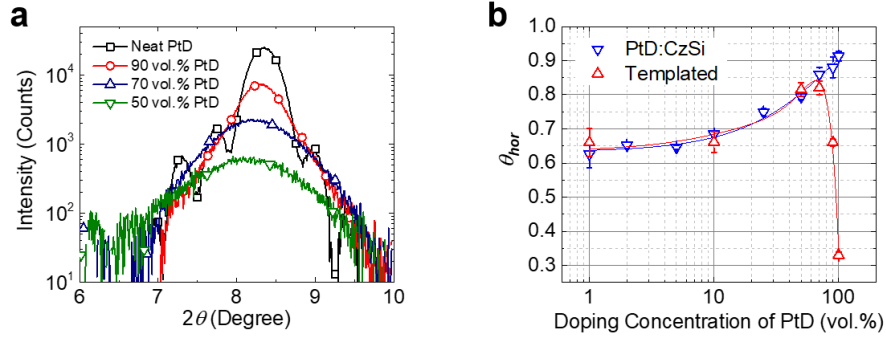


Figure 7.10 Relation between crystallinity and structural templating. (a) XRD patterns of PtD doped CzSi films as a function of PtD concentration. Background counts of the 50 vol.% PtD:CzSi film removed for clarity. (b) Measured θ_{hor} for the dimer emission TDM of PtD versus concentration in CzSi. The blue and red curves show θ_{hor} of films deposited on a bare substrate and on a pre-deposited PTCDA template, respectively.

The volume fraction of crystal domains within a CzSi film blended with PtD was measured as a function of doping concentration, with results shown in Fig. 7.10a. Vacuum deposited films of neat CzSi result in isotropic orientation (Fig. 7.11). A decreasing intensity and increasing full-width at half-maximum of the X-ray diffraction (XRD) peak [141] with decreasing PtD concentration indicates decreased film crystallinity and PtD domain size, as shown in Table 7.1. The TDM alignment measured by angle-dependent PL for each PtD:CzSi blend is shown in Fig. 7.10b. The alignment is random ($\theta_{hor} \sim 66\%$) at concentrations < 10 vol.%, while for the neat PtD film, an ordered morphology with $\theta_{hor} > 90\%$ is achieved. The TDM orientation was also measured for PtD:CzSi blends with a range of concentrations deposited on the NTCDA/PTCDA template, showing the controlled morphology of the film at PtD concentration of > 70 vol.%.

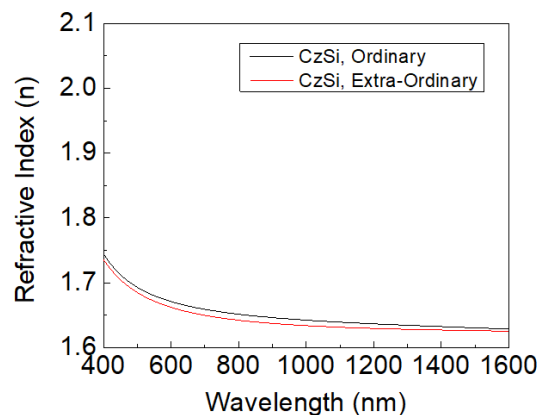


Figure 7.11 Refractive index measurement for neat CzSi film.

The CzSi ordinary and extraordinary refractive indices are nearly identical at all wavelengths, indicating the isotropic alignment of the TDM [83]. The random orientation of this molecule stems from its bulky molecular structure [142].

Table 7.1 Thin film morphology of CzSi films doped with PtD.

Doping Concentration [vol.%]	Peak 2θ [$^{\circ}$] ^(a)	FWHM [$^{\circ}$] ^(b)	d-spacing ^(c) [Å]	Crystallite Size ^(d) [nm]	θ_{hor}	
					Non-Templated	Templated
100	8.35	0.40 ± 0.01	10.6	20.8 ± 0.5	0.91 ± 0.01	0.33 ± 0.01
90	8.30	0.55 ± 0.01	10.6	15.1 ± 0.3	0.88 ± 0.03	0.66 ± 0.01
70	8.23	1.04 ± 0.02	10.7	8.0 ± 0.2	0.86 ± 0.02	0.82 ± 0.02
50	8.12	1.28 ± 0.01	10.9	6.5 ± 0.1	0.79 ± 0.01	0.82 ± 0.02

(a) Random error = $\pm 0.03^{\circ}$

(b) Calculation based on Gaussian Fitting model

(c) Random error = ± 0.1 Å

(d) Calculated utilizing Debye-Scherrer equation, $t = K\lambda/\beta\cos\theta$, where K is a crystallite shape dependent constant (0.94), $\lambda = 1.54$ Å is the wavelength of Cu- α x-ray source, β is the full width at half maximum of the peak, and θ is the Bragg angle.

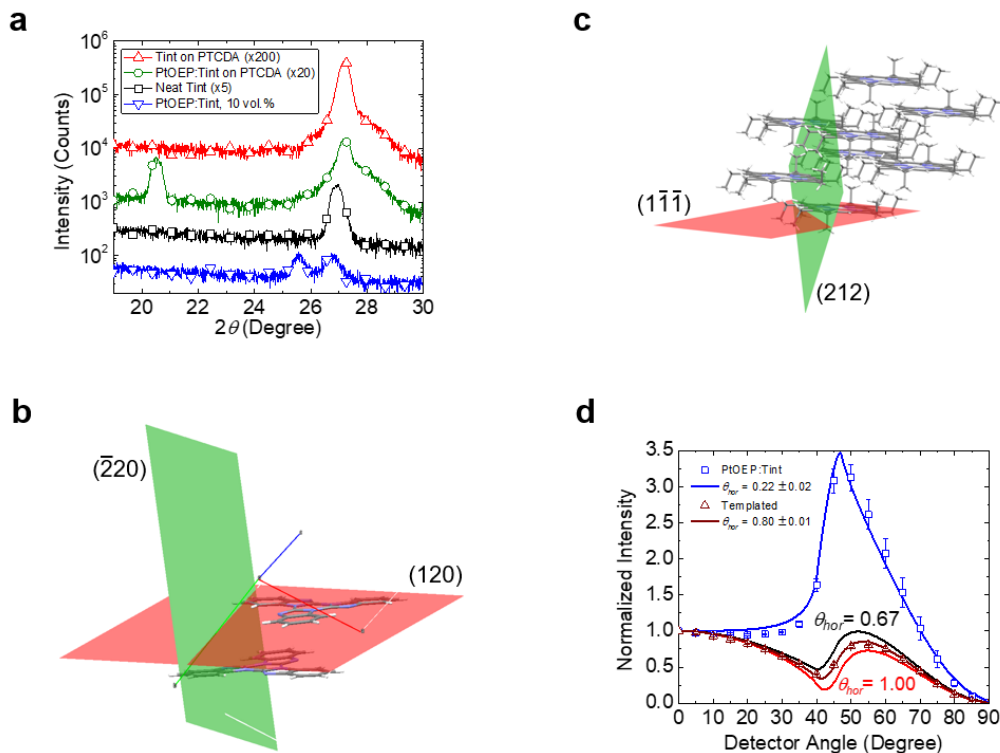


Figure 7.12 Control of the PtOEP:Tint TDM via templating.

(a) XRD patterns of the films with neat and blended Tint with PtOEP deposited on the template layer and on a bare sapphire substrate. Data are offset for clarity. (b) Tint crystal structure and diffraction planes from single crystal x-ray diffraction measurements. The diffraction peaks at $2\theta = 27.0^{\circ}$ and 27.3° correspond to the $(\bar{2}20)$ plane (green), (120) plane (red), respectively. (c) PtOEP crystal structure and diffraction planes from Cambridge Crystallographic Data library (CCDC-1167542). The

diffraction peaks at $2\theta = 25.9^\circ$ and 20.5° correspond to (212) (green), ($1\bar{1}\bar{1}$) (red) planes, respectively. (d) Angle dependent p-polarized photoluminescence of PtOEP:Tint films.

The orientations of the blended film comprising PtOEP doped in Tint at 10 vol.% deposited on the template and on a bare sapphire substrate are compared by x-ray diffraction in Fig. 7.12a. A monolayer of PTCDA is used as a template layer for x-ray diffraction. The neat Tint film deposited on the template compared to the bare substrate shows a peak shift from $2\theta=27.0^\circ$ to $2\theta=27.5^\circ$, corresponding to a morphological change from ($\bar{2}20$) to (120) diffraction plane. This peak shift of Tint molecules is also observed in the PtOEP:Tint blends. In the blended films, PtOEP peaks also shift when deposited on the template, from $2\theta=25.7^\circ$ to $2\theta=20.5^\circ$, corresponding to a change from (212) to ($1\bar{1}\bar{1}$) plane. The crystal structures and diffraction planes of PtOEP and Tint are shown in Fig. 7.12b and c. We also measured the TDM orientation of the blended film deposited on the NTCDA/PTCDA template showing an increased θ_{hor} compared to a bare substrate, from 0.22 ± 0.02 to 0.80 ± 0.01 as shown in Fig. 7.12d.

7.5 How interaction of ligands determines the orientation of Pt complex

The orientation of heteroleptic bidentate Pt complexes demonstrate the relative interactions of the two ligands with the organic surface. Specifically, if the interaction of both ligands with the surface is relatively weak, the molecular orientation is random. If the interaction of both ligands is similarly strong, a horizontal orientation relative to the substrate is promoted. However, if one ligand has a stronger interaction with the organic surface than the other, the molecule aligns vertically. Another possible way for the dopant molecule to self-organize is by aggregation with adjacent molecules forming polycrystalline islands within the film [143].

In Fig. 7.2a, the TDM of (dbx)Pt(dpm) shows a disproportionate vertical orientation. Since $\delta = 36.1^\circ$ is close to the c_2 axis, the vertically aligned TDM shows that one ligand of the

(dbx)Pt(dpm) has a markedly stronger interaction via edge-to-surface π - π interactions with the organic surface. To confirm that the vertical alignment is not due to aggregation, (dbx)Pt(acac) was doped at 10 and 1 vol.% into the host matrix in Fig. 7.2b and 2c. The ancillary dpm ligand was replaced by an acac ligand to promote aggregation, which is evident from the red-shifted spectrum of the 10 vol.% film in Fig. 7.4. As a result, (dbx)Pt(acac) doped at 1 vol.% showed similar alignment ($\theta_{hor} = 0.53 \pm 0.01$) to the 10 vol.% doped (dbx)Pt(acac) and (dbx)Pt(dpm) with no spectral red-shift. The similar orientation of (dbx)Pt(acac) with (dbx)Pt(dpm), regardless of the doping concentration, shows that the vertical orientation of the Pt complexes is not due to the dopant aggregation.

It is known that the intermolecular interaction strength is directly proportional to the size of the aromatic system [144]. Therefore, the smaller aromatic surface of ppy compared to dbx leads to a weaker interaction of (ppy)Pt(dpm) with the organic surface than the dbx based materials, and hence a reduced vertical molecular orientation relative to (dbx)Pt(dpm). To investigate whether the fraction of aromatic surface area in the ligand is tied to the molecular alignment, (dbx)Pt(dmes) with C^N and L^X ligands having substantial aromatic character. The horizontal component increased to $\theta_{hor} = 0.73 \pm 0.01$, leading to a net preferred horizontal alignment. The emission spectrum was unchanged since the chromophoric ligand also remained unchanged (Fig. 7.4). Adding a second Pt(dpm) to the dbx ligand producing (dbx)(Pt(dpm))₂ results in a further increase in θ_{hor} to 0.76 ± 0.01 , Fig. 7.3c, relative to (dbx)Pt(dpm). This is contrary to the hypothesis that the lower aromatic fraction of (dbx)(Pt(dpm))₂ promotes perpendicular alignment. Unlike the (C^N)Pt(L^X) complexes, the TDM of (dbx)(Pt(dpm))₂ lies at $\delta = -11^\circ$ relative to the Pt-N and Pt-C bonds (see inset, Fig. 7.3c). If (dbx)(Pt(dpm))₂ is aligned

perpendicular to the substrate, θ_{hor} is close to unity. The spectrum of $(dbx)Pt(dpm)_2$ red shifts due to the extended π -conjugation of the larger ligand [145,146].

7.6 Theory for vertical orientation of Pt complexes

The work of Hunter and Sanders [22,147] suggests that the $(dbx)Pt(dpm)$ molecule achieves vertical orientation via a balance between π - σ attraction (the attraction of the negatively charged π -electrons and a positively charged σ -framework), and π -electron repulsion. The edge-on geometry requires a strong π - σ attraction, whereas π - π repulsion and quadrupole attraction dominates in a cofacial, π -stacked geometry [23,24]. The dbx ligand shows a high net positive σ -framework due to the electron deficient π -system caused by two electron-withdrawing N atoms [24], leading to its edge-on geometry. We calculated the electrostatic potential surface of $(dbx)Pt(dpm)$ in Fig. 7.13 to compare the relative π - σ attraction of the two ligands. The average potential of the dbx ligand σ -framework shows 12.3 kcal/mol, with a peak potential of 17.9 kcal/mol near the N atoms. On the other hand, the dpm ligand shows an average 3.5 kcal/mol.

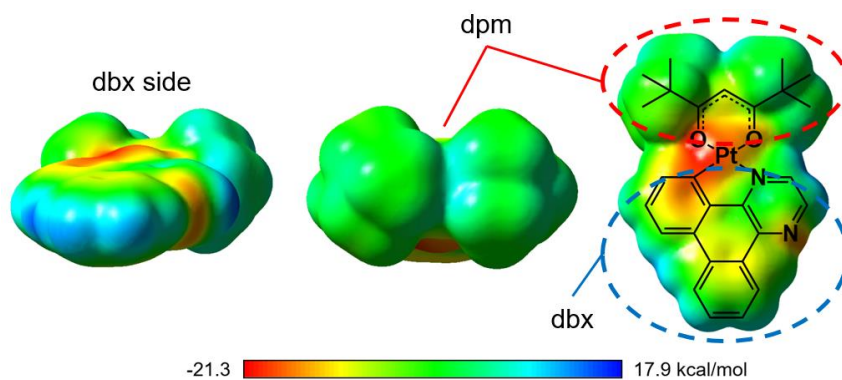


Figure 7.13 Calculated electrostatic potential surface of a $(dpm)Pt(dbx)$ molecule via DFT geometry optimization. The dpm shows almost neutral potential (3 kcal/mol) whereas the dbx ligand shows highly positive charge of 12.3 kcal/mol with the peak value of 17.9 kcal/mol near the nitrogen atoms.

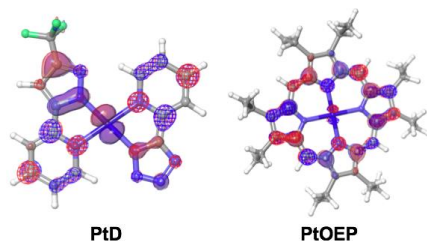
Pt complex molecules have planar structures, leading to strong π - π interactions with the surrounding environment, such as the host molecules. Thus, the orientation of the Pt complex

dopants is influenced by the host matrix. According to Huh, et al. [45], there is a lower fraction of horizontally aligned TDMs for Pt dopants in CBP compared to the other hosts. Therefore, changing the host molecule from CBP may increase the fraction horizontal alignment of Pt dopant molecules.

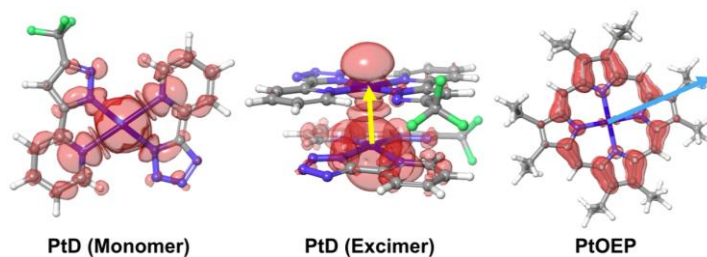
7.7 Structural analysis of PtD film

Density functional theory was used to investigate the relationship between the TDM of the PtD dimer and the molecular orientation in a neat crystalline PtD film (see Fig. 7.6). Calculations indicate that the TDM of the dimer lies perpendicular to the PtD monomer planes. The crystal structure of PtD features two unique emissive dimer configurations: one with a Pt-Pt separation of 3.35 Å and the other with 3.41 Å, henceforth referred to as 3.35-dimer and 3.41-dimer, respectively. The energy of the 3.35-dimer triplet (T_1) is 2.25 eV, compared with 2.27 eV for the 3.41-dimer (details found in Fig. 7.14). Also, the oscillator strength computed for T_1 of the former is almost twice that of the latter, indicating that emission in neat crystalline PtD films is likely to originate predominantly from the 3.35-dimer. The red arrow in Fig. 7.5a, inset, indicates that the 3.35-dimer TDM subtends a polar angle of 10° with the z-axis which lies along the Pt-Pt axis, and at an azimuthal angle of 99° with the x-axis that passes through the Pt-N(pyrazole-ring) bond of one of the monomers. The results from the DFT calculation and XRD data show that the TDM orientation is indeed controlled via templating.

a



b



c

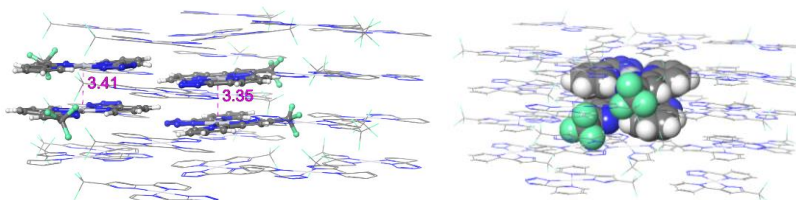


Figure 7.14 DFT calculation for PtD.

(a) Frontier molecular orbital plots for the Pt complexes computed for the S_0 optimized geometries. The solid surface denotes the HOMO while the LUMO is indicated by the meshed surface in each case. (b) Spin density plots computed using the T_1 optimized geometries. (c) The two different dimer configurations of PtD complexes derived from the single crystal packing data (left) and an illustration of the molecular clusters used for the ONIOM calculations (right) with the central dimer (QM region) shown as a space-filling structure while the surrounding molecular shell (MM region) is indicated by a wire-frame structure. (d) Table showing the calculated energies in eV (nm) and oscillator strengths (f) of the 3 T_1 sublevels for the complexes. The results are summarized in Table 7.2.

Table 7.2 Summarized results in Fig. 7.14.

	3.35-dimer (PtD)		3.41-dimer (PtD)		PtOEP	
	Energy	f	Energy	f	Energy	f
T₁ (I)	2.2515 (550.67)	0.25×10^{-5}	2.2682 (546.61)	0.17×10^{-5}	1.9197 (645.86)	0.85×10^{-7}
T₁ (II)	2.2519 (550.57)	0.16×10^{-4}	2.2689 (546.45)	0.85×10^{-4}	1.9197 (645.85)	0.72×10^{-7}
T₁ (III)	2.2533 (550.22)	0.15×10^{-3}	2.2698 (546.24)	0.75×10^{-4}	1.9204 (645.62)	0.11×10^{-4}

7.8 Structural templating of PtD film with varied crystallinity

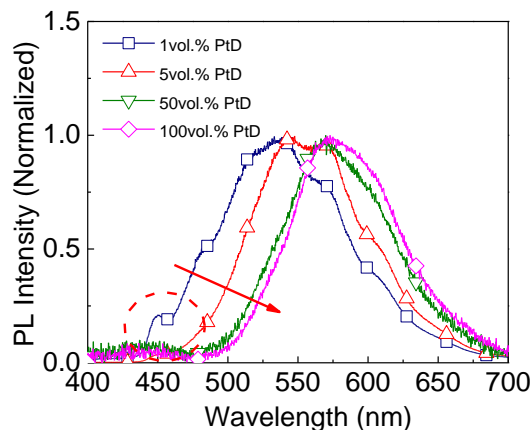
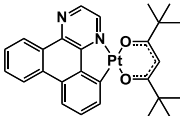


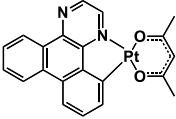
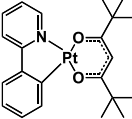
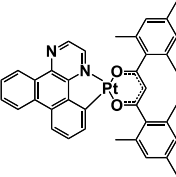
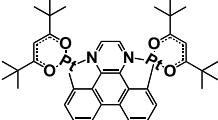
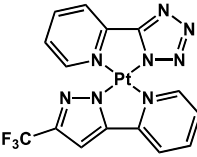
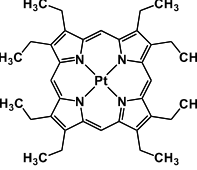
Figure 7.15 Spectrum vs. doping concentration of PtD in CzSi.

Bathochromic shifts follow the concentration of PtD due to the lattice strain relaxation. This results in a varied d -spacing between molecules as shown in Table 7.1. The DFT calculations of CzSi and PtD show similar permanent dipole moments ($\mu = 2.6$ vs. 2.2 Debye). Thus, the Bathochromic shift as a function of PtD doping concentration is mainly due to the strain relaxation of the PtD crystal domains. The monomer peak (green circle) appears at 450 nm wavelength by diluting PtD.

In Fig. 7.9a, the PtD (200) diffraction peak shifts toward an increased lattice constant with the reduced PtD domain size. The increased density of grain boundaries for smaller grains results in an increased lattice constant compared to bulk single crystals as a result of lattice strain relaxation [148]. The relaxed lattice also results in the hypsochromic shift of the dimer emission (Fig. 7.15), with results summarized in Table 7.2.

Table 7.3 Structural and emission data of reference Pt complexes

	Structure	Monomer Peak [nm]	Dimer Peak [nm]
(dbx)Pt(dpm)		563.82	-

(dbx)Pt(acac)		551.12	715.85
(ppy)Pt(dpm)		494.37 (First Peak)	-
(dbx)Pt(dmes)		559.67	-
(dbx)(Pt(dpm)) ₂		638.82	-
PtD		446.43 (First Peak)	572
PtOEP		653	783

Time-resolved photoluminescence of the films of PtD doped into CzSi at various doping concentrations was measured with results in Fig. 7.16. The data show a broad photoluminescence peak at $\lambda = 572$ nm that originates from the dimeric species. At 1 vol.% PtD, a monomer peak appears at $\lambda = 450$ nm (Fig. 7.15), showing biexponential decay with distinct exciton decay

lifetimes ($\tau_{dimer} = 0.88 \pm 0.12$ vs. $\tau_{monomer} = 0.10 \pm 0.01$), as shown in Fig. 7.16. This feature shows that monomer and dimer excitons coexist in 1 vol.% film, which corresponds to the spectrum in Fig. 7.15. However, single exponential decay is observed at higher doping concentrations with exciton lifetimes similar to the dimer exciton at 1 vol.%. Since only a broad photoluminescence peak at $\lambda = 550$ nm is observed at these higher concentrations, we conclude that the broad photoluminescence originates from dimer emission.

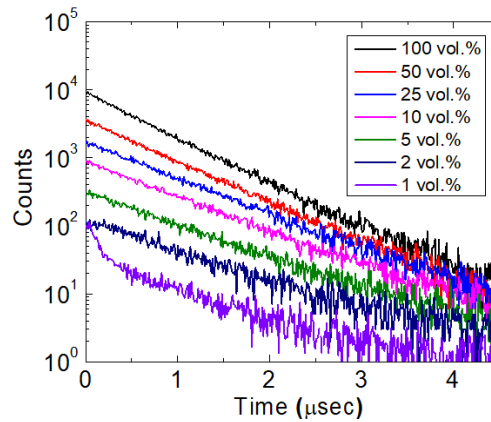


Figure 7.16 Time resolved photoluminescence of CzSi:PtD by varied doping concentration. The non-radiative rate of the excitons within the film was assumed to be negligible. Results are summarized in Table 7.4.

Table 7.4 Measured results in Fig. 7.16.

Lifetime (μsec)	100 vol.%	50 vol.%	25 vol.%	10 vol.%	5 vol.%	2 vol.%	1 vol.%
Dimer	0.64 ± 0.01	0.72 ± 0.01	0.82 ± 0.01	0.84 ± 0.01	0.90 ± 0.01	0.89 ± 0.03	0.88 ± 0.12
Monomer	-	-	-	-	-	-	0.10 ± 0.01

The TDM orientation was measured for PtD:CzSi blends with a range of concentrations deposited on the NTCDA/PTCDA template in Fig. 7.10b. The XRD results in Fig. 7.10a show that PtD molecules form highly crystalline films due to their discotic molecular structure that enables

efficient π -stacking. In the PtD:CzSi blend, however, the CzSi molecules interrupt the π -stacking of the PtD molecules at CzSi concentrations >30 vol.%, and hence the orientation of the template is not transferred to the PtD molecules. In contrast, for CzSi concentrations < 30 vol.%, the disruption of the stacks is limited, enabling the efficient transfer of the template orientation to PtD. Therefore, a concentration of polycrystalline discotic host molecule of > 70 vol.% is required to control the morphology of the blended film.

7.9 Controlling the TDM orientation of a mixed emissive layer film

Figure 7.12a shows the controlled morphology of PtOEP doped in Tint deposited with the PTCDA template by x-ray diffraction. The x-ray diffraction peaks of Tint ($\bar{2}20$) and PtOEP (212) planes in the film are shifted compared to the bulk (Tint ($\bar{2}20$), $2\theta = 27.2^\circ$; PtOEP (212), $2\theta = 26.0^\circ$) due to the lattice relaxation at grain boundaries. The blended film deposited on the bare substrate shows the edge-on diffraction for both Tint and PtOEP molecules (Fig. 7.12b and 12c, green) [149]. This geometry is caused by aggregation with adjacent molecules forming polycrystalline islands in the film, as Loi, et al. showed with the α -sexithiophene [143]. A neat Tint film on a PTCDA template shows its largest diffraction feature for the (120) plane, which is due to Tint crystallites (Fig. 7.12b, red) lying parallel to the substrate. The reorientation is due to matching to the α -phase PTCDA template ($2\theta = 27.5^\circ$) with a strain of $(a_{film} - a_{temp}) / a_{temp} = 0.7\%$, where a_{film} and a_{temp} are lattice constants of the Tint and PTCDA layers, respectively. Note that a peak appears at $2\theta = 27.5^\circ$ which corresponds to the α -phase PTCDA. Similarly, the PtOEP diffraction peak shifts to $2\theta = 20.5^\circ$, consistent with the (1 $\bar{1}\bar{1}$) plane being parallel to the substrate (Fig. 7.12c, red). This morphological control of the PTCDA template was also demonstrated via doped film deposited on the NTCDA/PTCDA template and

bare substrate, showing an increased θ_{hor} from 0.22 ± 0.02 to 0.80 ± 0.01 (Fig. 7.12d), consistent with the x-ray diffraction data.

Although PTCDA plays a central role in initiating structural templating, it has a low exciton energy, and therefore tends to quench excitons formed within the emissive layer. Identifying a molecule that has optimal energetics for an OLED while showing similar morphological characteristics as PTCDA remains a challenge.

7.10 Conclusion

We demonstrated that the interaction between the aromatic regions of the ligands and the organic surface drives the orientation of dihedral phosphor Pt complexes during the vacuum deposition. Accordingly, the molecular structure of the vertically aligning reference Pt complex, (dbx)Pt(dpm), was modified to increase the fraction of horizontally aligned TDM in the blended film. In one example, we introduced two mesityl groups to the ancillary ligand to increase the attraction of the molecule to the organic surface. In a second approach, the TDM of a binuclear Pt complex, (dbx)(Pt(dpm))₂, was shown to align parallel to the substrate due to the attraction of its aromatic region. Both methods showed an approximately 20% increased fraction of horizontally aligned TDMs compared to the reference Pt complex.

We also found that seeding the growth habit of the molecules in the blended emissive layer via an ordered NTCDA/PTCDA template results in a preferred horizontal alignment of the Pt phosphor emitter molecules. Polycrystalline emissive layers comprising single molecule or mixed host-dopant molecules were both shown to conform to the template orientation. The net horizontal fraction of the dopant TDM in the mixed host-dopant layer deposited on the template increased by approximately 60% compared to the film deposited directly onto bare sapphire and fused silica

substrates. Our findings demonstrate an efficient molecular design strategy and a method to control the optical outcoupling efficiencies of the OLEDs comprising Pt complex phosphors.

Chapter 8 Large Area Organic-Transition Metal Dichalcogenide Hybrid

Light Emitting Device

Two-dimensional (2D) layered materials show unusual physical properties that range from those of a wide-bandgap insulator to a semiconductor, a semimetal or metal [150]. Monolayer transition metal dichalcogenides (TMDCs), a subclass of 2D layered materials, have promising optical characteristics such as efficient photoluminescence (PL) [151,152], fast exciton decay [153], and high chemical and air stability [154]. As a result, TMDCs have been used in various optoelectronic devices, showing distinct characteristics from conventional bulk semiconductors [155–163]. For example, light emitting devices (LEDs) based on hexagonal boron nitrides (h-BN) insulators combined with TMDCs as the active luminescent materials have been demonstrated [159–162,164]. However, the LEDs require a sequence of complex layer transfers during the fabrication, and are constrained by the limited size of the 2D semiconductor flakes (several μm) [160,162]. Recently, a large area TMDC-based LED has been demonstrated, although its external quantum efficiency was low ($\sim 10^{-4}\%$) compared to LEDs based on exfoliated TMDCs [165,166].

8.1 Introduction

In this chapter, we demonstrate centimeter-scale LEDs using a monolayer of red emitting WS_2 (mWS_2) embedded within organic transport and host layers with an efficiency comparable to

much smaller, exfoliated-TMDC-based LEDs. The organic layers enable simplified deposition and precise placement of the TMDC within the structure to optimize the device characteristics. We transfer a 1 cm², chemical-vapor-deposition (CVD) grown mWS₂ onto a pre-deposited organic stack of the CBP host/TAPC hole transport layer/MoO_x hole injection layer/ITO anode. This is followed by deposition of the remainder of the host layer, thereby burying the mWS₂. The device is completed with a B3PYMPM electron transport layer and an Al cathode. Embedding a monolayer TMDC within the host enables efficient radiative emission via Förster transfer of excitons from the organic layers, while separating the TMDC from the heterointerface to avoid quenching at the heterointerface, especially at high current densities [167,168]. The LEDs show an average external quantum efficiency of $0.3 \pm 0.3\%$, with the highest value of 1%.

8.2 Experimental methods

8.2.1 Device fabrication

OLEDs were grown on glass substrates with a pre-deposited and patterned 150 nm thick ITO anode (Thin Film Devices, Inc.). The ITO-coated substrates were treated in a UV-ozone chamber for 15 min prior to organic film deposition. The organic film layers comprising CBP 12 nm / TAPC 50 nm / MoO₃ 2nm were grown by VTE in a chamber with a base pressure of 1×10^{-7} torr. The mWS₂ was dry-transferred onto the CBP surface following the procedure described in Fig. 8.1. After transfer, the sample was left in the VTE chamber for 2 h. The device was completed by depositing 100 nm Al / 1.5 nm LiQ / 55 nm B3PYMPM / 3 nm CBP on top of the mWS₂.

8.2.2 Dry transfer process

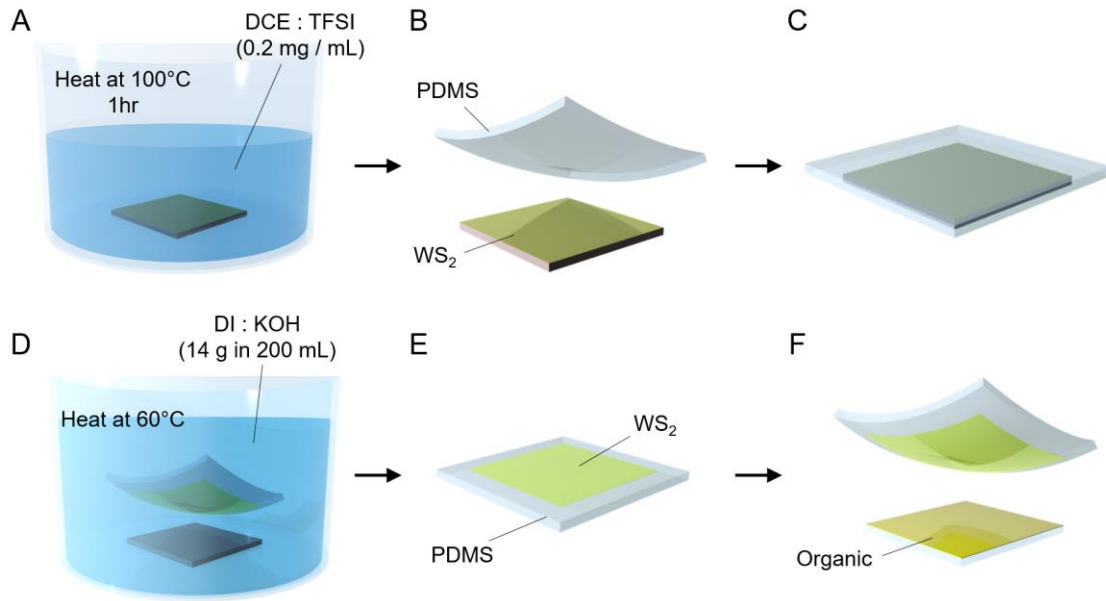


Figure 8.1 Schematic illustration of the monolayer WS₂ dry transfer procedure.

The CVD grown monolayer WS₂ on a SiO₂ substrate was purchased from 6Carbon Technology. We immerse the mWS₂ into the 100 mL of a solution comprising TFSI : DCE (0.2 mg/mL) and heat it for 50 mins at 100°C [169] as shown in Fig. 8.1 (A). After the TFSI treatment, we blow dry the sample surface with a N₂ gun. Then, we attach the PDMS on top of the mWS₂ as shown in Fig. 8.1, B and C. Then, we immerse the PDMS attached Si substrate into the KOH solution (14g KOH in 200 mL DI water) and apply 60°C heat to etch the SiO₂. Once the SiO₂/Si substrate drops off, we take out the mWS₂ attached PDMS (Fig. 8.1, E) and thoroughly blow dry the sample surface with a N₂ gun. Then we gently press the mWS₂ on PDMS onto the organic surface using an automated transfer stage and peel off the PDMS, leaving the mWS₂ on the organic surface.

8.2.3 Device characterization

The voltage-current density-*EQE* characteristics of the LEDs were measured using a parameter analyzer (HP4145, Hewlett-Packard) and a calibrated photodiode (S3584-08, Hamamatsu Photonics) following standard procedures [101]. The emission spectra were measured using a calibrated spectrometer (USB4000, Ocean Optics, Inc) connected to the device via an optical fiber (P400-5-UV-VIS, Ocean Optics, Inc.).

8.2.4 Electron- and hole-only device photoluminescence spectral fitting

The photoluminescence spectrum of mWS₂ in the EOD was fit using two Lorentzian curves following:

$$f(\lambda) = \frac{A \cdot \gamma^2}{(\lambda - \lambda_0)^2 + \gamma^2} \quad (8.3)$$

at center wavelengths of $\lambda_0 = 617$ nm and 628 nm, γ is the half-width at half-maximum, and A is the constant for the peak height. A least-squares algorithm was used to fit the measured photoluminescence data with the two Lorentzian curves.

8.2.5 Exciton formation analysis

The exciton density at the position x , $N(x)$, was mapped across the emissive layer using the sensing layer method [71,170]. Ultrathin ($\sim 1\text{\AA}$) red phosphorescent (PtOEP) layers were deposited at locations shown in Fig. 5a in a series of otherwise identical OLEDs. The emission spectra from the PtOEP sensing layer from each position (x) and the CBP organic host is:

$$I_{total}(\lambda, x) = a_{PtOEP}(x) \cdot I_{PtOEP}(\lambda) + a_{CBP}(x) \cdot I_{CBP}(\lambda), \quad (8.4)$$

where $I_{total}(\lambda, x)$ is the total emission spectrum comprising the spectra of PtOEP ($I_{PtOEP}(\lambda)$) and CBP host matrix ($I_{CBP}(\lambda)$), with the relative weights of $a_{PtOEP}(x)$ and $a_{CBP}(x)$, respectively. Then, the outcoupled exciton density at position x , $N(x) \cdot \eta_{out}(x)$, becomes as:

$$N(x) \cdot \eta_{out}(x) = \frac{J_0}{q} \cdot \eta_{EQE}(x) \cdot \frac{a_{PtOEP}(x) \cdot \int I_{PtOEP}(\lambda) / \lambda d\lambda}{a_{PtOEP}(x) \cdot \int I_{PtOEP}(\lambda) / \lambda d\lambda + a_{CBP}(x) \cdot \int I_{CBP}(\lambda) / \lambda d\lambda}, \quad (8.5)$$

where J_0 is the current density, $\eta_{out}(x)$ and $\eta_{EQE}(x)$ are the outcoupling and external quantum efficiencies of the sensing layer at position x . The $\eta_{out}(x)$ is calculated based on Green's function analysis [94] in Fig. 8.2. The range of $\sim 3\text{nm}$ [71] Förster energy transfer limits the spatial resolution of the measurement.

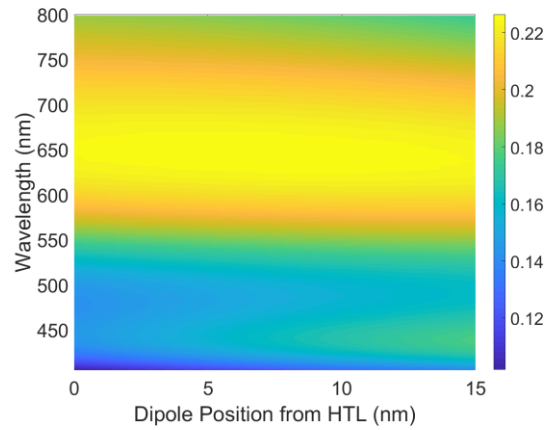


Figure 8.2 Calculated outcoupling efficiency of the sensing layers at various positions in the emissive layer.

8.3 LED fabrication and testing

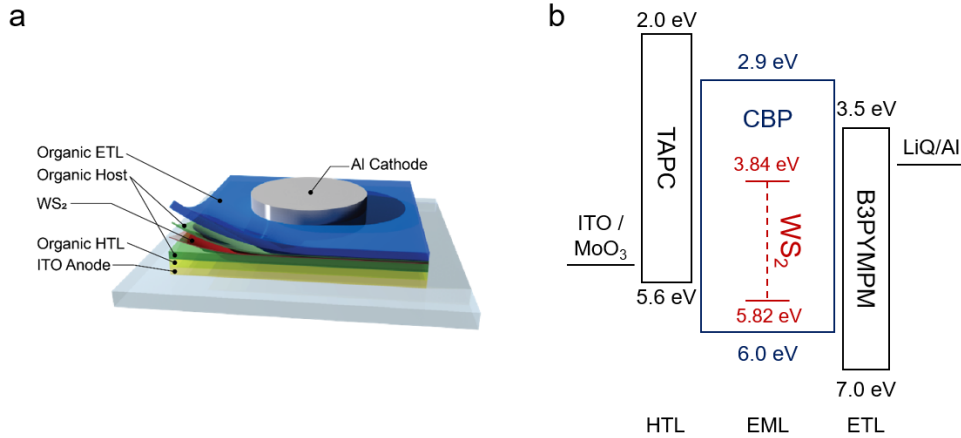


Figure 8.3 Device structure of the hybrid 2D-organic LED.

(a) Schematic illustration of the hybrid LED comprising a monolayer WS₂ active layer sandwiched between organic conducting and excitation generating layers. (b) Frontier orbital energies of the materials in eV.

Figure 8.3a shows the structure of the hybrid LED with the frontier energy levels in Fig. 8.3b. Organic HIL and HTL comprising 2 nm thick MoO₃ and 50 nm thick TAPC are deposited on top of the transparent anode (150 nm thick ITO), and then an organic host layer comprising 12 nm thick neat CBP is deposited. A mWS₂ is transferred onto the organic host by the method described in Fig. 8.1. After transfer, we deposit a 3 nm thick capping host (CBP) layer, 55 nm B3PYMPM ETL, and the top Al contact.

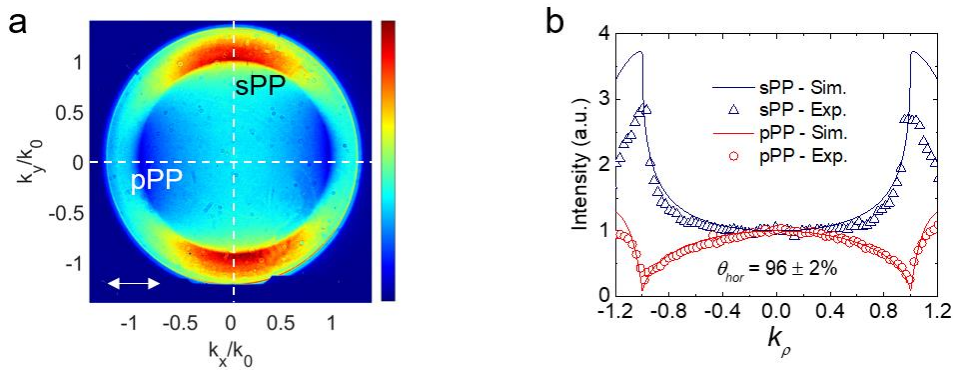


Figure 8.4 The TDM orientation of monolayer WS₂ in a CBP host matrix.

(a) Measured Fourier plane imaging microscopy polar plots for the monolayer WS₂ in the CBP host matrix. (b) Intensity profiles of the polar plot in the pPP and sPP (data points) along with the simulated fits (solid lines).

The percentage of TDM, θ_{hor} , of the mWS₂ in the CBP host aligned parallel to the substrate plane is measured via FIM [29,31,86,92,113]. When $\theta_{hor} = 100\%$, all TDMs are oriented parallel to the substrate, $\theta_{hor} = 67\%$ for random, and $\theta_{hor} = 0\%$ for a perfect vertical alignment. Figure 8.4a shows the polar emission pattern obtained from the mWS₂ embedded within the CBP host matrix measured by FIM. The intensity profiles (data points) in the pPP and sPP are fit to theory (solid line) in Fig. 8.4b, as described in ref. 15. The data show $\theta_{hor} = 96 \pm 2\%$, corresponding to near perfect horizontal orientation of the mWS₂ TDM. This leads to an exceptionally high light outcoupling efficiency of the LED, as shown in Fig. 8.5 [46,125].

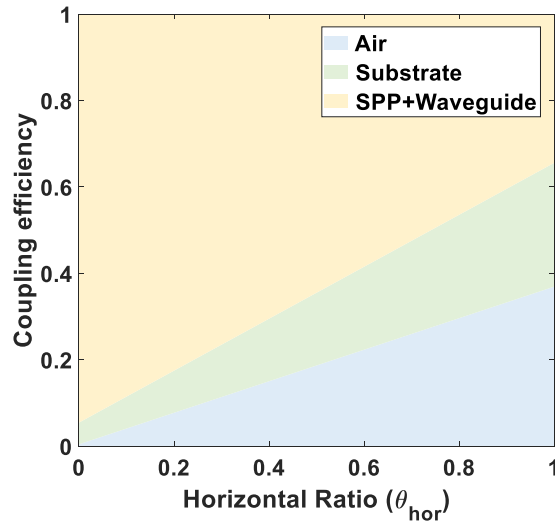


Figure 8.5 Calculated distribution of the modal power distribution vs. average TDM orientation.

The optimal position of the mWS₂ within the emission layer is determined by measuring the exciton density profile. To do this, we deposit an ultrathin (0.5 Å) layer of the phosphor, PtOEP at 2.5 nm intervals in a series of devices, starting from the hole HTL/EML interface, to the EML/ETL interface (see Fig. 8.6a). The frontier energy levels of PtOEP align with those of mWS₂. Hence, the emission intensity from the PtOEP at a fixed current density (J) is proportional to the

exciton density at its location. The measured exciton density profiles for various J are shown in Fig. 8.6b, with the peak near the EML/ETL interface. The peak position changes from $x=15$ nm to 12.5 nm at $J=100\text{mA/cm}^2$ due to increased exciton quenching near the heterointerface at high J . Figure 8.6c shows the EQE of each sensing layer sample, showing a decreasing efficiency as the sensing layer moves farther from the interface due to the reduced exciton density. The measured spectra of the samples are shown in Fig. 8.6d. We conclude from these data that the mWS₂ should be positioned ~ 3 nm away from the EML/ETL interface to enable harvesting of the highest density of excitons while preventing exciton quenching at J .

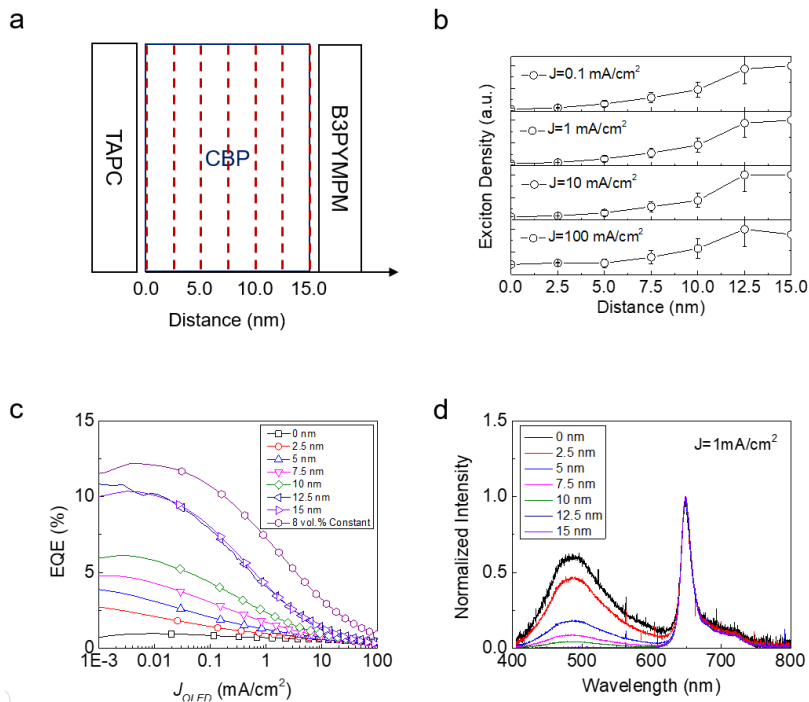


Figure 8.6 Exciton density profiles in the EML.

(a) Illustration showing the placement of the PtOEP MSLs within the emissive layer. (b) Measured exciton density profile at different current densities. (c) J - EQE characteristics of the samples with the sensing layer at each different positions. (d) Electroluminescence spectrum of samples with the sensing layer at different positions at $J = 1\text{mA/cm}^2$.

With the structural design in Fig. 8.6, a hybrid LED was fabricated following the procedure in Fig. 8.1, with the performance given in Fig. 8.7. Figure 8.7a shows EQE v. J , with an average peak $EQE = 0.3 \pm 0.3\%$, and the highest efficiency device with $EQE = 1\%$. The inset shows the

image of an array of 0.2 mm^2 devices. Figure 8.7b shows the J - V characteristics with a microscopic image of the device electroluminescence in the inset. The electroluminescence spectra at various J are shown in Fig. 8.7c, exhibiting a pronounced hypsochromic shift with current in the device. Note that the EQE in Fig. 8.7a increases with current at $J < 0.01 \text{ mA/cm}^2$. As shown in Fig. 8.7b, the device shows a noticeable leakage current at $V < 2.5 \text{ V}$, causing a significant quantity of charges to be lost rather than generate excitons. Thus, as the injected current surpasses the leakage current, EQE also increases.

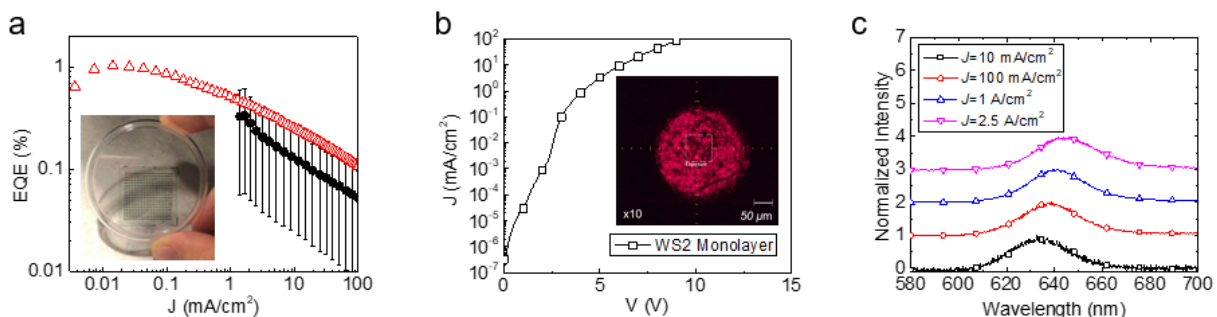


Figure 8.7 Performance characteristics of the hybrid LED.

(a) J - EQE characteristics of the hybrid LEDs. The average and the highest EQE data are shown in black and red data points, respectively. (Inset: photograph of the LEDs grown on a $2.5 \times 2.5 \text{ cm}^2$ glass substrate. (b) J - V characteristics of the hybrid LED. Inset: A photograph of the device electroluminescence. The diameter of the device is $250 \mu\text{m}$. (c) Current dependent electroluminescence spectrum of the hybrid LED.

Figures 8.8a and b shows the photoluminescence of the mWS₂ embedded within electron- and hole-only-devices (EOD and HOD, respectively) at several current densities. The device structures are 150 nm ITO (UV-ozone untreated) / 50 nm B3PYMPM / 12 nm CBP / monolayer WS₂ / 3 nm CBP / 55 nm B3PYMPM / 1.5 nm LiQ / 100 nm Al for EOD and 150 nm ITO (UV-ozone treated) / 2 nm MoO₃ / 50 nm TAPC / 12 nm CBP / monolayer WS₂ / 3 nm CBP / 45 nm TAPC / 5 nm MoO₃ / 100 nm Al for HOD with the J - V characteristics shown in Fig. 8.9. There is a pronounced hypsochromic mWS₂ photoluminescence peak shift with current in the EOD, which is absent in the HOD. We conclude that injected electrons in EOD combine with the generated

excitons to form negatively charged excitons, or trions [171,172]. The binding energy of trions has previously been shown to be 20-30 meV relative to the neutral exciton; [171,173] a value that corresponds to the energy shift in Fig. 8.8a. The absence of a peak shift of the mWS₂ photoluminescence in the HOD is due to the asymmetric charge trapping in the CBP-mWS₂-CBP quantum well structure. The energy barrier for electrons at the CBP LUMO-mWS₂ conduction band discontinuity (see Fig. 8.3b) is larger than the barrier at the CBP HOMO-mWS₂ valence band discontinuity for holes [174]. As a result, hole trions do not form as efficiently as electron trions, thus showing no apparent peak shift in Fig. 8.8b.

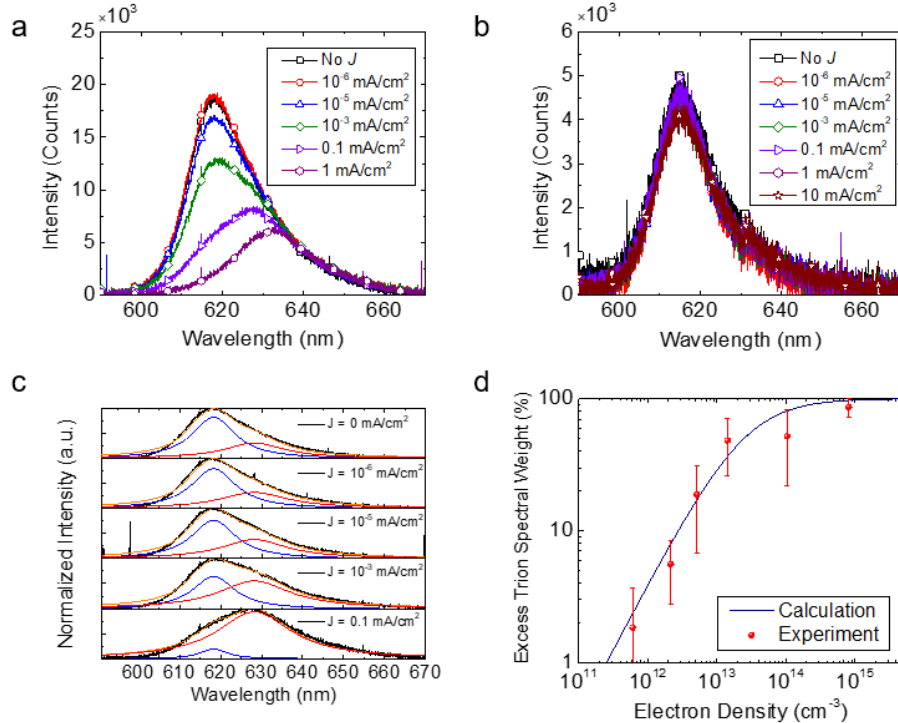


Figure 8.8 Photoluminescence of monolayer WS₂ embedded in single-charge device.

(a, b) Photoluminescence of a monolayer WS₂ within the (a) electron- and (b) hole-only-device with the varied injection current. (c) Photoluminescence of mWS₂ in the electron-only-device as a function of current density with the deconvolution of the spectrum using two Lorentzians with exciton and trion emission peaks. The blue, red and orange lines show the exciton, trion and the summed total spectrum, respectively, from the fits. (d) Increased spectral weight of trions compared the total emission from excitons and trions, as a function of the injected electron density (n_{el}).

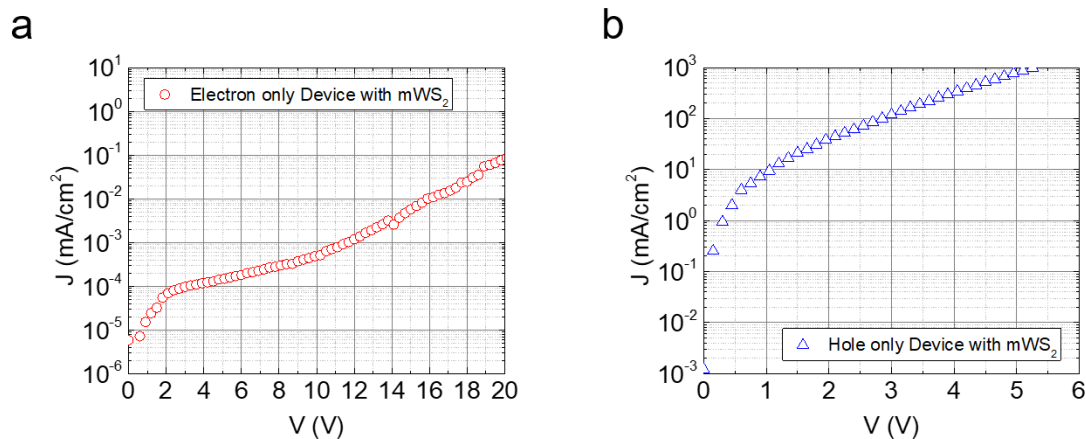


Figure 8.9 J-V characteristics of mWS₂ in the electron- and hole- only-device.

8.4 Device structure design concept

The introduction of an inorganic active layer into an OLED structure using dry transfer enables a variety of material selections to be combined with organic thin films in a hybrid LED. Using an organic host matrix separates charge conduction from the guest emission processes, allowing for optimization of each material to serve its intended purpose. Excitons are efficiently formed in the conductive host layer, and then transferred to the luminescent active material (mWS₂) which is positioned near the maximum exciton density within the Förster radius, as determined from the sensing layer experiments in Sec. II.

The use of host matrix differentiates the device structure from the previously reported TMDC LEDs [164,165] where the TMDCs are located directly between the hole- and electron-transport layers. However, according to Giebink, et al. [167] and Wang, et al. [168], the heterointerface is prone to charge/exciton accumulation and the coexistence of a high density of excitons and charges result in degradation of the active material or even morphological instabilities [175]. The use of host matrix enables placing the TMDC apart from the heterointerface with benefits to device stability.

8.5 Cause of limited external quantum efficiency

CVD-grown mWS₂ has a high defect density comprising S vacancies formed during the growth process, limiting the device efficiency. Also, cracks and holes are generated during the dry transfer since a mWS₂ is a polycrystal bound by weak van der Waals forces [176]. The S vacancies lead to emission from the defect levels in both the EOD and HOD, even when no charges are injected as shown in Fig. 8.8c [177,178]. The physical defects lead to the *EQE* to vary by orders of magnitude even within the same growth run. The defects are non-radiative, appearing as the dark spots on the device emitting surface, as shown by the image in Fig. 8.7b, inset.

8.6 Trion emission in device spectrum

The electroluminescence spectra show emission from mWS₂ but not from the organic host in Fig. 8.7c, demonstrating efficient Förster transfer of the excitons generated at the EML/ETL interface, into mWS₂. The spectrum shows a bathochromic shift depending on the drive current. In Fig. 8.8c, the photoluminescence of mWS₂ in the EOD, excited with a 532 nm laser, is shown as a function of current density, with the deconvolution of the spectrum using two Lorentzians with exciton and trion emission peaks at wavelengths of $\lambda = 617$ nm and 628 nm, respectively [177]. The trion peak intensity increases with the current density, as expected. The laser selectively excites A excitons of mWS₂ (~2.0 eV), but not the higher energy (~2.4 eV) B excitons, allowing us to not consider their spectra in the peak fits [179]. The ratio between the emission intensity of excitons and the increased emission intensity of trions due to the charge injection is found using the law of mass action [172,180,181]:

$$\frac{N_X n_{el}}{N_{X^-}} = \left(\frac{4\mu_X m_e}{\pi\hbar^2 \mu_{X^-}} \right) k_B T \exp\left(-\frac{E_B}{k_B T} \right), \quad (8.1)$$

where N_X , N_{X^-} and n_{el} are the concentrations of excitons, trions and electrons, with respective masses of μ_X , μ_{X^-} , and m_e [182], k_B is the Boltzmann coefficient, T is the temperature, E_B is the trion binding energy (20 meV) [171]. The reduced masses of electron trions and exciton are $\mu_{X^-}^{-1} = 2 \cdot m_e^{-1} + m_h^{-1}$ and $\mu_X^{-1} = m_e^{-1} + m_h^{-1}$. Equation (8.1) describes the ratio between the concentrations of excitons (N_X) and trions (N_{X^-}) in the presence of an electron concentration, It is apparent that the change of N_X/N_{X^-} is dependent on n_{el} within the mWS₂ film. The change of N_X/N_{X^-} is determined from the relative emission intensities of trions and excitons vs. J , which correspond to $\gamma_{tr}N_{X^-}$ and $\gamma_{ex}N_X$ where γ_{tr} and γ_{ex} are their intensity of each particle could be described as [180]:

$$\frac{I_{X^-}}{I_{total}} = \frac{g_{tr} \cdot N_{X^-}}{g_{ex} \cdot N_X + g_{tr} \cdot N_{X^-}} = \frac{g_{tr} \cdot N_{X^-}}{g_{ex} \cdot N_X} \left/ \left(1 + \frac{g_{tr} \cdot N_{X^-}}{g_{ex} \cdot N_X} \right) \right., \quad (8.2)$$

where γ_{tr} and γ_{ex} were obtained from fitting parameters in rate equations by Peimyoo, et al. [182]. Equation (8.2) yields the relation between the injected current density (n_{el}) vs. the amount of increased spectral weight of trions vs. electron density as shown in Fig. 8.8d. The theoretical fit and the measured data are in close correspondance, showing that the bathochromic shift of the electroluminescence occurs due to electron trion emission.

In addition to the spectral shift, the radiative decay rate of trions are less than 5 times that of the excitons [182], resulting in a reduction in mWS₂ photoluminescence intensity as a function of injected electron density in Fig. 8.8a. Therefore, the high electron density causes a decreased internal quantum efficiency of mWS₂ and a corresponding roll-off in EQE at $J > 0.01 \text{ mA/cm}^2$ (Fig 7a). As a result, placing mWS₂ in the region with reduced electron density while maintaining high exciton density enables efficient EQE with reduced roll-off.

8.7 Conclusion

We demonstrated an LED with an active layer comprising a CVD grown, large-area mWS₂ as the luminescent material, combined with organic buffer layers (charge transport and host matrix layers) that enable efficient charge transport and exciton generation. The use of a mWS₂ enables principally horizontally aligned TDMs and fast exciton decay leading to an enhanced outcoupling and device stability. Moreover, the organic host was used to efficiently generate and inject excitons into the mWS₂ via Förster transfer. Thus, the mWS₂ was positioned several nanometers distant from the heterointerface which prevents sites for non-radiative recombination and leads to morphological instabilities. LEDs with diameters of 250 μm exhibited average $EQE = 0.3 \pm 0.3\%$ with a peak of 1%. In addition, electron- and hole-only-devices indicated that the injected electrons in mWS₂ combine with excitons generating trions, reducing EQE at high current densities. Our results show an efficient way of incorporating promising luminescent materials into the organic device structure.

Chapter 9 Summary and Outlook

Works on OLED performance are related to four components comprising the external quantum efficiency: i) charge carrier balance; ii) spin factor; iii) photoluminescence quantum yield; and iv) outcoupling efficiency, as discussed in Chapter 4. Since the first demonstration of OLEDs by Tang and VanSlyke in 1987 [183], the material synthesis and device fabrication techniques have been matured to achieve nearly 100% for factors i) to iii). However, achieving 100% outcoupling efficiency is still a critical problem left to be solved. Other than the efficiency, process simplicity and large-area scalability are the other crucial aspects of OLED outcoupling technology which critically affect the product cost.

Therefore, this thesis mainly focused on methods improving the optical outcoupling of an OLED by controlling the film morphology, which is relatively simple and available in large-scale. The controlled morphology enables aligning the average TDM vectors within a film in a desirable way, which is highly correlated to the outcoupling efficiency of an OLED. The first approach, modifying the molecular structure, was helpful in discovering the main driving force of molecular alignment, however orienting molecules by molecular structural engineering does not seem to be a feasible strategy for the industry due to the added complication of molecular synthesis. This is because there are numerous elements to be considered to design a molecule, other than the outcoupling, such as conductivity, fragmentation, glass transition temperature, evaporation temperature, etc. On the other hand, the use of a structural template layer to orient the dopant molecule within the mixed emissive layer in a desired way seems to be an effective direction to

pursue due to its simplicity and effectiveness. However, the current structural templating molecule, PTCDA, has a low energy gap causing the excitons to be quenched, therefore developing a wide-energy gap templating molecule compatible with the emissive layer excitons is left as future work for an electroluminescent device with an embedded structural template layer.

Understanding how molecules orient within a film has led us to develop a technique to map the nanoscale morphology of a film using Fourier plane imaging microscopy. The unique feature of this technique is that it provides full 3-dimensional information of morphology, in a localized scale with a resolution of half of the visible wavelength and \sim Angstroms in the in-plane and depth axis, respectively. However, the resolution in the depth axis can vary due to the roughness of the film and the deposition technique that has Another advantage of the technique is its potential to be applied in various material systems. It can be applied in other vdW bonded solids such as 2-dimensional semiconductors, quantum dots and perovskites, and with appropriate modifications it can also be applied to covalent and ionically bonded materials. Furthermore, depositing the MSL between different spin-coated films is also possible for analyzing solution processed materials, which needs further demonstration in the future. While the technique suits OLED materials, it could not be applied to narrow-energy gap organic photovoltaic materials since the sensor dyes should be emissive at wavelengths distinct from that of the host. Thus, a technique to obtain the dye orientation via angle-resolved absorption should be developed in the future, which would make the technology a universal method for thin films of various energy gaps.

Another important demonstration in this thesis is the LED with an active layer comprising a CVD grown, large-area mWS₂ as the luminescent material, combined with organic buffer layers. The use of a mWS₂ enables principally horizontally aligned TDMs and fast exciton decay leading to an enhanced outcoupling and device stability. However, the *EQE* of the devices is limited at 1%

due to its high S-defect density of the CVD grown TDMC film. As the growth technique of large-area monolayer TDMCs is still nascent, the *EQE* will increase with the improvement of the film deposition technology in the future. In addition, an investigation of the degree of damage during dry transfer is needed to fully understand and improve the fabrication process, which will as well lead to the advanced device performance. On the other hand, adopting materials other than the 2-dimensional TMDC materials is another promising option to be investigated. Especially, since the display industry is having trouble with finding a long-lived stable blue LEDs that are simultaneously fabricated in large-areas, the development of a hybrid LED employing a GaN (or InGaN) active emitting layer with organic buffer layers would lead to a huge step forward towards the future display technology.

Appendix

A. List of Chemicals

acac acetylacetonate

Alq₃ tris-(8-hydroxyquinoline)aluminum

bppo benzopyranopyridinone

B3PYMPM 4,6-bis(3,5-di(pyridin-3-yl)phenyl)-2-methylpyrimidine

BCzTrz 9-(4-(4,6-diphenyl-1,3,5-triazin-2-yl) phenyl)-9'-phenyl-9H,9'H-3,3'-bicarbazole

BPhen bathophenanthroline

BP4mPy 3,3',5,5'-tetra[(M-pyridyl)-phen-3-yl]biphenyl

C₆₀ fullerene

CBP 4,4'-bis(9-carbazolyl)-1,1'-biphenyl

CuPC copper phthalocyanine

CzSi 9-(4-tert-butylphenyl)-3,6-bis(triphenylsilyl)-9H-carbazole

CzTrz 9-(4-(4,6-diphenyl-1,3,5-triazin-2-yl)phenyl)-9H-carbazole

dbx dibenzo-(f,h)quinoxaline

DCE dichloroethane

dmes 1,3-dimesitylpropane-1,3-dione

dpm dipivaloylmethane

FIrpic bis[2-(4,6-difluorophenyl)pyridinato-C₂,N](picolinato)Ir(III)

GaN Gallium Nitrides

HATCN dipyrazino[2,3-f:2',3'-h]quinoxaline-2,3,6,7,10,11-hexacarbonitrile

H₂ hydrogen

ITO indium tin oxide

IZO indium zinc oxides

Ir(btp)₂(acac) bis(2-(2'-benzo[4,5- α]thienyl)pyridinato-N,C3') (acetylacetonate)Ir(III)

Ir(ppy)₂(acac) bis[2-(2-pyridinyl-N)phenyl-C](acetylacetonate) Ir(III)
Ir(ppy)₃ tris[2-phenylpyridine] Ir(III)
Ir(MDQ)₂(acac) bis(2-methyldibenzoquinoline)(acetylacetonate)Ir (III)
LiQ 8-hydroxyquinolinato lithium
mCBP 4,40-bis(3-methylcarbazol-9-yl)-2,20-biphenyl
mWS₂ monolayer WS₂
(MAC)CuCz monoamido-aminocarbene Cu Carbazole
NTCDA 1,4,5,8-naphthalenetetracarboxylic dianhydride
PQIr bis(2-phenylquinolyl-N,C2')acetylacetonate Iridium(III)
PDMS Polydimethylsiloxane
PTFE polytetrafluoroethylene
PtOEP Pt(II) octaethylporphine
PMMA poly-methylmethacrylate
ppy 2-phenylpyridinate
PTCDA 3,4,9,10-perylenetetracarboxylic dianhydride
PtD (3-(trifluoromethyl))(5-(pyridyl)-pyrazolate 5-pyridyl-tetrazolate) Pt(II)
TAPC 4,4'-cyclohexylidenebis [N,N-bis(4-methylphenyl)benzenamine]
TFSI bis(trifluoromethane)-sulfonimide
TPBi 2,2',2''-(1,3,5-Benzinetriyl)-tris(1-phenyl-1-H-benzimidazole)
TCzTrz 9'-(4-(4,6-diphenyl-1,3,5-triazin-2-yl)phenyl)-9,9''-diphenyl-9H,9'H,9''H-3,3':6',3''-tercarbazole
Tint triindolotriazine

B. Efficient outcoupling of organic light emitting devices using a light scattering dielectric layer

Phosphorescent organic light-emitting devices (PHOLEDs) can achieve 100% internal quantum efficiency [1,184], although a considerable amount of light is lost within the device structure [69,70] due to the excitation of substrate [76,185], waveguide [186–192], and SPP modes [27,193,194], as well as absorption in the metal contacts. Substrate modes can be efficiently outcoupled by structuring the air-substrate interface such as by using microlens arrays [74,75]. However, reducing loss to waveguide and SPP modes, which is typically > 50% in conventional OLEDs, remains a significant hurdle. Several methods such as sub-anode structures [186,187,195,196], high refractive index substrates [197], scattering layers [76,191,198,199], corrugated structures [188,200,201], Bragg scatterers [190,202,203], and microcavities [204] have been demonstrated to overcome these losses, although near-field coupling into SPP modes by the metal electrode is more difficult to avoid.

In particular, top-emitting OLEDs efficiently excite both waveguide and SPP modes due to the strong optical cavity formed between the high reflectivity semitransparent top electrode and the thick metallic bottom electrode [205]. Several strategies such as thick electron transport layers [206], metallic grids [193], and periodically corrugated metal electrodes [190,202,203] suppress the losses. However, these methods are often wavelength and viewing-angle dependent, they are invasive of the device structure or are challenging to apply over large substrate areas.

B.1 Introduction

Here, we demonstrate the elimination of SPP modes by replacing the bottom metal electrode in top-emitting OLEDs with a transparent layer of ITO deposited on a PTFE (Teflon™) diffuse reflector. The rough reflector surface is planarized by a thick, integrated high index of refraction polymer slab waveguide. The outcoupling of this structure is wavelength and viewing-angle independent. There is no intrusion into the device structure itself since the OLED structure, including the ITO anode, is fabricated on the surface of the planar waveguide. This architecture achieves a 2.5-fold enhancement in outcoupling efficiency compared to an analogous device fabricated on an Al mirror. Simulations indicate that the enhancement can be further increased to 3.4. Importantly, no further light extraction method such as index matching layers or microlens arrays are required to enhance outcoupling, making this a simple and potentially low-cost design useful for OLED lighting appliances.

B.2 Optical design concept

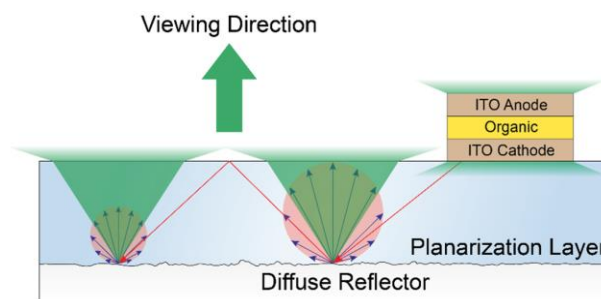


Figure B.1 Schematic illustration of the PHOLED on a diffuse reflector. Light incident to the diffuse reflector is scattered into a Lambertian profile (red circles), and light in the emission cone is scattered into the viewing direction (green cone).

A schematic cross-section of a top-emitting OLED with a PTFE reflector is shown in Fig. B.1. The surface of the reflector has a root mean square roughness of $6.7 \mu\text{m}$ (measured by

profilometry), which is planarized with a transparent polymer waveguide. Light emitted from the OLED is either directly emitted from the top surface into the viewing direction, or enters the waveguide layer where it propagates until it is incident on the rough reflector surface. There, the light is scattered into a Lambertian profile [207], and light within the emission cone exits into the viewing direction. Light incident at angles greater than that for total internal reflection at the polymer-air interface is returned to the diffuse reflector where it is scattered once again. This repeats until the light is either absorbed or scattered into the viewing direction. As shown in Fig. B.2a, the PTFE layer has a low loss even after multiple reflections, enabling multiple iterations of light scattering until the light is extracted.

For an ideal, lossless reflector, the ratio of incident to scattered light power towards the viewing direction from a single diffuse reflection (R_S) is determined using Snell's law, viz. $R_S = (n_{air}/n_P)^2$, where n_{air} and n_P are the refractive indices of the air and waveguide layer, respectively. Then, the ratio of the light intensity extracted into the viewing direction to that within waveguide layer (η_D) following the path shown in Fig. B.1, becomes:

$$\eta_D = R_S + (1 - R_S) \cdot R_S + (1 - R_S)^2 \cdot R_S + \dots = \sum_{n=0}^{\infty} (1 - R_S)^n \cdot R_S = 1 \quad (1)$$

In practice, absorption and reflection losses must be taken into account. To quantify the importance of these effects, we use ray tracing to calculate η_D as a function of waveguide layer thickness and absorption coefficient (α), assuming 5% loss at each reflection. As expected, the η_D increases as absorption and reflection losses are reduced, see Fig. B.2b and c, respectively. The only loss channel in this case is the light propagating to the substrate edge; $< 0.1\%$ for the $(2.5 \text{ cm})^2$ substrate used in the simulation. As shown in Fig. B.2c, the primary limit to η_D is the absorption in the waveguide layer.

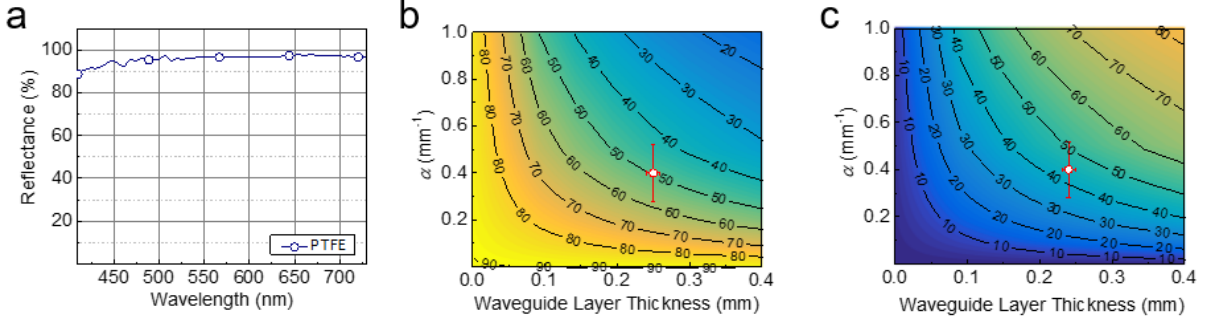


Figure B 2 Reflectance and outcoupling efficiency of the diffuser. (a) The reflectance of the PTFE diffuse reflector measured using an integrating sphere. Calculated (b) outcoupling efficiency (η_D) and (c) waveguide layer absorption of the light diffusing substrate as functions of waveguide thickness and absorption constant (α). The experimental results are indicated as points.

The outcoupling efficiency (η_{out}) of the OLED is, then:

$$\eta_{out} = \eta_{TA} + \eta_D \eta_S \quad (2)$$

where η_{TA} is the fraction of light emitted from the top surface and η_S is the fraction of light coupled into the slab waveguide. The simulated^{32,33} modal power intensity of both top and bottom OLED emission as a function of the normalized in-plane wave vector $u = k_{||}/(n_{EML} \cdot k_0)$ (here $k_{||}$ is the wave vector of the dipole radiation field in the plane of the interface, k_0 is the wave vector in vacuum, and n_{EML} is the refractive index of the organic layer) of the cavity at different waveguide layer refractive indices (n_P) at the wavelength of $\lambda=530$ nm are shown in Fig. B.3a and 3b, respectively. Top emission power propagating with wave vectors $0 < u < n_{air}/n_{EML}$, is emitted into the viewing direction (air modes). Modal power with wave vectors of $n_{air}/n_{EML} < u < n_P/n_{EML}$ is totally internally reflected at the air-top electrode interface. It is subsequently incident on the waveguide layer (substrate modes). All the bottom emitted power propagating with wave vectors $0 < u < n_P/n_{EML}$ couples into the waveguide. For $n_P/n_{EML} < u < 1$, both top and bottom emission propagates within the OLED active layer. Note that no power exists at $u > 1$, which corresponds to the power coupled into SPP modes. In Figs. 3a and b, vertical dashed lines correspond to

$n_{air}/n_{EML} = 0.55$, and $n_P/n_{EML} = 0.77, 0.88, 0.99$ for the substrate-waveguide mode boundary at each n_P . For $n_P = 1.8$, most of the non-radiative modal power propagates within the waveguide layer, and is subsequently extracted into the viewing direction via scattering from the rough diffuser interface at the bottom of the polymer waveguide. Figure B.3c is a plot of $\eta_{IQE} \cdot \eta_S$ vs. n_P , with the result that $\eta_{IQE} \cdot \eta_S = 67\%$ at $n_P = 1.8$.

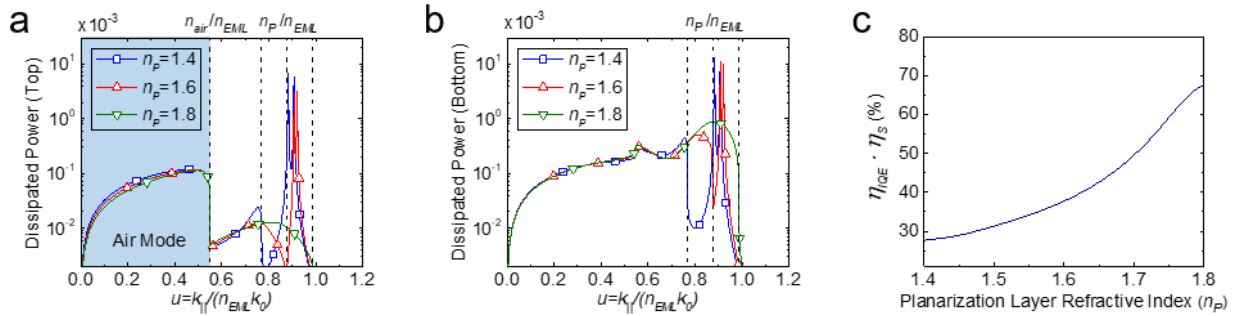


Figure B.3 Modal power distribution vs. in-plane wave vector for various waveguide layer refractive indices. Simulation of the dissipated optical power of the PHOLED emitted (a) from the top, and (b) the substrate surfaces at a wavelength of 530 nm, i.e., at the emission peak of $Ir(ppy)_2(acac)$ emission. (c) Calculated coupling efficiency into the waveguide layer (η_S) as a function of waveguide layer refractive index (n_P).

B.3 Device characteristics

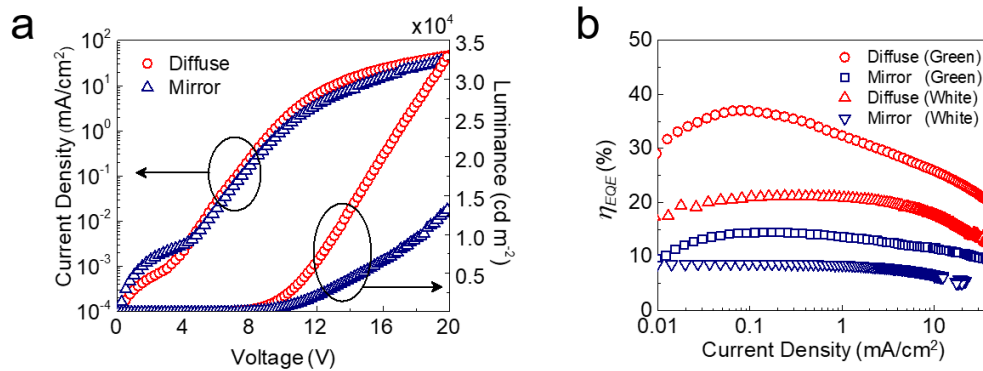


Figure B.4 Characteristics of PHOLEDs fabricated on metal mirror and diffuse reflector substrates. (a) Current density-voltage-luminance (J-V-L) characteristics of the green emitting PHOLED on the two substrates. (b) Current density versus external quantum efficiency (J- η_{EQE}) of the white and green PHOLEDs deposited on metal and diffuse reflecting substrates.

To demonstrate the enhancement in external quantum efficiency (η_{EQE}), green and white PHOLEDs with transparent top and bottom contacts were grown on diffuse and metal reflectors.

Figures B.4a and B.4b are plots of the current density-voltage (J - V) and external quantum efficiency characteristics of the PHOLEDs, respectively (see Methods for structures). The identical J - V characteristics of the PHOLED on the diffuser and the Al mirror shows that the flat top surface of the waveguide does not lead to a loss in performance of the subsequently deposited device. The green, diffuse reflecting PHOLED shows a peak $\eta_{EQE} = 37 \pm 4\%$, whereas with a metal mirror, $\eta_{EQE} = 15 \pm 2\%$. A similar enhancement is observed for the white-emitting PHOLED (W-PHOLED), where $\eta_{EQE} = 21 \pm 3\%$ for the diffuse compared with $9 \pm 1\%$ for the metal reflector.

The ability of the diffuse reflector to outcouple guided modes was quantified by comparing its performance with that of a green electrophosphorescent OLED fabricated on a sapphire substrate with a similar refractive index of $n_{saph} = 1.77$ at $\lambda = 530$ nm. The sapphire substrate yields $\eta_{IQE} \cdot \eta_{TA} = 7 \pm 2\%$, where η_{IQE} refers to the internal quantum efficiency. Therefore, from Eq. (2), the light coupled into the waveguide layer shows an outcoupling efficiency of $\eta_{IQE} \cdot \eta_S \cdot \eta_D = 30 \pm 5\%$ and $8 \pm 3\%$ for the diffuser and metal mirror structures, respectively, resulting in a 3.8 ± 1.5 fold increase in extraction into the viewing direction via diffuse scattering. In Fig. B.3c, $\eta_{IQE} \cdot \eta_S = 67\%$ for $n_P = 1.8$, yielding $\eta_D = 45\%$ and 12% for diffuse and Al mirror substrates, respectively. This corresponds to the ray tracing result in Fig. B.2b of $\eta_D = 49 \pm 6\%$ for $\alpha = 0.4 \pm 0.1 \text{ mm}^{-1}$ and a thickness $240 \pm 9 \text{ }\mu\text{m}$ measured for the waveguide (data point), compared to $\eta_D = 15 \pm 1\%$ for the $20 \pm 1 \text{ }\mu\text{m}$ thick waveguide used for the metal mirror reflector. These results are summarized in Table B.1.

Table B.1 Modal power distribution of scattering and specular (metal) reflector substrates.

	Diffuse Reflector	Metal Reflector
$\eta_{EQE}^{a)}$	$37 \pm 4\%$	$15 \pm 2\%$
$\eta_{IQE} \cdot \eta_{TA}^{\dagger}$	$7 \pm 2\%$	$7 \pm 2\%$
$\eta_{IQE} \cdot \eta_S \cdot \eta_D$	Active Area $14 \pm 5\%$	$8 \pm 3\%$
	Periphery $16 \pm 2\%$	
η_S^{\dagger}	67%	67%
η_D^{\ddagger}	$45\% (49\%)$	$12\% (15\%)$

^{a)} Measured

[†] Calculated based on Green's function analysis

[‡] Combined result from experiment and Green's function analysis. The result in parenthesis is from ray tracing analysis

The diffuser increases the étendue of the system, thus introducing emission outside of the PHOLED active area defined by the device contacts. Figures B.5a and b show the normalized radiated power intensities from the PHOLED deposited on a diffuse reflector and Al mirror, respectively. The calculations assume $\alpha = 0.4 \text{ mm}^{-1}$, a $(1 \text{ mm})^2$ device area, and with waveguide layer thicknesses of $240 \text{ }\mu\text{m}$ and $20 \text{ }\mu\text{m}$ for the diffuser and Al mirror, respectively. The black dashed lines define the device contact area. Photographic images of emission from PHOLEDs on each substrate are shown in Fig. B.5c and d, insets, showing similar behavior as the simulation. The redirection of the incident rays from the diffuse reflector isotropically redistributes the power, thus showing a circular emission pattern. Thinner waveguide layers suppress this effect due to the smaller subtended area. Contrary to the diffuse reflector, the specular reflection of the Al mirror does not affect the azimuthal ray direction, maintaining the defined device appearance.

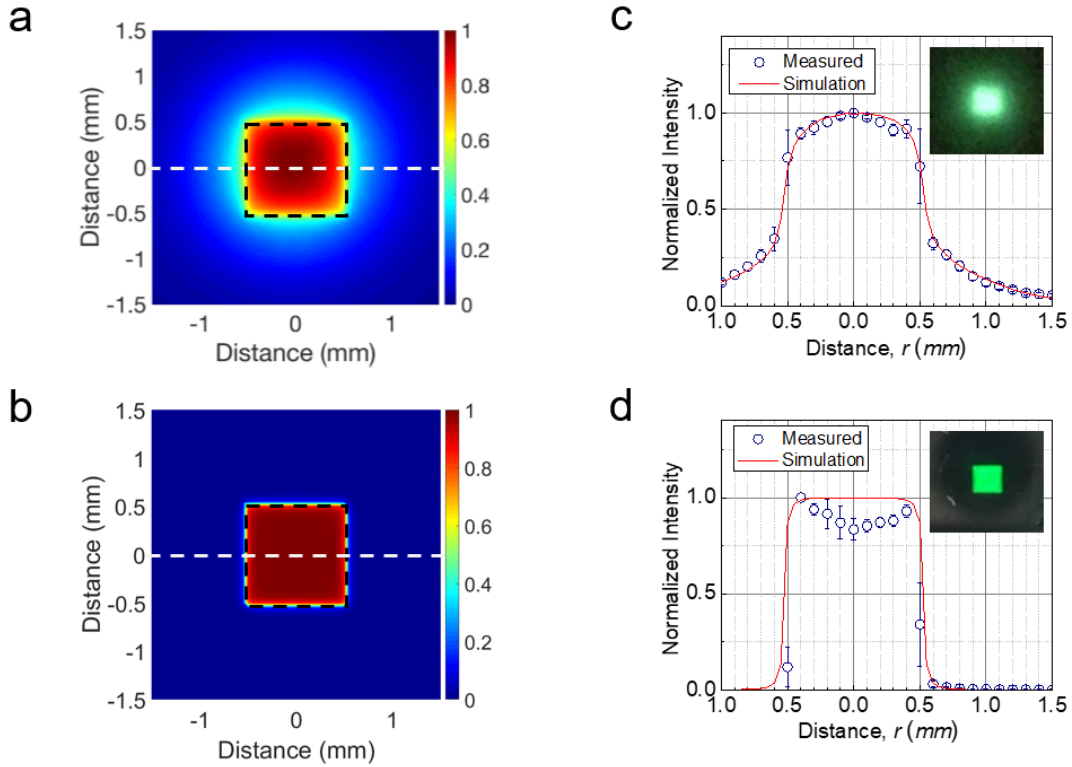


Figure B.5 Radiant power intensity profile for PHOLEDs on diffuse reflector and Al mirror substrates. (a) Simulated radiant power for a PHOLED on a diffuse reflector substrate. The white dashed line shows the measurement trajectory for 5c. The black dashed line indicates the device active area. (b) Simulated radiant power for the PHOLED on a specular (metal mirror) substrate. (c) (d) Measured (circles) radial peak intensity profiles along the white dashed line bisecting the PHOLED in (a) and (b) along with the ray tracing fit (lines). Insets: Photographs of emission from the green PHOLED deposited on each substrate.

To investigate the fraction of the peripheral emission for the PHOLED using the diffuser layer, we measured the radial intensity profile of the PHOLED following the trajectory of the dashed lines in Fig. B.5a and b, with the results given in Fig. B.5c and d along with a fit using ray tracing. The index of refraction at the top surface of the optical cavity changes from the ITO contact ($n_{ITO} = 2.1$) to the waveguide layer ($n_P = 1.8$), resulting in the emission peaks at the device edges in Fig. B.5d. Integrating the radiated power outside the device active area indicates that 54% of the total emission is emitted beyond the contact periphery for the diffuser, whereas Al mirror substrate showed $< 10\%$ of emission from the periphery. As expected, the fraction of peripheral emission decreases with device area.

We simulated η_D of OLEDs whose areas cover a large fraction of the substrate size (25 mm²), which is the common situation found in actual lighting panels, shown in Fig. B.6. We find that η_D is unchanged for device areas < 20 mm². At > 20 mm², η_D was reduced due to the waveguided emission reaching the substrate edge, although the effects were \leq 2%. The fraction of peripheral emission decreases with increased device area, resulting in the loss of only an insignificant fraction of the light in the waveguide layer at the substrate edge for large area devices.

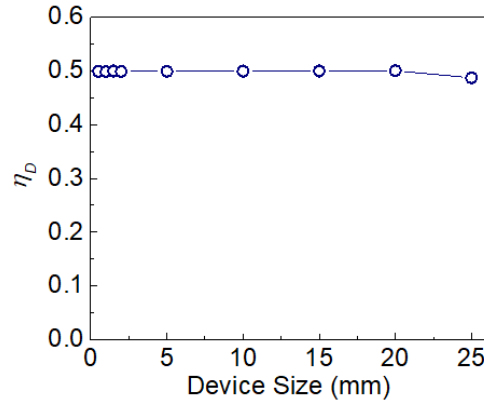


Figure B.6 Simulated fraction of light outcoupled from the light diffusing substrate vs. the size of the OLED. All devices are assumed to have square geometry. The square substrate size is 25 mm².

The spectrum of a conventional PHOLED depends on viewing angle due to weak optical microcavity effects³. Bulović, et al.³ measured the angular distribution of the radiant intensity and showed that the spectral shift in a green OLED exhibits a peak shift of approximately 30-40 nm depending on the device structure. Cavity effects are more pronounced for top emitting OLEDs due to the large difference in the refractive index between the transparent ITO top contact and air. This effect is especially critical for white light sources due to their broad spectra. The use of a high refractive index waveguide layer suppresses spectral shifts at large viewing angles²⁰, thus reducing cavity effects. As a result, the spectrum of the devices on both the mirror and the diffuse reflector substrates are independent of viewing angle, as shown in Fig. B.7a. The spectrum of the device on the mirror substrate measured perpendicular to the substrate (0°) shows Fabry-Perot resonances

due to the interference within the waveguide layer. Light scattering into all directions by the diffuse reflector eliminates the resonances. Furthermore, scattering by the diffuse reflector results in a Lambertian emission profile, shown in Fig. B.7b.

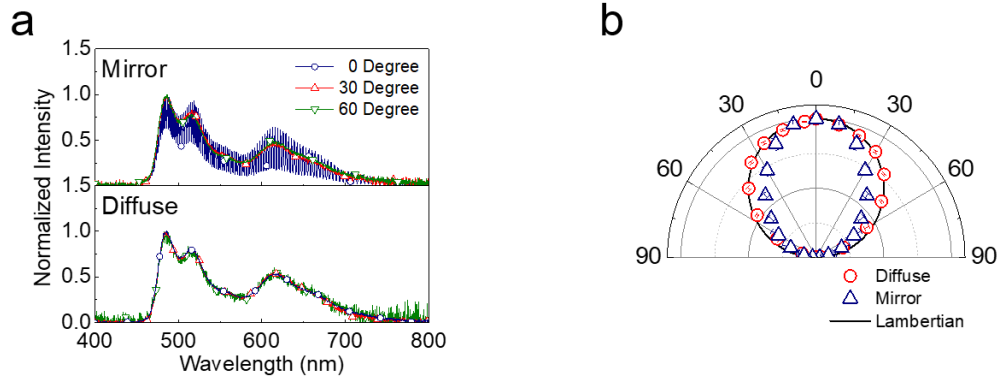


Figure B.7 Emission profile of the white PHOLED on the diffuser. (a) White PHOLED emission spectrum at viewing angles of 0°, 30°, and 60°. (b) Polar plot of the peak intensity. The solid line indicates a Lambertian profile.

The thickness of the waveguide affects the power lost via absorption. The ray tracing simulations show that η_D can approach 75% for a 50 μm thick waveguide layer at $\alpha=0.4 \text{ mm}^{-1}$, leading to $\eta_{EQE} = 68\%$ with 100% device internal quantum efficiency. From this we infer a 3.4-fold enhancement compared to the substrate with the metal mirror. The emission profile also depends on the waveguide layer thickness. This results since more reflections occur during lateral propagation in a thinner waveguide layer. A 50 μm waveguide layer is expected to show a peripheral emission of 13%.

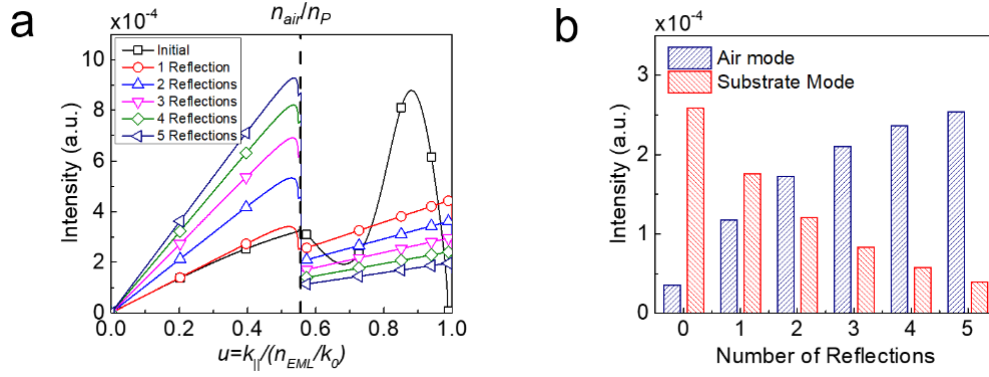


Figure B.8 Modal power distribution evolution with number of reflections. (a) Modal power distribution vs. the number of reflections in the waveguide layer. The dashed line represents the boundary between air and substrate modes at $u = n_{air}/n_P$. (b) Distribution of modal power in air and substrate modes following each reflection.

Since power coupled into non-radiative modes is not viewable, outcoupling schemes fall into two categories: concentrating power into air modes²⁷, or redirecting the wave vectors of the non-radiative modes. A means for redirecting the wave vector is via scattering^{7,8,24,25} which provides a route to reduce the in-plane momentum from $n_{air}/n_{EML} < u < 1$ to $0 < u < n_{air}/n_{EML}$. The Lambertian profile of the diffuse reflector shows that it evenly redistributes the incident power for each wave vector. Figure B.8a shows the variation in modal power distribution vs. the number of reflections in the waveguide layer. At each reflection the power confined in the waveguide layer ($n_{air}/n_P < u < 1$) is redistributed into all wave vectors, where wave vectors of $0 < u < n_{air}/n_P$ is extracted into the viewing direction. Thus, the power confined within the waveguide layer decreases as the wave propagates. The integrated modal power of air and substrate modes is given in Fig. B.8b.

A number of scattering methods redirect only a fraction of the scattered light into the viewing direction, and hence in those approaches, an outcoupling efficiency similar to that achieved here requires further enhancements by using microlens arrays or index matching fluid. In addition, the coupling into SPP modes and absorption by metal cathodes leads to additional losses, preventing wave propagation over long distances. The use of a diffuse reflector with a transparent

OLED completely avoids coupling into these loss channels. Therefore, efficient outcoupling is possible using only the diffuser and waveguide, making it considerably simpler and less costly to implement.

B.4 Conclusion

In conclusion, we demonstrate an efficient, transparent top emitting structure with a diffuse reflector planarized by a transparent slab waveguide. The diffuse reflector eliminates losses due to coupling to SPP modes, while redirecting the laterally propagating light within the waveguide layer into the viewing direction. The planarizing polymer with a high refractive index ($n_P = 1.8$) is deposited onto the diffuse reflector surface to maximize the light coupled into the diffuser, as well as to create a smooth surface on which to fabricate the PHOLED. The device on the diffuse reflector showed 2.5-fold enhancement in external quantum efficiency compared to an analogous PHOLED on a metal mirror. The architecture does not require additional outcoupling structures such as microlens arrays to enhance the outcoupling efficiency. The diffuse reflector shows no wavelength or viewing angle dependence, exhibiting a Lambertian emission profile. Our results provide a simple solution at a potentially low cost for OLED lighting applications.

Bibliography

- [1] M. A. Baldo, D. F. O'Brien, Y. You, A. Shoustikov, S. Sibley, M. E. Thompson, and S. R. Forrest, *Highly Efficient Phosphorescent Emission from Organic Electroluminescent Devices*, *Nature* **395**, 151 (1998).
- [2] J. L. Schmit, *Growth, Properties and Applications of HgCdTe*, *J. Crys. Growth* **65**, 249 (1983).
- [3] M. Shtein, H. F. Gossenberger, J. B. Benziger, and S. R. Forrest, *Material Transport Regimes and Mechanisms for Growth of Molecular Organic Thin Films Using Low-Pressure Organic Vapor Phase Deposition*, *J. Appl. Phys.* **89**, 1470 (2000).
- [4] M. Baldo, M. Deutsch, P. Burrows, H. Gossenberger, M. Gerstenberg, V. Ban, and S. Forrest, *Organic Vapor Phase Deposition*, *Adv. Mater.* **10**, 1505 (1998).
- [5] B. Qu, K. Ding, K. Sun, S. Hou, S. Morris, M. Shtein, and S. R. Forrest, *Fast Organic Vapor Phase Deposition of Thin Films in Light-Emitting Diodes*, *ACS Nano* **14**, 14157 (2020).
- [6] G. J. McGraw and S. R. Forrest, *Vapor-Phase Microprinting of Multicolor Phosphorescent Organic Light Emitting Device Arrays*, *Adv. Mater.* **25**, 1583 (2013).
- [7] S. Forrest and G. McGraw, *OVJP Patterning of Electronic Devices*, US10283737B2 (2013).
- [8] M. S. Arnold, G. J. McGraw, S. R. Forrest, and R. R. Lunt, *Direct Vapor Jet Printing of Three Color Segment Organic Light Emitting Devices for White Light Illumination*, *Appl. Phys. Lett.* **92**, 053301 (2008).
- [9] M. Shtein, P. Peumans, J. B. Benziger, and S. R. Forrest, *Direct, Mask- and Solvent-Free Printing of Molecular Organic Semiconductors*, *Adv. Mater.* **16**, 1615 (2004).
- [10] S. R. Forrest, *Organic Electronics: Foundations to Applications* (Oxford University Press, 2020).
- [11] A. Köhler and H. Bässler, *Electronic Processes in Organic Semiconductors: An Introduction* (John Wiley & Sons, 2015).
- [12] H. Uoyama, K. Goushi, K. Shizu, H. Nomura, and C. Adachi, *Highly Efficient Organic Light-Emitting Diodes from Delayed Fluorescence*, *Nature* **492**, 234 (2012).
- [13] R. R. Lunt, J. B. Benziger, and S. R. Forrest, *Relationship between Crystalline Order and Exciton Diffusion Length in Molecular Organic Semiconductors*, *Adv. Mater.* **22**, 1233 (2010).

- [14] B. P. Rand, D. P. Burk, and S. R. Forrest, *Offset Energies at Organic Semiconductor Heterojunctions and Their Influence on the Open-Circuit Voltage of Thin-Film Solar Cells*, Phys. Rev. B **75**, 115327 (2007).
- [15] L. Xiao, Y. Li, K. Ding, and S. R. Forrest, *Energy Loss in Organic Photovoltaics: Nonfullerene Versus Fullerene Acceptors*, Phys. Rev. Applied **11**, 024060 (2019).
- [16] M. A. Baldo, M. E. Thompson, and S. R. Forrest, *High-Efficiency Fluorescent Organic Light-Emitting Devices Using a Phosphorescent Sensitizer*, Nature **403**, 750 (2000).
- [17] A. Guerrero and G. Garcia-Belmonte, *Recent Advances to Understand Morphology Stability of Organic Photovoltaics*, Nano-Micro Lett. **9**, 10 (2017).
- [18] J. Ràfols-Ribé, P.-A. Will, C. Hänisch, M. Gonzalez-Silveira, S. Lenk, J. Rodríguez-Viejo, and S. Reineke, *High-Performance Organic Light-Emitting Diodes Comprising Ultrastable Glass Layers*, Sci. Adv. **4**, (2018).
- [19] V. Savikhin, L. K. Jagadamma, L. J. Purvis, I. Robertson, S. D. Oosterhout, C. J. Douglas, I. D. W. Samuel, and M. F. Toney, *Morphological, Chemical, and Electronic Changes of the Conjugated Polymer PTB7 with Thermal Annealing*, IScience **2**, 182 (2018).
- [20] M. J. Jurow, C. Mayr, T. D. Schmidt, T. Lampe, P. I. Djurovich, W. Brütting, and M. E. Thompson, *Understanding and Predicting the Orientation of Heteroleptic Phosphors in Organic Light-Emitting Materials*, Nat. Mater. **15**, 85 (2016).
- [21] E. Fermi, *Quantum Theory of Radiation*, Rev. Mod. Phys. **4**, 87 (1932).
- [22] C. A. Hunter and J. K. M. Sanders, *The Nature of π - π Interactions*, J. Am. Chem. Soc. **112**, 5525 (1990).
- [23] M. O. Sinnokrot and C. D. Sherrill, *Substituent Effects in π - π Interactions: Sandwich and T-Shaped Configurations*, J. Am. Chem. Soc. **126**, 7690 (2004).
- [24] C. Janiak, *A Critical Account on π - π Stacking in Metal Complexes with Aromatic Nitrogen-Containing Ligands*, J. Chem. Soc., Dalton Trans. 3885 (2000).
- [25] C. A. Hunter, *Meldola Lecture. The Role of Aromatic Interactions in Molecular Recognition*, Chem. Soc. Rev. **23**, 101 (1994).
- [26] J. Frischeisen, D. Yokoyama, C. Adachi, and W. Brütting, *Determination of Molecular Dipole Orientation in Doped Fluorescent Organic Thin Films by Photoluminescence Measurements*, Appl. Phys. Lett. **96**, 073302 (2010).
- [27] S. Nowy, B. C. Krummacher, J. Frischeisen, N. A. Reinke, and W. Brütting, *Light Extraction and Optical Loss Mechanisms in Organic Light-Emitting Diodes: Influence of the Emitter Quantum Efficiency*, J. Appl. Phys. **104**, 123109 (2008).
- [28] C.-K. Moon, S.-Y. Kim, J.-H. Lee, and J.-J. Kim, *Luminescence from Oriented Emitting Dipoles in a Birefringent Medium*, Opt. Express **23**, A279 (2015).
- [29] J. A. Schuller, S. Karaveli, T. Schiros, K. He, S. Yang, I. Kymissis, J. Shan, and R. Zia, *Orientation of Luminescent Excitons in Layered Nanomaterials*, Nat. Nanotechnol. **8**, 271 (2013).

- [30] D. Pommier, R. Bretel, L. E. P. López, F. Fabre, A. Mayne, E. Boer-Duchemin, G. Dujardin, G. Schull, S. Berciaud, and E. Le Moal, *Scanning Tunneling Microscope-Induced Excitonic Luminescence of a Two-Dimensional Semiconductor*, *Phys. Rev. Lett.* **123**, 027402 (2019).
- [31] M. J. Jurow, T. Morgenstern, C. Eisler, J. Kang, E. Penzo, M. Do, M. Engelmayr, W. T. Osowiecki, Y. Bekenstein, C. Tassone, L.-W. Wang, A. P. Alivisatos, W. Brütting, and Y. Liu, *Manipulating the Transition Dipole Moment of CsPbBr₃ Perovskite Nanocrystals for Superior Optical Properties*, *Nano Lett.* **19**, 2489 (2019).
- [32] S. S. Dalal, Z. Fakhraai, and M. D. Ediger, *High-Throughput Ellipsometric Characterization of Vapor-Deposited Indomethacin Glasses*, *J. Phys. Chem. B* **117**, 15415 (2013).
- [33] S. F. Swallen, K. L. Kearns, M. K. Mapes, Y. S. Kim, R. J. McMahon, M. D. Ediger, T. Wu, L. Yu, and S. Satija, *Organic Glasses with Exceptional Thermodynamic and Kinetic Stability*, *Science* **315**, 353 (2007).
- [34] E. Leon-Gutierrez, G. Garcia, A. F. Lopeandia, M. T. Clavaguera-Mora, and J. Rodríguez-Viejo, *Size Effects and Extraordinary Stability of Ultrathin Vapor Deposited Glassy Films of Toluene*, *J. Phys. Chem. Lett.* **1**, 341 (2010).
- [35] E. Leon-Gutierrez, A. Sepúlveda, G. Garcia, M. T. Clavaguera-Mora, and J. Rodríguez-Viejo, *Stability of Thin Film Glasses of Toluene and Ethylbenzene Formed by Vapor Deposition: An in Situ Nanocalorimetric Study*, *Phys. Chem. Chem. Phys.* **12**, 14693 (2010).
- [36] S. Y. Byeon, J. Kim, D. R. Lee, S. H. Han, S. R. Forrest, and J. Y. Lee, *Nearly 100% Horizontal Dipole Orientation and Upconversion Efficiency in Blue Thermally Activated Delayed Fluorescent Emitters*, *Adv. Opt. Mater.* **6**, 1701340 (2018).
- [37] A. Graf, P. Liehm, C. Murawski, S. Hofmann, K. Leo, and M. C. Gather, *Correlating the Transition Dipole Moment Orientation of Phosphorescent Emitter Molecules in OLEDs with Basic Material Properties*, *J. Mater. Chem. C* **2**, 10298 (2014).
- [38] S. Reineke, T. C. Rosenow, B. Lüssem, and K. Leo, *Improved High-Brightness Efficiency of Phosphorescent Organic LEDs Comprising Emitter Molecules with Small Permanent Dipole Moments*, *Adv. Mater.* **22**, 3189 (2010).
- [39] S. Reineke, G. Schwartz, K. Walzer, M. Falke, and K. Leo, *Highly Phosphorescent Organic Mixed Films: The Effect of Aggregation on Triplet-Triplet Annihilation*, *Appl. Phys. Lett.* **94**, 163305 (2009).
- [40] P. Liehm, C. Murawski, M. Furno, B. Lüssem, K. Leo, and M. C. Gather, *Comparing the Emissive Dipole Orientation of Two Similar Phosphorescent Green Emitter Molecules in Highly Efficient Organic Light-Emitting Diodes*, *Appl. Phys. Lett.* **101**, 253304 (2012).
- [41] K.-H. Kim, S. Lee, C.-K. Moon, S.-Y. Kim, Y.-S. Park, J.-H. Lee, J. Woo Lee, J. Huh, Y. You, and J.-J. Kim, *Phosphorescent Dye-Based Supramolecules for High-Efficiency Organic Light-Emitting Diodes*, *Nat. Commun.* **5**, 4769 (2014).
- [42] C.-K. Moon, K.-H. Kim, J. W. Lee, and J.-J. Kim, *Influence of Host Molecules on Emitting Dipole Orientation of Phosphorescent Iridium Complexes*, *Chem. Mater.* **27**, 2767 (2015).
- [43] K.-H. Kim, J.-Y. Ma, C.-K. Moon, J.-H. Lee, J. Y. Baek, Y.-H. Kim, and J.-J. Kim, *Controlling Emitting Dipole Orientation with Methyl Substituents on Main Ligand of*

- Iridium Complexes for Highly Efficient Phosphorescent Organic Light-Emitting Diodes*, Adv. Opt. Mater. **3**, 1191 (2015).
- [44] C.-K. Moon, K.-H. Kim, and J.-J. Kim, *Unraveling the Orientation of Phosphors Doped in Organic Semiconducting Layers*, Nat. Commun. **8**, 791 (2017).
- [45] J.-S. Huh, K.-H. Kim, C.-K. Moon, and J.-J. Kim, *Dependence of Pt(II) Based Phosphorescent Emitter Orientation on Host Molecule Orientation in Doped Organic Thin Films*, Org. Electron. **45**, 279 (2017).
- [46] J. Kim, T. Batagoda, J. Lee, D. Sylvinson, K. Ding, P. J. G. Saris, U. Kaipa, I. W. H. Oswald, M. A. Omary, M. E. Thompson, and S. R. Forrest, *Systematic Control of the Orientation of Organic Phosphorescent Pt Complexes in Thin Films for Increased Optical Outcoupling*, Adv. Mater. **31**, 1900921 (2019).
- [47] P. Sullivan, T. S. Jones, A. J. Ferguson, and S. Heutz, *Structural Templating as a Route to Improved Photovoltaic Performance in Copper Phthalocyanine/Fullerene (C₆₀) Heterojunctions*, Appl. Phys. Lett. **91**, 233114 (2007).
- [48] G. Giri, E. Verploegen, S. C. B. Mannsfeld, S. Atahan-Evrenk, D. H. Kim, S. Y. Lee, H. A. Becerril, A. Aspuru-Guzik, M. F. Toney, and Z. Bao, *Tuning Charge Transport in Solution-Sheared Organic Semiconductors Using Lattice Strain*, Nature **480**, 504 (2011).
- [49] J. Vogelsang, T. Adachi, J. Brazard, D. A. Vanden Bout, and P. F. Barbara, *Self-Assembly of Highly Ordered Conjugated Polymer Aggregates with Long-Range Energy Transfer*, Nat. Mater. **10**, 12 (2011).
- [50] A. L. Briseno, R. J. Tseng, M.-M. Ling, E. H. L. Falcao, Y. Yang, F. Wudl, and Z. Bao, *High-Performance Organic Single-Crystal Transistors on Flexible Substrates*, Adv. Mater. **18**, 2320 (2006).
- [51] J. Yang, D. Yan, and T. S. Jones, *Molecular Template Growth and Its Applications in Organic Electronics and Optoelectronics*, Chem. Rev. **115**, 5570 (2015).
- [52] B. E. Lassiter, R. R. Lunt, C. K. Renshaw, and S. R. Forrest, *Structural Templating of Multiple Polycrystalline Layers in Organic Photovoltaic Cells*, Opt. Express **18**, A444 (2010).
- [53] S. R. Forrest, *Ultrathin Organic Films Grown by Organic Molecular Beam Deposition and Related Techniques*, Chem. Rev. **97**, 1793 (1997).
- [54] L. S. Hung, C. W. Tang, and M. G. Mason, *Enhanced Electron Injection in Organic Electroluminescence Devices Using an Al/LiF Electrode*, Appl. Phys. Lett. **70**, 152 (1997).
- [55] H. Fujikawa, T. Mori, K. Noda, M. Ishii, S. Tokito, and Y. Taga, *Organic Electroluminescent Devices Using Alkaline-Earth Fluorides as an Electron Injection Layer*, Journal of Luminescence **87–89**, 1177 (2000).
- [56] H. Heil, J. Steiger, S. Karg, M. Gastel, H. Ortner, H. von Seggern, and M. Stöbel, *Mechanisms of Injection Enhancement in Organic Light-Emitting Diodes through an Al/LiF Electrode*, J. Appl. Phys. **89**, 420 (2000).

- [57] T. M. Brown, R. H. Friend, I. S. Millard, D. J. Lacey, J. H. Burroughes, and F. Cacialli, *Efficient Electron Injection in Blue-Emitting Polymer Light-Emitting Diodes with LiF/Ca/Al Cathodes*, *Appl. Phys. Lett.* **79**, 174 (2001).
- [58] Q. T. Le, L. Yan, Y. Gao, M. G. Mason, D. J. Giesen, and C. W. Tang, *Photoemission Study of Aluminum/Tris-(8-Hydroxyquinoline) Aluminum and Aluminum/LiF/Tris-(8-Hydroxyquinoline) Aluminum Interfaces*, *J. Appl. Phys.* **87**, 375 (1999).
- [59] Z. Liu, O. V. Salata, and N. Male, *Improved Electron Injection in Organic LED with Lithium Quinolate/Aluminium Cathode*, *Synthetic Metals* **128**, 211 (2002).
- [60] T. Matsushima, G.-H. Jin, and H. Murata, *Marked Improvement in Electroluminescence Characteristics of Organic Light-Emitting Diodes Using an Ultrathin Hole-Injection Layer of Molybdenum Oxide*, *J. Appl. Phys.* **104**, 054501 (2008).
- [61] J.-H. Lee, H. Shin, J.-M. Kim, K.-H. Kim, and J.-J. Kim, *Exciplex-Forming Co-Host-Based Red Phosphorescent Organic Light-Emitting Diodes with Long Operational Stability and High Efficiency*, *ACS Appl. Mater. Interfaces* **9**, 3277 (2017).
- [62] S. Lee, K.-H. Kim, D. Limbach, Y.-S. Park, and J.-J. Kim, *Low Roll-Off and High Efficiency Orange Organic Light Emitting Diodes with Controlled Co-Doping of Green and Red Phosphorescent Dopants in an Exciplex Forming Co-Host*, *Adv. Funct. Mater.* **23**, 4105 (2013).
- [63] Y. Sun, N. C. Giebink, H. Kanno, B. Ma, M. E. Thompson, and S. R. Forrest, *Management of Singlet and Triplet Excitons for Efficient White Organic Light-Emitting Devices*, *Nature* **440**, 908 (2006).
- [64] B. W. D'Andrade and S. R. Forrest, *White Organic Light-Emitting Devices for Solid-State Lighting*, *Adv. Mater.* **16**, 1585 (2004).
- [65] M. C. Gather, A. Köhnen, and K. Meerholz, *White Organic Light-Emitting Diodes*, *Adv. Mater.* **23**, 233 (2011).
- [66] J.-S. Huh, Y. H. Ha, S.-K. Kwon, Y.-H. Kim, and J.-J. Kim, *Design Strategy of Anthracene-Based Fluorophores toward High-Efficiency Deep Blue Organic Light-Emitting Diodes Utilizing Triplet-Triplet Fusion*, *ACS Appl. Mater. Interfaces* **12**, 15422 (2020).
- [67] H. Uoyama, K. Goushi, K. Shizu, H. Nomura, and C. Adachi, *Highly Efficient Organic Light-Emitting Diodes from Delayed Fluorescence*, *Nature* **492**, 7428 (2012).
- [68] M. Furno, R. Meerheim, S. Hofmann, B. Lüssem, and K. Leo, *Efficiency and Rate of Spontaneous Emission in Organic Electroluminescent Devices*, *Phys. Rev. B* **85**, 115205 (2012).
- [69] V. Bulović, V. B. Khalfin, G. Gu, P. E. Burrows, D. Z. Garbuzov, and S. R. Forrest, *Weak Microcavity Effects in Organic Light-Emitting Devices*, *Phys. Rev. B* **58**, 3730 (1998).
- [70] W. Brütting, J. Frischeisen, T. D. Schmidt, B. J. Scholz, and C. Mayr, *Device Efficiency of Organic Light-Emitting Diodes: Progress by Improved Light Outcoupling*, *Phys. Status Solidi A* **210**, 44 (2013).
- [71] Y. Zhang, J. Lee, and S. R. Forrest, *Tenfold Increase in the Lifetime of Blue Phosphorescent Organic Light-Emitting Diodes*, *Nat. Commun.* **5**, 5008 (2014).

- [72] Y. Kawamura, K. Goushi, J. Brooks, J. J. Brown, H. Sasabe, and C. Adachi, *100% Phosphorescence Quantum Efficiency of Ir(III) Complexes in Organic Semiconductor Films*, *Appl. Phys. Lett.* **86**, 071104 (2005).
- [73] S. Möller and S. R. Forrest, *Improved Light Out-Coupling in Organic Light Emitting Diodes Employing Ordered Microlens Arrays*, *J. Appl. Phys.* **91**, 3324 (2002).
- [74] Y. Sun and S. R. Forrest, *Organic Light Emitting Devices with Enhanced Outcoupling via Microlenses Fabricated by Imprint Lithography*, *J. Appl. Phys.* **100**, 073106 (2006).
- [75] J.-J. Kim, J. Lee, S.-P. Yang, H. G. Kim, H.-S. Kweon, S. Yoo, and K.-H. Jeong, *Biologically Inspired Organic Light-Emitting Diodes*, *Nano Lett.* **16**, 2994 (2016).
- [76] T.-W. Koh, J. A. Spechler, K. M. Lee, C. B. Arnold, and B. P. Rand, *Enhanced Outcoupling in Organic Light-Emitting Diodes via a High-Index Contrast Scattering Layer*, *ACS Photonics* **2**, 1366 (2015).
- [77] W. L. Barnes, A. Dereux, and T. W. Ebbesen, *Surface Plasmon Subwavelength Optics*, *Nature* **424**, 824 (2003).
- [78] A. Salehi, X. Fu, D.-H. Shin, and F. So, *Recent Advances in OLED Optical Design*, *Adv. Funct. Mater.* **29**, 1808803 (2019).
- [79] W. L. Barnes, *Fluorescence near Interfaces: The Role of Photonic Mode Density*, *J. Modern Optics* **45**, 661 (1998).
- [80] D. Chen, A. Nakahara, D. Wei, D. Nordlund, and T. P. Russell, *P3HT/PCBM Bulk Heterojunction Organic Photovoltaics: Correlating Efficiency and Morphology*, *Nano Lett.* **11**, 561 (2011).
- [81] Y. Watanabe, H. Sasabe, and J. Kido, *Review of Molecular Engineering for Horizontal Molecular Orientation in Organic Light-Emitting Devices*, *Bull. Chem. Soc. Jpn.* **92**, 716 (2019).
- [82] T. D. Schmidt, T. Lampe, D. Sylvinson M. R., P. I. Djurovich, M. E. Thompson, and W. Brütting, *Emitter Orientation as a Key Parameter in Organic Light-Emitting Diodes*, *Phys. Rev. Applied* **8**, 037001 (2017).
- [83] D. Yokoyama, Y. Setoguchi, A. Sakaguchi, M. Suzuki, and C. Adachi, *Orientation Control of Linear-Shaped Molecules in Vacuum-Deposited Organic Amorphous Films and Its Effect on Carrier Mobilities*, *Adv. Funct. Mater.* **20**, 386 (2010).
- [84] G. R. Mitchell, *A Wide-Angle X-Ray Study of the Development of Molecular Orientation in Crosslinked Natural Rubber*, *Polymer* **25**, 1562 (1984).
- [85] J. Als-Nielsen, D. Jacquemain, K. Kjaer, F. Leveiller, M. Lahav, and L. Leiserowitz, *Principles and Applications of Grazing Incidence X-Ray and Neutron Scattering from Ordered Molecular Monolayers at the Air-Water Interface*, *Phys. Rep.* **246**, 251 (1994).
- [86] M. A. Lieb, J. M. Zavislan, and L. Novotny, *Single-Molecule Orientations Determined by Direct Emission Pattern Imaging*, *J. Opt. Soc. Am. B* **21**, 1210 (2004).
- [87] M. Böhmeler, N. Hartmann, C. Georgi, F. Hennrich, A. A. Green, M. C. Hersam, and A. Hartschuh, *Enhancing and Redirecting Carbon Nanotube Photoluminescence by an Optical Antenna*, *Opt. Express* **18**, 16443 (2010).

- [88] S. J. Brown, R. A. DeCrescent, D. M. Nakazono, S. H. Willenson, N. A. Ran, X. Liu, G. C. Bazan, T.-Q. Nguyen, and J. A. Schuller, *Enhancing Organic Semiconductor–Surface Plasmon Polariton Coupling with Molecular Orientation*, *Nano Lett.* **17**, 6151 (2017).
- [89] S. J. Brown, R. A. Schlitz, M. L. Chabinyk, and J. A. Schuller, *Morphology-Dependent Optical Anisotropies in the n-Type Polymer P(NDI2OD-T2)*, *Phys. Rev. B* **94**, 165105 (2016).
- [90] A. Fieramosca, L. De Marco, M. Passoni, L. Polimeno, A. Rizzo, B. L. T. Rosa, G. Cruciani, L. Dominici, M. De Giorgi, G. Gigli, L. C. Andreani, D. Gerace, D. Ballarini, and D. Sanvitto, *Tunable Out-of-Plane Excitons in 2D Single-Crystal Perovskites*, *ACS Photonics* **5**, 4179 (2018).
- [91] Y. Gao, M. C. Weidman, and W. A. Tisdale, *CdSe Nanoplatelet Films with Controlled Orientation of Their Transition Dipole Moment*, *Nano Lett.* **17**, 3837 (2017).
- [92] T. H. Taminiau, S. Karaveli, N. F. van Hulst, and R. Zia, *Quantifying the Magnetic Nature of Light Emission*, *Nat. Commun.* **3**, 979 (2012).
- [93] R. R. Chance, A. Prock, and R. Silbey, *Lifetime of an Emitting Molecule near a Partially Reflecting Surface*, *J. Chem. Phys.* **60**, 2744 (1974).
- [94] K. Celebi, T. D. Heidel, and M. A. Baldo, *Simplified Calculation of Dipole Energy Transport in a Multilayer Stack Using Dyadic Green's Functions*, *Opt. Express* **15**, 1762 (2007).
- [95] J. W. Goodman, *Introduction to Fourier Optics*, 2nd ed. (McGraw Hill, New York, 1996).
- [96] L. Penninck, P. De Visschere, J. Beeckman, and K. Neyts, *Dipole Radiation within One-Dimensional Anisotropic Microcavities: A Simulation Method*, *Opt. Express* **19**, 18558 (2011).
- [97] M. K. Callens, D. Yokoyama, and K. Neyts, *Anisotropic Materials in OLEDs for High Outcoupling Efficiency*, *Opt. Express* **23**, 21128 (2015).
- [98] W. S. Weiglhofer, *Dyadic Green's Functions for General Uniaxial Media*, *IEE Proc. H Microw. Antennas Propag. UK* **137**, 5 (1990).
- [99] Z. Xiong, *Electromagnetic Fields of Electric Dipoles Embedded in a Stratified Anisotropic Earth*, *Geophysics* **54**, 1643 (1989).
- [100] J. A. Kurvits, M. Jiang, and R. Zia, *Comparative Analysis of Imaging Configurations and Objectives for Fourier Microscopy*, *J. Opt. Soc. Am. A* **32**, 2082 (2015).
- [101] S. R. Forrest, D. D. C. Bradley, and M. E. Thompson, *Measuring the Efficiency of Organic Light-Emitting Devices*, *Adv. Mater.* **15**, 1043 (2003).
- [102] C. Mayr and W. Brütting, *Control of Molecular Dye Orientation in Organic Luminescent Films by the Glass Transition Temperature of the Host Material*, *Chem. Mater.* **27**, 2759 (2015).
- [103] S. Shi, M. C. Jung, C. Coburn, A. Tadde, D. Sylvinson M. R., P. I. Djurovich, S. R. Forrest, and M. E. Thompson, *Highly Efficient Photo- and Electroluminescence from Two-Coordinate Cu(I) Complexes Featuring Nonconventional N-Heterocyclic Carbenes*, *J. Am. Chem. Soc.* **141**, 3576 (2019).

- [104] F. Yang, M. Shtein, and S. R. Forrest, *Controlled Growth of a Molecular Bulk Heterojunction Photovoltaic Cell*, *Nat. Mater.* **4**, 37 (2005).
- [105] D. Yokoyama, *Molecular Orientation in Small-Molecule Organic Light-Emitting Diodes*, *J. Mater. Chem. C* **21**, 19187 (2011).
- [106] C. Kim, A. Facchetti, and T. J. Marks, *Polymer Gate Dielectric Surface Viscoelasticity Modulates Pentacene Transistor Performance*, *Science* **318**, 76 (2007).
- [107] H. Sirringhaus, P. J. Brown, R. H. Friend, M. M. Nielsen, K. Bechgaard, B. M. W. Langeveld-Voss, A. J. H. Spiering, R. a. J. Janssen, E. W. Meijer, P. Herwig, and D. M. de Leeuw, *Two-Dimensional Charge Transport in Self-Organized, High-Mobility Conjugated Polymers*, *Nature* **401**, 685 (1999).
- [108] H.-W. Lin, C.-L. Lin, H.-H. Chang, Y.-T. Lin, C.-C. Wu, Y.-M. Chen, R.-T. Chen, Y.-Y. Chien, and K.-T. Wong, *Anisotropic Optical Properties and Molecular Orientation in Vacuum-Deposited Ter(9,9-Diarylfluorene)s Thin Films Using Spectroscopic Ellipsometry*, *J. Appl. Phys.* **95**, 881 (2004).
- [109] K. Ding, X. Liu, and S. R. Forrest, *Charge Transfer and Collection in Dilute Organic Donor–Acceptor Heterojunction Blends*, *Nano Lett.* **18**, 3180 (2018).
- [110] W. Chen, M. P. Nikiforov, and S. B. Darling, *Morphology Characterization in Organic and Hybrid Solar Cells*, *Energy Environ. Sci.* **5**, 8045 (2012).
- [111] M. Rohlfing, R. Temirov, and F. S. Tautz, *Adsorption Structure and Scanning Tunneling Data of a Prototype Organic-Inorganic Interface: PTCDA on Ag(111)*, *Phys. Rev. B* **76**, 115421 (2007).
- [112] Z. J. W. A. Leijten, A. D. A. Keizer, G. de With, and H. Friedrich, *Quantitative Analysis of Electron Beam Damage in Organic Thin Films*, *J. Phys. Chem. C* **121**, 10552 (2017).
- [113] J. Kim, H. Zhao, S. Hou, M. Khatoniar, V. Menon, and S. R. Forrest, *Using Fourier-Plane Imaging Microscopy for Determining Transition-Dipole-Moment Orientations in Organic Light-Emitting Devices*, *Phys. Rev. Applied* **14**, 034048 (2020).
- [114] P. J. Low, M. A. J. Paterson, D. S. Yufit, J. A. K. Howard, J. C. Cherryman, D. R. Tackley, R. Brook, and B. Brown, *Towards an Understanding of Structure–Property Relationships in Hole-Transport Materials: The Influence of Molecular Conformation on Oxidation Potential in Poly(Aryl)Amines*, *J. Mater. Chem.* **15**, 2304 (2005).
- [115] J.-S. Huh, K.-H. Kim, and J.-J. Kim, *Emitting Dipole Orientation and Molecular Orientation of Homoleptic Ir(III) Complexes*, *Org. Electron.* **82**, 105715 (2020).
- [116] H.-W. Lin, C.-L. Lin, C.-C. Wu, T.-C. Chao, and K.-T. Wong, *Influences of Molecular Orientations on Stimulated Emission Characteristics of Oligofluorene Films*, *Org. Electron.* **8**, 189 (2007).
- [117] P. Peumans, V. Bulović, and S. R. Forrest, *Efficient Photon Harvesting at High Optical Intensities in Ultrathin Organic Double-Heterostructure Photovoltaic Diodes*, *Appl. Phys. Lett.* **76**, 2650 (2000).
- [118] P. Peumans, S. Uchida, and S. R. Forrest, *Efficient Bulk Heterojunction Photovoltaic Cells Using Small-Molecular-Weight Organic Thin Films*, *Nature* **425**, 158 (2003).

- [119] J. H. Magill, *Review Spherulites: A Personal Perspective*, Journal of Materials Science **36**, 3143 (2001).
- [120] X. Cheng, Y.-Y. Noh, J. Wang, M. Tello, J. Frisch, R.-P. Blum, A. Vollmer, J. P. Rabe, N. Koch, and H. Sirringhaus, *Controlling Electron and Hole Charge Injection in Ambipolar Organic Field-Effect Transistors by Self-Assembled Monolayers*, Adv. Funct. Mater. **19**, 2407 (2009).
- [121] P. Fenter, F. Schreiber, L. Zhou, P. Eisenberger, and S. R. Forrest, *In Situ Studies of Morphology, Strain, and Growth Modes of a Molecular Organic Thin Film*, Phys. Rev. B **56**, 3046 (1997).
- [122] D. Yokoyama, A. Sakaguchi, M. Suzuki, and C. Adachi, *Horizontal Orientation of Linear-Shaped Organic Molecules Having Bulky Substituents in Neat and Doped Vacuum-Deposited Amorphous Films*, Org. Electron. **10**, 127 (2009).
- [123] Y. Watanabe, H. Sasabe, D. Yokoyama, T. Beppu, H. Katagiri, Y.-J. Pu, and J. Kido, *Simultaneous Manipulation of Intramolecular and Intermolecular Hydrogen Bonds in N-Type Organic Semiconductor Layers: Realization of Horizontal Orientation in OLEDs*, Adv. Opt. Mater. **3**, 769 (2015).
- [124] H.-F. Xiang, Z.-X. Xu, V. A. L. Roy, C.-M. Che, and P. T. Lai, *Method for Measurement of the Density of Thin Films of Small Organic Molecules*, Review of Scientific Instruments **78**, 034104 (2007).
- [125] M. Flämmich, J. Frischeisen, D. S. Setz, D. Michaelis, B. C. Krummacher, T. D. Schmidt, N. Danz, and W. Brütting, *Oriented Phosphorescent Emitters Boost OLED Efficiency*, Org. Electron. **12**, 1663 (2011).
- [126] H. Shin, J.-H. Lee, C.-K. Moon, J.-S. Huh, B. Sim, and J.-J. Kim, *Sky-Blue Phosphorescent OLEDs with 34.1% External Quantum Efficiency Using a Low Refractive Index Electron Transporting Layer*, Adv. Mater. 4920 (2016).
- [127] T. Lee, B. Caron, M. Stroet, D. M. Huang, P. L. Burn, and A. E. Mark, *The Molecular Origin of Anisotropic Emission in an Organic Light-Emitting Diode*, Nano Lett. **17**, 6464 (2017).
- [128] K.-H. Kim, J.-L. Liao, S. W. Lee, B. Sim, C.-K. Moon, G.-H. Lee, H. J. Kim, Y. Chi, and J.-J. Kim, *Crystal Organic Light-Emitting Diodes with Perfectly Oriented Non-Doped Pt-Based Emitting Layer*, Adv. Mater. **28**, 2526 (2016).
- [129] K. T. Ly, R.-W. Chen-Cheng, H.-W. Lin, Y.-J. Shiau, S.-H. Liu, P.-T. Chou, C.-S. Tsao, Y.-C. Huang, and Y. Chi, *Near-Infrared Organic Light-Emitting Diodes with Very High External Quantum Efficiency and Radiance*, Nat. Photonics **11**, 63 (2017).
- [130] T. Fleetham, Z. Wang, and J. Li, *Efficient Deep Blue Electrophosphorescent Devices Based on Platinum(II) Bis(n-Methyl-Imidazolyl)Benzene Chloride*, Org. Electron. **13**, 1430 (2012).
- [131] G. E. Norby, C.-D. Park, B. O'Brien, G. Li, L. Huang, and J. Li, *Efficient White OLEDs Employing Red, Green, and Blue Tetradentate Platinum Phosphorescent Emitters*, Org. Electron. **37**, 163 (2016).

- [132] T. B. Fleetham, L. Huang, K. Klimes, J. Brooks, and J. Li, *Tetradentate Pt(II) Complexes with 6-Membered Chelate Rings: A New Route for Stable and Efficient Blue Organic Light Emitting Diodes*, Chem. Mater. **28**, 3276 (2016).
- [133] L. H. Smith, J. a. E. Wasey, I. D. W. Samuel, and W. L. Barnes, *Light Out-Coupling Efficiencies of Organic Light-Emitting Diode Structures and the Effect of Photoluminescence Quantum Yield*, Adv. Funct. Mater. **15**, 1839 (2005).
- [134] K. S. Yook, B. D. Chin, J. Y. Lee, B. E. Lassiter, and S. R. Forrest, *Vertical Orientation of Copper Phthalocyanine in Organic Solar Cells Using a Small Molecular Weight Organic Templating Layer*, Appl. Phys. Lett. **99**, 043308 (2011).
- [135] A. D. Bochevarov, E. Harder, T. F. Hughes, J. R. Greenwood, D. A. Braden, D. M. Philipp, D. Rinaldo, M. D. Halls, J. Zhang, and R. A. Friesner, *Jaguar: A High-Performance Quantum Chemistry Software Program with Strengths in Life and Materials Sciences*, Int. J. Quantum Chem. **113**, 2110 (2013).
- [136] E. van Lenthe, E. J. Baerends, and J. G. Snijders, *Relativistic Regular Two-component Hamiltonians*, J. Chem. Phys. **99**, 4597 (1993).
- [137] M. J. Frisch, G. W. Trucks, J. R. Cheeseman, G. Scalmani, M. Caricato, H. P. Hratchian, X. Li, V. Barone, J. Bloino, G. Zheng, T. Vreven, J. A. Montgomery, G. A. Petersson, G. E. Scuseria, H. B. Schlegel, H. Nakatsuji, A. F. Izmaylov, R. L. Martin, J. L. Sonnenberg, J. E. Peralta, J. J. Heyd, E. Brothers, F. Ogliaro, M. Bearpark, M. A. Robb, B. Mennucci, K. N. Kudin, V. N. Staroverov, R. Kobayashi, J. Normand, A. Rendell, R. Gomperts, V. G. Zakrzewski, M. Hada, M. Ehara, K. Toyota, R. Fukuda, J. Hasegawa, M. Ishida, T. Nakajima, Y. Honda, O. Kitao, and H. Nakai, *Gaussian 09* (2016).
- [138] Y. Chi and P.-T. Chou, *Transition-Metal Phosphors with Cyclometalating Ligands: Fundamentals and Applications*, Chem. Soc. Rev. **39**, 638 (2010).
- [139] K. Xiao, W. Deng, J. K. Keum, M. Yoon, I. V. Vlassiuk, K. W. Clark, A.-P. Li, I. I. Kravchenko, G. Gu, E. A. Payzant, B. G. Sumpter, S. C. Smith, J. F. Browning, and D. B. Geohegan, *Surface-Induced Orientation Control of CuPc Molecules for the Epitaxial Growth of Highly Ordered Organic Crystals on Graphene*, J. Am. Chem. Soc. **135**, 3680 (2013).
- [140] V. R. Gangilenka, L. V. Titova, L. M. Smith, H. P. Wagner, L. A. A. DeSilva, L. Gisslén, and R. Scholz, *Selective Excitation of Exciton Transitions in PTCDA Crystals and Films*, Phys. Rev. B **81**, 155208 (2010).
- [141] A. L. Patterson, *The Scherrer Formula for X-Ray Particle Size Determination*, Phys. Rev. **56**, 978 (1939).
- [142] M.-H. Tsai, H.-W. Lin, H.-C. Su, T.-H. Ke, C. -c. Wu, F.-C. Fang, Y.-L. Liao, K.-T. Wong, and C.-I. Wu, *Highly Efficient Organic Blue Electrophosphorescent Devices Based on 3,6-Bis(Triphenylsilyl)Carbazole as the Host Material*, Adv. Mater. **18**, 1216 (2006).
- [143] M. A. Loi, E. da Como, F. Dinelli, M. Murgia, R. Zamboni, F. Biscarini, and M. Muccini, *Supramolecular Organization in Ultra-Thin Films of α -Sexithiophene on Silicon Dioxide*, Nat. Mater. **4**, 81 (2005).

- [144] E. R. Vorpagel and J. G. Lavin, *Most Stable Configurations of Polynuclear Aromatic Hydrocarbon Molecules in Pitches via Molecular Modelling*, *Carbon* **30**, 1033 (1992).
- [145] K. Hanson, L. Roskop, P. I. Djurovich, F. Zahariev, M. S. Gordon, and M. E. Thompson, *A Paradigm for Blue- or Red-Shifted Absorption of Small Molecules Depending on the Site of π -Extension*, *J. Am. Chem. Soc.* **132**, 16247 (2010).
- [146] T. Sajoto, P. I. Djurovich, A. Tamayo, M. Yousufuddin, R. Bau, M. E. Thompson, R. J. Holmes, and S. R. Forrest, *Blue and Near-UV Phosphorescence from Iridium Complexes with Cyclometalated Pyrazolyl or N-Heterocyclic Carbene Ligands*, *Inorg. Chem.* **44**, 7992 (2005).
- [147] C. A. Hunter, K. R. Lawson, J. Perkins, and C. J. Urch, *Aromatic Interactions*, *J. Chem. Soc., Perkin Trans. 2* 651 (2001).
- [148] E. J. Mittemeijer and P. Scardi, *Diffraction Analysis of the Microstructure of Materials* (2010).
- [149] L. R. Milgrom, R. N. Sheppard, A. M. Z. Slawin, and D. J. Williams, *X-Ray Crystal Structure of 2,3,7,8,12,13,17,18-Octaethylporphyrinatoplatinum(II) (PtOEP): Potential for Correlation of Meso-Carbon Bond-Angle ($\hat{C}m$) With One-Bond $^{13}C_{meso}$ \rightarrow $^1H_{methine}$ Coupling Constant in Some Diamagnetic Metal Complexes of OEP*, *Polyhedron* **7**, 57 (1988).
- [150] A. Castellanos-Gomez, *Why All the Fuss about 2D Semiconductors?*, *Nat. Photonics* **10**, 202 (2016).
- [151] M. Amani, R. A. Burke, X. Ji, P. Zhao, D.-H. Lien, P. Taheri, G. H. Ahn, D. Kirya, J. W. Ager, E. Yablonovitch, J. Kong, M. Dubey, and A. Javey, *High Luminescence Efficiency in MoS_2 Grown by Chemical Vapor Deposition*, *ACS Nano* **10**, 6535 (2016).
- [152] H. Kim, D.-H. Lien, M. Amani, J. W. Ager, and A. Javey, *Highly Stable Near-Unity Photoluminescence Yield in Monolayer MoS_2 by Fluoropolymer Encapsulation and Superacid Treatment*, *ACS Nano* **11**, 5179 (2017).
- [153] M. Palummo, M. Bernardi, and J. C. Grossman, *Exciton Radiative Lifetimes in Two-Dimensional Transition Metal Dichalcogenides*, *Nano Lett.* **15**, 2794 (2015).
- [154] K. S. Novoselov, A. Mishchenko, A. Carvalho, and A. H. C. Neto, *2D Materials and van Der Waals Heterostructures*, *Science* **353**, (2016).
- [155] J. Wang, I. Verzhbitskiy, and G. Eda, *Electroluminescent Devices Based on 2D Semiconducting Transition Metal Dichalcogenides*, *Adv. Mater.* **30**, 1802687 (2018).
- [156] X. Zhou, X. Hu, J. Yu, S. Liu, Z. Shu, Q. Zhang, H. Li, Y. Ma, H. Xu, and T. Zhai, *2D Layered Material-Based van Der Waals Heterostructures for Optoelectronics*, *Adv. Funct. Mater.* **28**, 1706587 (2018).
- [157] C. Wang, F. Yang, and Y. Gao, *The Highly-Efficient Light-Emitting Diodes Based on Transition Metal Dichalcogenides: From Architecture to Performance*, *Nanoscale Advances* **2**, 4323 (2020).

- [158] B. W. H. Baugher, H. O. H. Churchill, Y. Yang, and P. Jarillo-Herrero, *Optoelectronic Devices Based on Electrically Tunable p - n Diodes in a Monolayer Dichalcogenide*, Nat. Nanotechnol. **9**, 262 (2014).
- [159] Y. J. Zhang, T. Oka, R. Suzuki, J. T. Ye, and Y. Iwasa, *Electrically Switchable Chiral Light-Emitting Transistor*, Science **344**, 725 (2014).
- [160] F. Withers, O. Del Pozo-Zamudio, S. Schwarz, S. Dufferwiel, P. M. Walker, T. Godde, A. P. Rooney, A. Gholinia, C. R. Woods, P. Blake, S. J. Haigh, K. Watanabe, T. Taniguchi, I. L. Aleiner, A. K. Geim, V. I. Fal'ko, A. I. Tartakovskii, and K. S. Novoselov, *WSe₂ Light-Emitting Tunneling Transistors with Enhanced Brightness at Room Temperature*, Nano Lett. **15**, 8223 (2015).
- [161] W. Yang, J. Shang, J. Wang, X. Shen, B. Cao, N. Peimyoo, C. Zou, Y. Chen, Y. Wang, C. Cong, W. Huang, and T. Yu, *Electrically Tunable Valley-Light Emitting Diode (VLED) Based on CVD-Grown Monolayer WS₂*, Nano Lett. **16**, 1560 (2016).
- [162] J. Gu, B. Chakraborty, M. Khatoniar, and V. M. Menon, *A Room-Temperature Polariton Light-Emitting Diode Based on Monolayer WS₂*, Nat. Nanotechnol. **14**, 11 (2019).
- [163] J. Pak, I. Lee, K. Cho, J.-K. Kim, H. Jeong, W.-T. Hwang, G. H. Ahn, K. Kang, W. J. Yu, A. Javey, S. Chung, and T. Lee, *Intrinsic Optoelectronic Characteristics of MoS₂ Phototransistors via a Fully Transparent van Der Waals Heterostructure*, ACS Nano **13**, 9638 (2019).
- [164] F. Withers, O. Del Pozo-Zamudio, A. Mishchenko, A. P. Rooney, A. Gholinia, K. Watanabe, T. Taniguchi, S. J. Haigh, A. K. Geim, A. I. Tartakovskii, and K. S. Novoselov, *Light-Emitting Diodes by Band-Structure Engineering in van Der Waals Heterostructures*, Nat. Mater. **14**, 301 (2015).
- [165] D. Andrzejewski, H. Myja, M. Heuken, A. Grundmann, H. Kalisch, A. Vescan, T. Kümmell, and G. Bacher, *Scalable Large-Area p - i - n Light-Emitting Diodes Based on WS₂ Monolayers Grown via MOCVD*, ACS Photonics **6**, 1832 (2019).
- [166] D. Andrzejewski, R. Oliver, Y. Beckmann, A. Grundmann, M. Heuken, H. Kalisch, A. Vescan, T. Kümmell, and G. Bacher, *Flexible Large-Area Light-Emitting Devices Based on WS₂ Monolayers*, Adv. Opt. Mater. **8**, 2000694 (2020).
- [167] N. C. Giebink, B. W. D'Andrade, M. S. Weaver, J. J. Brown, and S. R. Forrest, *Direct Evidence for Degradation of Polaron Excited States in Organic Light Emitting Diodes*, J. Appl. Phys. **105**, 124514 (2009).
- [168] Q. Wang and H. Aziz, *Degradation of Organic/Organic Interfaces in Organic Light-Emitting Devices Due to Polaron-Exciton Interactions*, ACS Appl. Mater. Interfaces **5**, 8733 (2013).
- [169] M. Amani, D.-H. Lien, D. Kiriya, J. Xiao, A. Azcatl, J. Noh, S. R. Madhvapathy, R. Addou, S. Kc, M. Dubey, K. Cho, R. M. Wallace, S.-C. Lee, J.-H. He, J. W. Ager, X. Zhang, E. Yablonovitch, and A. Javey, *Near-Unity Photoluminescence Quantum Yield in MoS₂*, Science **350**, 1065 (2015).
- [170] C. Coburn, J. Lee, and S. R. Forrest, *Charge Balance and Exciton Confinement in Phosphorescent Organic Light Emitting Diodes*, Adv. Opt. Mater. **4**, 889 (2016).

- [171] K. F. Mak, K. He, C. Lee, G. H. Lee, J. Hone, T. F. Heinz, and J. Shan, *Tightly Bound Trions in Monolayer MoS₂*, Nat. Mater. **12**, 207 (2013).
- [172] J. S. Ross, S. Wu, H. Yu, N. J. Ghimire, A. M. Jones, G. Aivazian, J. Yan, D. G. Mandrus, D. Xiao, W. Yao, and X. Xu, *Electrical Control of Neutral and Charged Excitons in a Monolayer Semiconductor*, Nat. Commun. **4**, 1474 (2013).
- [173] T. C. Berkelbach, M. S. Hybertsen, and D. R. Reichman, *Theory of Neutral and Charged Excitons in Monolayer Transition Metal Dichalcogenides*, Phys. Rev. B **88**, 045318 (2013).
- [174] J. Kang, S. Tongay, J. Zhou, J. Li, and J. Wu, *Band Offsets and Heterostructures of Two-Dimensional Semiconductors*, Appl. Phys. Lett. **102**, 012111 (2013).
- [175] Q. Wang, B. Sun, and H. Aziz, *Exciton–Polaron-Induced Aggregation of Wide-Bandgap Materials and Its Implication on the Electroluminescence Stability of Phosphorescent Organic Light-Emitting Devices*, Adv. Funct. Mater. **24**, 2975 (2014).
- [176] A. Gurarslan, Y. Yu, L. Su, Y. Yu, F. Suarez, S. Yao, Y. Zhu, M. Ozturk, Y. Zhang, and L. Cao, *Surface-Energy-Assisted Perfect Transfer of Centimeter-Scale Monolayer and Few-Layer MoS₂ Films onto Arbitrary Substrates*, ACS Nano **8**, 11522 (2014).
- [177] G. Plechinger, P. Nagler, J. Kraus, N. Paradiso, C. Strunk, C. Schüller, and T. Korn, *Identification of Excitons, Trions and Biexcitons in Single-Layer WS₂*, Physica Status Solidi RRL **9**, 457 (2015).
- [178] H. Lu, A. Kummel, and J. Robertson, *Passivating the Sulfur Vacancy in Monolayer MoS₂*, APL Mater. **6**, 066104 (2018).
- [179] H. Zeng, G.-B. Liu, J. Dai, Y. Yan, B. Zhu, R. He, L. Xie, S. Xu, X. Chen, W. Yao, and X. Cui, *Optical Signature of Symmetry Variations and Spin-Valley Coupling in Atomically Thin Tungsten Dichalcogenides*, Sci. Rep. **3**, 1 (2013).
- [180] S. Mouri, Y. Miyauchi, and K. Matsuda, *Tunable Photoluminescence of Monolayer MoS₂ via Chemical Doping*, Nano Lett. **13**, 5944 (2013).
- [181] J. Siviniant, D. Scalbert, A. V. Kavokin, D. Coquillat, and J.-P. Lascaray, *Chemical Equilibrium between Excitons, Electrons, and Negatively Charged Excitons in Semiconductor Quantum Wells*, Phys. Rev. B **59**, 1602 (1999).
- [182] N. Peimyoo, W. Yang, J. Shang, X. Shen, Y. Wang, and T. Yu, *Chemically Driven Tunable Light Emission of Charged and Neutral Excitons in Monolayer WS₂*, ACS Nano **8**, 11320 (2014).
- [183] C. W. Tang and S. A. VanSlyke, *Organic Electroluminescent Diodes*, Appl. Phys. Lett. **51**, 913 (1987).
- [184] M. A. Baldo, S. Lamansky, P. E. Burrows, M. E. Thompson, and S. R. Forrest, *Very High-Efficiency Green Organic Light-Emitting Devices Based on Electrophosphorescence*, Appl. Phys. Lett. **75**, 4 (1999).
- [185] K. M. Lee, R. Fardel, L. Zhao, C. B. Arnold, and B. P. Rand, *Enhanced Outcoupling in Flexible Organic Light-Emitting Diodes on Scattering Polyimide Substrates*, Org. Electron. **51**, 471 (2017).

- [186] Y. Sun and S. R. Forrest, *Enhanced Light Out-Coupling of Organic Light-Emitting Devices Using Embedded Low-Index Grids*, Nat. Photonics **2**, 483 (2008).
- [187] Y. Qu, M. Sloatsky, and S. R. Forrest, *Enhanced Light Extraction from Organic Light-Emitting Devices Using a Sub-Anode Grid*, Nat. Photonics **9**, 758 (2015).
- [188] W. H. Koo, S. M. Jeong, F. Araoka, K. Ishikawa, S. Nishimura, T. Toyooka, and H. Takezoe, *Light Extraction from Organic Light-Emitting Diodes Enhanced by Spontaneously Formed Buckles*, Nat. Photonics **4**, 222 (2010).
- [189] L. Zhou, Q.-D. Ou, J.-D. Chen, S. Shen, J.-X. Tang, Y.-Q. Li, and S.-T. Lee, *Light Manipulation for Organic Optoelectronics Using Bio-Inspired Moth's Eye Nanostructures*, Sci. Rep. **4**, (2014).
- [190] T. Bocksrocker, J. B. Preinfalk, J. Asche-Tauscher, A. Pargner, C. Eschenbaum, F. Maier-Flaig, and U. Lemme, *White Organic Light Emitting Diodes with Enhanced Internal and External Outcoupling for Ultra-Efficient Light Extraction and Lambertian Emission*, Opt. Express **20**, A932 (2012).
- [191] H.-W. Chang, J. Lee, S. Hofmann, Y. Hyun Kim, L. Müller-Meskamp, B. Lüssem, C.-C. Wu, K. Leo, and M. C. Gather, *Nano-Particle Based Scattering Layers for Optical Efficiency Enhancement of Organic Light-Emitting Diodes and Organic Solar Cells*, J. Appl. Phys. **113**, 204502 (2013).
- [192] J. Lee, T.-H. Han, M.-H. Park, D. Y. Jung, J. Seo, H.-K. Seo, H. Cho, E. Kim, J. Chung, S.-Y. Choi, T.-S. Kim, T.-W. Lee, and S. Yoo, *Synergetic Electrode Architecture for Efficient Graphene-Based Flexible Organic Light-Emitting Diodes*, Nat. Commun. **7**, 11791 (2016).
- [193] Y. Qu, C. Coburn, D. Fan, and S. R. Forrest, *Elimination of Plasmon Losses and Enhanced Light Extraction of Top-Emitting Organic Light-Emitting Devices Using a Reflective Subelectrode Grid*, ACS Photonics **4**, 363 (2017).
- [194] P. A. Hobson, S. Wedge, J. A. E. Wasey, I. Sage, and W. L. Barnes, *Surface Plasmon Mediated Emission from Organic Light-Emitting Diodes*, Adv. Mater. **14**, 1393 (2002).
- [195] M. Sloatsky and S. R. Forrest, *Enhancing Waveguided Light Extraction in Organic LEDs Using an Ultra-Low-Index Grid*, Opt. Lett. **35**, 1052 (2010).
- [196] Y. Qu, J. Kim, C. Coburn, and S. R. Forrest, *Efficient, Nonintrusive Outcoupling in Organic Light Emitting Devices Using Embedded Microlens Arrays*, ACS Photonics **5**, 2453 (2018).
- [197] S. Mladenovski, K. Neyts, D. Pavicic, A. Werner, and C. Rothe, *Exceptionally Efficient Organic Light Emitting Devices Using High Refractive Index Substrates*, Opt. Express **17**, 7562 (2009).
- [198] S. Jeon, S. Lee, K.-H. Han, H. Shin, K.-H. Kim, J.-H. Jeong, and J.-J. Kim, *High-Quality White OLEDs with Comparable Efficiencies to LEDs*, Adv. Opt. Mater. **6**, 1701349 (2018).
- [199] Z. Tang, A. Elfving, J. Bergqvist, W. Tress, and O. Inganäs, *Light Trapping with Dielectric Scatterers in Single- and Tandem-Junction Organic Solar Cells*, Adv. Energy Mater. **3**, 1606 (2013).

- [200] J. B. Kim, P. Kim, N. C. Pégard, S. J. Oh, C. R. Kagan, J. W. Fleischer, H. A. Stone, and Y.-L. Loo, *Wrinkles and Deep Folds as Photonic Structures in Photovoltaics*, Nat. Photonics **6**, 327 (2012).
- [201] Q. Ou, L. Zhou, Y. Li, S. Shen, Chen Jing-De, Li Chi, Wang Qian-Kun, S. Lee, and J. Tang, *Extremely Efficient White Organic Light-Emitting Diodes for General Lighting*, Adv. Funct. Mater. **24**, 7249 (2014).
- [202] S. Wedge, A. Giannattasio, and W. L. Barnes, *Surface Plasmon–Polariton Mediated Emission of Light from Top-Emitting Organic Light-Emitting Diode Type Structures*, Org. Electron. **8**, 136 (2007).
- [203] Y.-G. Bi, J. Feng, Y.-S. Liu, Y.-F. Li, Y. Chen, X.-L. Zhang, X.-C. Han, and H.-B. Sun, *Surface Plasmon-Polariton Mediated Red Emission from Organic Light-Emitting Devices Based on Metallic Electrodes Integrated with Dual-Periodic Corrugation*, Sci. Rep. **4**, 7108 (2014).
- [204] Z. B. Wang, M. G. Helander, J. Qiu, D. P. Puzzo, M. T. Greiner, Z. M. Hudson, S. Wang, Z. W. Liu, and Z. H. Lu, *Unlocking the Full Potential of Organic Light-Emitting Diodes on Flexible Plastic*, Nat. Photonics **5**, 753 (2011).
- [205] S. Hofmann, M. Thomschke, B. Lüssem, and K. Leo, *Top-Emitting Organic Light-Emitting Diodes*, Opt. Express **19**, A1250 (2011).
- [206] R. Meerheim, M. Furno, S. Hofmann, B. Lüssem, and K. Leo, *Quantification of Energy Loss Mechanisms in Organic Light-Emitting Diodes*, Appl. Phys. Lett. **97**, 253305 (2010).
- [207] B. van Ginneken, M. Stavridi, and J. J. Koenderink, *Diffuse and Specular Reflectance from Rough Surfaces*, Appl. Opt. **37**, 130 (1998).